LA-7755-PR
Progress Report

UC-21
Issued: November 1980

Inertial Fusion Program

July 1—December 31, 1978

Roger B. Perkins and the
Laser Fusion Program Staff

Compiled by
Frederick Skoberne

Dr. 2233

CONTENTS

INERTIAL FUSION PROGRAM
July 1—December 31, 1978

by

Roger B. Perkins and the
Laser Fusion Program Staff

ABSTRACT

Progress at Los Alamos Scientific Laboratory (LASL) in the development of high-energy short-pulse CO_2 laser systems for fusion research is reported. Improvements to LASL's two-beam system, Gemini, are outlined and experimental results are discussed. Our eight-beam system, Helios, was fired successfully on target for the first time, and became the world's most powerful gas laser for laser fusion studies. Work on Antares, our 100- to 200-TW target irradiation system, is summarized, indicating that design work and building construction are 70 and 48% complete, respectively. A baseline design for automatic centering of laser beams onto the various relay mirrors and the optical design of the Antares front end are discussed.

Optical phase conjugation as a means of automatic target alignment is summarized, and we report on work with SF_6-based gas isolators containing H_2, which may lead to almost total recovery of isolator absorption in a few tens of nanoseconds. In experiments with exploding-pusher targets, neutron yields exceeding 10^8 were obtained for the first time with CO_2 radiation. Progress in the development of x-ray diagnostics is outlined, including the fast high-voltage triggering of our x-ray streak camera. Ultraviolet spectroscopy of highly ionized beams yielded results that had not been observed previously. Multiburst simulation and opacity experiments, part of our modest military applications effort, are described. Improvements in calculational techniques, and results of studies on optical loading of targets and their energy absorption by shifted laser foci are presented. Significant problems in the fabrication of laser fusion targets culminating in the successful manufacture of the 20-times-liquid-density target are outlined, and the development of a heat-transfer code that calculates the nonuniformity of DT ice layers on opaque inner target shells is discussed.

The results of various fusion reactor studies are summarized, as well as investigations of synthetic-fuel production through application of fusion energy to hydrogen production by thermochemical water splitting. Studies on increased efficiency of energy extraction in CO_2 lasers and on lifetimes of cryogenic pellets in a reactor environment are summarized, as well as the results of studies on pellet injection, tracking, and beam synchronization.

SUMMARY

(R. B. Perkins and Laser Fusion Staff)

The Laser Fusion Program at the Los Alamos Scientific Laboratory (LASL) is pursuing the dual goal of developing inertial confinement fusion for commercial and military applications. It is essential for both goals to achieve scientific breakeven; that is, a fusion energy output that equals the laser energy incident on the target. For this purpose, we invented, and are developing, high-power short-pulse carbon-dioxide gas lasers that will provide the efficiency and repetition-rate capability required for use in commercial power plants. As our gas laser systems become available, they are used intensively in a vigorous experimental program aimed at achieving thermonuclear burn of fuel pellets. This goal requires that we perform basic physics experiments to provide an understanding of the processes involved, and integral pellet burning experiments, which we expect to achieve breakeven by the mid-1980s. In our experimental program, we are expending significant effort in target design, target fabrication, laser facility support, and diagnostics development. In addition, a modest experimental effort directed toward military applications is under way. Last, a systems group is exploring design concepts for future commercial fusion and fusion-fission hybrid reactor systems and subsystems to identify potential problems.

CO_2 LASER PROGRAM

Gemini

The Two-Beam Laser System, Gemini, was devoted primarily to target experimentation and, to a small degree, to system characterization. During the past six months, 170 target shots were fired, 73% of which produced the desired energy on target with no measurable prelasing. Some experiments were delayed because of problems with the pumping-chamber pulsers. The following salient features characterized the Gemini operations during the past six months.

- Encircled energy of the focal spot was measured.
- The internal saturable-absorber gas cell was received.
- A single-target insertion mechanism was designed.
- A new oscillator-preamplifier system was designed to replace the existing front end.

Helios

In late July, we entered a new era in the laser fusion program when the Helios laser system was fired successfully on target for the first time. Although the initial energy on target was limited to only 1.6 kJ because of a target-amplifier parasitic mode, investigations into the nature of this mode enabled us to develop a means to increase the on-target energy to the 6-kJ level. At these levels the Helios laser facility now ranks among the world's most powerful laser systems, and is the world's most powerful gas laser. Because the carbon dioxide laser is considered by most people the most promising candidate for a laser-fusion-driven reactor, our recent Helios results will play a significant, if not critical, role in determining the direction of this country's overall laser fusion program. The results are preliminary, but experimental evidence of the first high-density core compressions has generated a good deal of excitement throughout the laser fusion community.

Antares

Substantial progress was made in all areas of the Antares project. Raising the prestressed concrete walls of the larger buildings that will house Antares and the target systems was the most obvious undertaking. All long-lead-time Antares laser components were released to vendors for fabrication in preparation for the start of installation in August 1979.

A baseline design for automatic centering of the laser beams on the power-amplifier and target-system relay mirrors was completed. We subsequently prepared variations on the baseline system and an alternative concept to allow an assessment of the impact on cost and performance.

The suggestion to sample the full system of the output with wire transmission gratings was accepted after tests of the gratings on Gemini. The gratings were fabricated in-house on a winding machine designed to produce wire spark and drift chambers.

The optical design of the Antares front end was completed. Preamplifiers were ordered and delivered, and one of the required six driver amplifiers was ordered for evaluation. A prototype of the Antares front end was

assembled in the old Single-Beam System area. Evaluation and development of multiline oscillators and multipass amplifier geometries were planned for the prototype.

We reactivated the power-amplifier prototype to evaluate modifications in the Antares power-amplifier design that were a result of the prototype program. Reliability and control of the gridded cold-cathode gun were improved. Stands, pressure vessels, and gun parts—all long-lead-time items—for the power-amplifier proper were promised for delivery in mid-1979.

A firm, fixed-price contract for the engineering design and fabrication of the Antares energy storage system was awarded. All prospective vendors were willing to quote on a fixed-price basis because a prototype unit had been designed and tested by LASL. This prototype Marx unit met the specified inductance requirements as well as the basic voltage and energy requirements. In addition, we developed a spark gap that transfers the charge and current anticipated under fault conditions without failure.

A design-construct contract for the Antares target-chamber and vacuum system was also awarded. A unique feature of this 1300-m^3 system was the requirement that the pumping units be cryogenic pods. The contractor was to proceed with the procurement of long-lead-time items before final design review.

A tree-structured hierarchical architecture was defined for the controls system. Detailed specifications for the control computers and the communications networks were released for competitive quotations.

Because construction was three months behind schedule, the Department of Energy negotiated with the Contractor to obtain beneficial occupancy of the Laser Hall by mid-July 1979.

CO_2 LASER TECHNOLOGY

Optical phase conjugation continues to promise improved beam quality and, possibly, automatic target alignment in laser fusion systems. The use of longer germanium samples permitted us to increase the observed efficiency of phase-conjugate wave generation from 2 to 20%. Also, conjugation in inverted CO_2 was seen for the first time. In a hybrid arrangement where the CO_2 medium helped to amplify the conjugated wave, efficiencies as high as 250% were measured without loss of wave quality; the conjugated signal was stronger than the original aberrated signal

In related work designed to identify upper limits to improving phase-conjugation efficiency in germanium by using higher 10-μm intensities, we found that dense, bulk plasma forms in intrinsic and in optical-grade germanium above 200 MW/cm^2 with associated free-carrier densities as high as $2 \times 10^{15}/cm^3$ without permanent material damage. However, p-type germanium did not show these effects, renewing our interest in doped germanium for conjugation.

In the gas-isolator development area, absorption recovery was studied to better understand the potential impact of these systems on the retropulse problem. We found that the recovery rate of the SF_6-based mixtures depends only weakly on the saturating wavelength, and slows with increasing optical fluence. However, by adding H_2 to the isolator mixture, the absorption at some wavelengths recovered up to four times faster than previously. The goal is to obtain almost total recovery of isolator absorption in a few tens of nanoseconds.

Work on the reinjection laser prototype culminated in demonstration of reliable operation at pressures up to 7600 torr. Results of a full characterization are reported, including an operation reliability level of 99.95 during a 4000-shot sequence. This laser uses multiple passes to generate energetic, subnanosecond pulses, and will be used in the upgraded Gigawatt Test Facility (GWTF) system.

A prototype of the GWTF was also characterized, revealing some discrepancies between predicted and observed propagation of subnanosecond multiline pulses. Although predicted and observed extracted energies agreed well in these tests for 1.0- and 0.5-ns final-amplifier-input-pulse durations, the amplified pulse was substantially broader than expected in the latter case.

Investigations begun this period include the first direct measurement of the nonlinear 10-μm refractive index (n_2) in germanium via ellipse rotation and determination of an upper limit to n_2 in NaCl.

EXPERIMENTS, DIAGNOSTICS, AND MILITARY APPLICATIONS

Experiments

The Helios laser has delivered previously unattainable CO_2 laser power and energy to various targets. Exploding-pusher targets served as a test of the new facility. Neutron yields exceeding 10^8 were obtained for the first time using CO_2 radiation. Plastic-coated glass

microballoon (GMB) targets designed to achieve high fuel density were used in experiments aimed at targets that are direct predecessors to fusion reactor targets. These targets yielded sufficient neutrons for meaningful parametric studies. High-density targets are difficult to diagnose, but initial experiments are providing information consistent with our code calculations, which intensifies our diagnostic development efforts. The measured speed of the fastest plasma protons at Helios gave further support to the expressions for hot-electron temperature scaling, $(I\lambda^2)^{1/3}$, where I is the ratio of focal power vs unit area and λ is the laser wavelength.

Diagnostics Development

The laser fusion program depends on our ability to provide the instruments required. This is increasingly true with large complex laser facilities and complex targets.

During this reporting period, researchers tried to improve the time resolution of neutron detectors so as to more clearly separate the effects of ion temperature, burn time, and run-in time on neutron spectra.

We have continued our vigorous program of x-ray diagnostics development. Advances during the past 6 months clarified the triggering problems that have plagued our x-ray streak camera work. We continued fast high-voltage switching and triggering studies, which should be useful for various diagnostics. Optical telephotography with high resolution is evolving toward the use of precisely timed optical probe beams.

Military Applications

Many feasibility studies were performed and a considerable amount of data was collected during the past two years using the two-beam glass laser.

The work on vacuum uv spectroscopy of highly ionized metals has been concluded successfully, and we obtained good, usable spectra of 22 metals. Many of the results had never before been observed.

By contrast, the GEAR x-ray streak camera continued to have triggering problems in its internal circuitry, and no satisfactory data have been obtained.

Our equation-of-state (EOS) studies continue along two distinct lines: impedance matching and shockwave structure. We are using a fast, visible-light streak camera to observe the shock front emerging from the rear of multistep targets. Because the EOS is known for the substrate, it can be deduced for the other layers. Work to date has confirmed the feasibility of this technique.

The work on multiburst simulation and blast waves used two-wavelength, visible-light holographic interferometry to observe one- and two-dimensional shocks in air at various pressures. Experimental results to date do not agree completely with calculations; i.e., gas densities are in approximate agreement but electron densities are not.

In the opacity experiments, we made progress in observing optical self-emission from the back of aluminum foil targets simultaneously along a 30° and a normal line of light. Analysis indicates a time-dependent anisotropy in this emission.

THEORETICAL SUPPORT AND DIRECTION

The final report of the DOE Ad Hoc Experts' Group on Fusion (chaired by J. S. Foster) was issued in June 1978. One recommendation was that DOE establish a full-spectrum design and theory effort at LASL to cover the range of possible ICF (Inertial Confinement Fusion) drivers, rather than CO_2 lasers only. We have presented detailed plans to the DOE Office of Laser Fusion, and anticipate that our effort will increase in that direction in both depth and scope over the next year.

Significant work was performed in the four sections of our theoretical group. Our unclassified target-design effort concentrated on the two Helios experiments: the 20-Times-Liquid-Density Milestone experiment, also discussed in preceding reports, and the Exploding-Pusher designs reported herein. An important achievement in our code development effort was the preparation of an off-axis ray-trace procedure, which modifies previous treatment that caused us to *overemphasize* the nonspherical optical loading and to overcorrect our two-dimensional designs. Our laser physics work shows improved calculations of the small-signal gain coefficient in CO_2 lasers.

Our theoretical target design studies produced results on the optical loading and absorption by shifted laser foci and on an extension of the suprathermal electron scaling law; progress was also made in understanding the coherent acceleration of hot electrons and their subsequent transport in the plasma. Finally, we present corrected calculations on the loss of fast ions from the tails of the fuel-ion distribution in low-ρR pellets.

LASER FUSION TARGET FABRICATION

General

Our ability to fabricate targets for laser fusion experiments has increased in several areas, culminating in the successful manufacture of the 20-times-liquid-density (20XLD) target. In meeting this goal, we improved our plastic-coating techniques and can now apply plastic (CH) coatings up to 350 μm thick with a peak-to-valley surface smoothness better than 1 μm to stalk-mounted GMBs. In addition, we were able to remove the coated stalk, leaving an imperfection of only ~ 1 μm in smoothness and uniformity at the stalk location. Also, we can coat about 100 unmounted, quality-selected GMBs with up to 15 μm of very-smooth-surfaced plastic and recover essentially all the coated shells. Metal coatings of gold and molybdenum up to 5 μm thick were applied to levitated GMBs by sputtering. Both uniformity and surface smoothness are adequate for our 20XLD target.

In cryogenics, we developed a heat-transfer computer code that calculates the nonuniformity of the DT ice layer in a target frozen by the fast-isothermal-freezing (FIF) technique. We are applying this code to targets with opaque inner shells in which the DT layer cannot be measured directly.

Target Assembly Progress

We supplied more than 1000 targets to our three operating laser systems and made more than 100 parts for diagnostic devices. About 320 targets were fabricated for Main-Sequence experiments. Another 340 were supplied for a wide variety of Target-Essentials and Support Physics experiments, and over 400 were made for military applications experiments. We completed the development of fabrication techniques for 20XLD targets to be tested on Helios.

During development of the 20XLD target, we developed a micromachining technique to remove the coated stalk from the plastic-coated GMB and to remount the resulting spherical target. To fill these high-aspect-ratio glass shells with 30 atm of DT fuel gas, we measured the GMB crush strength and optimized our pressure-staging procedures.

Metal Coatings Development

In preparation for fabricating the Rigel-B target (20XLD with a metal pusher layer) we developed techniques to coat small numbers of quality-selected GMBs with metal layers. We applied coatings up to 5 μm thick of sputtered gold and molybdenum to GMBs levitated by our gas-jet levitator. The surface smoothness of these coatings is better than 1 μm peak-to-valley.

To improve the quality of all-metal pushers, we are trying to make free-standing, high-quality metal shells by metal-coating a removable spherical mandrel. Spheres of polymethyl methacrylate (PMMA) made by our droplet generator technique were overcoated with ~2 μm of CVD nickel and leached in solvent. Although some of the resulting hollow shells were of high quality, some crumpled without the mandrel support.

Plastic-Coatings Development

We finally discovered how to plastic-coat a few preselected GMBs by low-pressure plasma polymerization without losing them or fusing them to the coater in the process. Up to 15 μm of poly p-xylene was applied to as few as 8 GMBs, with 100% recovery and extremely smooth surfaces. For the thicker coatings needed for the 20XLD target, we applied poly p-xylylene by the vapor-phase pyrolysis technique in coatings up to 350 μm thick. Surface smoothness was improved by lowering the deposition rate, applying a 20-nm-thick passivating layer of aluminum to the GMB before coating, or by adding a comonomer during deposition. Surfaces with $< \pm 0.2$-μm peak-to-valley variation are achieveable.

All experiments to produce small-cell-size, low-density plastic foam failed to achieve one of these requirements. We are, therefore, reassessing foam fabrication methods and investigating alternative buffer materials.

Organometallic Coatings Development

Because we cannot measure the uniformity of a DT ice layer inside a metal pusher shell, we developed a heat-transfer computer code to calculate the freezing rate and DT shell nonuniformity for complex, multilayer, multishell targets. Calculated nonuniformities for glass

shell targets were in good agreement with experimental data, and we are trying to compare calculated and experimental data for different configurations of glass shells.

Work on the cryogenic-target freezing apparatus for Helios is under way. The present retraction speed of the heat shield is 3 cm in 6.8 ms, which is probably fast enough, but more work is needed on the shock absorber system that stops the retracting shroud.

APPLICATIONS OF LASER FUSION SYSTEMS STUDIES

In our reactor design studies we programmed the mathematical description of the new plasma model representing the magnetically protected reactor cavity for use on the CRAY computer. We also investigated methods of removing the significant amount of fuel-pellet microexplosion energy by means of magnetic fields in a magnetohydrodynamic (MHD) energy converter that decelerates the ions without suffering excessive wall erosion and even generates electric energy in the process. The concept of absorbing the neutron energy at high temperature in a blanket of boiling lithium-containing metal was studied further and led to conceptual solutions to the production of high-temperature process heat for more efficient energy conversion.

Our studies of proliferation-resistant fuel cycles, based on laser-driven ICF reactor technology, focused on quasisymbiotic concepts that maximize fissile-fuel production and minimize heat production.

Hydrogen production studies continued. They are coordinated with a parallel study, supported by the Office of Fusion Energy, of thermochemical hydrogen production. As part of this effort, we are also engaged in process design of a bismuth-oxide electrothermochemical cycle.

Finally, in engineering development studies that attest to the impact of advanced technologies on long-life, high-repetition-rate ICF systems, we investigated means of increasing the efficiency of energy extraction in CO_2 lasers and calculated the lifetime of cryogenic pellets in a reactor environment. Results of a study performed for us by United Technologies Research Center on pellet injection, tracking, and laser beam synchronization are also reported.

I. CO_2 LASER PROGRAM
(G. Schappert)

Research and development programs on high-energy short-pulse CO_2 lasers began at LASL in 1969. The first system, the Single-Beam System, was designed in 1971, began operation in 1973, and was phased out in November 1977. Two large systems now operating are the Two-Beam System called Gemini, and the Eight-Beam System called Helios. Target experimentation continued on Gemini, which will ultimately generate pulses of 2 to 4 TW for target-irradiation experiments. Helios became operational in April 1978, and surpassed the design goal on June 21, 1978, with an output of 10 kJ at a power level of ~20 TW. The third system, Antares, is in the design and prototype stage. This system, described separately in Sec. II, will generate laser pulses of 100 to 200 TW, with the objective of demonstrating scientific breakeven.

GEMINI SYSTEM

Introduction (J. P. Carpenter)

The Gemini System was devoted primarily to target experimentation and, to a small degree, to system characterization. During the past 6 months, 170 target shots were fired and 73% of those produced the desired energy on target with no measurable prelasing. Some experiments were delayed by problems with the pumping-chamber pulsers.

Laser Performance and Diagnostics (J. P. Carpenter, J. J. Hayden, J. McLeod)

Measurements of encircled energy at the focal spot showed that 70% of the total beam energy passed through a 100-μm-diam pinhole. The Strehl ratio of ~0.25 derived from these data should improve substantially with the addition of adaptive optics to the triple-pass amplifiers. The adaptive-optics contract with Hughes Research Laboratories entered the final hardware phase.

The internal saturable-absorber gas-cell hardware was received and inspected. This cell will house the deformable recollimating mirror and should allow the delivery of ~1 TW to a target.

A target insertion mechanism that holds one target at a time was designed and should be installed during the second quarter of FY-79. This insertion system will permit an unlimited number of target shots before breaking the vacuum in the target chamber. The present target wheel holds seven targets, but the vacuum must be broken each time a new wheel is inserted.

The optical diagnostics facility can now measure pre- and postpulsing power to 10^{-3} of the main pulse peak.

Oscillator-Preamplifier System (P. Goldstone, V. Romero)

A new oscillator-preamplifier system, to be installed early in FY-80, was designed to replace the existing front end. A smoothing tube in addition to a switched-out oscillator, similar to that in the Helios system, will be used. The new front end will be installed directly east of the dual-beam module. Downtime will be minimal because the present front end will remain operational until the new system is installed. The new oscillator-preamplifier room is shown in Fig. I-1.

Computer and Control System (S. Hackenberry, P. Castine)

A computer simulation of our pulse-power capacitor banks was started. This computer model, which should simplify troubleshooting the pulse-power systems, uses the NET-2 electronics code in the LASL Central Computing Facility.

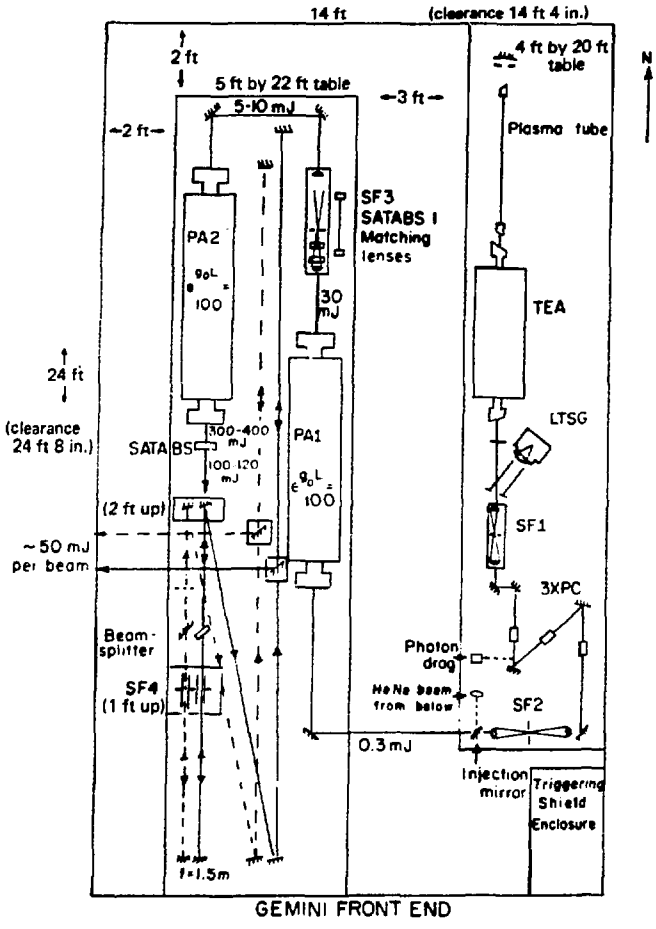

Fig. I-1.
Gemini front end.

HELIOS SYSTEM

Introduction (J. S. Ladish)

The second half of 1978 marked the transition of the Helios Laser Fusion Facility from construction to the target-irradiation phase. After successfully firing the laser in excess of the design output of 10 kJ into calorimeters in June 1978 (FIST II), we decided to perform the Earliest Laser On-Target (ELOT) experiment as soon as possible to gain experience and to become familiar with the problems to be encountered in target-irradiation tests. On July 27, 1978, ELOT was performed at an on-target energy of 1.6 kJ and peak intensity of just over 2 TW. The energy on target in that experiment was limited because of a parasitic oscillation mode caused by target feedback coupling to the amplifier gain medium.

The discovery of the parasitic mode triggered a considerable effort to determine the feedback source at the amplifier end, which would lead to its elimination. A more suitable gas mix (Mix 907) was subsequently developed for the amplifier saturable-absorber cell, and the entrance beam tube used in the power amplifier was removed. Also, we discovered a small, cone-shaped depression, made by micromachining, at the center of the large micromachined recollimating mirror. We used Nextel paint to cover the depression because the cone shape could act as a direct retroreflector, which would produce parasitic paths involving the power-amplifier gain medium and the target and/or diagnostics located near the target. These modifications raised the on-target energy to ~6 kJ, equal to a peak power of ~13 TW.

Although Helios is still in the shakedown phase, our target experimentation has already provided valuable new information regarding laser plasma interaction, and has produced the first clear evidence of high-density target implosions.

Target experimentation provided the principal excitement during the second half of 1978, but most of our effort on Helios centered on many less exciting but equally essential tasks, which are described below.

Front End (R. Carlson, R. Quicksilver, M. Weber)

The eventual requirement on beam simultaneity in Helios has been set at ±1 cm (±33.3 ps). In preparation for ELOT. the individual beam paths of the eight Helios beams were adjusted for a beam simultaneity of ±50 ps, using a method similar to that used in the Gemini system. The time of flight (TOF) of a front-end pulse to the target was measured by the time difference between the arrival of an optical pulse on a fast pyroelectric detector (Molectron P5-00) referenced against the laser-triggered spark-gap pulse (LTSG) of the three-stage Pockels-cell system. The simultaneity measurements were made with the LASL-built 3-GHz oscilloscope to record the optical and the LTSG pulses; a sweep calibration trace was added to each record to permit future temporal deconvolution. About 1300 photographs were taken yielding 200 records that met the pulse amplitude requirements. The final data after several iterations of path-length adjustment are presented in Table I-I.

TABLE I-I

BEAM SIMULTANEITY DATA FOR HELIOS

Primary Beams	Path Difference from Mean (ps)
1A, 2B	+51 ± 40
1B, 2A	−24 ± 33
3B, 4A	−5 ± 43
3A, 4B	−23 ± 61

This method of beam simultaneity measurement is tedious and can cause several systematic errors. Therefore, we developed, prototyped, and tested an improved technique that enables us to perform routine measurements of beam simultaneity with a resolution of less than ±5 ps. Briefly, the cw (continuous wave) CO_2 alignment laser in the front end will be modulated electro-optically at 40 MHz and aligned onto a surrogate reflecting sphere located in the target chamber. The reflected return signal will be detected by a HgCdTe detector located in the front end. The phase of this return signal will be compared continuously to the phase of the electrical signal that drives the modulator; this phase difference is proportional to the path difference. The system is shown schematically in Fig. I-2. All equipment for this system is on hand, and installation is ~30% complete.

As part of our continuing improvements to the Helios facility, we installed the following components:

- An improved oil-filled TEA oscillator and its associated Invar-stabilized optical support structure;
- Four motorized mirror slides at Spatial Filter 2 to permit repeatable injection of the krypton-ion visible alignment laser; and
- A 16-port voltage divider that provides an LTSG pulse to Gallery West (our diagnostics setup) and to the target diagnostics room for timing purposes.

Laser Physics (G. T. Schappert, J. S. Ladish, D. Casperson, R. F. Haglund)

The first eight-beam target shots on Helios were performed during the second half of 1978. On July 27, the entire system was fired for the ELOT test at reduced PFN voltage (42 kV/stage) with 6 torr of Mix 804 in each saturable-absorber cell. The total energy output on these shots was 1.6 kJ and was limited because of parasitic instabilities brought about when the entire system was carefully aligned onto a GMB target. An inside view of the Helios target chamber is shown in Fig. I-3.

After these first successful low-energy eight-beam shots, we performed a systematic study of the parasitic thresholds with targets in place. We used several techniques to identify the transitions involved in the self-lasing from a target. An Optical Engineering spectrometer, and

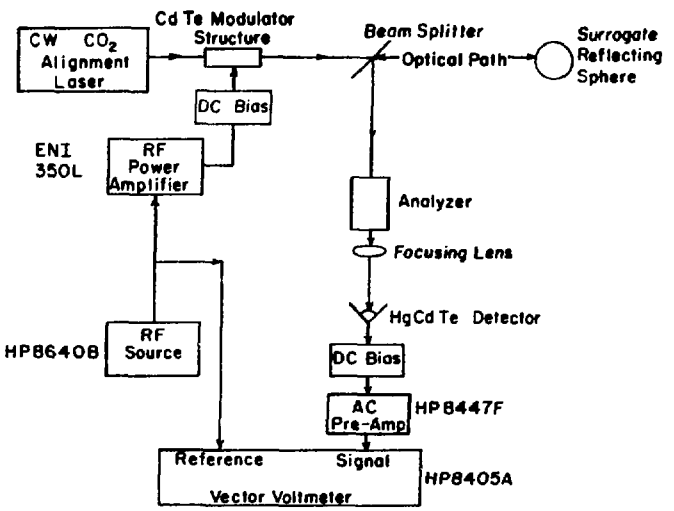

Fig. I-2.
Beam simultaneity schematic.

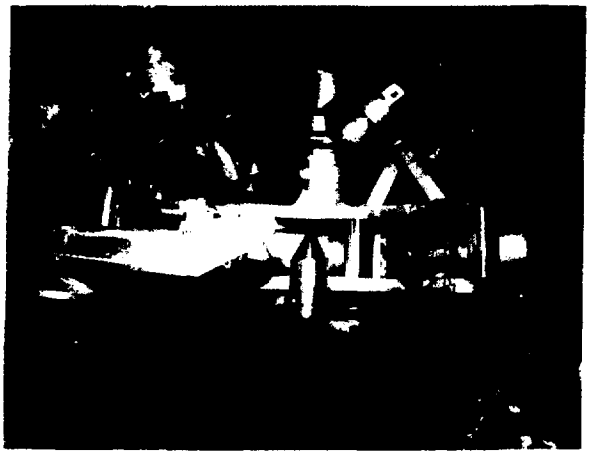

Fig. I-3.
Inside view of Helios target chamber.

later, 9- and 10-μm bandpass filters were placed at Gallery West to detect any energy due to self-lasing. However, these efforts were unsuccessful because of alignment problems and because of the low energy available at Gallery West. The most useful technique was to use various absorber gases in the amplifier side arm and in the saturable-absorber cell to differentially quench 9- and 10-μm light. Mix 804 did not perform well at 9 μm and was replaced with Mix 907.

With this new mix, the stable pump voltage attainable on the power modules was raised from 46 to 50 kV, with a corresponding increase in energy from ~200 to ~500 J per beam.

To determine the sources of parasitic instabilities in a module, we disassembled the saturable-absorber cell of Amplifier 1A and removed the reentrant beam tube. This tube guides the oscillator pulse through the absorber cell without attenuation, but may offer a partially reflecting surface that, in combination with the target, can produce self-lasing. In addition to having the input-beam tube removed, Amplifier 1A was also corrected for a machining fault in its 40.5-cm (16-in.) recollimating mirror. The single-point diamond turning process leaves a small cone-shaped depression at the very center of the mirror, which can reflect light at angles other than those intended. The fault was corrected by painting the center with Nextel paint.

Subsequent threshold measurements with Amplifier 1A aligned onto a target indicated that the amplifier was stable at 54 kV, with only 11 torr of Mix 907 in the absorber cell. Energy extraction measurements later showed that the energy output of this amplifier under these conditions is ~800 J. The same corrective procedure was then carried out on the remaining power amplifiers. With these modifications and with Mix 907 in the saturable-absorber cells, Helios can stably produce more than 6 kJ on target.

After retropulse damage was observed on the 10-cm (4-in.)-diam NaCl windows that separate the laser gas mix in each amplifier from the 3 torr of air in the sidearm, a Mylar transporter system was installed in Module 3A, which placed a "sacrificial" 1/4-mil film of Mylar over this window. The forward pulse passed through the Mylar after the first pass of the triple-pass amplifier at an energy density of ~0.1 J/cm^2 with only slight attenuation. The retropulse, however, struck the window at >5 J/cm^2 and created a plasma that blocked most of the retropulse from reaching the 10-cm (4-in.) NaCl window. The window has remained undamaged after ~15 shots since installation of the transporter. Similar systems have been installed in all modules.

Other modifications include the replacement of the straight amplifier anodes with curved anodes, which show improved gain uniformity.

Controls (E. L. Jolly, M. D. Thomason, J. Sutton, D. Remington, F. D. Wells, W. Hanna, K. M. Spencer, L. Sanders)

The Helios master control program evolved into a three-task multiple overlay (three overlay areas) with almost 28 k of core storage on the Data General Eclipse S/200 control computer, using the latest revision of Data General's operating system, QDOS, Rev. 6.32. Recent changes to the control program were the addition of absorber-gas pressure-change routines and the replacement of the monitor task with a more efficient version.

Work on supporting stand-alone programs is summarized as follows.

- The saturable-absorber control program was written.
- Studies continued of the new Asynchronous Line Multiplexor (ALM) and of its interface with the remote microprocessor substation, to be used for beam diagnostics. Some subroutines to support the ALM were written and tested. The ALM will be used to communicate with several microcomputers within the Helios facility and with the PDP 11/70 computer of the Target Diagnostics Group.

- The front-end checking program was modified to accommodate changes in the front-end hardware.
- The support programs for Helios, CRASHSV and TAPESEV. are being updated. CRASHSV was written to allow data retrieval from the digitizers in the event of a system crash at shot time, whereas TAPESV allows data retrieval from the on-line target if data are lost from the disk. Both support programs were modified to update the operations log file.
- The front-end spectral-line-content program LINES was used in conjunction with laser system firings by running the background terminal. This program will soon be incorporated into Helios.
- Testing of the prototype microprocessor-based target-chamber mirror-position encoding system revealed problems in both software and hardware. The system works well with a smoothly rotating motor driving the mirror mount, but does not always count correctly when a stepping-motor driver is used. Several test programs were written to diagnose the problem; some progress has been made.[1]
- The automatic alignment program was completed with the addition of a subroutine to operate the cw CO_2 alignment laser. This program is used routinely.

To carry out the necessary microprocessor programming, we developed the capability to assemble programs and to encode them into programmable read-only memories (PROM) automatically. A cross assembler (which allows us to assemble Intel 8085 assembly language programs) was obtained from Boston Systems, Inc., and installed on the Eclipse S/200. A program to encode automatically from the cross-assembler output was developed. Object files from the disk are sent across our Asynchronous Line Multiplexer (ALM) to a borrowed portable PROM programmer. Another PROM programmer was ordered for exclusive use on Helios.

The second computer processor for Helios arrived in early December 1978. Installation is about half complete and proceeding well. No computer downtime is anticipated as a result of the installation.

In addition to these tasks, the following hardware control systems were completed, installed, and made operational.

- The target-chamber vacuum control
- The target three-axis manipulator control
- The building safety and warning control
- The saturable-absorber-gas control
- The amplifier side-arm pressure control
- The motorized mirror-mount beam-positioner control

We designed and fabricated an optical isolation scheme to eliminate all wired inputs to the shielded control computer room. A total of 124 digital lines and 8 analog lines will be transmitted optically through the screen-room/control-room interface.

Mechanical Assembly and Engineering (E. L. Zimmermann, B. Maestas, D. Martinez, J. Valencia, L. Rodriguez)

Although mechanical assembly was completed some time ago, Helios upgrading and maintenance work continued.

Several titanium foils (windows) separating the evacuated and pressurized sections in the power modules developed pin-hole leaks and were replaced. Data accumulated indicate an average window life of ~75 shots with a typical foil-replacement time of less than a day. Although the phenomenon of pin-hole leak formation was investigated in some detail, no satisfactory explanation has been found. Helios operations are not affected too severely.

The following steps were taken to ensure a constant available supply of foil windows.

- A contract was awarded to produce acceptable window assemblies routinely.
- A metal-fabrication group at LASL was funded to produce foil-window assemblies (at present as the primary source).
- A mill run of titanium foil was purchased to ensure an adequate supply.
- An inventory of at least ten complete assemblies is maintained.

The new curved anodes are showing signs of fatigue-cracking in the weld joints, and an investigation of possible solutions to the problem is under way.

The electron-beam vacuum metal bellows are beginning to crack from fatigue and will be replaced soon with stainless steel bellows.

Miscellaneous tasks that were completed include

- installation of safety chains, work platforms, and railings on the power modules;
- installation of rupture disks on two of the amplifier modules;

- design of safety covers for the amplifier output salt windows; and
- design of oil troughs for the amplifier modules to eliminate oil overflow.

Concrete pads were poured to support the temporary modular building, which will be used until the permanent Helios addition is completed. The vestibules for the south doors were completed. Plans for the permanent addition are nearly complete, with groundbreaking scheduled for April 1979.

Two 1/24th-scale Helios models were completed by the Model Shop and displayed at several meetings. One model will be housed in LASL's Science museum.

Helios Laser Beam Diagnostics (I. Bigio, S. Jackson, R. Ainsworth, C. Smith, A. Laird)

A 1-W krypton-ion laser was installed in the front end as an alignment aid for Gallery West. Alignment time required by Gallery West for preparing a shot sequence was thereby reduced to less than one hour.

Initial optical problems were resolved by the implementation of CaF_2 beamsplitters and of a redesigned optical layout to collimate the sample beams to the shielded screen room. Studies have shown that careful placement of lead shielding is required to protect the liquid-helium-cooled prepulse detectors from x rays. At the end of 1978, the electrical problems were being solved and the last of the beam lines were made operational. Preliminary plans for an automatic alignment system were initiated.

The following laser beam parameters can now be monitored.

- Total-energy—all eight beams on target
- "3Q" ratio (ratio of prepulse: main-pulse: post-pulse energy)—one beam only
- Temporal pulse shape—one beam only
- Front-end energies—all four beams
- Front-end spectral content

In addition, both 8085 microcomputer substations became operational, and the optical fiber links from the substations to the main computer were installed and are also operational. The final link to the ALM remained to be made, but the remote substations can be operated from the main control room.

Optical Systems (J. Hanlon, V. K. Viswanathan, M. D. Bausman, J. J. Hayden, J. Murphy, P. Bolen, R. Parnell, I. Liberman)

The optical systems tasks fall into four major categories: day-to-day alignment and maintenance of the Helios laser alignment system; evaluation of adaptive optics; design and manufacture of the ir microscope; and salt-window control, recoating, and refurbishing.

Day-to-day alignment and maintenance tasks have included upkeep of the automatic alignment system; aligning the laser for firing; installing the remote-control motorized mounts for the orthogonal alignment telescopes inside the target chamber; changing optics; initiating the design of new holders for the Hartmann mirrors; initiating the design of covers for the power-amplifier windows; transferring maintenance of the Hartmann cameras from EG&G to L Division; removing all beam tubes; reestablishing the beam lines for all amplifiers; cleaning mirrors; and making and installing new masks for the 7.1-cm (3-in.) mirrors inside the power amplifiers. Attempts to automate Spatial Filter 4 were not successful; this task should be completed early in 1979.

Primary efforts in the Rocketdyne and Hughes adaptive optics contract centered on liaison and on the manufacture and use of a CO_2 Smartt interferometer to evaluate the adaptive optics. Preparations for testing these optics in our optics laboratory were made.

The overall mechanical design of the ir microscope is complete, but some detailing of parts remains to be done. The lenses for the system were designed and ordered. A major future task will focus on establishing and designing an evaluation system for processing the relayed image.

Five coated salt windows for the Helios system were received. These windows were coated on one side only and will be used on the target chamber. One new window was installed; recordings of the pulse shape indicate that the second surface reflection has been eliminated by coating, as expected. The worst of the existing windows will be replaced as AR-coated salts arrive. The present salt windows will be gradually replaced with coated ones. Windows that can be refurbished will be returned to Harshaw for repolishing.

Monitoring, documenting, and coordinating the shipping, refurbishing, and coating of salt windows remained an important task.

Experimental Plan 13 (Target Alignment Accuracy in Helios) was carried out successfully. As the principal result, we established that the average pointing error for the GMBs tested is 34 μm. By improving the tests, we expect to reduce this error to less than 25 μm, as required.

An important modification made to the optical transport code LOTS enables us to routinely calculate the interferogram produced by an arbitrary optical system in conjuction with a Twyman-Green or Smartt interferometer. This important accomplishment permits us to compare the observed and calculated interferograms and allows us to make specific statements about system alignment and about the sensitivity of the wavefront error affected by individual optical components. Applications of this powerful code to the Helios system are being considered. Experimental verification of its prediction capability and a general description of the work was presented at the Optical Society Conference in San Francisco.[2]

An ir interferometer was constructed in-house and is being used routinely in conjunction with LOTS.

REFERENCES

1. F. D. Wells and D. Remington, "Mirror Position Display Equipment for the Target Chamber Mirror Mounts of the Helios Laser Fusion Research Facility," Proc. CUBE Symposium, Los Alamos, 1978.

2. B. D. Seery, "Design and Assembly of Carbon Dioxide Laser Systems Using IR Interferometry," presented at the Optical Society Conference, San Francisco, 1978.

II. ANTARES—HIGH-ENERGY GAS LASER FACILITY
(T. F. Stratton)

Antares and associated facilities are being constructed to provide a CO_2 laser fusion system with an optical output of 100 to 200 TW with a maximum energy of 100 kJ. We believe that scientific breakeven is within reach of this machine. All laser-system section work proceeded on schedule toward the 1983 completion date.

INTRODUCTION (T. F. Stratton, J. Jansen)

Substantial progress was made in all areas of the project. Raising the mostly prestressed concrete walls of the larger buildings that will house Antares and the target systems was the most eye-catching undertaking; all long-lead-time Antares laser components were released to vendors for fabrication in preparation for the start of installation in August 1979.

A baseline design for automatic centering of the laser beams on the power amplifier and target-system relay mirrors was completed. We prepared variations of the baseline system and an alternate concept to allow assessments of the effect on cost and performance.

The suggestion to sample the full system output with wire transmission gratings was accepted after tests of the gratings on Gemini. The gratings were fabricated in-house on a winding machine designed to produce wire spark and drift chambers.

The optical design of the Antares front end was completed. Preamplifiers were ordered and delivered, and one of the required six driver amplifiers was ordered for evaluation. A prototype of the Antares front end was set up in the old Single-Beam System area. Evaluation and development of multiline oscillators and multipass amplifier geometries were planned for the prototype.

We reactivated the power-amplifier prototype to evaluate modifications incorporated in the Antares power-amplifier design as a result of the prototype program. Reliability and control of the gridded cold-cathode gun were improved. Stands, pressure vessels, and gun parts—all long-lead-time items—for the power-amplifier proper were to be delivered in mid-1979.

A firm, fixed-price contract for the engineering design and fabrication of the Antares energy storage system was placed with Maxwell Laboratories. All prospective vendors were willing to quote on a fixed-price basis because a prototype unit had been designed and tested by LASL. This prototype Marx unit met the specified inductance requirements, which was a primary uncertainty, as well as the basic voltage and energy requirements. In addition, we developed a spark gap that transfers the charge and current anticipated under fault conditions without failure.

A design-construct contract for the Antares target-chamber and vacuum system was awarded to the Pittsburgh-Des Moines Steel Company (PDM). A unique feature of this 1300-m^3 system was the requirement that the pumping units be cryogenic pods. We advised PDM to proceed with the procurement of long-lead-time items before the final design review.

A tree-structured hierarchical architecture was defined for the controls system. Based on this definition, we released detailed specifications for the control computers and the communications networks for competitive quotations. Digital Equipment Corp. was the successful bidder.

Finally, because facility construction was three months behind schedule, the Department of Energy negotiated with the Contractor to obtain beneficial occupancy of the Laser Hall, the most critical part of the facility, by mid-July 1979.

OPTICAL SYSTEM (A. Saxman, D. Blevins, W. Miller, J. L. Munroe, W. H. Reichelt, C. Silvernail, J. Sollid, T. Swann, W. Sweatt, P. Wolfe)

Introduction

The Antares beam-alignment and diagnostic conceptual designs and analyses are partially completed. The optical-mechanical end-to-end system performance requirements have been specified. The initial analysis of subsystems indicated that the required hardware is available commercially. The bigger part of the initial analysis has involved choosing cost-effective hardware to modify and integrate into the Antares design.

Prototype beam alignment, beam diagnostics, and mirror positioners are in the initial design phase, with

some of the follow-on initial prototypes being tested, such as centering detectors, power detectors, signal-conditioning electronics, and large-mirror positioners. Final designs of the support structure for the beam-alignment and diagnostics package are being incorporated into the power-amplifier and target-system designs.

Beam Alignment

A number of beam-alignment tasks were completed successfully and new efforts were started. Descriptions of some of these tasks follow.

Hughes Research Laboratories Study Contract. Phase II of the Hughes Research Laboratories (HRL) study contract for a conceptual baseline design of a complete beam-alignment system for the Antares power-amplifier system was completed. The task had the following engineering objectives: to ensure that an alignment beam entering the power amplifier is colinear with the output beam of the front-end driver amplifier; that it is properly centered and pointed into the power amplifier; that it remains aligned as it passes through various elements, including all mirrors, windows, and spatial filters; and to ensure that the beam exiting the power amplifier reaches the target area without vignetting. The equipment proposed in the baseline design would allow automatic alignment of each of the 72 optical paths through the 6 power amplifiers between the front-end output and the back reflector of the power amplifier. The details of the proposed flip-in detector system were outlined in the last semiannual report, LA-7587-PR.

Baseline Design Effort and Analysis. Using the basic power-amplifier beam-alignment conceptual design generated by HRL and LASL as a baseline design, our beam-alignment group initiated a design and analysis effort to simplify the mechanical, electrical, and electro-optical designs of the alignment laser source and its beam sector insertion device, the beam-centering and positioning sensor package, beam sensor positioning devices, and the general approach of maintaining the precise placement of components and devices. These design considerations greatly reduced the projected cost of the system hardware and its integration as compared to an estimate generated for the baseline concept.

Alternative Beam-Alignment Technique. We generated another beam-alignment technique for the entire Antares system. The conceptual design is referred to as a "See-Through Imaging System," in which each of the 72 optical beam paths from the front end to the target is manually or automatically aligned. The basic system uses a visible imaging system positioned at the output of each driver amplifier. The system colinearizes its optical axis with the driver-amplifier output beam and then properly centers each component of the entire optical train through to and including the target. Studies began on a number of technical areas for this system, such as solid-angle constraints, reflection losses from the diamond-turned mirrors, various combinations of visible imaging camera systems, optics, and image centroid-determining hardware and software packages.

Conceptual Beam Alignment. A conceptual beam-alignment design effort for the target system with Hughes Aircraft Corporation (HAC), was initiated and will continue through March 1979. The basic tasks involve upgrading an analytical model to describe the target system optics, performing a sensitivity analysis of the Antares optical train, verifying our analysis that indicated noninterference of the target-system beams and optical elements, developing conceptual alignment schemes for the target-system optics, selecting an overall baseline alignment scheme, and identifying long-lead-time items required for a prototype single-beam alignment subsystem for the entire optical train.

Beam Diagnostics

Design efforts were started on the diagnostic package for the Antares system as referenced in the last semiannual report (LA-7587-PR).

Wire Diffraction Grating. The final design of the wire diffraction grating and support structures was completed, and in-house fabrication was initiated. A development prototype wire grating was tested successfully on Gemini. The grating sustained fluxes exceeding 3 J/cm^2 without damage and sampled the total beam energy as predicted.

Spatial-Filter/Thermal-Detector Testing. Initial testing of the spatial-filter/thermal-detector assembly was completed. The net repositional error product (REP) of beam

displacement and energy was 5 mm·mJ; that is, with 1 mJ of total energy on the detector, it resolved the beam position accurately, to within 5 mm. Typically, we anticipate a total energy deposition of 150 mJ, which implies a resolution of 0.04 mm under Antares conditions.

Input Diagnostics Package Designs. Design started on the retropulse and power-amplifier input diagnostic packages, the output-beam sampling calorimeters for the turning chambers that collect the 12-sectored, high-power, wire-grating-sampled beams from the power amplifier; and the diagnostic spool calorimeter that collects the special-purpose full output of a power amplifier.

A beam diagnostic and alignment test facility was partially constructed to evaluate the detector packages and the CAMAC/computer data collection and analysis system.

Window and Mirror Fabrication

Harshaw Chemical Company (HCC) produced their first three successful forgings of Antares windows. The production-process checkout remained promising. If the whole production can be judged by these results, no delay in meeting schedule requirements is anticipated. Recent HCC in-house efforts in Kyropoulos crystal growth were encouraging. Boules grown by this technique had minimum haze and sparkle. In fact, HCC delayed the procurement of the last four Antares growth furnaces until the results of this new growth technique are evaluated. The salt window and cell pressure tests were concluded successfully. Mechanical and optical parameters were well within tolerances up to the operating pressure, and no plastic flow of the salt was detected after a 35-day pressure soak.

Orders for 82 periscope substrates and 48 rear reflector substrates were placed. The polyhedron beam reflector design was reviewed and the first attempt to machine it was scheduled for April 1979. A preliminary analytical design for the parabolic-mirror fixture was completed.

The Y-12 Plant of Union Carbide Corporation demonstrated repeatable surface figures of less than 1000 nm rms at 10.6 μm and surface finishes of less than 500 nm peak-to-valley. These values are adequate for the Antares system.

Mirror Positioners and Mirror Cells

All the parts for the mirror positioners were received. Tests on the motorized positioner continued. The fine-screw actuator responded and repeated reliably; the coarse-screw actuator needed minor rework. The University of Tennessee made a detailed deflection analysis of the periscope mirrors supported by the three-post kinematic mount. Initial results indicated less than 125-nm peak-to-valley distortion of a mirror in the worst possible attitude. An alternative kinematic mounting post was designed in which flexures replace spherical ball bearings. Trial parts were ordered.

FRONT-END SYSTEM (W. Leland, M. Kircher, C. Knapp, D. Swanson, G. York)

Introduction

A detailed design of a one-beam prototype front end was completed, and procurement of hardware began as design drawings and specifications became available. A baseline design of the Antares front end was also prepared. The oscillator systems for Antares and the prototype are different, but all other features of the prototype front-end design are identical to those of one beam line in Antares. However, the Antares design duplicates the one-beam design six times for all major components after a six-way beam splitter. The Antares oscillator complex will produce a multiline pulse output with the capability of shaping the pulse, whereas the prototype beam line will, at least initially, use a multiline oscillator complex without beam-shaping capabilities. The one-beam prototype preserves important distances between major components but has a different configuration from the Antares front end to permit installation in an existing building.

General Description of Beam Line and Arrangment of Components

A schematic layout for the one-beam prototype is shown in Fig. II-1. The Antares layout is shown in Fig. II-2. The following description of the prototype beam

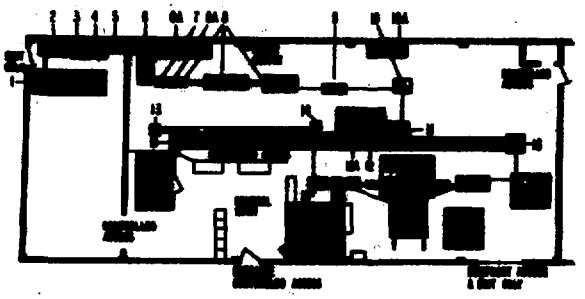

Fig. II-1.
Layout for one-beam Antares prototype front end.

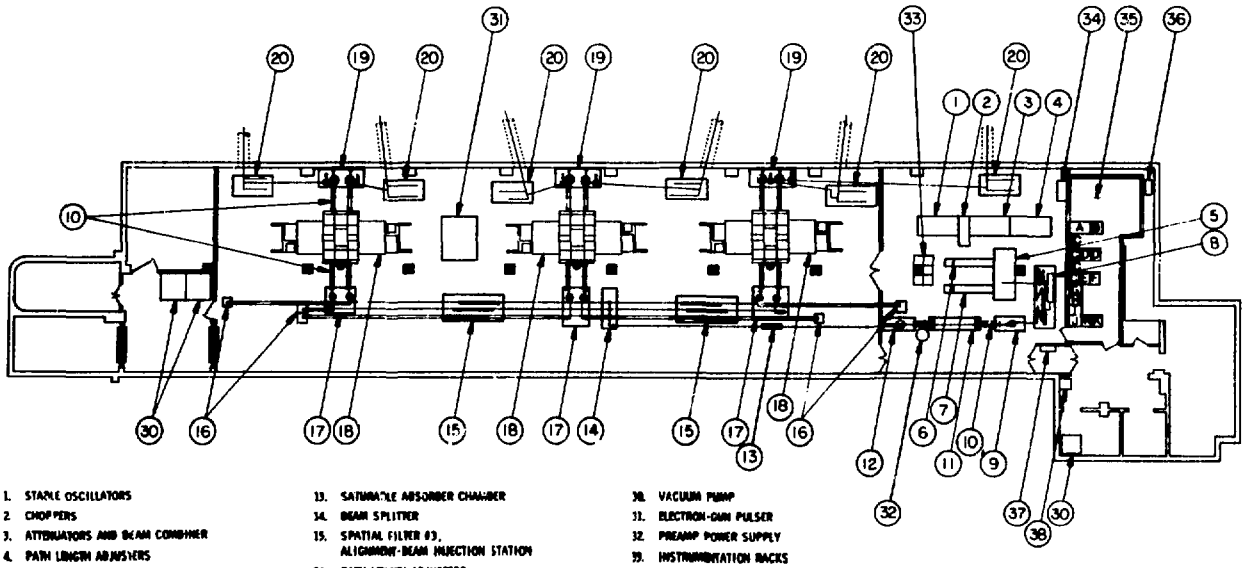

1. STABLE OSCILLATORS
2. CHOPPERS
3. ATTENUATORS AND BEAM COMBINER
4. PATH LENGTH ADJUSTERS
5. PREAMP OPTICS TABLE
6. 4-PASS BOOSTER PREAMP (LUMONICS 922)
7. 2-PASS BOOSTER PREAMP (LUMONICS 922)
8. SPATIAL FILTER #1, SWITCH OUT, SPATIAL FILTER #2, ALIGNMENT-BEAM INJECTION STATION
9. PREAMP INPUT OPTICS TABLE, ALIGNMENT TELESCOPE, BEAM STEERING STATION, PRIMARY CASSEGRAIN OPTICS
10. PARASITIC SUPPRESSION CHAMBER
11. PREAMP (LUMONICS 400)
12. PREAMP OUTPUT OPTICS TABLE, SECONDARY CASSEGRAIN OPTICS, BEAM STEERING STATION
13. SATURABLE ABSORBER CHAMBER
14. BEAM SPLITTER
15. SPATIAL FILTER #3, ALIGNMENT-BEAM INJECTION STATION
16. PATH LENGTH ADJUSTERS
17. DRIVER INPUT OPTICS TABLE, ALIGNMENT TELESCOPE, BEAM STEERING STATION, PRIMARY CASSEGRAIN OPTICS
18. DRIVER AMPLIFIER
19. DRIVER OUTPUT OPTICS, SECONDARY CASSEGRAIN OPTICS, BEAM STEERING STATION, CALORIMETER
20. PAM ALIGNMENT STATION
30. VACUUM PUMP
31. ELECTRON-GUN PULSER
32. PREAMP POWER SUPPLY
33. INSTRUMENTATION RACKS
34. OSCILLATOR DIAGNOSTICS
35. SCREEN ROOM
    A. PDP 11/60
    B. DEC WRITER
    C. FIBER OPTICS INTERFACE
    D. PDP 11/40
    E. CAMAC RACK
    F. SPARE RACK
    G. FLOPPY DISK
    H. COMPUTER TERMINAL
    I. HARD COPY UNIT
    J. TIMING AND COMMUNICATIONS RACK
    K. DISPLAYS
36. TRANSFORMER
37. CLEAN ROOM CLOTHING SHELVES
38. SINK

Fig. II-2.
Layout of six-beam Antares front-end system.

line applies in all important respects to the Antares system, with a sixfold duplication required in Antares after the beam splitter. In the following paragraphs, numbers in parentheses refer to numbers associated with parts shown in Fig. II-1.

The beam, which originates in a multiline oscillator (1), is sent through a spatial filter (2), a beam-steering station (3), and a switchout station (4). At this point it emerges from the oscillator complex as a multiline millijoule pulse of the desired duration (typically, 1 ns). The spatial profile is Gaussian with a characteristic width (1/e) of about 0.6 cm. The beam proceeds from the switchout station to a beam-steering station (5), and then through another spatial filter (6). An alignment-beam insertion station (6a) is coupled to the spatial filter. Visible or CO_2 alignment beams are inserted at this point.

The alignment beam is adjusted to be colinear with the main beam as defined by the spatial filter. Divergence of the alignment beam is also adjusted to be equal to the divergence of the main beam. After passing through the spatial filter and another beam-steering station (7), the beam travels through a preamplifier complex (8). The preamplifier is fitted with on-axis Cassegrain optics to provide three-pass amplification. Parasitic suppression cells are located at each end of the preamplifier. Provision is made to insert an optical tooling telescope just before the preamplifier at station (8a). The Cassegrain optics and preamplifier produce an annular beam of 9-cm o.d. and 3-cm i.d. with a nominal energy density of 50 mJ/cm^2. Next, the annular beam passes through a saturable-absorber cell (9), and is then directed into a beam-splitter station (10). The beam splitter geometrically cuts out a 2.5-cm circular beam (six beams for Antares). The unused beams are routed to the diagnostics station (10a), but the 2.5-cm beam cut out by the beam splitter passes through a beam-steering station (11), where it is directed to another spatial filter (12). The alignment-beam insertion station (12a) is associated with the spatial filter (12) and has the same functions as stations (6) and (6a). After the spatial filter (12) the beam passes through a path-length adjustment complex (13) and (14), through another beam-steering station (15), and then through the driver-amplifier complex (16). Provision is made to insert an optic tooling telescope at (16a) just before the driver complex. The driver complex consists of half an Antares dual-beam amplifier fitted with on-axis Cassegrain optics and parasitics-suppression cells at each end. The dimensions of the annular output beam are 15-cm o.d. and 9-cm i.d., with a 1-J/cm^2 energy density of the multiline output beam. The output beam is directed either to a beam-diagnostic station (17) or to the retropulse simulators (18) and (19). The retropulse simulator can produce a backward-running pulse, which is delayed as it would be if it were reflected by a target in Antares, by reflecting a chosen fraction of the output pulse. Implementation of the retropulse simulator is not planned for early prototype beam operation.

As noted earlier, the Antares beam layout shown in Fig. II-2 follows the same general sequence of components. Output from each of the six driver amplifiers is directed onto stations that are a part of the optical subsystem.

Description of Major Components

Driver Amplifiers. Driver-amplifier procurement continued. Systems, Science and Software (S^3) was selected to build the three dual-beam units according to our detailed specifications. Design reviews were held with S^3 in August 1978, and fabrication was started. Due to unfavorable component delivery schedules and other difficulties, the driver could not be used in the prototype front end by the requested December completion date.

The driver amplifiers are high-pressure (1200-torr) electron-beam-type amplifiers. They are packaged as dual-beam units with two high-pressure discharge chambers coupled to a single, two-sided, gridded, cold-cathode gun. Each high-pressure discharge has its own energy supply, but all three electron guns are connected to a common energy supply. Switching relays provide for operation of any subset of the three electron guns.

The 2-m gain length will provide gain-length (gL) products up to 7, although adequate output energy is predicted at gL products of 6. A parasitics-suppression cell is attached at each end of the amplifier to ensure stable operation with triple-pass, on-axis Cassegrain optics. The 21-cm-diam, 4.5-cm-thick NaCl windows are tilted 15° to the optic axis to avoid on-axis reflection. Beam diagnostics can be performed by using the reflected energy from the salt windows of the parasitics suppression cells. Optics are mounted on support stands outside the amplifier isolator cells. Margin to provide additional output or to compensate for unforeseen problems is provided by the capability for higher-than-nominal gL products and by the designed ability to operate at 1500 torr rather than at the nominal pressure of 1200 torr.

Preamplifier. We selected a standard commercial unit (Lumonics 602) for the preamplifier. The amplifier and most auxiliary equipment (e.g., stands, power supplies, parasitic isolator cells, windows) were delivered and assembled. The unit was operated routinely at specified gain (gL = 4) and gain uniformity. Tests with the triple-pass Cassegrain optics awaited delivery of the optics.

Oscillator and Switchout. The oscillator to be used first in the prototype front end is a modified Laser

Development Corporation (LDC) unit. The LDC oscillator combines a pulsed TEA laser of our design with multiple low-pressure plasma tubes, one for each desired line. The optical cavity for each line includes one low-pressure plasma tube, but shares the TEA laser. A grating combines the beams to give the unidirectional multiline operation. The switchout is a standard LASL design with three stages of CdTe Pockels cells and germanium plate polarizers. The Pockels cells are driven by a fast (nanosecond) high-voltage (25-kV) pulse generated by a charged line and a spark-gap switch. All equipment for the prototype oscillator-switchout system was delivered, and checkout was begun.

Laser energy extraction calculations and predictions of the performance of some target designs indicate the need for pulse-shaping. In the LDC design, the common beam volume in the TEA laser (part of the oscillator cavity) produces coupling between lines and precludes positive relative-line-amplitude adjustment. The Antares oscillator design provides an extremely versatile system, which allows positive amplitude control for each line as well as pulse shaping by variable timing of pulses from each line. The final switchout unit is identical to the prototype unit and can, in principle, also provide pulse-shaping by control of the switchout voltage pulse. The Antares oscillator design uses six stable, 1-W, cw lasers, each operating on a selected line. Each of the six beams is switched out individually and directed through its own path-length adjuster before being combined into a common beam path. Adjustment of the relative timing of the pulses from different lines, either electrically or by path-length difference, will produce pulse-shaping. Control over the individual line amplitude further adds to the line-shaping capability. Amplitudes can be adjusted by varying the power input to the cw lasers and by inserting attenuators. The 1-W power level in the cw lasers must be amplified to 1 MW. The desired amplification is accomplished with four-pass amplification in a commercially available laser (Lumonics K922S), which has a gL product of 4. Amplification is performed after combining the six beams into a single beam by combinations of zinc-selenide beam splitters. No serious problems with coupling between lines are expected because we are operating the Lumonics laser in the small-signal regime (output energy of 1 mJ vs available stored energy in excess of 100 mJ). The four-pass amplification design depends on a polarization rotator, germanium Brewster-angle plates, and a Pockels-cell switch with germanium plate polarizers. All four passes lie on a common path that requires a minimum of gain volume. Good contrast ratio is obtained because two passes are made through the Pockels-cell switch. Design of the unit was completed except for some detail drawings of minor parts. Parts were ordered and fabrication was initiated.

The repetition rate for the Antares oscillator complex can be as high as 3 Hz. Longer pulses, along with the high repetition rate, will give output power useful for some alignment tasks.

Beam-Line Components Not Associated Directly with Amplifier. The spatial filters consist of two powered mirrors with a pinhole of appropriate size located between them at the focal point of the input mirror. The filters are used in the front end for spatial beam quality control; beam-line definitions for use in alignment; alteration of beam characteristics (size and divergence); and retropulse interruption. The design of these units is complete, and parts were either delivered or have been ordered.

Beam-steering stations are used at various locations to adjust beam position and direction, and to facilitate positioning of the beam line relative to large units such as amplifiers. These designs are complete, and parts were delivered or have been ordered.

The saturable-absorber cell is included to enhance the contrast ratio as needed. It is different from the parasitics-suppression cells in that it needs to function only on the selected lines of operation, whereas the parasitics cells must cope with all lines that can produce parasitics. The gas filling for the saturable absorber is SF_6. Design was completed and procurement started.

The beam splitter is a perforated mask whose holes separate the number of needed beams. Appropriate optics pick up these physically operated beams and direct them as needed. Design was completed and parts have been ordered.

The path-length adjuster compensates for the differing locations of amplifiers (and hence, for the path length to the target) by adding length to the shorter paths. Design was completed and parts were ordered.

The alignment-beam insertion stations are similar to those in Helios. The design was completed and parts were ordered.

Controls and Diagnostics

The prototype front-end controls are identical to the manual backup, checkout, and maintenance controls designed for Antares. The manual controls are compatible with switchover to computer control when computers, interface hardware, and software become available. Diagnostic or monitoring information from the various components in the prototype front end is obtained by Antares design sensors, signal generators, and transmitters. The design incorporates fiber optics for signal transmission wherever possible. The output of the oscillator complex, the preamplifier, and the driver amplifier will be examined for total energy and for the temporal and spatial character of the pulse.

Detailed lists specifying type and characteristics (e.g., voltage levels and impedance) of all Antares control and monitor signals were prepared.

System Studies

Performance. Pulse energy and temporal characteristics were calculated for the system. Our results indicated acceptable performance, but uncertainties existed in the characterization of parasitics suppression by saturable-absorber gases under the wide range of operating conditions considered.

Gaussian-beam propagation calculations were made to account for first-order diffraction effects. We examined beam stability and factored it into the design of all components. The geometric magnification produced by the Cassegrain optics used on the driver amplifier and preamplifier desensitizes the system to directional changes of the beam at the input end, but it enhances the displacement sensitivity. All beam-line components are mounted directly and rigidly to the building floor. Whenever possible, mirror combinations are mounted in such a way as to desensitize effects of their motion on beam-line direction and position.

Reliability and Maintenance. Reliability received high priority in all design work. We used conservative design and specifications to achieve an expected misfire rate of less than 1%. Maintenance for Antares was designed for replacement of readily accessed components or groups of components. Diagnostics were included for rapid identification of the faulty replaceable part or group of parts. Routine maintenance of energy storage units was planned.

Safety. All components presenting electrical hazards were designed with regard to personnel safety considerations. Radiation hazards were addressed by controlled-access procedures. Both the prototype front end and the Antares front end were designed for a single controlled access whenever radiation hazards are present. Special handling equipment was designed or specified to eliminate mechanical hazards to personnel.

Equipment is protected by hard-wired interlocks and through computer check routines.

POWER-AMPLIFIER SYSTEM (R. Stine, R. Scarlett, G. Ross, W. Turner, W. Miller, E. Yavornik, N. Wilson, G. Allen, W. Gaskill)

The Antares power amplifier and a cross section are shown in Figs. II-3 and -4. The unit is 16 m long, 3.7 m in diameter, and the centerline is 3.2 m above the floor. The basic design incorporates a centrally located 12-sided grid-controlled cold-cathode electron gun, which discharges radially into 4 annular pumping volumes.

Fig. II-3.
Antares power amplifier.

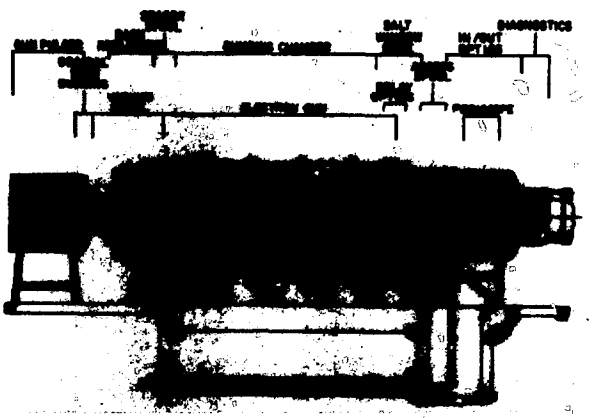

Fig. II-4.
Cross section of Antares power amplifier.

All large long-lead-time components for the pressure-vessel and electron-gun portions of the power amplifier were ordered. The first electron gun, as well as the support stand for the first power amplifier, will be delivered by July 1979. The pressure-vessel components will be delivered soon thereafter for installation on the support stand.

The first electron gun will be tested in Building 85, independent of the Laser Hall.

Pumping Chamber

Electrical Design and Testing. We designed and tested a solid anode bushing using a compressed-rubber dielectric. Initial voltage testing at 600 kV showed adequate holdoff, but lifetime data were still required. A metal-powder-loaded epoxy bushing was fabricated and awaited testing. The backup position depended on the water-graded bushing tested in the prototype power amplifier. The bushing holes in the pumping chamber were enlarged to a diameter of 35 cm, to accept any of the bushings under consideration. We completed a dielectric divider design that is consistent with the revised electron-gun support system. The dielectric divider is not an integral part of the support system, but it prevents ring-mode optical parasitics and improves gain uniformity and efficiency by containing the electron flux.

Mechanical. The pumping-chamber and spacer-spool sections are being fabricated; delivery is expected in May 1979. The salt-window domes and back-reflector domes were redesigned to eliminate costly forgings. These units were ordered, and delivery is expected in September 1979. The design of the electron-gun support system was nearly completed.

Electron Gun

Electrical Tests. Modifications were made to the prototype power amplifier to allow in-depth testing of electron-beam characteristics for the final Antares design. The modifications included a new control-grid design, improvements to the vacuum system, some additional corona rings on the cathode assembly, viewing ports in the grid, and a careful cleaning of all parts of the electron gun. The major problem to be solved by these modifications was grid emission at high voltages and at grid resistance, which led to a loss of control of the electron-beam current. In addition to the physical modifications to the electron gun, we also developed a grid-conditioning procedure, which consisted of shorting the grid to the cathode and then operating the gun with a series of pulses of increasing voltage. We tested these changes in a series of runs at voltages between 300 and 500 kV and grid resistances between 250 and 1200 Ω. The improvements allowed operation at higher voltages and grid resistances than previously possible, and there was decreased frequency of grid emission at all voltages. The results of these tests, which were incorporated into the Antares electron-gun design, showed that the Antares electron gun should perform well within the required specifications.

We also conducted tests to determine the electrical performance of the prototype dielectric dividers at low voltage. When the electron-gun voltage was reduced to 300 kV, flashover was observed between the ribs of the dividers. At 400 kV the flashover stopped. The new Antares designs for anodes and dielectric dividers were installed and will be tested.

We selected a test facility for the electron guns. Drawings of building modifications required for the testing program were submitted for approval. The modifications included a pit for the vacuum system, lead shielding, and a large screen room. We considered these provisions necessary because of the late completion date for the HEGLF laser building.

Mechanical. All four electron-gun weldments were machined successfully. A typical weldment with the machined hibachi slots is shown in Fig. II-5. The weld

Fig. II-5.
Typical electron-gun weldment with the machined hibachi slots.

test program proceeded well, with all the flat samples completed. Once the final ring sample is welded and tested, the electron-gun section will be machined in preparation for final welding and will be shipped to the welding shop. We designed a revised sealing concept for the junction of electron gun and pressure vessel. This concept uses bellows and eliminates tight tolerances in these large parts.

Three vacuum spools were being fabricated, with delivery starting May 1979. Both the coaxial feed bushing and the electron-gun support bushings were being fabricated, with delivery expected in April 1979. Brazed-foil and glued-foil electron-gun windows were ordered for the first electron gun.

Gas and Vacuum Subsystem

The electron-gun high-vacuum turbomolecular pump with its associated mechanical backing pumps was received. We will install the system in an existing building for electron-gun testing. Detail drawings of the complete gas and vacuum system were started. The Vacuum System Evaluation and Test Laboratory was completed.

Handling Equipment

We emphasized the completion of the electron-gun handling equipment because it is needed first. A low-boy fixture, which will serve both as a handling fixture and a test fixture for the electron-gun testing, was designed. The fixture can be rotated to allow easy access to all 48 foil windows. Drawings for the grid/cathode assembly fixture and for the 3.2-m-high gun-insertion fixture to be used in the Laser Hall were completed.

Diagnostics

The design of the small-signal gain measurement system was completed. We ordered the CO_2 laser as well as all mirrors, mirror mounts, and other accessories. This system will require a screen room in the Laser Hall, which will be shared with the optical diagnostics.

A completely computer-integrated diagnostics system was designed for the electron-gun testing.

Optical Support Structures

Detailed structural analyses of the back reflector, relay optics, and in/out optics support structures were completed. The drawing for the optical support structure of the back reflector was completed; the relay and in/out optical support-structure drawings will follow. The long-lead-time aluminum plate for these elements was ordered.

The optical components and their locations on the optical support structures were defined. The first turning mirror will have the same kinematic mount as the back reflector and the periscope mirrors. The second turning mirror and the focusing mirror will use a modified commercial mirror mount. Prototypes of the trombone and spatial filter were fabricated. A small mirror clamping design was detailed, and mirrors were fabricated and tested. The transmission gratings for large beam sampling were integrated into the optical support structures, and three prototypes are being fabricated.

Support Stand

Weldment fabrication and final machining of the power-amplifier support stand were ordered. The steel box beams were ordered earlier and will be delivered to the stand fabricator in mid-February 1979. The first support stand was scheduled to arrive by July 1979.

High-Voltage Cable

Both General Cable Company and Sieverts Kabelverk dry-cured high-voltage cables were certified for use at 550 kV in the power amplifier. Specifications for both cables were completed and sent out for bid.

Air Bearings

A new set of electron-gun air bearings was installed and tested on the test vehicle during December 1978 (Fig. II-6). The new air bearings were a second-generation version of the prototype bearings tested in July 1978. The major difference between the prototype and the new air bearings was the size of the internal air-supply line, which was increased to 1.3-cm o.d. This

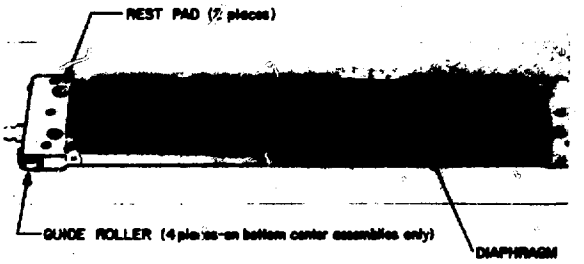

Fig. II-6.
Antares electron-gun air-bearing assembly (shown inverted).

change was made to improve the performance of the air-bearing assemblies. The smaller copper tubing on the prototypes appeared to restrict the air flow to the bearings, resulting in nonuniform lift and high frictional drag. Our test results showed that the new air bearings had more uniform lift, operated at a lower pressure, exhibited a higher flow rate through the assembly, and required a lower tow load than the prototype. These improvements in performance were the direct result of increasing the size of the air-supply line.

ENERGY STORAGE SYSTEM (K. Riepe, G. Allen, J. Bickford)

The Energy Storage System supplies the high-power high-voltage pulses to the gas discharges and electron guns in the power amplifiers. The system consists of 24 gas pulsers storing 300 kJ each, and of 6 gun pulsers that store 70 kJ each.

The gas pulsers will be built by a contractor. We built a prototype gas pulser to provide information for evaluation of proposals, to help us review the contractor's designs as they progress, and to provide a test bed for controls and diagnostics.

Because requirements for the gun pulser have not been fully defined, these pulsers will be designed and fabricated in-house.

Gas Pulsers

Requests for quotation for 25 Marx generators (including 1 spare) were sent to 4 vendors. Basic specifications were

Energy, kJ	300.
Voltage, MV	1.2
Inductance, μH	<3.0
Jitter, rms, ns	<20
Prefire Rate	<0.01

The contractor will be required to build one Marx in his facility and to run it for 2000 shots to allow us to evaluate its reliability. The first trigger system will be tested for 50 000 shots. Bids were received from three vendors. After some changes in specifications, best and final offers were received in November 1978. Letter-contract approval was predicted for late January 1979.

Testing of the prototype gas pulser was slowed by failure of the charging-power supply. Because a power supply of comparable size was not available, testing continued with a much smaller power supply.

The Marx generator was reconfigured to measure the effect of spark-gap position on inductance. In the original configuration, the spark gaps were placed away from the centerline of the stage, toward the centerline of the Marx. It was thought that this would minimize the loop and, thus, the total inductance. However, we found that moving the gaps back to the centerline of the stage, and thus decreasing the stage inductance while increasing the loop inductance, decreased the Marx inductance from 2.7 to 2.4 μH.

New spark gaps, based on the spark-gap test programs, were installed in the Marx. Before installation, these gaps were tested to determine the effect of dimensions and electrode condition on the self-breakdown voltage (SBV) measured at atmospheric pressure with a slight flow of air through the gap. The gap was isolated from the power supply with a large (1-MΩ) resistor, and a small capacitor (2.4 nF) was charged and discharged through the gap. SBV was measured after several tens of conditioning shots. The standard deviation of the 17 gaps tested was 1.8%, and the largest difference was 3.4%, indicating an acceptable tolerance stack-up.

The coated Carborundum resistors to be installed in the gas-pulser prototype were received and tested before installation. The test consisted of soaking the resistors in oil for one week. The resistance increased if there were large holes in the coating. A 10-kJ, 10-kV capacitor was then discharged through each resistor. When the resistor was heated by the dissipated energy (10 kJ produced a temperature rise of 50 K), a stream of small bubbles was emitted from any pinhole leaks. About 20% of the resistors failed this test. We continued to work on this

problem with Carborundum Corporation. They recommended a double coating of polyurethane, rather than the usual polyurethane-over-epoxy coating.

Electron-Gun Pulser

The electron gun pulsers provide the energy to drive the electron guns. The beams from the electron guns control the ionization density, hence the impedance, of the gas discharges. The gun current density controls the overall impedance, whereas the voltage controls the electron range, and thereby controls the gain distribution. We conducted a theoretical and experimental program to determine the optimum voltage and waveform.

If the optimum waveform is square or trapezoidal, a Guillemin network can be used. We built and tested to full voltage a megavolt, two-mesh, type-A Guillemin-Marx generator. In addition, we used the Marx portion of the network to life-test the high-voltage cable samples. This procedure provided a good life-test of the Marx itself. The disadvantage of the Guillemin network was that it limited the risetime. Experiments indicated that a voltage rise of several kilovolts per nanosecond was required for uniform ignition of the cathode. Thus, the Guillemin network required a peaking capacitor and switch to provide this voltage rise.

Theory indicated that the optimum gun waveform was a high-voltage spike (500-600 kV), followed by a lower voltage plateau (300-400 kV). The high-voltage spike occurred before voltage was applied to the gas, fully ionizing the entire volume. After voltage was applied to the gas, the applied electric field allowed the use of lower energy electrons, while maintaining ionization across the full discharge gap. We found experimentally that, without the initial high-voltage spike, gas breakdown occurred. This waveform can be generated by a Guillemin network. However, a good approximation may also be generated by a straight Marx generator, which has the advantage that it may be built with low inductance, and thus does not require a peaking circuit to provide good ignition of the electron gun. These considerations led to the selection of a simple inexpensive Marx generator as the Antares gun pulser.

Component Development

After completion of the spark-gap life-testing under fault conditions, we performed some experiments to characterize the gap under normal operating conditions. A dummy load was inserted in series with the spark gap to limit the peak current to ~250 kA with 25% reversal. The parameters of interest were trigger jitter and prefire rate.

It is difficult to relate spark-gap jitter to Marx jitter because the Marx jitter depends on the internal coupling of the Marx. However, if the spark-gap jitter is high, the Marx jitter will obviously also be high. Switch jitter was less than 10 ns with a 200-kV trigger pulse at 120 kV and at a safety factor of 2. This implied that a trigger pulse of more than 200 kV, and probably at least 300 kV, will be needed for the Marx to achieve a Marx jitter of <20 ns.

To achieve the specified Marx prefire rate of about 1 in 100, the individual spark-gap prefire rate should be less than 1 in 2500. Verification of this value would take more than 5000 shots. This was not considered reasonable, and a less direct approach was taken. The distribution of SBV at a pressure corresponding to a mean SBV near 100 kV was measured, and the probability of self-breakdown at or below one-half the mean SBV was calculated by assuming that the distribution was Gaussian, and that the standard deviation was independent of pressure. The standard deviation of SBV was between 2 and 3% of SBV over the range of 50 to 120 kV. If the distribution is Gaussian, then the prefire probability at one-half SBV is negligible ($<10^{-100}$). From experience, we know that the prefire rate will be higher, so either or both assumptions were incorrect. However, the standard deviation of gaps operating at much lower current is also on the order of 2 to 3%, so we may expect that the prefire rate of the Antares gaps will be no worse than that of conventional gaps.

Power Supplies

Specifications for the Antares power supplies were written. We require a gas-pulser power supply that will charge four gas pulsers in one minute. Six will be required. The gun-pulser power supplies will charge one gun pulser in ~20 s, depending on the gun-pulser energy. Six will be required. One spare of each will be purchased.

The first unit of each power supply will be required to undergo a proof-of-design performance test at the manufacturer's facility, as follows.

a. Operate high-voltage transformers without rectifiers at 200% of rated voltage for 7200 cycles.

b. Short the output through a 100-ft-long cable at 60-kV charge with a vacuum relay.

c. Operate the full power supply into an open circuit at 130% of maximum charge voltage (78 kV) or at maximum open-circuit voltage, whichever is higher, for 6 hours.

d. Operate with both polarities short-circuited for 1 hour;

e. Operate at full power into a resistive load for 1 hour.

We expect these tests to guarantee the reliability of the power supplies. Each power supply will be required to pass an acceptance test consisting of the transformer test at 200% of rated voltage, and of 2-hour open- and short-circuit tests.

TARGET SYSTEM (P. Wolfe, J. Allen, W. Sweatt, N. Wilson, V. Zeigner)

Introduction

The scope of the target system is illustrated in Fig. II-7, an artist's sketch of the target vacuum system. Six beam tubes, each 1.7 m in diameter and ~35 m long, extend underground from the north wall of the Laser Hall to the Target Building, where they connect to six 3-m-diam turning-mirror chambers. Six smaller beam tubes lead to a centrally located target chamber, a 7-m-diam vessel that houses a space frame, which, in turn, carries arrays of folding and focusing mirrors for each beam, as well as a precision target-insertion mechanism. Figure II-7 shows the space frame in its rolled-out position, which requires the removal of one target-chamber end dome and of three short beam tubes. This position will be used primarily for initial installation and major overhaul of the 12 mirror arrays. For normal operation the target chamber will remain closed; targets and diagnostic equipment will be changed by means of air locks without breaking vacuum; and minor maintenance will be carried out by backfilling the target vacuum system with air and entering through a man-access hatch.

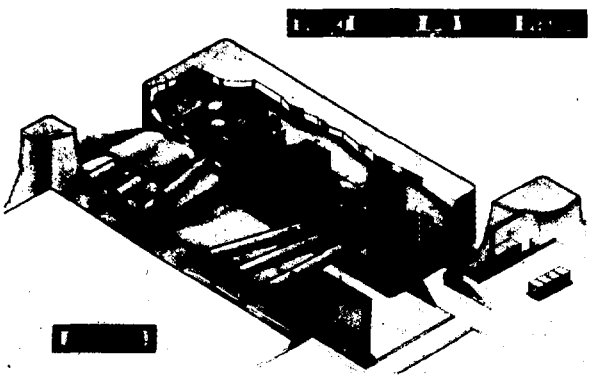

Fig. II-7.
Artist's sketch of Antares target vacuum system.

Activity related to the target system was markedly increased, which made it appropriate to organize a more formal target system team, made up of the regular contributors from the various design disciplines, primarily from L-Division's Antares Group, and of representatives from the Target Diagnostic and Target Fabrication Groups. Brief weekly coordination meetings were valuable for spotting action items and for keeping the effort on schedule.

Optical Train

As described in some detail in the previous semiannual progress report (LA-7587-PR), the portion of the optical system within the target chamber was radically redesigned to decrease the focal length of the focus mirrors that illuminate the target. Although this change had the desired effect of decreasing the spot size on target, it made the layout of components in the space frame and the use of space near the target for experiments much more critical. In addition, it increased the diversity of required sector mirror shapes over that of the earlier, more symmetric design. Therefore, we conducted several detailed studies of outline ray trajectories between mirrors and of beam footprints on mirrors and mirror arrays before completing the design. An independent check of the representative results of our in-house calculations was performed on the Antares optical train as a part of the Hughes Aircraft study contract.

Target Positioner

This component of the target system might be described more properly as a target insertion and precision positioning mechanism. As a key element in the optical train, its design must satisfy not only obvious functional requirements, but also must provide for reproducibly locating targets within a few tens of

micrometers of a fixed point in space, and for accommodating optical alignment tooling to ensure that the remainder of the optical train is aligned and focused on that point. In addition, for cryogenic targets, the positioner must incorporate retractable means for cooling the target up to a few milliseconds before shot time.

On the basis of the successful design developed for the Helios system we commissioned the same LASL group to develop a successor for use on Antares. A design and development schedule consistent with the overall target system schedule was worked out, and design work began, with first tasks consisting of firming the requirements for precise target positioning and for interfaces of the alignment system.

Space Frame

Upon completion of interference checks for the revised optical layout within the target chamber, we reinitiated the design effort on the space frame. The general frame envelope of this structure was already fairly well defined, because it had to be established to permit the design of the target chamber to proceed (see Target Vacuum System, below). The remaining structure consists of 12 supplementary frames to hold the 6 folding-mirror arrays and the 6 focusing-mirror arrays, plus members to provide rigidity. We could not use a common design for the supplementary support frames; this added complexity to the task of designing and analyzing the overall space frame. Overlying the integration of these members into an overall structure were the requirements that no optical-beam interferences be introduced, and that adequate target access be provided for fusion experiments.

Two design layouts were generated and supplementary scale models were built. These models permitted a critique of structural-member placement from the standpoint of the frame's probable rigidity; provided clear insight on interferences and accesses; and served as indispensable aids in setting up the necessary mathematical models of the overall structure for rigidity and vibration analyses. At the end of 1978, we selected one design and initiated mechanical analyses.

Target Vacuum System

This part of the target system composes the entire vacuum envelope, as shown in Fig. II-7 and described in the introduction to Sec. II.F, together with the pumps and controls needed to rough and maintain an operating pressure of 2×10^{-6} torr in the target chamber. In August 1978, we awarded a contract to design and build this system to the Pittsburgh-Des Moines Steel Company (PDM), and a meeting of PDM and LASL design groups was held at LASL.

At the end of a 10-week conceptual design effort by PDM, a 3-day preliminary design review was held in Pittsburgh. Structural concepts presented by PDM were accepted with minor revisions, such as providing access stairs instead of ladders, and aluminum platforms rather than steel. However, acceptance of the high-vacuum-system design was delayed, pending further calculations and verification of pumping capabilities and compatibilities of the proposed combination of Freon-chilled baffles to handle water vapor, and helium-refrigerated surfaces to pump other gases.

A review of a revised pumping scheme was held in December 1978, but some apprehensions remained, and an alternative design based on helium-refrigerated pumps alone was requested by LASL. Our experience with this approach on Helios led us to believe it to be reliable and adequate; to our knowledge, the combination system has never been tried on applications like ours. PDM accepted our recommendation.

In December, authorization was given PDM to initiate procurement of certain long-lead-time items and materials. A final design review was scheduled for March 1979, before beginning fabrication.

CONTROLS SYSTEM (M. Thuot, D. Call, D. Carstensen, D. Gutscher, A. Kozubal, R. Lindberg, F. Maestas, F. McGirt, W. Seifert, B. Strait)

General

Final requirements for the Antares Controls System were established. These requirements are listed below.

Absolute Requirements

- Accept and execute operator commands according to predetermined algorithms.
- Prepare and fire the laser in a specified sequence.
- Acquire, store, and display laser and control system information.
- Meet the schedule determined by the installation and checkout of other Antares subsystems.

Design constraints that tend to limit the manner in which absolute requirements are met are listed below,

followed by additional design constraints ordered according to priority.

Absolute Design Constraints

- Personnel must be protected from severe safety hazards.
- The control system must operate in an adverse EMI environment over a large area.
- The control system must have sufficient generality and flexibility to accommodate change.
- A comfortable man-machine interface must be provided.
- System control from a central location must be provided.
- Distributed subsystem control must be provided.

Additional Design Constraints, Priority-Ordered

- The control system will be hierarchical and tree-structured.
- The control elements will be designed for high reliability and low mean repair time.
- The control system will be implemented according to the best techniques available for specification, design, and documentation.
- Testing and integration will proceed at many levels simultaneously, with tools and controls that prevent hazards to personnel and equipment.
- A common control language, common hardware, and a common operating environment will be supported at each level of control.
- Decisions to make or buy hardware and software will be based on requirements, interfacing, support, schedule, and budget.
- Command acknowledgment and command execution times will be minimized.
- A programmable central control sequencer will be provided to fire the laser.
- All laser data and status information will be available at the central control station.
- The control system will provide archival storage of laser and control data.
- Computer-generated hard copy will be available at the central and subsystem levels.

The configuration of the Antares control system as specified above was established as shown in Fig. II-8. This configuration is a four-level hierarchical tree-structured network of 11 minicomputers and ~100 microcomputers.

The top-level processor, the Integrated Control Center (ICC), provides an integrated central control point for all of Antares. In addition, auxiliary support functions such as data-base management will also be provided at this level.

The second-level processors, the Subsystem Control Centers (SCC), provide individual control of each major Antares subsystem.

The third-level processors, Beam Line Controllers (BLC), exist only under the Laser Hall SCC and serve as controllers for each Antares beam line. The fourth-level processors, Machine Interface (MI) processors, execute the desired control and data-acquisition functions.

The experimental data-system node of the control network refers to the experimental data system, which is unspecified at present.

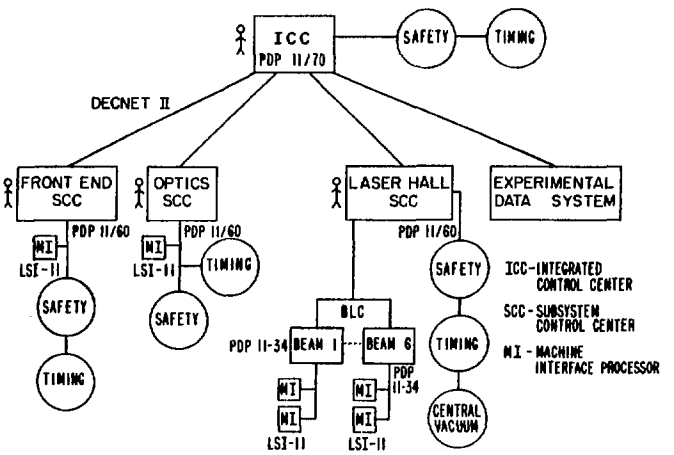

Fig. II-8.
Antares control-system configuration.

Communication facilities between all network nodes will be supplied by a commercially available package.

Hardware

After competitive bidding, computer hardware was selected as shown in Fig. II-8 with Digital Equipment Corporation (DEC) supplying all the computers and communication facilities. The network hardware will be ordered in stages. The first stage, obligated from FY-79 funds, includes the ICC processor; the three SCC processors for the front end, laser hall, and optics systems; and two third-level processors. The remaining five third-level processors for beam-line control will be procured from FY-80 and FY-81 funds.

The configuration of the machine interface processor (MI) has not been finally determined. Work is in progress to establish the control and data-acquisition interfaces to be supported.

Software

Schedule and budget required that as much of the Antares software be purchased as possible. This particularly applied to operating systems, communications support, and even to the use of device drivers, where appropriate. Only in the case of specialized applications tasks or when vendor-supplied software is not available will we write our own software.

Design and implementation of these application tasks began with the definition of software modules. The first or top-level modules for the Antares software are shown as a hierarchy chart in Fig. II-9, which only describes the major software functions and the interrelationships between these functions. The data paths are not described. Lower level modules are shown in Figs. II-10 to II-12.

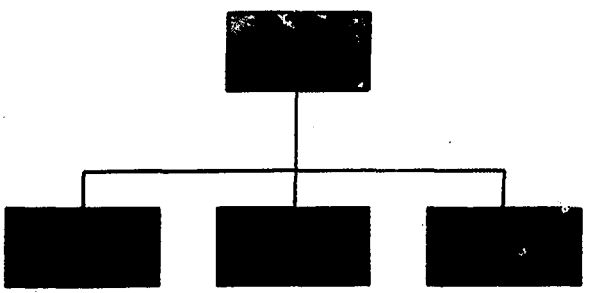

Fig. II-9.
Antares software hierarchy chart.

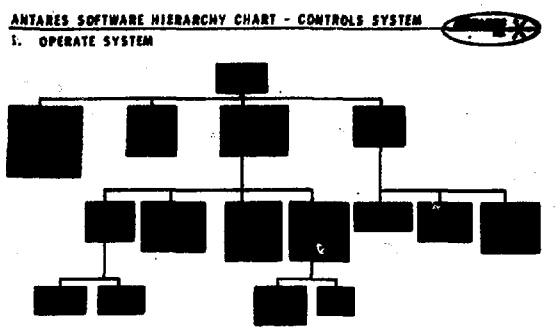

Fig. II-10.
Antares software hierarchy chart of the lower level modules (Operate System).

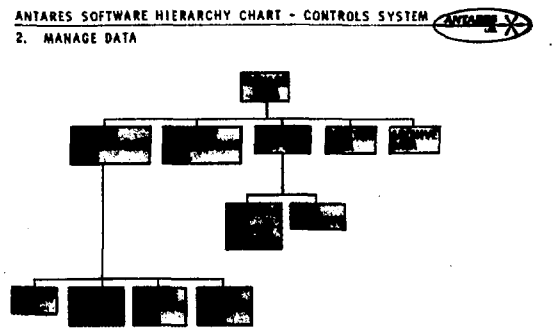

Fig. II-11.
Antares software hierarchy chart of the lower level modules (Manage Data).

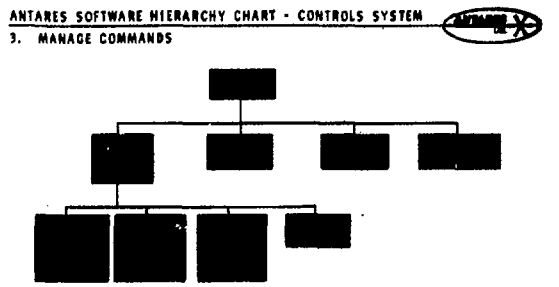

Fig. II-12.
Antares software hierarchy chart of the lower level modules (Manage Commands).

Front-End Controls

Detailed control requirements, complete with cost and manpower estimates and schedules, were integrated into the total control-system effort, which contributed to final definition of the overall control structure described above. Tests of hardware in several areas such as CAMAC crate controllers for the LSI-11 microprocessors were completed. A specification was written for the standard Antares crate controller.

Laser Hall Controls

Detailed control requirements specified by System Managers for the power amplifiers, electron-gun test, laser diagnostics, and energy storage were integrated into the overall control-system effort. Interactions with other systems were also specified. This work contributed to the establishment of the controls-system architecture and general approach.

Beam Alignment

Hardware designs for stepping-motor controls, hand-held controllers, and sensor electronics were completed.

Network Management

Most of our effort was expended for site preparation and procurement of computer hardware. In addition, plans for computer relocation in the Antares central-control screen room and installation of DECNET II between a PDP 11/60 processor and an LSI-11 processor were completed.

Antares Timing System

Requirements for the Antares timing system were specified. These requirements will be used to write a specification before design, implementation, and procurement of the timing system.

ICC and Central Control

Requirements for the operator-machine interfaces for Antares are being established, including specifying operator control and status displays, video and audio signals, control panels, and terminals. In addition, a large amount of time was spent in specifying the data archival system for Antares.

MI Configuration

A team was formed to establish the MI configuration required for Antares control. Work was started on an evaluation of the input/output interfaces, the fiber-optic packaging, and an EMI enclosure specification.

Antares Software

A team was formed to implement the Antares production software using structured programming methods. Work on the top-level modules was begun.

Early Support

A team was formed to provide early temporary support for data-acquisition and control activities in the following areas.

- Electron-gun test facility
- Small-signal gain measurement development
- Optical systems development
- Laser diagnostics
- Front-end systems development

Work has begun to establish a general package for the parallel I/O interface driver for PDP 11/03 computers.

HEGLF SITE AND STRUCTURES (J. Allen)

Construction Package I

As of December 31, 1978, the job was 48% complete with 74% of the time consumed. This meant a rescheduling of the completion date from mid-July to late September 1979. The delay was caused by abnormally bad weather, change orders, bad concrete samples, and improper planning by the Contractor. Figure II-13 is an aerial view of the site, taken in late summer 1978. The status of the elements that make up Package I is outlined below.

Laser Building. The high-bay portion of the laser building, which houses the power amplifiers and energy-storage equipment, is shown in Fig. II-14. According to the construction sequence chosen by the Contractor, this part of the package will be completed later than most of the other elements. Power-amplifier installation in this area is to start by early August 1979. A joint-occupancy arrangment must be worked out between LASL and the Contractor if this schedule is to be maintained.

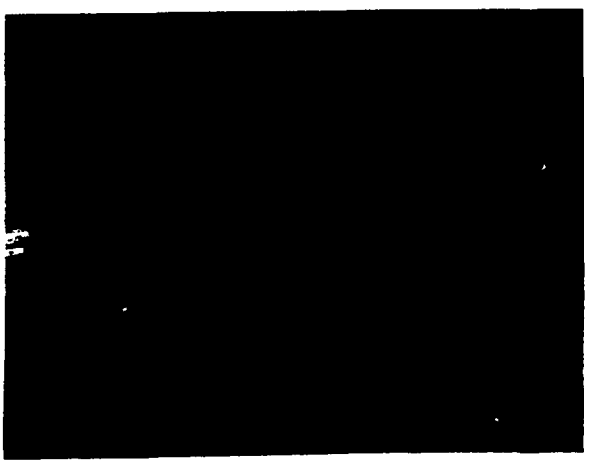

Fig. II-13.
Aerial view of HEGLF site.

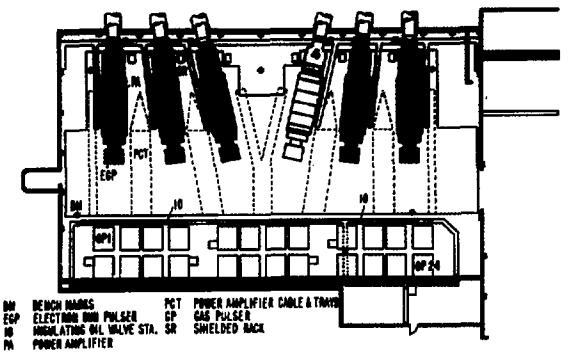

Fig. II-14.
High-bay portion of laser building housing the power amplifiers and energy-storage equipment.

Most of the wall panels were erected and a portion of the support slab for the power amplifiers was poured. A fortunate selection of a low-profile crane allowed us to gain 2 ft of hook height with only a minor change to the column design.

The office, laboratory, and shop portions of the laser building have progressed farther than the high bay, with grade beams poured and the T-beam roofing sections installed over two-thirds of this area. All underground conduit and piping were installed.

The front-end room received one coat of paint and the air-conditioning ducting was installed.

Mechanical Building. The floors, equipment pads, walls, and roof concrete work were completed. The mechanical building and the laser-building shops and laboratory areas were completed first to accommodate the mechanical and electrical subcontractors' work. Water chillers, boilers, an air conditioner, and some piping were installed. Part of the tritium stack was erected.

Office Building. The walls and T-beam roof sections were installed. The underground conduit and piping were installed. Some concrete test specimens taken from the T-beam pours had low 28-day break values, but additional cores taken from the T beams later, showed adequate concrete strength. Office and laser-building construction was delayed until the discrepancy was resolved.

Warehouse. A prefabricated design that satisfied everybody was selected. Construction will start when the ground thaws—probably in April 1979.

Package II

The north and west walls of the target building were completed. The south wall was two-thirds complete, with the beam-tube penetration inserts in place. The scaffolding to support the forms for the 5-ft-thick roof was in place. This building should be finished in July 1979, which is compatible with the scheduled start date of August 1, 1979 for target vacuum system installation. This package was 42% complete with 76% of the time consumed.

The 500 000-gal. water tank and the backup fire protection system were nearly complete. The tank was not painted, pending resolution of safety procedures to be used by the Contractor.

The rebuilding of the power line leading into the site to accommodate the extra HEGLF load was completed.

High-Voltage and Optical Evaluation Laboratories

Both laboratories were essentially complete. The laboratories were scheduled for occupancy in mid-January 1979. The original contract completion date of October 23, 1978 was missed because of late delivery of the boiler and hot-water pumps. Several design deficiencies became apparent during the final walk-through and contributed to the delay.

III. CO_2 LASER TECHNOLOGY
(J. F. Figueira)

Each of our CO_2 laser systems described earlier represents a significant advance in the state of the art of reliable CO_2 laser subsystems, components, and diagnostics. The design, construction, and improvement of the systems require, therefore, basic support of CO_2 technology. Some important areas are the development of short-pulse multifrequency oscillators; amplifier optimization; development of subsystems for the prevention of system self-oscillation and removal of prepulse energy, including the study of relaxation processes in bleachable gases; and the development of passive means to enhance laser beam quality and simultaneously to provide automatic target alignment through phase conjugation.

PROPAGATION STUDIES (S. J. Czuchlewski, J. F. Figueira, A. V. Nowak, E. J. McLellan, C. E. Knapp)

Introduction

We evaluated the performance of a 10-GW subnanosecond CO_2 laser system prototype capable of reliably generating pulses of good optical quality and high peak irradiance at a repetition rate of 0.1 Hz. This system will be used to conduct development studies in support of our CO_2 Laser Fusion program, including target diagnostics development, optical damage threshold studies, the evaluation of gaseous and solid-state saturable-absorber isolators, and the development of phase-conjugate reflectors. Comparisons were made between the energy and pulse shapes obtained with this system and those predicted by a theoretical model that has been used extensively in high-power CO_2 amplifier design. In this case, the model is examined in a regime where the input pulse width is less than half the effective rotational relaxation time, a domain in which it has not previously been tested.

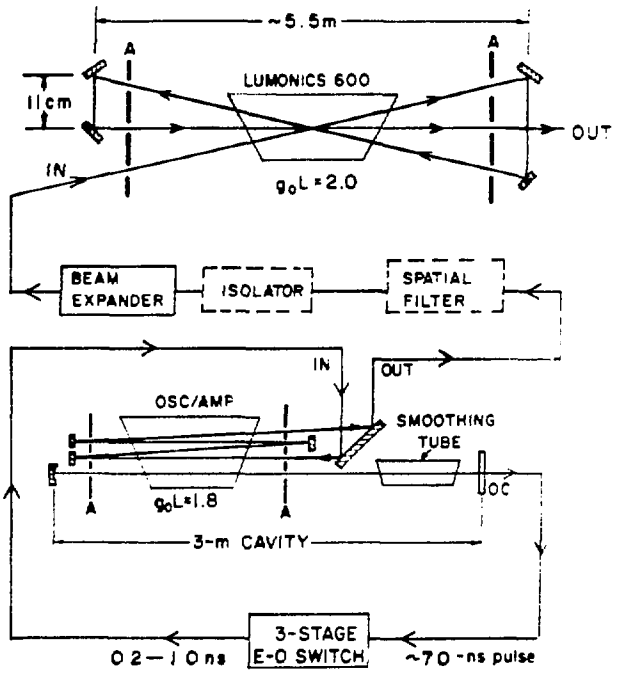

Fig. III-1.
Two-stage TEA laser system, showing the reinjection oscillator, the electro-optic switch, and the triple-passed Lumonics power amplifier.

Apparatus

The prototype consisted of a reinjection CO_2 oscillator, an electro-optic switch system for producing subnanosecond pulses, and a power amplifier (Fig. III-1). A commercial TEA laser was used as the power amplifier. Both the oscillator and the power amplifier were multipassed to optimize system performance.

The oscillator and electro-optic switch were described previously.[1] The Lumonics-600A TEA power amplifier is a double-discharge, uv-preionized device with an active volume of 8.9 by 10 by 50 cm,[2] capable of operating at a repetition rate of 0.1 Hz. The gas mix used was 61:15:24::He:N_2:CO_2 at 580 torr. Small-signal gain was 4%/cm, measured with an attenuated multiline, gain-switched pulse that sampled a 25-cm^2 cross section of

the active region on a path inclined 2.5° relative to the axis of the device.

Experimental Procedure

Two types of measurements were made. First, we determined the response of the full system to a 1-ns input pulse, and second, we took a set of measurements to investigate pulse shaping with a 570-ps input pulse.

Case 1. One-Nanosecond Pulses. For the first experiment, 2-mJ, 1-ns FWHM pulses with 200-ps risetime were produced by adjusting the Pockels cells in the electro-optic switch for in-phase operation. Reinjection to the oscillator medium for four stages of amplification yielded a 230-mJ, 1.02-ns FWHM pulse with a 190-ps risetime for input to the Lumonics amplifier. The pulse energy was distributed among the 10-μm P(16), P(18), and P(20) lines. The beam diverged slightly as it passed through the amplifier, occupying a cross-sectional area of ~25, 40, and 46 cm^2 on the three successive passes.

Energy and pulse shape measured and calculated after each pass are shown schematically in Fig. III-2. The pulse width decreased appreciably on the second and third passes, giving an 8.7-J output pulse with 778-ps FWHM duration. Because the amplifier was underfilled, these values can be increased by 30% to produce an output power of 12 GW.

Beam quality was evaluated by measuring the Strehl ratio for the system via a diffraction-grating technique. The measured ratio of 0.25 would allow a focused intensity of 10^{14} W/cm^2 with an f/2 optical system.

Case 2. One-Half-Nanosecond Pulse. The theoretical model we use predicts that a 1.0-atm CO_2 amplifier system should effectively amplify pulses as short as 250 ps when the optical flux is sufficient to saturate the amplifier medium. To test this prediction, the electro-optic switch was adjusted for out-of-phase operation, yielding a 0.3-mJ, 270-ps FWHM pulse with 120-ps risetime for second measurement series. During passage through the four-pass reinjection amplifier, the pulse energy increased to 19 mJ, but the pulse broadened to 570 ps.

Because we wanted to study the performance of the power amplifier for short pulses under saturation conditions, the beam expander was adjusted to provide a smaller beam than that used in the first experiment. The

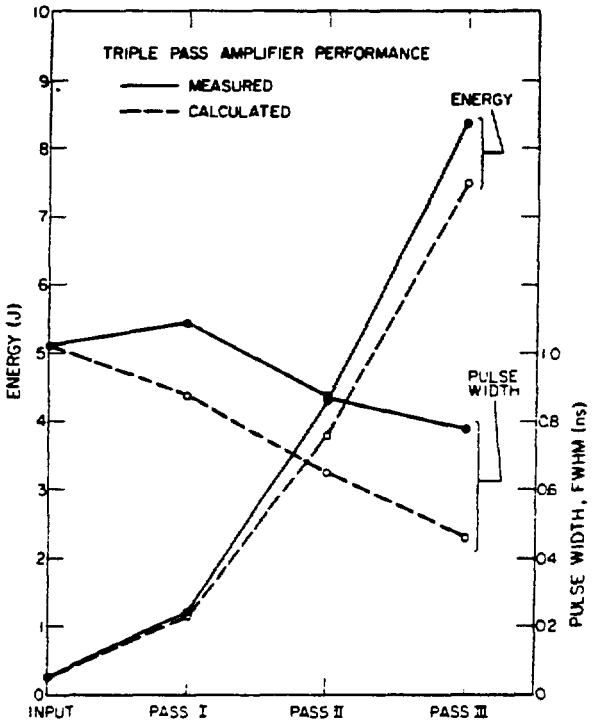

Fig. III-2.
Performance of the tripled-passed TEA amplifier with a laser mixture of 61:15:24::He:N_2CO_2 at 580 torr total pressure. Length of active gain region was 50 cm.

area of the diverging beam during the third pass was 6.1 cm^2 compared with 46 cm^2 in the previous case. Input-output parameters and pulse shapes for the Lumonics amplifier under these conditions are shown in Fig. III-3. Note that, in this case, the injected pulse was broadened significantly, to 880 ps FWHM, from the predicted value of 370 ps.

Theory

The performance of the Lumonics amplifier has been modeled by using a coherent density-matrix kinetics code developed by Feldman,[2,3] which describes the propagation of pulses shorter than about 5.0 ns. This code accurately predicts the energies and shapes of 200-J, 1.5-ns pulses propagated through our 2000-torr electron-beam-controlled Gemini system.[3] However, the model has not been fully tested with subnanosecond

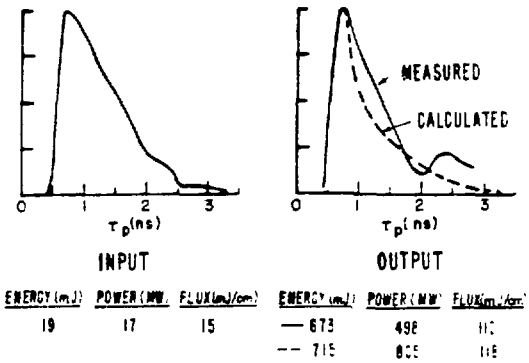

Fig. III-3.
Pulse parameters and shapes from the triple-passed Lumonics power amplifier for a 570-ps input pulse. Solid curves are experimental; dashed curves are theoretical.

pulses. Because the characteristic relaxation times of the laser medium vary inversely with pressure, the present work explores a substantially different regime from that studied in Ref. 3.

Modeling a strongly saturated, multipassed amplifier requires accounting for the energy extracted from the medium on preceding passes. In addition, the 16-ns interval between passes may require accounting for additional kinetic processes. The first of these processes is intramode V-V relaxation.[4] In addition to the upper (001) and lower (100) CO_2 laser levels, higher lying vibrational levels are also excited by the discharge. These levels can relax to the (001) state, thus repumping the upper laser level. Because this relaxation time has been estimated to be ~50 ns,[4] we ignored this process in our present work. However, this relaxation time has not been accurately established and may be shorter.

The second process that must be considered is relaxation of the lower (100) laser level. By using Stark's experimental data,[5] this relaxation time is estimated to be 45 ns for our conditions, whereas the Jacobs et al. data[6] predict a value of ~7 ns. Because the latter results were obtained more directly, we assumed in our model that the lower laser level relaxes completely between passes. Nevertheless, the discrepancy in the measured time constants for this process warrants further investigation. Under these assumptions, the gains on the second and third passes of the amplifier are reduced slightly from the initial values (80% of maximum gain in the extreme case).

Discussion

Because of the difficulty of modeling a multipassed system, comparison between theory and experiment must be somewhat qualitative, and agreements within 25% are considered good. Figures III-2 and -3 show that, although the theoretical and experimental energies agree to within 15%, the predicted pulse shapes are consistently 40 to 60% narrower than those observed. With 1.0-ns injected pulses, the pulse did narrow significantly, although not as much as expected. However, with 570-ns input pulses, the width of the observed pulse increased from 570 to 880 ps instead of decreasing to 370 ps as predicted. Figure III-3 shows that the second peak of the observed output pulse is higher than predicted. This reinforces the conclusion that the amplifier is not saturating as completely as expected.

Two parameters affect the response time of the laser medium: the dipole dephasing time T_2 and the effective rotational relaxation time τ'_{rot}.

$$\tau'_{rot} = T_1/(M\kappa), \qquad \text{(III-1)}$$

where T_1 is the longitudinal relaxation time, M is the number of laser transitions on which the system is operating, and κ is the rotational partition function.[7] The latter function is obtained from a "reservoir" model of the rotational equilibration process within a given vibrational state. The ratios τ_{rise}/T_2 and τ_{FWHM}/τ'_{rot}, where τ_{rise} and τ_{FWHM} are the risetime and width of the input pulse, should then characterize the response of the medium to a given pulse. These characteristic ratios are listed in Table III-1 for our two experiments and for the experiment reported for the high-pressure amplifier.[3] In all three cases, the input-pulse risetimes were longer than

TABLE III-I

CHARACTERISTIC LASER-MEDIA RESPONSE TIMES FOR THREE EXPERIMENTS

	T_2 (ps)	τ'_{rot} (ns)	τ_{Rise}/T_2	FWHM/τ_{rot}
Case 1	83	1.03	2.0	1.0
Case 2	83	1.54	2.3	0.37
Ref. 3	27.3	0.88	22.0	1.9

T_2, and the risetimes should not have been degraded by the amplifiers, which agrees with the experimental data. For Case 2, however, the pulse width equals 0.4 τ'_{rot}, which may explain why the pulse broadened as it traveled through the amplifier. The reservoir model used in the computer code has not been tested in this regime (especially for multiline pulses), which could explain the apparent discrepancy with theory.

Conclusions

The performance of a highly reliable, relatively simple and compact, 10-GW, subnanosecond CO_2 laser system has been demonstrated successfully. Results suggest that the 1.0-atm TEA amplifier is not effective at propagating pulses shorter than ~780 ps. Our experimental results do not agree with calculations of short-pulse propagation. This discrepancy has not been resolved. Further experimental work is under way to study the propagation of intense subnanosecond pulses during a single pass of the Lumonics amplifier, when the process has not been complicated by multipass phenomena. A new high-pressure (2000—8000 torr) double-discharge reinjection oscillator is being installed to facilitate this investigation.

The present study has also demonstrated the need for more detailed measurements on the kinetics of CO_2 laser media for pulse durations >10 ns, to determine the effects of repumping by intramode V-V processes.

SATURABLE-ABSORBER RECOVERY (A. V. Nowak)

Introduction

An earlier report[8] described double-resonance experiments designed to measure the relaxation behavior of 10.6-μm gaseous saturable absorbers after excitation by a 1-ns pulse from a CO_2 laser. We continued these recovery measurements primarily to clarify several unresolved questions.

Experimental

Three modifications were made to the double-resonance apparatus previously described. The Hg:Cd:Te detector was replaced by a faster, more sensitive liquid-helium-cooled Hg:Ge detector; the 10-cm gas cell in which the two laser beams cross was replaced by a 3.1-cm cell tilted ~45° with respect to the beams; and a germanium polarizer stack was placed in the monitor beam between the double-resonance cell and the Hg:Ge detector to reduce the intensity of unwanted scattered light.

Results and Discussion

The relaxation rates for vibrationally excited SF_6 in 10 torr of Mix 804 (1.5% total SF_6 content), extrapolated to zero pump-pulse energy are shown in Table III-II. Note that the relaxation time varies from a maximum of 1200 ns for 20M14 [i.e., pump laser tuned to the P(20) CO_2 laser line, monitor laser tuned to the P(14) line] to a minimum of 210 ns at 20M20. The relaxation times are similar for a fixed monitor and varying pump wavelength, but are very dissimilar for a particular pump line and changing monitor line.

We show the dependence of the relaxation rate on pump-pulse energy and mix pressure in Fig. III-4. Note that the relaxation time slows with increasing pulse energy. This trend was observed for all pump-monitor pairs studied, although the actual value of the slope $d\tau/dE$ differed from pair to pair. The $P\tau$ values extrapolated to zero energy are 7.84, 7.88, and 8.43 μs·torr at 5.06, 10.0, and 19.93 torr, respectively. Here, P is the pressure of Mix 804 and τ is the corresponding relaxation time.

We also studied the relaxation of SF_6 in a system consisting of Mix 804 and hydrogen. We chose H_2 because

TABLE III-II

RELAXATION TIME FOR VARIOUS PUMP LINES

10-μm Monitor Lines	Relaxation Times for 10-μm Pump Lines (ns)		
	P(14)	P(18)	P(20)
P(14)	---	---	1200
P(18)	<450	350	350
P(20)	---	240	210
P(26)	---	---	800

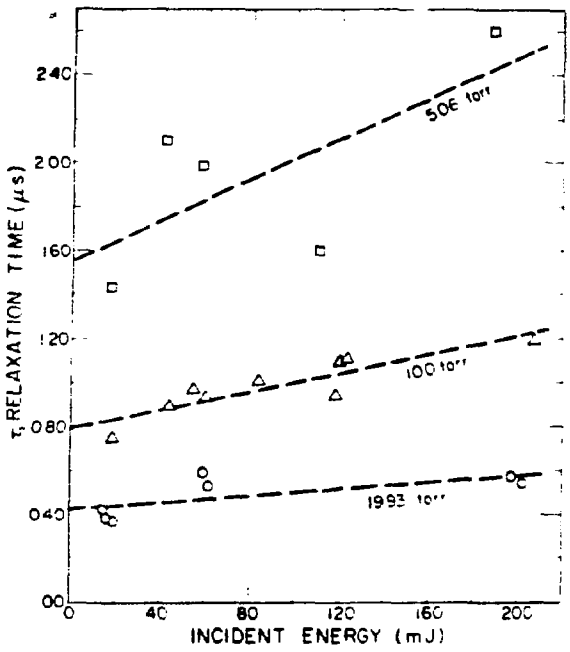

Fig. III-4.
Relaxation time τ for Mix 804 at 20M26 after excitation by a 1-ns CO_2 laser pulse. The dashed lines are a least-squares fit. The slopes are 4.66, 2.13, and 0.77 ns/mJ.

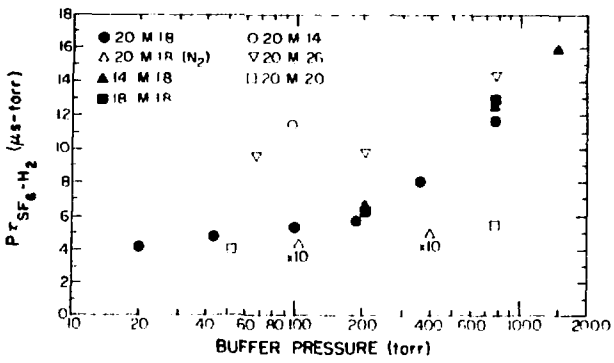

Fig. III-5.
Pτ values for the relaxation of SF_6 by H_2 molecules in the system Mix 804 + H_2, extrapolated to zero pump-pulse energy. The pressure of Mix 804 was 10 torr in all cases. The symbol XMY refers to a 10-μm P(X) pump line and to a 10-μm P(Y) monitor line.

it is among the most effective known deactivators of vibrationally excited SF_6.[9] If used as an additive to any SF_6-based saturable-absorber mix, it could produce a relaxation rate fast enough to protect against retropulse amplification in large CO_2 laser fusion systems.

Our measurements of the relaxation rate of SF_6 in Mix 804 buffered by H_2 are summarized in Fig. III-5. The pressure of Mix 804 was 10 torr. The relaxation due to H_2 was separated from that caused by Freons in the mix by use of the relation

$$P\tau = P\left[\frac{1}{\tau_{804+P}} - \frac{1}{\tau_{804}}\right]^{-1} \qquad \text{(III-2)}$$

where τ_{804} is the relaxation time observed in 10 torr of unbuffered Mix 804, and τ_{804+P} is the relaxation time observed in 10 torr of Mix 804 buffered by P torr of H_2. Note that at monitor lines P(18) and P(26) the Pτ value increases with H_2 pressure above 100 torr. This behavior is inconsistent with a simple bimolecular model for V-T relaxation of SF_6 by H_2. If the relaxation in the 804 + H_2 system were dominated by the bimolecular process

$$SF_6^* + H_2 \rightarrow SF_6 + H_2 \qquad \text{(III-3)}$$

where SF_6^* denotes a vibrationally excited SF_6, then τ would be inversely proportional to the H_2 pressure, or Pτ = constant.

We also studied the relaxation of the bimolecular mix SF_6 + H_2. Figure III-6 illustrates two extreme cases. For 20M26, the relaxation time increased drastically with pump pulse energy at 10.8 torr of H_2, but only moderately at 37.9 torr of H_2. For 14M18, we observed the opposite effect: the relaxation time decreased with increasing energy, very noticeably at 9.99 torr, but only slightly at 20.1 torr. Only 18M20 at 21.3 torr of H_2 showed a very pronounced increase in the relaxation time with increasing energy. The other cases studied, including 20M14, 18M18, and 20M40, showed only a mild increase of the relaxation time with pulse energy.

The Pτ values extrapolated to zero pulse energy for SF_6 buffered by H_2 are summarized in Fig. III-7. Note that our data are consistent with those of Steinfeld at al.[9] for the one value at which our results can be compared. The agreement is striking when we consider that their pulse was longer (0.5 μs vs 1 ns), and weaker (several kW vs several MW), and that the H_2 pressure was much lower (160 to 430 mtorr vs 10 to 80 torr).

We offer these results without interpretation. The SF_6 system has a long and deserved history for being difficult to model. We will defer any complete interpretation of

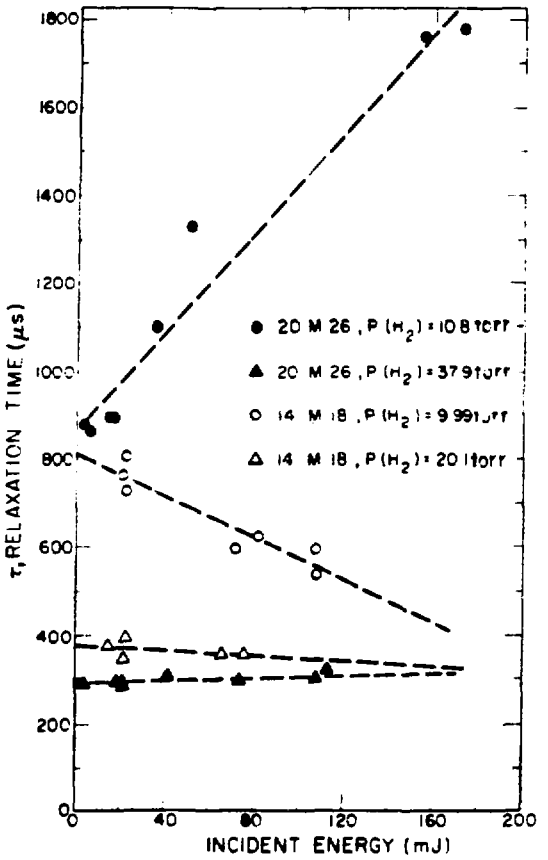

Fig. III-6.
Relaxation time τ for SF_6 in the bimolecular gas mix SF_6 + H_2, following excitation by a 1-ns CO_2 laser pulse. The SF_6 pressure was 155 ± 5 mtorr. The slopes for the case 20M26 are 5.66 and 0.151 ns/mJ, and for the case 14M18, are −2.39 and −0.313 ns/mJ.

the data until a more comprehensive data base is obtained.

Future Experiments

More work remains to be done to completely characterize the relaxation of Mix 804. First, we will prepare a table similar to Table III-II, to include five lines at which the Helios CO_2 laser amplifiers operate, P(14) through P(22). Second, we will firmly establish the dependence of the relaxation of Mix 804 on the energy of the pump pulse.

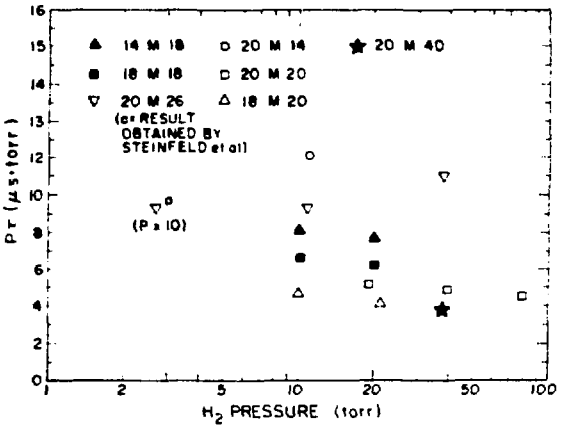

Fig. III-7.
Pτ values for the relaxation of SF_6 by H_2 in bimolecular gas mix SF_6 + H_2 extrapolated to zero pump-pulse energy. The SF_6 pressure was 155 ± 5 mtorr in all cases.

It would also be desirable to perform a detailed study of the bimolecular system SF_6 + buffer gas. This mix is easier to model than multicomponent mixes. The results on these types of systems, for example, the relaxation time as a function of the buffer series He, Ne, Ar, Kr, and Xe, could yield a useful pattern of information and would be substantially more interesting to the scientific community than the results for multicomponent mixes.

HIGH-EFFICIENCY PHASE-CONJUGATE REFLECTION IN GERMANIUM AND IN INVERTED CO_2 (B. J. Feldman, R. A. Fisher, I. J. Bigio, E. E. Bergmann)

Introduction

During this period, we generated phase-conjugate, 10.6-μm reflections from the phase grating established with counterpropagating waves in germanium samples located within an oscillating TEA double-discharge CO_2 laser cavity as well as in the CO_2 gain medium itself. The work reported[8] for germanium was the first demonstration of nonlinear phase conjugation in the infrared, and, more generally, of *intracavity* degenerate four-wave mixing. The work within the CO_2 gain medium is the first

demonstration of infrared phase-conjugation in an inverted medium. These intracavity techniques have general applicability for any laser system.

In such a conjugation process, a nonlinear interaction (such as stimulated Raman scattering, stimulated Brillouin scattering, or degenerate four-wave mixing) causes a "reflected" wave, which is the amplitude complex conjugate of the incident wave. Characteristic of the process is the fact that a phase-conjugate reflection exactly retraces the optical path of an incident wave, regardless of any phase distorters that may be in the path of the incident wave. In contrast to a normal mirror (which inverts only the component of the k-vector normal to its surface), a conjugating mirror inverts all three components.

Conjugate optics can improve the double-pass operation of laser amplifiers. As a high-quality optical beam traverses an optical system, it is unavoidably distorted because of imperfections, improper surfaces, and inhomogeneities in the gain medium. If the distorted beam is reflected by a phase conjugator, it is redirected in such a way that each distorted ray returns to its corresponding aberrating spot and the beam emerges with excellent optical quality. If so, large optical systems could be arranged so that there are many elements whose imperfect optical quality would not impair the passage of a diffraction-limited beam, and this could result in large savings for high-power laser designs.

Among the many potential applications of such a phase-conjugator, the application to laser fusion is perhaps the most exciting. In one arrangement, the fusion target is diffusely illuminated. The scattered light could travel backward through the amplifier chain, be reflected by a conjugating four-wave mixing medium, and return through the imperfect optical elements; an amplified pulse would then impinge directly on the target, obviating the need for ultraprecise target alignment. Such a phase-conjugating mirror will undoubtedly find other applications, such as providing stable laser operation even in a gain medium experiencing time-varying inhomogeneities, and, possibly, diagnosing laser-plasma interactions.

How Four-Wave Mixing Produces Phase Conjugation

For the simplest example of this effect, consider a material in which the index of refraction depends linearly upon intensity. Such a material would, for example, cause strong self-focusing or strong self-defocusing (depending on whether the refractive index increased or decreased with intensity). The nonlinear response can be described as an index of the form $n = n_0 + n_2 \langle E^2 \rangle$, or as a polarizability $\chi = \chi^{(0)} + \chi^{(3)} E^2$. The coefficients are related through $n_2 = 2\pi\chi^{(3)}/n_0$.

Consider waves E_1, E_2, and E_3 (all of the same frequency) propagating through this nonlinear material. Waves E_1 and E_2 are arranged to be precisely counter-propagating plane waves and both are assumed to be far stronger than E_3. In the [illegible]fied theory, the pair of oppositely propagating ([illegible]up) waves (at the same frequency ω) in a material exhibiting a nonlinear index of refraction, provides the conditions for which a third (probe) wave E_3, also at frequency ω, incident on the material from *any* direction, would result in a fourth wave being emitted from the sample precisely retracing the k-vector of the third wave. Although a nonlinear phenomenon is utilized, the effect is *linear* in the field to be conjugated. Therefore this technique is far more attractive than, say, stimulated Brillouin backscattering. Because the effect is linear, a superposition of E_3's will generate a corresponding superposition of E_4's, and one can readily see that any complex field is time-reversed in such an arrangement.

It is valuable to consider how the interference gives a conjugated E_4 wave. Consider first the interaction of the weak wave E_3 and of one strong wave E_1. The index change contains the term $(E_1 + E_3)^2$, which includes a cross term corresponding to a phase grating perfectly phase-matched so that the other strong wave E_2 is Bragg-scattered into the E_4 wave. Concurrently, E_2 and E_3 interfere to form a phase grating that scatters E_1 into the E_4 wave. This process is analogous to volume holography in which the writing and reading are done simultaneously.

Experimental Results in Germanium. Numerous demonstrations of *extracavity* phase-conjugate reflection via degenerate four-wave mixing in the visible have been described recently. These experiments used beams from frequency-doubled YAG lasers, from dye lasers, from ruby lasers, and from cw argon-ion lasers; four-wave mixing media included liquid CS_2; resonant, near-resonant, and two-photon resonant absorbing sodium vapor; and ruby crystal. Yet, before our work, no experiments had been performed at 10.6 μm. Demonstrating this effect in the infrared was made difficult because (1)

the effect has an ω^2 dependence, and thus, is reduced by a factor of 400 from the corresponding visible effect, (2) very strong pump waves are needed, and (3) the pump waves must be perfectly collimated and precisely retrodirected.

We recognized that one could reduce the constraints on the pump waves by requiring that they merely be complex conjugates of each other. This means that if E_1 is diverging, E_2 must be converging, and vice versa. Because the two counterpropagating waves inside an oscillating laser cavity are already complex-conjugates of each other, if the nonlinear material is placed *within* the cavity of an oscillating stable-mode laser, the material is guaranteed to be a conjugator for light of the laser frequency. As an added bonus, the circulating power within a laser can be much higher than the output power.

In our first experiments,[8,10] we obtained 2% phase-conjugate reflection by reversing a 95% flat germanium output coupler so that the substrate was internal to the optical cavity. The laser output was then used to probe the sample's conjugate reflectivity. In our recent experiments, we used thicker germanium samples. A 2.5-cm-thick, 95% reflecting end piece gave a conjugate reflectivity of 10%, whereas a 15-cm-long single-crystal boule placed in the center of the cavity gave 20% conjugate reflection efficiency. The effect did not scale simply as the sample length squared because, as the length of the nonlinear sample was increased, the circulating power within the cavity decreased. This behavior may be due to the intensity-dependent formation of an electron-hole plasma[11] in the germanium, to surface damage, or to phase-front durations of the pump waves due to nonlinear refraction. To verify that the gain medium does not impair the conjugation effect, we first passed the beam through a different path in the amplifier on the way to the germanium conjugator. When including the gain of the amplifier, the effective conjugate reflectivity of the hybrid system was 40% (using a 0.5-cm-thick germanium conjugator).

Conjugate Reflection in Inverted CO_2

In the second set of experiments, we chose to obtain conjugation using the nonlinear properties of the resonance associated with the CO_2 gain medium *itself*, and again, our intracavity technique used the counterpropagating waves already present in the oscillating laser cavity. As an added bonus of working with the nonlinearity of a partially saturated gain medium, the phase-conjugate signal is automatically amplified if the probe beam is directed through "unused" gain volume on its way to and from the interaction region.

The nonlinear process used in the CO_2 gain resonance is not merely the four-wave mixing process; because of saturation, the effect is the coherent superposition of four-wave, six-wave, eight-wave, ... processes. Because of the ambiguity in the number of waves involved, we prefer to identify this mixing process as resonant light-by-light scattering. The theory of phase-conjugate resonant light-by-light scattering was first developed by Abrams and Lind.[12] They used the well-known nonlinear susceptibility of a homogeneously broadened two-level absorber (or amplifier) which, on resonance, sets up an amplitude grating that couples the standing field and the probe field to generate the conjugate wave. As should be expected, the maximum scattering efficiency is attained when the strong counterpropagating standing waves only *partially* saturate the transition. Consequently, a limitation occurs because the depth of the amplitude grating becomes reduced as the strong waves exceed the saturation flux, and this, in turn, explains why the effect is not merely a third-order (four-wave) process.

In this experimental setup, our conventional hybrid high-pressure/low-pressure TEA laser is operated with a 10-m radius of curvature, a 35% reflecting mirror, and a flat 10% reflecting mirror. These unusually low reflectivities were chosen to reduce the circulating power within the cavity. The laser operated on the P(20) line of the 10-μm CO_2 branch; the pulse emitted from the curved output coupler was ~150 ns (FWHM) and had an energy of ~100 mJ. This corresponded to a circulating intensity of ~1.5 MW/cm^2 inside the cavity. The output of the laser was attenuated, passed through a beam splitter, and redirected through the TEA laser gain medium. Phase-conjugate reflectivity was diagnosed by using an infrared vidicon or a high-speed SAT detector on the return-signal reflection from the beam splitter. The phase-conjugate nature of the reflected light was confirmed by studying the spatial characteristics of the beam in the presence of an aberrator and in the presence of a cross-hair image placed on the beam in front of the beam splitter. In both cases the initial incident probe-beam image was preserved in the reflected image. In a single-pass configuration where the probe beam overlapped the lasing region of the gain medium only in the last 10 cm of the 91-cm discharge length, effective reflectivity was 0.5% (reflectivity defined as the peak intensity

of the phase-conjugate beam divided by the peak intensity of the incident probe beam). In a double- and triple-pass arrangement, where only the last 10 cm of the final pass through the gain medium overlapped, the lasing-region reflectivities were 35 and 250%, respectively. The enhanced reflectivity in these cases is due entirely to the amplification of the outgoing probe and incoming phase-conjugate signal en route to and from the conjugation region. The actual phase-conjugate reflectivity in the 10-cm overlap region is, in all cases, less than 10^{-2}, in accord with the Abrams and Lind theory[12] for the field and gain-medium parameters involved.

Concluding Remarks

We demonstrated that a very simple intracavity arrangement is useful in obtaining phase-conjugate reflections. The technique is readily applicable to any nonlinear material placed in an oscillating laser cavity; if the laser operates, the material is guaranteed to be a conjugate reflector for light of that frequency. Table III-III indicates the conjugate reflectivities we obtained.

By using this technique, we demonstrated for the first time a phase-conjugate reflection in the infrared using both germanium and the CO_2 gain medium itself.

TABLE III-III

PHASE-CONJUGATION RESULTS IN THE INFRARED OBTAINED WITH GERMANIUM

Interaction Length (cm)	Power (MW/cm^2)	Reflectivity (%)
1	40	2
2.54	8.7	0.8
5.08	8.7	2.3
5.08	8.0	3.4
10.16	8.0	10.3
15	25	20
Hybrid	12	40

CALCULATION OF SMALL-SIGNAL GAIN COEFFICIENTS IN CO_2 (J. C. Goldstein)

The small-signal gain coefficient of a CO_2 amplifier is frequently used as a measure of the energy stored in the device, and therefore, as an indicator of the amplifier's performance. The stability of a laser amplifier system with respect to the growth of spurious parasitic modes of oscillation—and the suppression of such parasitics by saturable absorbers—is determined in large measure by the magnitude and frequency variation of the small-signal gain coefficient. It is important, therefore, to be able to infer accurately the molecular energy-level population densities from small-signal gain measurements, and conversely, to be able to predict the small-signal gain coefficient from calculated medium conditions (such as vibrational and rotational temperatures).

The usually straightforward relationship of the small-signal gain coefficient to molecular populations is somewhat obscured in CO_2 by the presence of gain on many closely spaced lines. The gain coefficient at any particular frequency is the sum of the gains, each one evaluated at that frequency, contributed by many different transitions. In addition to the contributions from various rotational lines of the main vibrational transition (the $00^0 1 \rightarrow 10^0 0$ transition in the case of the 10.6-μm band), there can also be contributions from transitions between higher lying vibrational states due to near coincidences of some of the rotational lines of these transitions with those of the main transition.

We constructed a code to compute the small-signal gain coefficient at any specified frequency by summing over P- and R-branches of the following transitions in CO_2.

10 μm		9 μm
$00^0 1 \rightarrow 10^0 0$	main	$00^0 1 \rightarrow 02^0 0$
$00^0 2 \rightarrow 10^0 1$	sequence	$00^0 2 \rightarrow 02^0 1$
$00^0 3 \rightarrow 10^0 2$	sequence	$00^0 3 \rightarrow 02^0 2$
$01'1 \rightarrow 11'0$	hot	$01'1 \rightarrow 03'0$

This notation abbreviates the correct notation of the lower levels, which are coupled Fermi resonance pairs; e.g., "10°0" means $|10°0, 02°0|_I$ and "02°0" means $|10°0, 02°0|_{II}$. Only the principal isotopic variant is considered $|C^{12}(O^{16})_2$; natural abundance, 98.4%|.

The code was used to compute the line-center absorption coefficient of the 10.6-μm P(20) line in pure CO_2 and of mixtures of He, N_2, and CO_2 in thermal equilibrium at various temperatures and pressures. The results agree with recent published measurements[13,14] to within a few percent—better in most cases than the claimed experimental uncertainty. In comparing the predictions of the code with a recent gain measurement,[15] we varied the vibrational and rotational temperatures until we obtained good agreement between the code and the measured value of the 10.6-μm P(20) line-center small-signal gain coefficient. We then computed the line-center gain coefficients for other lines without changing any parameter in the code. The results are shown in Figs. III-8 and -9 for various lines of the P- and R-branches of the 10.6-μm transition. The effects of including all overlapping lines (as opposed to a single transition) in the calculations are shown in Fig. III-10.

The code appears to calculate small-signal gain or absorption coefficients in CO_2 to an accuracy of a few percent. It is conceivable, however, that for higher temperatures and gas pressures, it may be necessary to include more transitions in the calculation.

DIRECT MEASUREMENT OF NONLINEAR DIELECTRIC PROPERTIES IN GERMANIUM (D. E. Watkins, C. R. Phipps, Jr., S. J. Thomas)

Introduction

The use of germanium in high-power infrared laser systems and in four-photon mixing[16] and phase-conjugation[17] experiments has renewed interest in its nonlinear optical properties. Conversion efficiencies obtained in these experiments suggested very large values for the infrared nonlinear susceptibility in germanium. In addition, more accurate knowledge of the nonlinear index of refraction in NaCl and germanium are of great importance for our Helios and Antares laser systems, but no direct measurements of these crucial quantities in the 10-μm region were available. We initiated some appropriate experiments and used time-resolved rotation of the axes of elliptically polarized light to measure the nonlinear dielectric tensor in germanium at 10-μm wavelength.

Owyoung[18] has shown that, for an elliptically polarized plane wave propagating along a 100 axis in a transparent cubic crystal, the angle of rotation can be determined when the major axis of the ellipse lies along a 100- or 110-crystal axis.

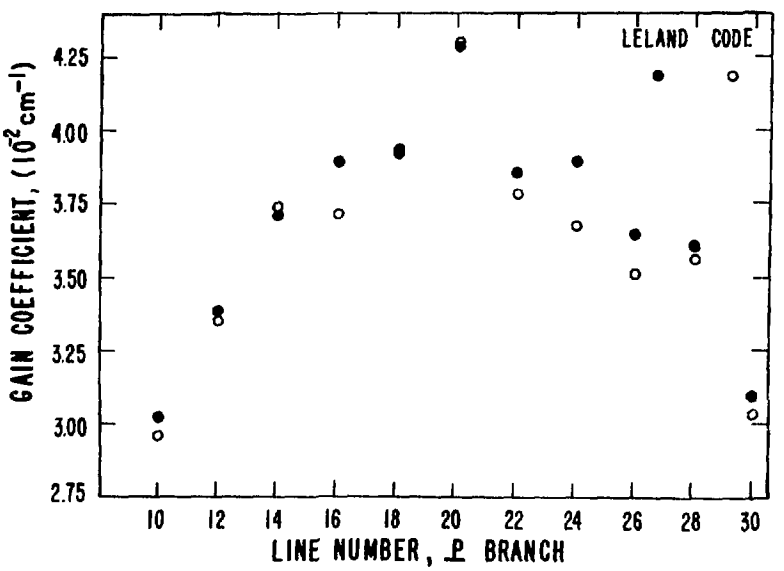

Fig. III-8.
Calculated and measured[16] line-center gain coefficients for several lines of the P-branch of the 10-μm transition.

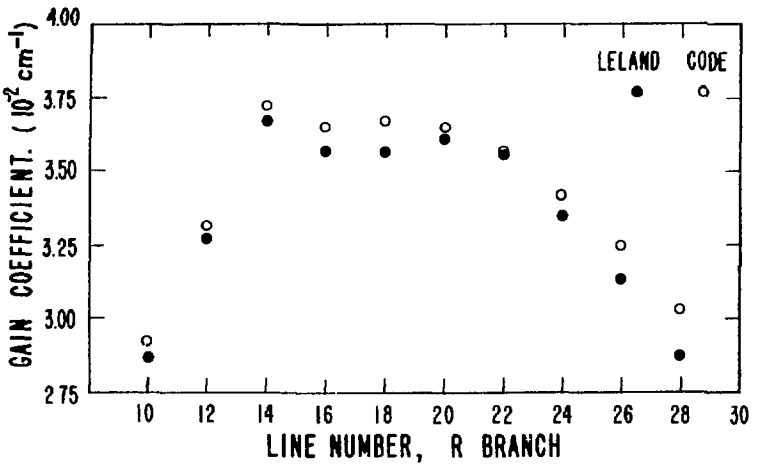

Fig. III-9.
Calculated and measured[16] line-center gain coefficients for several lines of the R-branch of the 10-μm transition.

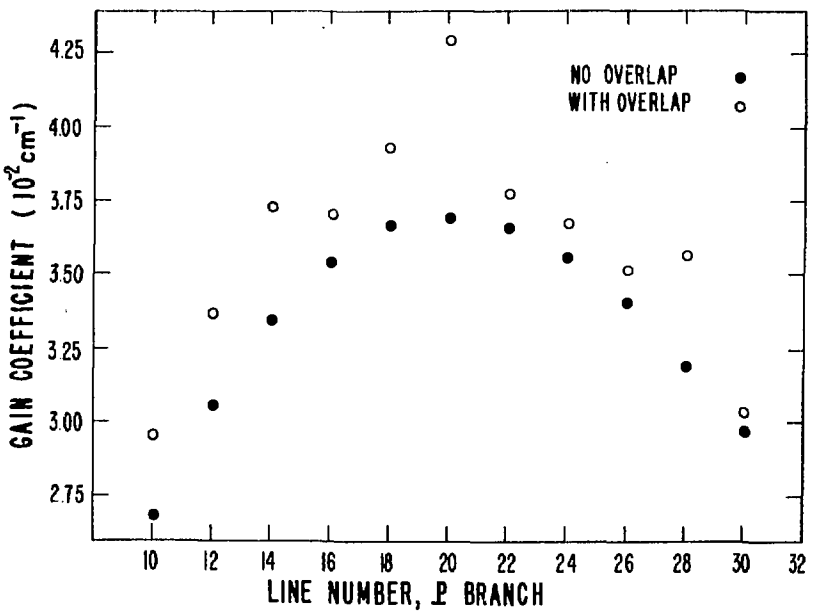

Fig. III-10.
Comparison of calculated gain coefficients showing the effects of neglecting overlapping spectra from adjacent lines.

Results

An elliptically polarized CO_2 laser beam was passed through samples of Ge, CS_2, and NaCl. A polarization splitter was oriented at 45° to the axis of the ellipse. The separated S- and P- polarized signals were time-resolved via fast pyroelectric detectors to obtain peak intensities I_s and I_p. The ratio of these intensities can be related to the angle of ellipse rotation, and hence, to the components of the nonlinear susceptibility of the material.

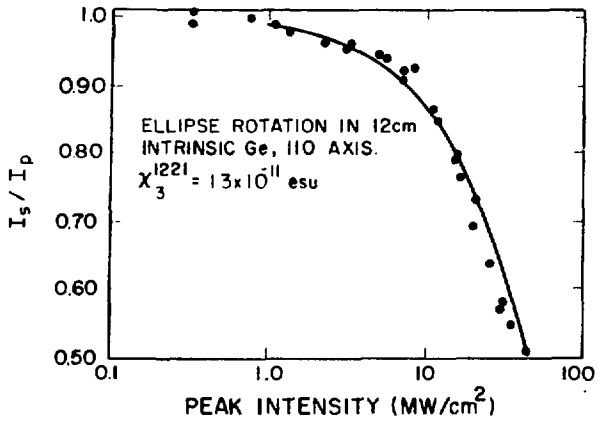

Fig. III-11.
Dependence of ratio I_s:I_p on peak intensity for the value of nonlinear susceptibility χ_3 given. The dots are experimental values.

Our system was calibrated against CS_2. In 10 cm of CS_2, we found $\chi_3^{1221} = (3.9 \pm 1.0) \times 10^{-13}$ esu compared to $(4.7 \pm 1.6) \times 10^{-13}$ esu reported by Moran et al.[19]

Measurements made on a 12-cm-long single-crystal intrinsic germanium sample are shown in Fig. III-11. The values obtained from this sample are $\chi_3^{1111} = (2.5 \pm 0.3) \times 10^{-11}$ esu and $\chi_3^{1221} = (1.3 \pm 0.2) \times 10^{-11}$ esu. These values are substantially lower than previously reported. Wynne[20] used third-order optical mixing to infer $\chi_3^{1111} = (1 \pm 0.5) \times 10^{-10}$ esu and $\chi_3^{1221} = 0.6\ \chi_3^{1111}$. However, recent work in four-photon mixing[16] and phase conjugation[17] has produced smaller effects than expected on the basis of Wynne's work.

A 17.8-cm-long piece of polycrystalline NaCl produced no measureable result. This experiment would have been sensitive to $\chi_3^{1221} = 3 \times 10^{-14}$ esu in NaCl, consistent with Smith et al.,[21] who found $\chi_3^{1221} = (2.6 \pm 1.3) \times 10^{-14}$ esu via four-photon mixing in NaCl at 1.06 μm.

The results for germanium indicate a lower efficiency for four-photon mixing and phase conjugation than previously assumed. Also, they imply a 1/4-wavelength distortion for intensity-length products of ~0.5 GW/cm, which has been confirmed by brightness degradation measurements.[22] In NaCl, these measurements imply that 1/4-wavelength phase distortion will occur for intensity-length products that are greater than 45 GW/cm. Further measurements with 20 times greater sensitivity are under way to correct the upper bound reported here with accurate measurements of χ_3 in NaCl.

SUBNANOSECOND EXTINCTION OF CO_2 LASER SIGNALS VIA BULK PHOTOIONIZATION IN GERMANIUM (C. R. Phipps, Jr., S. J. Thomas, D. E. Watkins)

Introduction

Recent reports of efficient phase conjugation[23] and four-wave mixing[24] of CO_2 laser signals in germanium have renewed interest in the nonlinear optical properties of this material. The ultimate efficiency of these processes is limited by the magnitude of the nonlinear susceptibility and by the intensity-length product available in the interaction region. The former is somewhat smaller than had been supposed,[25] and the useful interaction length has practical limits set by loss, nonlinear refraction, or the signal duration itself.

We found that a definite intensity limit also exists for propagation in intrinsic or optical-grade germanium, determined by the sudden onset of bulk photoionization at levels only moderately higher than those required for efficient mixing or conjugation. The threshold intensity was relatively independent of wavelength in the 9- to 10-μm region, and varied only slightly for pulse durations ranging from 1 to 50 ns. Ionization thresholds were lower in optical grade than in intrinsic material, but much higher in p-type gallium-doped germanium. Because the saturation intensity[26] of the intraband hole absorption is 3.2 MW·cm^{-2}, and because the Abrams-Lind Model[27] predicts efficient phase-conjugation in such saturable absorbers, the increased threshold in p-type germanium may permit the attainment of four-wave mixing efficiencies considerably higher than those seen previously.

Experiments and Results

The effects studied were completely reversible, using intensities well below surface damage thresholds. Bulk ionization was revealed by transverse photoconductive signals with decay times varying from nearly 1 ms in pure germanium to 50-100 μs in optical-grade material. These results were consistent with absorption decay rates observed in low-power, 9-μm probe measurements. Transmission was measured for intense, collimated, single- or multiline CO_2 laser signals in samples of various lengths. Both time-averaged and instantaneous quantities were measured; time resolution of our diagnostic system was 100 ps.

The time-resolved data for uniform illumination clearly show that the instantaneous, high-intensity transmission function drops to zero (irreversibly on nanosecond time scales) whenever the input intensity exceeds a critical value $I_b \approx 200$ MW·cm^{-2}. The peak output intensity is essentially a constant, and the fall time of the output signal can be as small as 400 ps, indicating very rapid plasma formation.

Bearing in mind that absorption in germanium is dominated by the intravalence-band transitions in this spectral range, and taking proper account of saturation, we infer peak photoplasma densities of 2×10^{15} cm^{-3} from the experimental transmission data, as indicated in Fig. III-12.

We also used a second method to measure the nonlinear transmission properties of germanium, with the input CO_2 laser beam brought to a real internal focus. We observed that internal damage was prevented by plasma formation. In addition, the transmission for a space-time Gaussian beam in this configuration was highly predictable over four orders of magnitude in input intensity. Applications of this highly reproducible transmission function include passive intensity-limiting for detector protection, and passive pulse-shortening. An additional application of this work is passive intensity-range compression for more effective comparison of prepulses and main pulses in target-illumination diagnostics, where the intensities to be compared differ by many orders of magnitude.

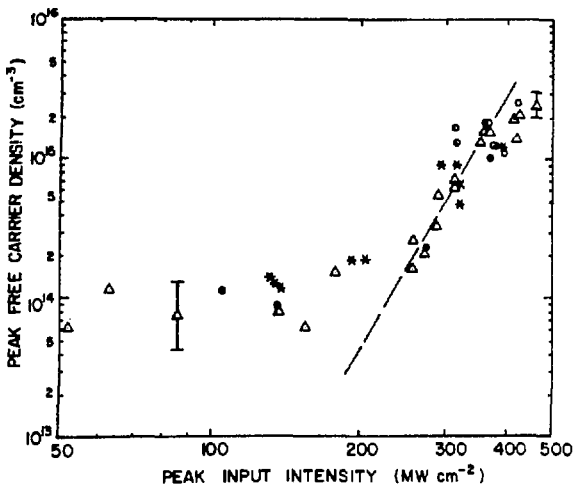

Fig. III-12.

Free carrier densities vs input intensity inferred from residual transmission measurements on germanium samples for lengths of 5.7 cm (0), 9.7 cm (Δ), and 14.2 cm (*). The trend line represents $n \propto I^6$.

HIGH-PRESSURE ENRICHMENT OF LIGHT ISOTOPES (J. B. Marling, I. P. Herman, LLL; S. J. Thomas)

Introduction

A series of joint LLL-LASL experiments, designed to demonstrate enhanced deuterium enrichment in certain Freon compounds by using ns-duration CO_2 laser signals, was completed successfully at LASL. Higher than 1000-fold enrichment was obtained, and the short laser pulses permitted the use of relatively high gas pressures for this type of work.

Laser separation of light isotopes by multiple-photon dissociation is becoming more attractive, using pulsed CO_2 lasers as an excitation source. Very high single-step enrichment factors were observed when the proper working molecule was chosen. For deuterium separation, single-step enrichment factors above 1000 with high yield have been obtained in 2,2-dichloro-1,1,1, -trifluoroethane (Freon 123) at 0.5 torr using standard CO_2 TEA laser technology near 10.65 μm.[28] For ^{13}C separation, single-step enrichment factors up to 65 were observed in CF_3Br at room temperature,[29] but enrichment dropped rapidly above 1 torr.[29]

Extension of these performance parameters into the 100-times higher pressure regime is essential to reduce gas pumping costs to competitive levels and to achieve a realistic photochemical reactor size, especially for deuterium separation. Deuterium and ^{13}C enrichment using these molecules was studied experimentally and is reported here as a function of pressure and incident fluence for a variety of CO_2 laser pulse lengths (2 to 1000 ns).

Experiment and Results

The CO_2 laser used was either an oscillator-amplifier with variable short-pulse duration or (at LLL) a standard TEA laser with a 100-ns gain-switched initial spike followed by a weak 1-μs tail. The LASL oscillator was modelocked with a 12-ns switchout gate for selection of a single 2-ns FWHM pulse for amplification. With the modelocker turned off, a 12-ns FWHM pulse was switched out for amplification. Pulses of 80 ns without

tails were available by bypassing both the switchout and modelocker, and by controlling the laser gas composition.

We evaluated deuterium using mixtures of CF_3CHCl_2 (Freon-123) containing ~0.4% CF_3CDCl_2. We also performed several experiments using Freon-123 with natural deuterium isotopic abundance (~0.015% D). The primary deuterium-containing photoproduct is trifluoroethene, ($CF_2 = CFD$),[28] and the isotope content of the product was determined by mass spectrometry. The CF_3Br (bromotrifluoromethane) decomposes to yield ^{13}C-enriched CF_3CF_3 as primary photoproduct;[29] CF_3Br of natural isotopic abundance, containing ~1.1% ^{13}C, was always used. For deuterium separation, we used the P(26) 10.65-μm line for photolysis, and for ^{13}C, we used the P(24) 9.59-μm CO_2 laser line.

In the initial ^{13}C enrichment studies in CF_3Br, reported in Ref. 29, the low-pressure single-step enrichment factor of 65 dropped 50% by 0.8 torr and dropped 10-fold by 3 torr. By using 2-ns CO_2 laser pulses in our study, the single-step ^{13}C enrichment factor at 3 torr was 43. It decreased as a very slow function of pressure to 27 at 100 torr, and to 22 at 225 torr.

Deuterium enrichment was measured by using 12-ns dissociating pulses at a peak focal fluence of 8 to 10 J/cm^2. The single-step deuterium enrichment factor was constant at 900 ± 50 in the trifluoroethene product over the range 1 to 600 torr. However, the yield at 100 torr was too low to determine isotopic enrichment. Hence, high pressure quenched the photoproduct yield without decreasing the enrichment. Use of shorter (2-ns) dissociating pulses again resulted in near-1000-fold enrichment, but with apparently higher yield because we obtained a sufficient amount of photoproduct at 100 torr for isotope analysis. Freon-13 of natural isotopic abundance was also examined, and yielded a deuterium enrichment factor of 1900 ± 400 at 30 torr, and of 1500 ± 100 at 100 torr. The use of relatively long (80-ns) dissociating pulses did not significantly decrease the isotopic enrichment at higher pressures. However, a higher fluence of 20 J/cm^2 was used, reducing overall enrichment (see Fig. 2 of Ref. 28), but it remained as high as 220 ± 50 throughout the pressure range from 0.3 to 30 torr.

In ir photolysis of a sample in which the minority isotope is the absorbing molecule, the effect of collisions on yield should be analyzed as a function of laser fluence. Above the saturation fluence (for the resonantly absorbing molecule of the minority), an increase in pressure can lead to increased ir dissociation of the nonresonant species, which can absorb photons only after collisions with the resonant molecule. The increase occurs without greatly decreasing the association yield of the resonantly absorbing minority isotope. Therefore, at high fluences the isotopic enrichment will fall with increasing pressure, perhaps with little change in yield. However, at fluences between dissociation threshold and saturation, collisions will quench the resonant isotope, and the nonresonant species, therefore, will not be able to dissociate. Consequently, as pressure increases, net yield will fall, but isotopic enrichment may vary only slightly. However, we ignore the importance of collisions in removing the multiple-photon absorption bottleneck that appears at very low fluences. Our conclusions seem to be especially true for deuterium separation in Freon-123 where the single-step enrichment factor is very fluence-sensitive,[28] but showed only slight sensitivity to operating pressure.

Conclusion

The practicality of using lasers for the separation of light isotopes has been greatly enhanced by demonstrating that high single-step isotope enrichment can be maintained even at pressures up to 1/3 atm. Isotopically selective multiple-photon dissociation was achieved with 2-ns CO_2 laser pulses, permitting 1500-fold enrichment of naturally occurring deuterium in pure Freon-123 at 100 torr and 22-fold enrichment of ^{13}C in CF_3Br at 225 torr.

The LASL part of this work was supported by the Inertial Confinement Fusion Program because of the existence of high-intensity, short-pulse CO_2 lasers. Improved efficiency of deuterium separation will benefit the fusion program by providing an improved fuel source.

REFERENCES

1. F. Skoberne, Comp., "Laser Fusion Program, July 1—December 31, 1977," Los Alamos Scientific Laboratory report LA-7328-PR (December 1978).

2. B. J. Feldman, "Multiline Short Pulse Amplification and Compression in High-Gain CO_2-Laser Amplifiers," Opt. Commun. 14, 13 (1975).

3. H. C. Volkin, "Calculation of Short-Pulse Propagation in a Large CO_2-Laser Amplifier," J. Appl. Phys., to be published.

4. R. J. Harrach, "Effect of Rotational and Intramode Vibrational Coupling on Short-Pulse Amplification in CO_2," IEEE J. Quantum Electron. QE-11, 349 (1975).

5. E. E. Stark, Jr., "Measurement of the 10°0-0-02°0 Relaxation Rate in CO_2," Appl. Phys. Lett. 23, 335 (1973).

6. R. R. Jacobs, K. J. Pettipiece, and S. J. Thomas, "Rate Constants for the CO_2 020-100 Relaxation," Phys. Rev. A 11, 54 (1975).

7. G. T. Schappert, "Rotational Relaxation Effects in Short-Pulse CO_2 Amplifiers," Appl. Phys. Lett. 23, 319 (1973).

8. F. Skoberne, Comp., "Inertial Fusion Program, January 1—June 30, 1978," Los Alamos Scientific Laboratory report LA-7587-PR (May 1980).

9. J. I. Steinfeld, I. Burak, D. G. Sutton, and A. V. Nowak, J. Chem. Phys. 52, 5421 (1970).

10. E. E. Bergmann, I. J. Bigio, B. J. Feldman, and R. A. Fisher, Opt. Lett. 3, 82 (1978).

11. C. R. Phipps, Jr., Los Alamos Scientific Laboratory, private communication (1978).

12. R. L. Abrams and R. C. Lind, Opt. Lett. 2, 94 (1978), and Erratum, Opt. Lett. 3, 205 (1978).

13. A. M. Robinson and Y. -K. Hsieh, J. Appl. Phys. 48, 1589 (1977).

14. A. M. Robinson and N. Sutton, Appl. Opt. 16, 2632 (1977).

15. W. T. Leland, M. J. Kircher, M. J. Nutter, and G. T. Schappert, J. Appl. Phys. 46, 2174 (1975).

16. N. Lee, R. Aggarwal, and B. Lax, Opt. Commun. 9, 401 (1976).

17. E. Bergmann, I. Bigio, B. Feldman, and R. Fisher, Opt. Lett. 3, 82 (1978).

18. A. Owyoung, I.E.E.E. J. Quantum Electron. QE-9, 1064 (1973).

19. M. Moran, C. She, and R. Carman, I.E.E.E. J. Quantum Electron. QE-11, 259 (1975).

20. J. Wynne, Phys. Rev. 178, 1295 (1969).

21. W. Smith, J. Bechtel, and N. Bloembergen, Proc. Laser Induced Boulder Damage in Optical Materials, 7th Annual Symp. (1976), p. 321.

22. C. Phipps, Jr., Los Alamos Scientific Laboratory, unpublished data (1978).

23. E. E. Bergmann, I. J. Bigio, B. J. Feldman, and R. A. Fisher, Opt. Lett. 3, 82 (1978).

24. N. Lee, R. L. Aggarwal, and B. Lax, Opt. Commun. 19, 401 (1976).

25. D. E. Watkins, University of Washington, unpublished data (1978).

26. C. R. Phipps, Jr., and S. J. Thomas, Opt. Lett. 1, 93 (1977).

27. R. L. Abrams and R. C. Lind, Opt. Lett. 2, 94 (1978).

28. J. B. Marling and I. P. Herman, Appl. Phys. Lett. 34 (February 1979).

29. M. Gauthier, P. A. Hackett, M. Drovin, R. Pilon, and C. Willis, Can. J. Chem. 56, 2227 (1978).

IV. TARGET EXPERIMENTS, DIAGNOSTICS, AND MILITARY APPLICATIONS
(G. H. McCall)

In an integrated program of target experiments, theory, and design, we are establishing a fundamental understanding of laser-target interactions, particularly of the relevant plasma physics and hydrodynamics. Experimental and theoretical efforts have addressed the scaling of consistent models to higher laser intensities. Emphasis has been on the development and demonstration of experimental techniques that will determine conclusively the performance of present and future targets. A modest experimental effort is directed toward military applications.

The laser fusion process calls for new diagnostic techniques having spatial and temporal resolutions in the submicrometer and 1- to 100-ps regime. These needs are being met with a vigorous diagnostics program in such areas as laser calorimetry, charged-particle and neutron detection, x-ray spectrometry, and subnanosecond streak camera development.

EXPERIMENTS (R. P. Godwin, D. B. Giovanielli)

Introduction

This reporting period was an exciting one. The Helios laser is maturing as a complete laser-fusion research facility. It has delivered previously unattainable CO_2 laser power and energy to various targets. Exploding-pusher GMB targets served as a test of the new facility and verified our confidence in the understanding and intensity scaling of those targets. Neutron yields exceeding 10^8 were obtained for the first time using CO_2 radiation powers of 3 TW. In our first experiments, we used plastic-coated GMB targets designed to achieve high fuel density, but relatively low temperature. These targets were direct predecessors of long-range fusion reactor targets. Their neutron yields (up to 10^8) provided enough data for statistically meaningful parametric studies. This class of targets is sensitive to such important aspects of laser fusion as hot-electron preheat, which is unimportant in exploding-pusher experiments. Although these high-density targets are difficult to diagnose by simple techniques that provide uniquely interpretable information, initial experiments are providing information consistent with our code calculations and are determining our diagnostic development efforts, particularly in the areas of neutron diagnostics with high temporal resolution and x rays. The measurement of the fastest plasma protons at Helios gives additional support to the hot-electron temperature scaling as $(I\lambda^2)^{1/3}$, where I is the focal power/area and λ the laser wavelength, which has proved to be a useful laser diagnostic. Energy transport questions continue to be dominant in laser-plasma interactions, particularly in the interpretation of experiments. Conceptually simple experiments performed at Gemini showed that electron currents flowing toward targets through support structures, and through target potentials of several hundred kV may be important vectorial factors in transport—factors previously discounted in hydrodynamics calculations.

Helios Exploding-Pusher Experiments (D. Giovanielli)

Exploding-pusher experiments were the first to be undertaken at the Helios laser facility. Because the behavior of such targets is well known, they were chosen for the first full-scale integration of laser operations, beam diagnosis, alignment and focusing, target handling, and target diagnosis systems. Performance of all of those system elements can be normalized against earlier experience.

In the first sequence, 32 DT-filled GMB targets were irradiated with total laser energies varying from 750 to 4100 J. Simultaneity of the eight Helios laser beams was previously measured to be within 50 ps. Several targets were irradiated with fewer than eight beams, but the suprathermal electrons, which drive the explosion of the thin-walled glass shell, symmetrized the target. There was no loss of ability to calculate target thermonuclear

yield when two or more laser beams were used to irradiate the targets (single-beam experiments were not attempted).

Target diagnostics included neutron yields, fast (isothermal front) ion velocities, x-ray pinhole images, high-resolution x-ray spectra (Si lines), and multichannel x-ray spectra from 10 eV to 4 keV.[1] The high-resolution spectroscopy used instruments placed within 3 cm of the target position. No reduction in parasitic oscillation threshold of the laser amplifiers could be observed in such proximity. X-ray line spectra displayed features not previously observed, such as both hydrogen-like and helium-like silicon continuum edges simultaneously, allowing triply redundant temperature determinations. The successful operation of these instruments verified our ability to design and produce thin filter window assemblies that can be used near the Helios targets. Integration of the multichannel spectrometer and x-ray diode data yielded x-ray emission efficiencies (incident laser light re-emitted as x rays) of 2%, in agreement with previously obtained values.

X-ray pinhole camera images from seven shots are shown in Fig. IV-1. Rippling of the inner imploded glass surface is suggestive of hydrodynamic instability; however, because laser light remains incident long after the time of peak compression, and these are time-integrated photographs, deduction of quantitative information from this apparent shell breakup is difficult. Radiochemical diagnostics now being developed may be more sensitive to shell breakup at the time of peak compression and thermonuclear burn.

Table IV-I lists the initial target parameters, equivalent trapezoidal laser pulse shapes, calculated and measured neutron yields, and velocities of the fastest ions observed. The ion velocities match data obtained at the Single Beam System and Gemini, and lead to a scaling of suprathermal electron temperature with incident laser intensity of $I^{1/3}$, in agreement with simulation results. Neutron yields were calculated by using an analytical model[2] and the measured target and laser parameters. The absorbed laser energy fraction was not measured in these experiments; however, in the calculations of expected yield we assumed 25% absorbed energy, as measured previously with spherical targets.[3] We assumed 35% of the absorbed energy to be lost to reradiation, fast-ion production,[4] suprathermal electron emission,[5] and conduction along the supporting stalk.[6] The excellent agreement between measured and calculated neutron yields confirms both the model and our input assumptions.

Evidence of Adiabatic Implosion of GMBs (T. H. Tan)

A most significant result from our target experiments at Helios is evidence of adiabatic implosion. It is essential for the success of the laser fusion program that adiabatic implosion processes be investigated as soon as possible. Exploding-pusher experiments have contributed valuable information, but the conditions that exist in these targets are far from those that are believed required to produce breakeven of higher yields. Helios now produces enough energy on target so that, for the first time, we can design targets with predicted densities higher than that of solid DT, and we can produce the same adiabatic conditions in the fuel as those of current breakeven designs.

The 20XLD goal (4 g/cm^3) was chosen even though predictions indicate that, for certain designs, much higher densities can be reached by targets irradiated by Helios. Also, it is important to study phenomena associated with the early adiabatic phases of laser-driven implosions, and complicated targets depend on poorly understood physical processes that are extraneous to the study of the implosion itself. Therefore, we needed as simple a target as possible so that the implosion system could be diagnosed in a straightforward way that would require only modest extrapolation from existing experimental results.

The achievement of adiabatic compression to high fuel densities requires, first, adequate shielding of the target interior against laser preheat, and second, efficient conversion of absorbed laser energy into compressional motion. In our targets, shielding from hot-electron preheat is accomplished by adding a low-density parylene ablator to a bare GMB (exploding-pusher) target. The low-density material allows a geometrically thick ablator. This results in the largest possible outer radius for a target of given mass. Assuming the laser beams can be defocused to flood the target surface nearly uniformly, thereby minimizing the intensity, the energy spectrum of hot electrons produced during laser absorption should be cooler for these than for smaller targets. Thus, less material is required for hot-electron preheat shielding because the electron range decreases rapidly with energy.

With such targets, we have measured neutron production time-delays that are significantly longer than the 1-ns laser pulse, implying that the implosion is sustained adiabatically after the laser pulse has been turned off. The experimental data are crucial for demonstrating the

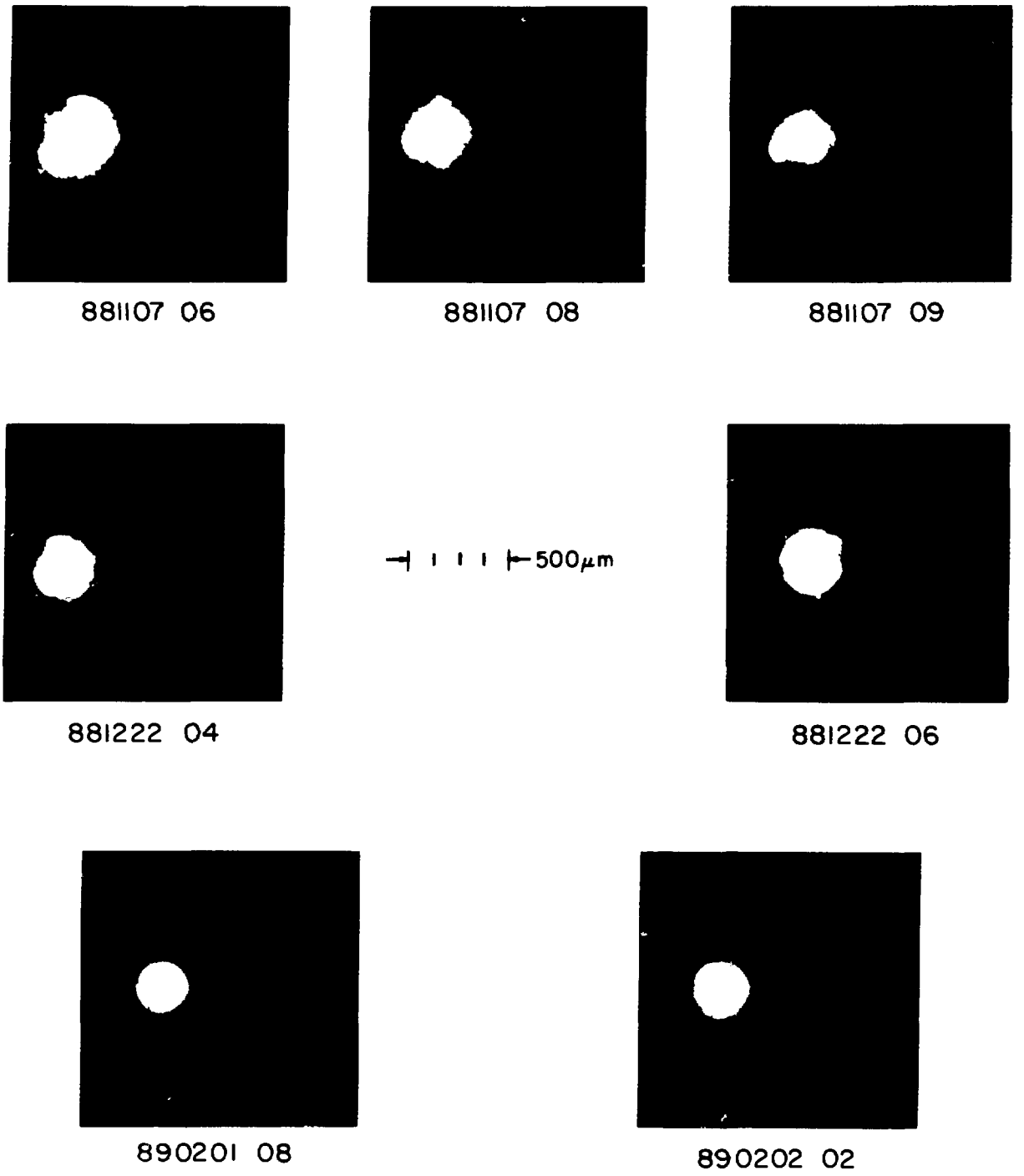

Fig. IV-1.
Time-integrated x-ray pinhole camera images from seven exploding-pusher shots at Helios.

TABLE IV-I

INITIAL TARGET PARAMETERS AND DATA FROM 32 EXPLODING PUSHER EXPERIMENTS AT HELIOS USING DT-FILLED GMB TARGETS

	Initial Target Parameters				Equivalent Trapezoidal Laser Pulse						Neutron Yield		
Shot Number	Radius (μm)	Wall Thickness (μm)	DT Fill (mg/cm³)	Ion Front Velocity (10^7 cm/s)	Rise-time (ps)	Peak Time (ps)	Fall Time (ps)	Total Energy (J)	Peak Power (TW)	No. of Laser Beams	Obs. (10^8)	Calc. (10^8)	Obs. Calc
88100517	196	0.99	2.0	3.40	374	115	855	2905	4.0	7	1.6	5.4	0.30
88101215	162	1.29	2.0	3.32				2189	3.0	7	1.42	1.7	0.84
88102411	150	1.0	6.75	3.45				3990	5.5	7	0.42	3.4	0.12
88102602	168	1.22	2.0	3.12				3984	5.5	8	2.0	8.1	0.25
88102603	117	1.08	2.0	2.30				753	1.0	2	.066	.074	0.89
88102604	159	0.99	5.85	3.21				3217	4.4	7	0.8	2.3	0.35
88102605	258	1.25	2.25	2.83				2154	3.0	5		2.2	
88102607	275	1.01	1.58	3.54				1494	2.1	4	0.26	0.79	0.33
88110705	173	1.57	2.0	2.95	471	068	636	1428	2.3	4	0.41	0.41	1.00
88110706	217	0.98	2.25	2.89	320	071	989	2476	3.4	6	2.3	5.4	0.43
88110708	189	0.88	1.8	3.07	360	110	763	2329	3.5	6	3.5	4.2	0.83
88110709	198	1.18	2.25	3.04	375	198	729	1840	2.5	6	1.1	1.25	0.88
88110916	225	1.16	2.255	2.97	374	115	855	2296	3.2	6	2.3	2.9	0.79
88112803	195	0.99	6.75	3.25				1770	2.4	4	0.22	0.27	0.81
88113002	195	0.95	2.0	3.19			1179	2693	3.1	6	2.2	2.7	0.81
88113004	200	0.83	2.0	3.39				3133	3.5	7	1.6	4.2	0.38
88113005	183	0.85	2.25	3.39				3015	3.3	7	0.57	3.1	0.18
88113007	144	0.99	6.75	3.20				2529	2.8	6	.05	0.48	0.10
88113008	140	1.02	6.5	2.60				1537	1.7	4	0.14	0.10	1.40
88122107	101	0.99	1.8	3.20				2356	2.6	8		0.53	
88122204	148	1.05	6.75	2.52				1841	2.0	6	.045	0.18	0.25
88122206	145	1.13	6.75	2.52				~1616	1.8	6	.055	0.12	0.46
89010405	099	1.11	2.0	2.50	221	097	1191	4100	5.1	7		6.7	
89012310	168	0.58	2.25	2.50	374	115	1179	717	0.79	2		.042	
89012311	161	1.03	2.25	2.90				1395	1.5	4	0.13	0.29	0.45
89012903	175	1.12	2.25	2.40				689	0.76	2		.021	
89012904	165	0.85	2.25	2.30				684	0.76	2	.04	0.3	1.33
89012905	158	0.88	2.25	2.76				1444	1.6	4	0.3	0.34	0.88
89013003	157	1.16	6.75	2.90				2280	2.5	6	0.4	0.39	1.03
89013005	142	1.1	6.75	2.95				3040	3.4	8	1.3	0.90	1.44
89020108	148	148	1.05	6.75	2.90			2820	3.1	8	0.56	0.71	0.79
89020202	146	0.80	6.5	2.90				2634	2.9	6	0.51	0.49	1.04

achievement of high fuel compression and high burn efficiency by inertial confinement. They also provide an important check on the reliability of the code prediction that is so necessary to the laser fusion program.

These results were obtained with GMB targets tailored for systematic investigation of high-density pellet compression. Each GMB is 300 μm in diameter with a wall thickness of 1 μm. They are coated with different thicknesses (0-100 μm) of parylene and filled with 30 atm of DT gas.

The implosion time is measured as a delay in excess of the expected arrival-time difference between the x-ray fiducial and the prompt-neutron pulse from an exploding-pusher target. Ultrafast TOF detectors and scopes are used.

Targets with coatings of parylene 54-62 μm thick produced consistent data. By increasing the amount of laser energy on target from 2.2 to 3.0 kJ, the neutron yield increased from 9×10^6 to 2.6×10^7, while the neutron production time delay decreased from 2 ± 0.5 ns to 1.5 ± 0.5 ns, in agreement with code predictions. Longer drive-in time is due to smaller energy transfer resulting in lower fuel temperature and smaller yield. The longest implosion time was 2.8 ± 0.5 ns on a target with a plastic coating 88 μm thick and illuminated by 3.6 kJ of laser energy. It produced 3×10^6 neutrons. X-ray pinhole photography corroborated the behavior of these targets that we inferred from neutron measurement.

Preliminary data and code predictions both indicate a consistent relationship among implosion time, yield, and compressed fuel density.

Measurement of Fastest Ion Velocity (T. H. Tan)

The measurement of the fastest ion velocity has been a powerful plasma diagnostic for laser-matter interactions. These fastest ions, which are protons with velocities exceeding 10^9 cm/s, were first detected by us in measurements done at KMS Fusion with a scintillator-photomultiplier detector designed for measuring charged nuclear reaction products.

We reported previously[7] that $v_i \propto \phi_L^{1/6}$, where v_i is the fastest ion velocity and ϕ_L is the laser flux. From the isothermal expansion model (Ref. 8) $v_i \propto C_s$, where C_s is the ion sound speed, the hot-electron temperature T_e can be related to ϕ_L as $T_e \propto \phi^{1/3}$. This agrees with computer plasma simulation work,[9] which suggests the prominence of resonant absorption and strong density-profile steepening due to the presence of the ponderomotive force. The data have been extended using the Helios system to about 5×10^{16} W/cm^2. Figure IV-2 shows the data points ranging over four decades in intensity. The relationship established earlier at lower intensities remains valid.

Fluctuations of ion velocity for a given ϕ_L are due to the systematic uncertainties in the laser pulse and plasma interaction parameters rather than to any statistical error associated with the measurement. Possible uncertainties include laser risetime and pulselength, focused spot on target, presence of hot spots in the beam, low-level precursors, and coherent effects in the simultaneous presence of several laser beams. Analysis reveals that the

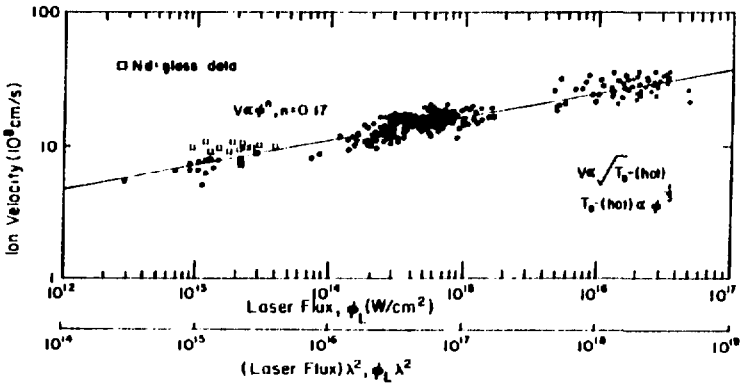

Fig. IV-2.
Plot of the fastest ion velocity (v_i) vs laser flux on target.

cause of variation in ion velocity can be accounted for by these kinds of uncertainties.

For any target design, two critical code inputs that generate the simulated implosions are fraction of energy absorbed and hot-electron temperature. The agreement of the fast-ion data with the simulations implies that the assumption of $T_{e-} \propto \phi_L^{1/3}$ is still valid at an intensity of 10^{17} W/cm^2. Because the analysis assumes a constant absorption fraction, it suggests that the absorptance is the same as that measured at lower intensity.[10] Both inputs were incorporated into our high-compression target design. The agreement between the experimental results and calculations[11] bears out the diagnostic capability of fast-ion detection.

We have also established direct correlation between fast-ion spectrum and target implosion as seen by the x-ray pinhole camera. The abrupt appearance of the fastest ions essentially guarantees a bright core in the implosion center. Furthermore, for DT-filled GMBs, the measured neutron yield increases as a direct function of fast-ion velocity. This implies that, as long as the target shell thickness is comparable to or less than the range of the hot electrons, which is true in the case of exploding-pusher targets, the yield is determined primarily by hot-electron temperature, and hence, by the laser irradiance.

Line and Continuum Spectra from Laser-Irradiated GMB Targets (K. Mitchell, A. Hauer, W. Priedhorsky)

X-ray spectroscopy provides a variety of information crucial to the understanding of laser-plasma interactions. High-energy bremsstrahlung provides the temperature of suprathermal electrons important to fusion target design because of the fuel preheat they cause. Low-energy bremsstrahlung is important to the energy balance of laser fusion targets and provides the thermal electron temperature. Line spectra offer a multitude of diagnostic possibilities and very selective sampling of various target regions by using the lines of various materials.

Very strong silicon spectra were observed from 300-μm-diam GMB targets irradiated by the Helios laser. Two spectra taken at laser energies of 2 and 4 kJ are shown in Figs. IV-3 and -4. These spectra are spatially integrated so that the radiation is observed from both the laser interaction region and the compressed core. The spectra are qualitatively different from those obtained in lower energy experiments. This is the first time that free-bound continua have been seen from 10-μm laser-produced plasmas. If the log of continuum intensity is plotted as a function of energy, the electron temperature can be estimated from the slope of the curve. The temperature indicated from the ($1s^2$-continuum) spectrum shown in Fig. IV-3 is 310 eV. Figure IV-4 shows both the "helium-like" ($1s^2$-continuum) and "hydrogen-like" spectra, but they exhibit different slopes. This indicates that the two continua are emitted from different regions in space or are emitted at different times.

The arrow on the x-axis in Fig. IV-3 shows the position of the helium-like ($1s^2$-continuum) recombination edge for an atom in vacuum. As shown, the actual position of this edge is shifted considerably toward lower energies. This effect is caused by high-density plasma microfields that reduce the ionization potential. For the

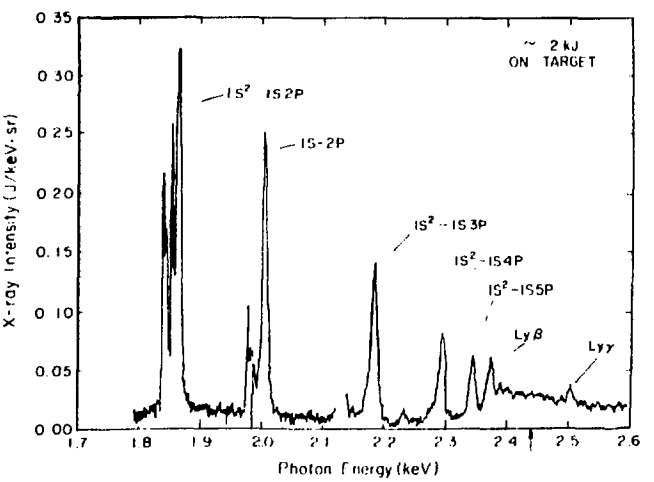

Fig. IV-3.
Spectrum from 300-μm-diam GMB irradiated with laser energy of 2 kJ.

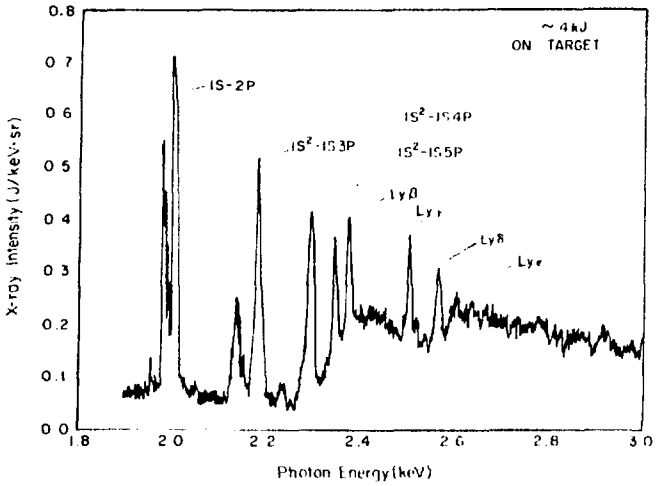

Fig. IV-4.
Same as Fig. IV-3 at 4 kJ.

case shown, the helium-like recombination edge is gradual, which indicates a density gradient in the source. The density of the compressed silicon determined by this method is at least $10^{23}/cm^3$.

The temperature of 310 eV, derived from the slope of the free-bound continuum, appears to be inconsistent with the broad-band temperature estimate of 580 eV. A limited number of space-resolved spectra from 200-μm GMB targets show the free-bound continuum emitted principally from the core region. Also intensity ratios of hydrogen-like and helium-like lines indicate that the core is hotter than the coronal region. As far as temperature measurements are concerned, these data appear to raise more questions than they answer. More space-resolved spectra from GMB targets are expected in the near future. Also, we are proceeding to analyze the intensity distribution among the "satellite" lines.

Broad-Band X-Ray Spectral Measurements on GMB Targets (P. Lee, K. Mitchell)

Broad-band spectrometers were used to record x-ray spectra in the range 30 eV to 5 keV for several Helios shots >2 kJ on GMB targets. Spectral discrimination was obtained with K- or L-edge absorption filters. Spectra in the region 30 to 600 eV were recorded with XRDs, whereas spectra from 780 eV to 5 keV were recorded with NE III fluor photomultiplier-tube detectors. Examples of spectra from two shots on 300-μm-diam GMB targets are shown in Fig. IV-5. Spectra in the range 1 to 5 keV are identified principally as x-ray continua due to free-free bremsstrahlung. There is some blend of line and free-bound continuum that contributes to the signal, particularly in the 2.6-keV channel, but this is not evident from these data. Assuming x-ray continuum, the slope of the curve between 1 and 5 keV indicates an electron temperature of 580 eV.

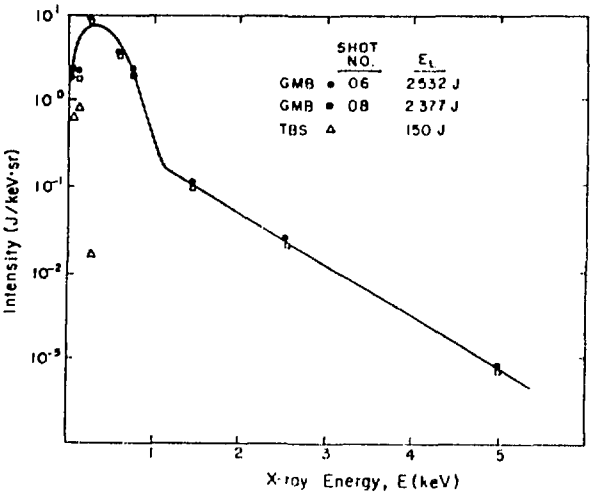

Fig. IV-5.
Broad-band x-ray spectra—6 beams of Helios system on GMB targets.

About 90% of the x-ray emission occurs below energies of 0.8 keV. The character of this x-ray emission is unknown. The total x-ray emission into 4π steradians is about 2% of the laser energy incident on target. This is consistent with the x-ray emission measured at Gemini with about 0.25 TW on target. Hence, the bulk of the x-ray emission at energies below 0.8 keV scales with laser energy.

Experiments using the Gemini system, with <1.0 TW on 180-μm GMB targets, shows that the electron temperature $T_e \propto 500\ I_L^{0.37}$. For a laser power I_L of 2.4 TW, we would expect T_e to be 680 eV; data from Helios showed T_e to be 580 eV. This difference, which is not great, probably exists because the GMBs used in Helios and in Gemini experiments were different sizes.

Analysis of Pinhole Camera Images (W. Priedhorsky)

X-ray imaging on the Helios system is performed by two pinhole cameras (Fig. IV-6). Each has a pinhole 13 μm in diameter located 4.5 cm from the target and shielded by a beryllium window 7.5 μm thick. As currently operated, with a pinhole-film separation of 39.87 cm, the camera magnification is 8.86. At that magnification, the x-ray flux from GMBs coated with up to 50 μm of plastic is enough to produce an optical density >1.5 on Kodak 2490 film. The camera resolution is limited by the geometric size of the pinhole, rather than by diffraction effects.

Fig. IV-6.
Pinhole camera for the Helios laser system.

The analysis of pinhole images for quantitative information about target performance (e.g., compression) is complicated by the fact that the x-ray emission per unit volume from a compressed target is a function of both density and temperature. It is not possible to distinguish between a density spike and a temperature spike from image data alone. Moreover, the targets currently being shot are, in many cases, optically thick at soft x-ray energies, making recovery of density information from x-ray images difficult. Because of these problems, we have chosen to compare the pinhole images obtained experimentally with intensity profiles calculated by a modeling program in an attempt to correlate predicted and actual target behavior.

The code uses a one-dimensional calculation; thus, the target and implosion were assumed to be spherically symmetric. The code uses the laser pulse profile and target parameters to calculate radial profiles of density, temperature, emission, etc., as functions of time. The emission profile is folded with the response of 2490 film and the pinhole camera filter transmission function; it is then integrated over time and summed over the line of sight (LOS) to yield the two-dimensional radial intensity profile expected for the pinhole images. The calculated emission comes primarily from the glass shell.

Figure IV-7 shows the pinhole image obtained from the parylene-coated GMB that had the greatest apparent compression of the Helios shots to date. The film was raster-scanned by a microdensitometer to produce two-dimensional, digitized density data. The center of weight of each image was then calculated, and a mean radial-density profile was obtained by averaging the density samples in a series of annuli about the center. Inspection of the images revealed that they were not entirely symmetrical, as can be seen in Fig. IV-7. The effect of such asymetry on the profile was estimated by comparing the profiles from 20° wedges to the 360° average profile. We concluded that, for the images examined thus far, the mean profile accurately represented the local profile: the profile was not significantly flattened by the averaging process. Film density was converted to x-ray intensity

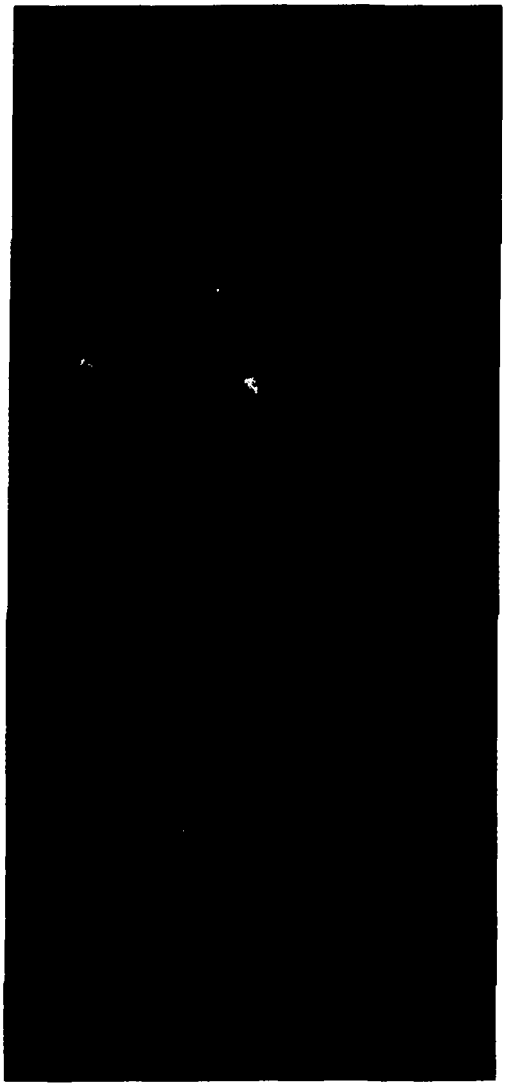

Fig. IV-7.
Pinhole picture of Shot 88110707, 145-μm-radius GMB with 55-μm CH coating, 2232 J on target.

via the known calibration of 2490 film. Because the film gamma is a function of photon energy, the characteristic curve appropriate to 2.62 keV was chosen as typical for the calculated x-ray spectrum. The characteristic curve for 2490 film shows little change in shape over the region 1.2-3.0 keV.

Figure IV-8 shows the experimental (error bars) and calculated (solid line) radial x-ray intensity profiles from the plastic-coated high-density sequence target of Fig. IV-7. The laser and target parameters assumed in the calculations were chosen to match the experimental configuration as closely as possible. The target was a 145-μm-radius GMB coated with 55 μm of plastic (CH density, 1.0). Energy on target was 2232 J from six of the eight Helios beams. The simulation assumed spherically symmetric illumination and implosion. The calculated profile was scaled to fit peak experimental intensity because we are interested in comparing the shapes of the profiles only. Though the shapes of the calculated and observed profiles are similar, the observed profile is slightly broader than the calculated profile at its half-width and has a longer tail. The maximum compression achieved in the simulation was 7 times liquid density.

The minimum radii of the fuel-glass and the glass-plastic interfaces obtained in the simulation run are indicated by the arrows in Fig. IV-8. Neither interface corresponds to any feature in the calculated profile. Thus, there appears to be no way to estimate target performance for such targets without resorting to a detailed simulation. The analysis of more shots using a comparison with code simulations is in progress.

Return-Current Heating (R. F. Benjamin, G. H. McCall, A. W. Ehler)

Our interest in lateral heat transport at long distances (i.e., more than several focal radii from the irradiated region) is motivated by observations during exploding-pusher experiments. X-ray photographs revealed that the glass stalk that supports the gas-filled GMBs is self-luminous in x-rays. This heat flow along the support fiber can influence implosions by modifying the heating symmetry or the electron spectrum or by simply draining energy.

We performed two experiments to determine that the dominant mechanism for this energy transport is return current. The first experiment was to irradiate a target consisting of a tortuous path of 10-μm-diam fibers (see target schematic in Fig. IV-9a). A focused CO_2 beam (300 J, 1.5 ns) impinged on a GMB at point A, producing heat that traversed the fibers. Assuming that optical luminosity is a signature of heating, we identified the heat-flow path using time-integrated optical photographs (Figs. IV-9b, -9c). The most luminous path, ABCJ, is between the irradiated region at point A and the nearest electrical ground, the target holder, as seen in the photographs. This indicates that the heat flow is driven

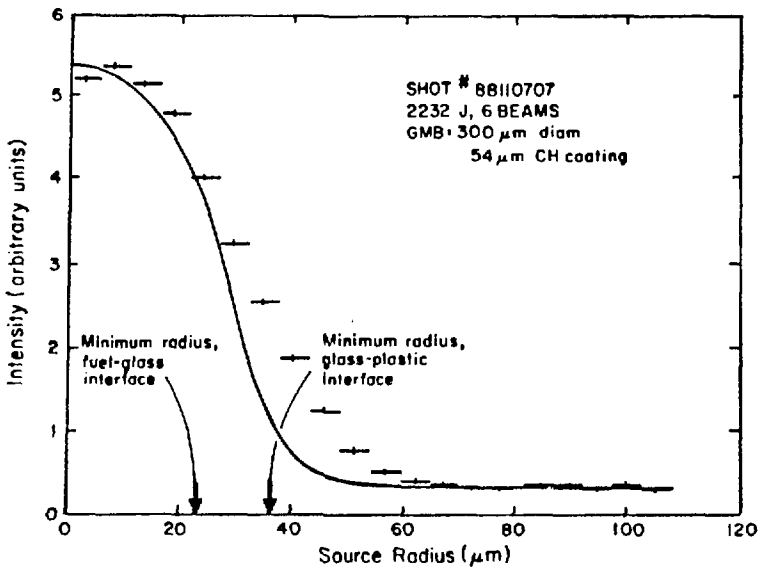

Fig. IV-8.

Mean radial intensity profile, Shot 88110707. Solid line indicates calculated profile for similar conditions.

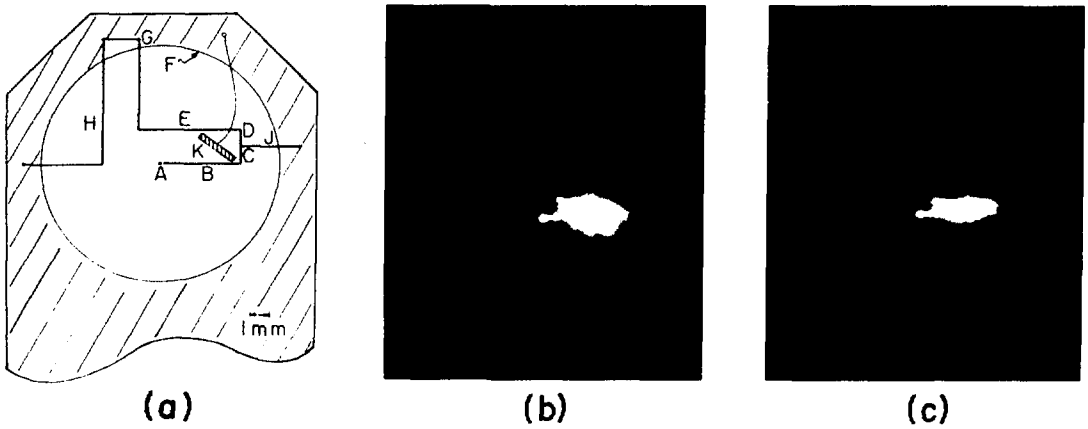

Fig. IV-9.

(a) Schematic of target and heat flow in target consisting of tortuous path of 10-μm-diam fibers. (b) and (c) Time-integrated photographs of heat flow along fibers.

by an electrical mechanism. We also observed that when the fiber section CJ was removed, making ABCDEG the shortest ground path (Fig. IV-9c), the fibers shielded by K were as luminous as those between points A and G that were directly exposed to the illuminated region. Thus the electrical mechanism is more important than plasma radiation or scattered light.

The second experiment discriminated between the directions of electrical current flow. An aluminum slab mounted on the center conductor of a 50-Ω coaxial cable was irradiated by 150 J of CO_2 laser light (1.5-ns pulse width). The voltage pulse, shown in Fig. IV-10, was 180 kV positive, indicating a net flow of electron return current *toward* the target.

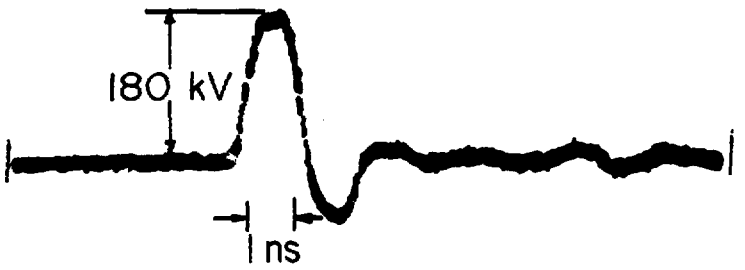

Fig. IV-10.
Positive voltage pulse indicating new flow of current toward target.

We conclude that lateral heat transport at long distances along support fibers is driven by return current that replenishes emitted hot electrons. The optical luminosity is ohmic heating. A simple theoretical model based on a Maxwellian electron distribution with a measured temperature agrees with the value of the voltage pulse and the number of emitted electrons. More sophisticated current flow treatments must be implemented in computer simulations as a result of this experiment.

DIAGNOSTIC DEVELOPMENT (R. P. Godwin)

Introduction

A viable laser fusion experimental program depends in large part on being able to anticipate and develop the kinds of instruments required. This is increasingly true with large, complex laser facilities and ever more complex targets.

During this reporting period, the researchers who developed the invaluable fast charged-particle detectors turned to the problem of improving the time resolution of neutron detectors. Their objective is to improve our ability to separate the effects of ion temperature, burn time, and run-in time on neutron spectra.

We have continued our vigorous program of x-ray diagnostics development with a balance of near-term goals (such as the development of a PIN diode x-ray spectrometer) and longer term goals (such as charge-coupled imaging devices, which eventually should replace film detectors). Our x-ray streak camera work was plagued with triggering problems that were more difficult than we anticipated. Advances made during the past six months, however, clarified the problems in this area. In addition, we have a general project in the area of fast high-voltage switching and triggering, which should be useful for various diagnostics, including optical probe beams and x-ray backlighting.

Although a superficial glance at 10.6-μm laser-plasma interactions indicates that we should concentrate either on infrared or x-ray photons, experience has shown that visible-light imaging or spectroscopy provides important information. Seeing is believing. Systematic development of optical telephotography with high spatial resolution is evolving from time-integrated photographs through temporally resolved photography to the use of precisely timed optical probe beams.

Ultrafast Neutron Diagnostics (T. H. Tan, A. Williams)

Recently, we developed several fast particle detectors that can generate a signal pulse with a full width at half maximum (FWHM) of 600 ps or less. Each detector is assembled by coupling an ultrafast, quenched scintillator[12] of some optimum size to a high-gain ITT microchannel plate photomultiplier (MCP-PMT). A typical assembly of the detector is shown in Fig. IV-11. Figure IV-12 shows the response of such a system. With a fast GHz oscilloscope as recorder, it is possible to obtain time resolution of less than 100 ps in time shift and pulse broadening. This greatly extends our capability to diagnose the performance of the high-compression laser fusion targets.

For example, measurement of the implosion time from the delay of the neutron arrival provides the first experimental clue of the hydrodynamic process associated with laser fusion. With greater yield, the time history of

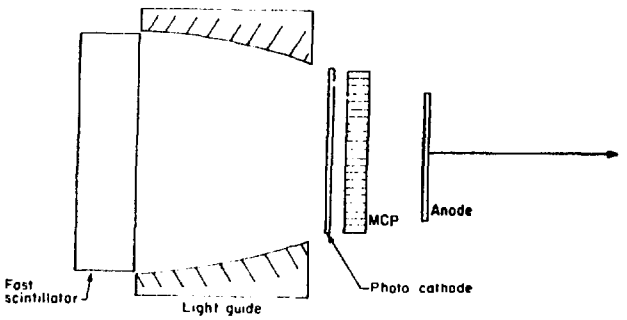

Fig. IV-11.
Typical assembly of an ultrafast neutron detector.

neutron production can be streaked by these electrons to yield more refined details of the implosion processes. Let us consider the relationship $Y \sim n^2 \langle\overline{\sigma v}\rangle\ t_c\ V = N^2/V \langle\overline{\sigma v}\rangle\ t_c$, where Y is yield, N is number of DT atoms (known), V is instantaneous volume, t_c is burn time, and $\langle\overline{\sigma v}\rangle$ is cross-section rate, which is a function of fuel temperature Ti alone; t_c can be measured from pulse broadening at short distances and T_i at larger distances. The burn volume and the final density can be deduced directly.

We are pursuing the experiments to achieve high compression at high enough yield to use this fast diagnostic capability. Such diagnostics of laser fusion performance become easier as the yield and confinement time increase. At near breakeven, when it may not be possible to use other diagnostics in the harsh environment near the target, these fast neutron diagnostics may provide much of the important data relevant to laser-induced fusion processes.

(a)

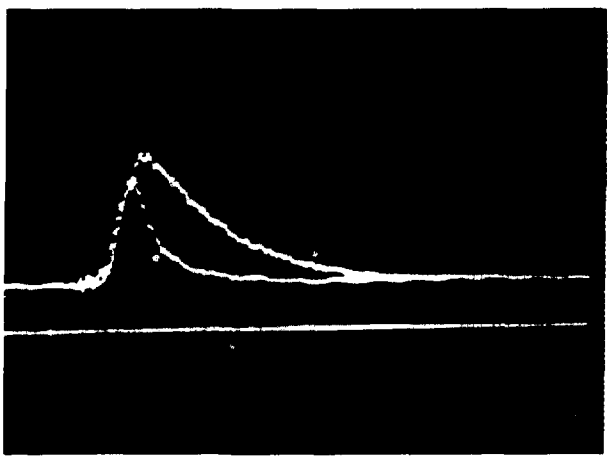

(b)

Fig. IV-12.
Typical response of the ultrafast detector to a 50-ps e-beam pulse. (a) Intrinsic response of the detector as calibrated by the Cerenkov light. (b) Comparison of detector response between 3% quenched NE III scintillator and the standard NE III scintillator.

PIN Diode X-Ray (PDX) Spectrometer (P. Rockett)

A PIN diode x-ray spectrometer has been designed to operate in the 4.5- to 29.2-keV range. The instrument, complete except for K-edge filters, will be mounted on the Helios vacuum chamber to monitor the spectral region between that covered by photomultiplier tube/NE III scintillators on the low-energy end and CsF detectors on the high-energy end.

Calculations were completed on optimizing PIN diode thickness and sensitivity with K-edge filter transmission and x-ray spectral form. An analytical model was generated, describing the response of the filter-diode combination (in C/mJ) to any given spectral input. Variations of the diode thickness show clearly its effect as a low-pass filter. A thin diode simply cut off the high-energy response. This enhanced the amount of energy

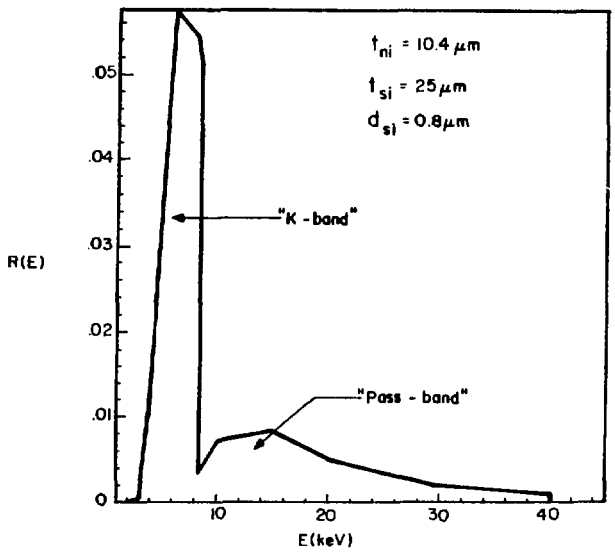

Fig. IV-13.
Spectral sensitivity of filtered diode detector for silicon depletion layer thickness t_{s_i} = 25 μm.

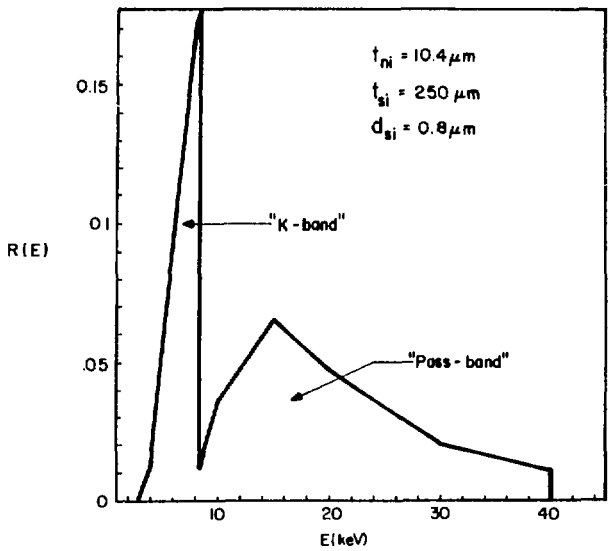

Fig. IV-14.
Same as Fig. IV-13 for t_{s_i} = 250 μm.

recorded in the K-edge region relative to that in the higher energy pass-band. The dramatic effect of diode thickness is illustrated in Figs. IV-13 and -14. Here, one sees the spectral sensitivity of the filtered diode detectors for two different silicon depletion layer thicknesses (t_{s_i}). The K-edge-detected energy constitutes the primary portion of the total signal for t_{s_i} = 25 μm (Fig. IV-13), but only a minor portion of the total signal for t_{s_i} = 250 μm (Fig. IV-14). These design principles were used in choosing both the diodes and filters for the PDX spectrometer.

X-Ray-Sensitive Charge-Coupled Device (CCD) Development (P. Rockett)

A contract has been awarded to Westinghouse Corporation for fabrication of an x-ray-sensitive (1-10 keV) CCD to replace film in x-ray pinhole cameras. The proposed device will have a sensitive area 3 mm by 6 mm with 30-μm resolution at the detector and 2×10^4 imaging pixels. It will be highly quantum-efficient over the entire range of 1-10 keV. Detailed high-resolution images at 10 keV will enhance our insight into the source of high-energy electrons in laser-induced plasmas. The readout into our PDP 11/70 computer will be immediate, allowing shot analysis on a real-time basis.

X-Ray Streak Camera Development (P. Rockett, J. S. McGurn)

A streak camera mount for the Helios vacuum chamber was designed and drawings were completed. The mount provides tracks along which the camera may be transported. An air lock allows the camera to be removed from the chamber without breaking vacuum. This will permit film to be reloaded without interfering with experiments. Repositioning accuracy will be ±10 μm with a remote station for motor control.

A pinhole translator was constructed for use with the x-ray streak camera in an imaging mode. The positioning accuracy will be ±2 μm in 2-μm steps with both x- and y-control. The translator will be attached to the streak camera mounting rail independent of the camera. The target, pinhole, and streak camera slit will be aligned using a telescope of high magnification.

A new 36-stage, avalanche transistor trigger unit was received from General Engineering and Applied Research (GEAR) and was installed in the GEAR Pico-X x-ray streak camera. This replaced the original fast optical-spark-gap trigger, which could not be triggered with 10.6-μm light. Tests indicated a sweep rate of 100 ps/mm.

We used our two-beam Nd:glass laser to determine the transition trigger delay (by finding the x-ray streak in time) and to calibrate the streak rate and linearity.

The laser provided a 300-ps FWHM, 1.06-μm pulse to illuminate a 200-μm nickel microballoon. Two beams were incident upon the target with 5 to 20 J per beam, one beam delayed 1.5 ns with respect to the other. A trigger beam was picked off and directed into a fast photodiode, whose output then triggered the avalanche stack in the Pico-X. Triggering delay, measured by oscilloscope, was 16 ns with <0.5 ns jitter when the unit was fired into a 10-kΩ, high-voltage probe.

When the camera was placed in the vacuum chamber, however, the temporal location of the streak could not be found. Occasional appearances of partial streak images indicated that the avalanche stack did not function properly and was randomly triggering on noise during laser flashlamp discharge. Direct-current shots proved that the streak tube was functioning and that sufficient x-ray flux was being generated for film exposure. Inspection of the trigger unit showed that many transistors were being biased within a few volts of breakdown. The camera is being relocated to our single-beam Nd:glass laser (5 J, 30 ps) where the lower background noise level is more suitable for further tests of delay, jitter, and sweep rate.

Spectral calibration of the camera will continue at 4.93 keV (Ti Kα), and at or near 17.8 keV (Zr Kα). These will provide six performance data points and will give us an accurate picture of the Pico-X spectral sensitivity.

X-Ray Scaling Experiments (W. Priedhorsky, K. Mitchell)

An investigation was made to determine whether x-ray calorimetry could be performed using intensity measurements of the Si resonance line ($1s2p - 1s^2$) to determine absorbed laser energy on target.

Spectrometer and spectrograph data were obtained from 50 shots with the south beam of the Gemini system in and out of focus (to vary intensity) on a variety of SiO_2 targets. Laser energy on target was varied through nominal values of 50, 100, 200, and 300 J.

Figure IV-15 shows the integrated signal in the Si XIII resonance line ($1s2p - 1s^2$) as a function of laser energy. The upper line is the least-squares linear fit to the focused shots on target (slab, lollipop, and GMB), whereas the lower line is a fit of shots -360 μm from focus on glass slab targets. There is a notable difference between the focused and unfocused shots: none of the points from the unfocused shots falls above the mean line of the focused shots.

The focused shots fit the relationship

$$I_{line} \propto E_L^{1.10 \pm 0.33}, \qquad \text{(IV-1)}$$

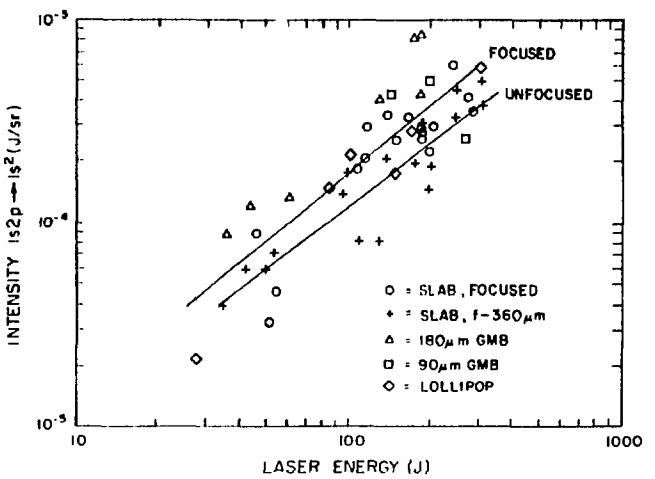

Fig. IV-15.
Integrated signal in the Si XIII resonance line ($1s2p - 2s^2$) as a function of laser energy.

where I_{line} is the intensity of the Si ($1s2p - 1s^2$) line and E_L is the laser energy. The unfocused shots fit the relationship

$$I_{line} \propto E_L^{1.02 \pm 0.26}. \quad \text{(IV-2)}$$

We conclude that there is a small but consistent intensity dependence of the resonance line in this range of shot parameters. The focused and unfocused data are consistent with a common fit of

$$I_{line} \propto E_L\, I_L^{0.25}, \quad \text{(IV-3)}$$

where I_L is the laser intensity. For a constant spot size, such a fit would require

$$I_{line} \propto E_L^{1.25}, \quad \text{(IV-4)}$$

This is consistent with the data.

A second measurement was made with a K-edge filter spectrometer, which includes the Si line ($1s2p - 1s^2$), in channel 4 covering the range from 1.8 to 2.45 keV. This resonance line represents a sizeable fraction of the total energy recorded by this channel. The spectrometer data for focused and unfocused shots are shown in Fig. IV-16. The two lines that are linear fits to the focused and unfocused points are given by

$$I_{ch\ 4} \propto E_L^{1.68 \pm 0.26} \quad \text{(focused)} \quad \text{(IV-5)}$$

and

$$I_{ch\ 4} \propto E_L^{1.29 \pm 0.15} \quad \text{(unfocused)}, \quad \text{(IV-6)}$$

where $I_{ch\ 4}$ is x-ray intensity in channel 4 and E_L is laser energy. Hence, the difference between the focused and unfocused shots in the channel 4 signal is less than measured with the spectrograph. The spectrometer provides more detailed data than film recording in a spectrograph because the spectrometer signal is a blend of lines and some continuum. In any event, the laser energy on target can be estimated to within a factor of 2 with 90% confidence from spectrometer measurements of the resonance line x-ray intensity.

Narrow-Aperture Methods for Determining the Emission Structure of Imploded Targets (M. M. Mueller)

A general treatment of single-aperture imaging was given for slit, square, and circular apertures as summarized in the last progress report.[13] It was shown that, for irradiance data of sufficient quality to allow meaningful first derivatives, a simple technique deconvolves a wide-aperture image to give the image that would have been obtained using an infinitesimal slit.

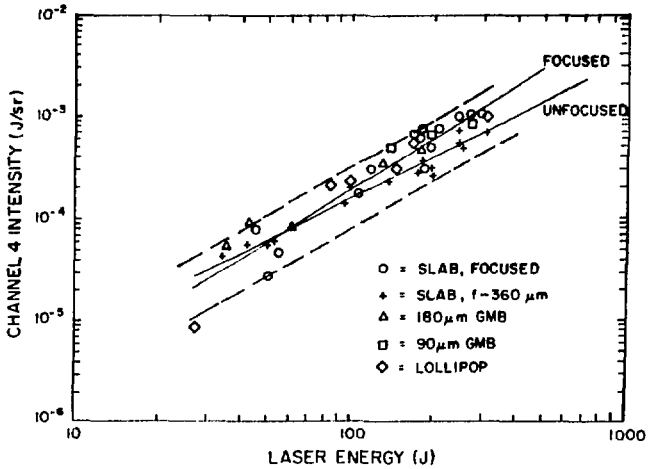

Fig. IV-16.
Measurements made with a K-edge filter spectrometer from 1.80-2.45 keV, including the Si line ($1s2p - 1s^2$).

Although the problem of instrumental broadening has thus been overcome in principle, wide-aperture deconvolution is often limited in practice because the data are too noisy to yield useful first derivatives. Usually, because of diffraction as well as limited source radiances, very small apertures are also prohibited. Thus, there is a need for methods to handle noisy data taken with narrow apertures. Such methods, with particular reference to microballoon targets, are the subject of this study. The numerical simulations were carried out using a version of the code developed during the previous study.[13]

The two main questions to be addressed are:

- Can the base-intercept method be used to determine the size of a small part of a radiating source? In particular, can the diameter of an imploded core be determined from its image, even though the image is perturbed by the irradiance from the unimploded microballoon wall? An ancillary issue is whether the FWHM is a valid measure of the imploded core diameter.
- Can a method be developed to determine the emittance of the core relative to that of the imploded wall from images formed by pinholes of narrow aperture? This question bears directly on the issue of inner-wall (pusher-fuel) stability during implosion. If significant instability occurs, mixing of the wall material with the nearly nonradiant DT gas would be expected to produce radiant cores without much "hollowness" at the center. Conversely, a core that is nearly nonradiant or "hollow" at the center would indicate pusher-fuel hydrodynamic fuel stability.

Figure IV-17 is a microdensitometer trace through the center of the time-integrated, x-ray pinhole image of an imploded microballoon target (Shot VV29 #4). It is a good example of images obtained with the Gemini laser system. They exhibit a dim outer ring having a diameter approximately equal to that of the original microballoon, and a brighter core about one-fourth the original diameter. While some asymmetry in the core is usually apparent, it will be ignored in this discussion.

Such time-integrated x-ray images may be interpreted as being the superposition of two "snapshots"—one of the laser-heated microballoon wall before the implosion has begun and the other of the compressed core at "turnaround" before disassembly has begun. According to the simulations, a model based on the superposition of these snapshots is adequate to explain the measured image distributions. Thus, we tentatively conclude that the remainder of the implosion history, when the glass shell of reduced density moves at high speed, contributes only a background irradiance to the time-integrated image. However, a possibility remains that the core diameter deduced from such photographs is appreciably larger than the minimum core diameter attained.

The first question has been addressed by numerical simulations using a variety of source emission models.

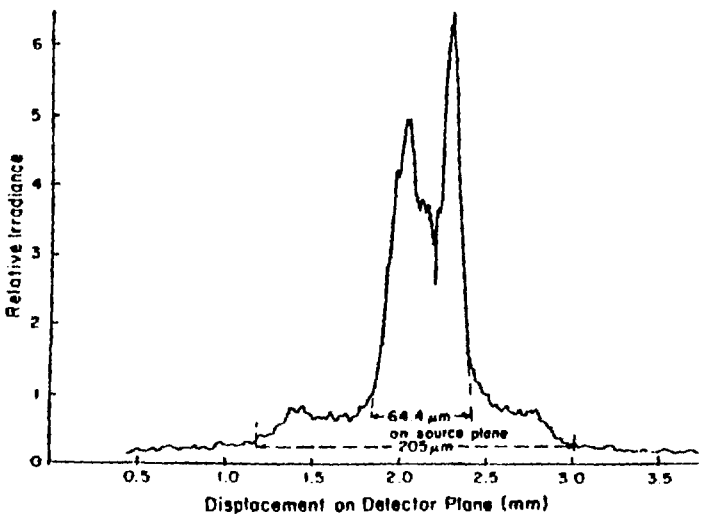

Fig. IV-17.
Microdensitometer trace through the center of a time-integrated x-ray pinhole image of a microballoon target imploded by the Gemini CO_2 laser system.

The conclusion is that the base-intercept method of determining the core diameter is not only valid in the normal range of experimental conditions, but is accurate to one part in a thousand even when the emittance from the unimploded shell is 30 times that from the imploded core. Hence, we infer that the base-intercept method of determining the sizes of "hot-spots" within a target is amazingly robust against smooth but intense perturbation from other parts of the source. Of course, the method fails if the images of two or more hot-spots overlap. The answer to the ancillary question is that the FWHM is not generally a valid measure of the core diameter, which is strongly dependent on core structure. For example, for a homogeneous core, use of the FWHM would result in overestimating the volume compression by about a factor of 2.

The answer to the second question is more involved, for we have developed two independent methods for determining the x-ray emission from the central region of an imploded microballoon. Both methods assume that the absorption of the x-rays by the target is negligible, as is reasonable for targets that have been used until now.

The first method is straightforward and potentially accurate, even with data noise, but is tedious. It involves assuming a source emission model, calculating the radiance distribution, performing a two-dimensional convolution under the experimental configuration, and then performing a second convolution under the conditions of the microdensitometer scan. This procedure is then iterated until the calculated irradiance pattern best fits the data from the microdensitometer scan. Although this method cannot provide a unique solution, our limited experience indicates that uniqueness is not a problem for realistic source models.

An example of the modeling procedure will be given without demonstrating the iterative process. The parameter values have been chosen to give approximate congruence with the data of Fig. IV-17. The emission model used is an outer (unimploded) shell of 180-μm o.d. and an inner (imploded) shell of 45-μm o.d., with respective wall thicknesses of 1.8 and 5.6 μm. The resulting radiance pattern is then convolved with a 12-μm-diam pinhole with a system magnification of 9, as shown in Fig. IV-18 in isometric projection. A microdensitometer scan convolution using a 6.1-μm-square aperture (referred to the plane of the source) of this irradiance distribution is shown in Fig. IV-19. This second convolution partially fills in the central dip and broadens the base intercepts, but leaves the FWHM of the core practically unchanged.

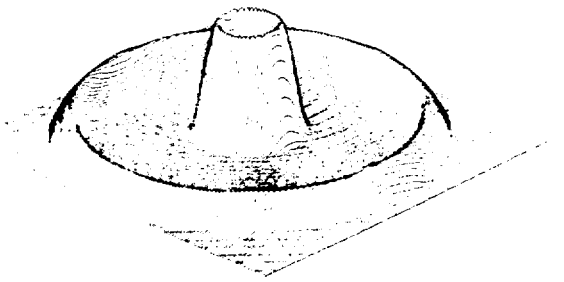

Fig. IV-18.
Irradiance distribution in the pinhole image of the emission model.

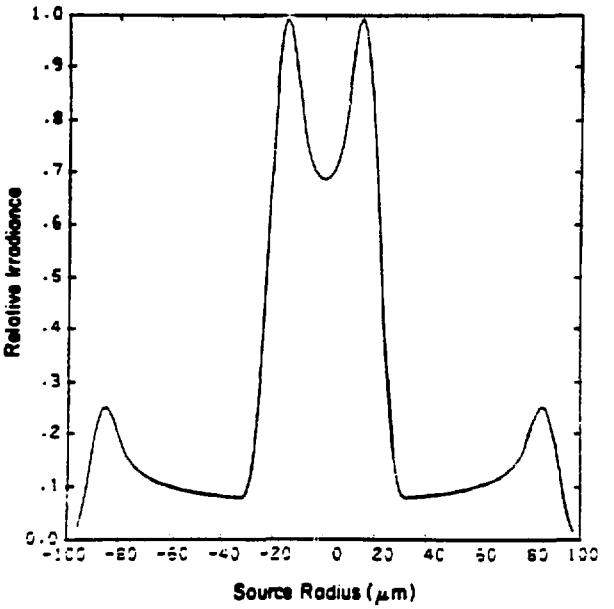

Fig. IV-19.
Simulated microdensitometer scan through the center of the irradiance distribution shown in Fig. IV-18.

The main features of the simulated microdensitometer scan in Fig. IV-19 are similar to those of Fig. IV-17. The measured base intercept widths in Fig. IV-17 are reduced by the standard method[13] to give 185-μm o.d. for the unimploded shell and 45-μm o.d. for the imploded shell. The microballoon target had a shell diameter of 180 μm. It seems remarkable that such a simple source model can give good congruence with a time-integrated photograph. Many other simulations with varying source models have been computed, and imply that the

data of Fig. IV-17 are consistent only with a model of low central emission, which is consistent with the hypothesis of pusher-fuel hydrodynamics stability.

When the model-adjusting method is used with a rather narrow pinhole, the emission structure of the imploded core can be determined accurately. However, it can be time-consuming, so it would be desirable to have a more expedient method to serve as a first diagnostic.

To this end, we have investigated the effectiveness of the ratio of the FWHM of the core image to the core diameter in determining the emission from the central part of the core.

We found that the above ratio can indicate the relative emission of the central region for a broad class of realistic models. It appears that the FWHM could be developed into a useful diagnostic of central core emission and that the FWHM method could be used with larger apertures than those of the model-adjusting method.

Reconstruction of Source Emission Structures from Slit Images (M. M. Mueller)

The methods of source reconstruction discussed above are integral methods that are generally superior for noisy data, but they cannot guarantee a unique solution. For cases in which useful first derivatives can be obtained, the derivative methods would be valuable as a check on the uniqueness of integral methods, or as the primary method, because they are suitable for automatic calculation without human intervention. However, the derivative methods require irradiance data from infinitesimal slits, which leaves only data from the wide-aperture deconvolution method.[13] Because wide-aperture deconvolution is itself a differential method, its use to provide input to other differential methods compounds the requirement of low noise levels to impracticable stringency. Hence, we are forced to consider the use of differential methods on image data taken with practical realizable slits.

Both available differential source-reconstruction methods, a dual-sequential Abel inversion or the Vest and Steel method,[14] require radial source symmetry and infinitesimal-slit images. However, the simpler Vest and Steel method (dI/xdx, where I is the irradiance and x the displacement) is the one to be discussed here. Our question is whether we can use the Vest and Steel method with undeconvolved irradiance data taken with practical, narrow-slit apertures.

Although the answer depends somewhat on source structure and the investigation is not completed, the Vest and Steel method does not appear to work well with practical apertures. The matter has been investigated analytically for sources that give a uniform disk of radiance and numerically for spherical-shell sources.

The conclusion is that appreciable source distortion occurs for ratios of aperture width to overall target diameter greater than ~0.01. For aperture ratios as large as 0.03, which is about the lower limit of practical, diffraction-free slit imaging for larger targets, source emission structure is rather grossly distorted. However, the *locations* of emission structures are correctly preserved and the width of spherical shells can be roughly determined by the naive application of the base-intercept method, even though this method is strictly correct only when applied to source diameters, not to shell widths. Hence, the Vest and Steel method may be of some value in source reconstruction from practical slit images even though the emittance ratios between different parts of the source may be badly distorted. Also, numerical simulation could help in estimating the sense and magnitude of the distortion, thus allowing correction.

The issue is complicated and is still under investigation. There is a possibility that a modified and elaborate version of the Vest and Steel method could be devised to give adequate source reconstruction from real data, but it is clear that the straightforward application of this method cannot give accurate emission ratios when practical slit widths are used.

Extension and Generalization of Two-Dimensional Image Simulations (M. M. Mueller)

The convolution code[13] developed to simulate single-aperture images of randomly asymmetrical sources was modified to provide more realistic simulations. One modification replaces the circular or square aperture with something intermediate: the generalized circle (Überkreis) $x^p + y^p = 1$. At $p = 2$, the circular aperture is recovered, while the square aperture is approached as $p \rightarrow \infty$. Because small "pinhole" apertures are never really circular, a more general aperture shape for the simulation is usually desirable, and in many cases considerably improves the simulation accuracy.

Another modification improves the calculation of the radiance from a three-dimensional source, which is basically an Abel integral for cases of radial symmetry.

In the interest of more realistic simulations, another independent two-dimensional convolution was added to simulate the effect of a microdensitometer scan of the film image. In many cases this second (microdensitometer) convolution is quite important.

Uniformly Redundant Array Imaging of Laser-Driven Compressions (E. E. Fenimore, P Division; T. M. Cannon, M Division)

We have been investigating the problem of artifacts from the image process of coded apertures. These artifacts can obscure portions of the image, but images produced by uniformly redundant arrays (URAs) are supposed to be free of artifacts. An x-ray camera based on coded-aperture imaging with URAs was tested using the Gemini laser system. Five single-pinhole pictures were also taken to test the faithfulness of the URA image.

Figure IV-20 is a single-pinhole x-ray picture of a laser-driven compression of a DT-filled GMB, which is scaled to correspond to the URA image of a similar target (Fig. IV-21). Figures IV-22 and -23 are one-dimension intensity scans through Figs. IV-20 and -21, respectively. These figures show two important features. (1) The URA produced a faithful picture without the artifacts common to other coded aperture imaging systems. We believe that the small differences between the URA and the single pinhole in these pictures are due to the pictures being taken from different angles. The lack of artifacts (and the fact that a digital analysis avoids the nonlinear problems of optical reconstruction) means that the URA has a larger dynamic range and that intensity ratios from different parts of the image can be determined accurately. (2) The URA consisted of 9521 apertures and, therefore, collected many more photons than did the camera with the single pinhole. Note that the peak in the URA intensity trace (Fig. IV-23) represents ~7100 times more photons than the peak in the pinhole camera trace (Fig. IV-22). This is near the theoretical maximum for the URA, which would be 9521 times as many photons, or a total of 6.60×10^4.

With its much greater photon-collecting ability, the URA can form images in a weak x-ray flux where the single pinhole cannot. Also, the URA can be mounted farther from the target, thus avoiding debris and making space available for other diagnostics nearer the target.

Optical Telephotography (R. Benjamin, J. Riffle)

We developed an optical telephotographic system for experiments on the Gemini target chamber. During this reporting period, we used this instrument on lateral heat flow experiments, discussed elsewhere in this report, and on parametric studies involving GMB targets. In the former experiment, the photographs produced by this camera were crucial in discovering the importance of heating due to electrical return current along target support fibers. The latter experiment produced a variety of features that we shall attempt to correlate with other diagnostic results. Preliminary comparisons indicate that we can detect prelase by an excessive amount of luminous plasma blowoff and we can detect vertical alignment errors by the location of intensely luminous regions at the GMB. Many photographs showed dramatic plasma blowoff from the interface between the GMB and mounting stalk.

The telephotographic system produces high-resolution images covering a wide latitude of optical exposure. The photographs are time-integrated visible images as defined by the ir cutoff of the film and the uv cutoff of the glass optics. The lens is a modified commercially available 90-mm-diam telescope, and the film holder is a modified tri-plane camera with two internal pellicles. The components are rigidly mounted on a plate and attached directly to a vacuum flange, as shown in Fig. IV-24. Because the instrument is entirely external to the chamber, film-handling, alignment, and focusing are easily performed. To cover a wide latitude of exposure, we typically use two black and white films (ASA 75 and 1000) and a color transparency film. The deployed instrument has a spatial resolution of 80 lp(live pairs)/mm referenced to the source and a magnification of 12.

Optical Probe (R. Benjamin, J. Riffle)

In preparation for the optical probe experiments at the Gemini and Helios lasers, an optical system based on a high-power, pulsed argon laser has been designed and fabricated. The source assembly, shown in Fig. IV-25, consists of a commercial argon laser (modified to synchronize it with the CO_2 laser), an autocollimating alignment telescope, and beam transport optics. The structure is extremely stable, yet portable. Initial experiments using this system will study plasma expansion, thermal

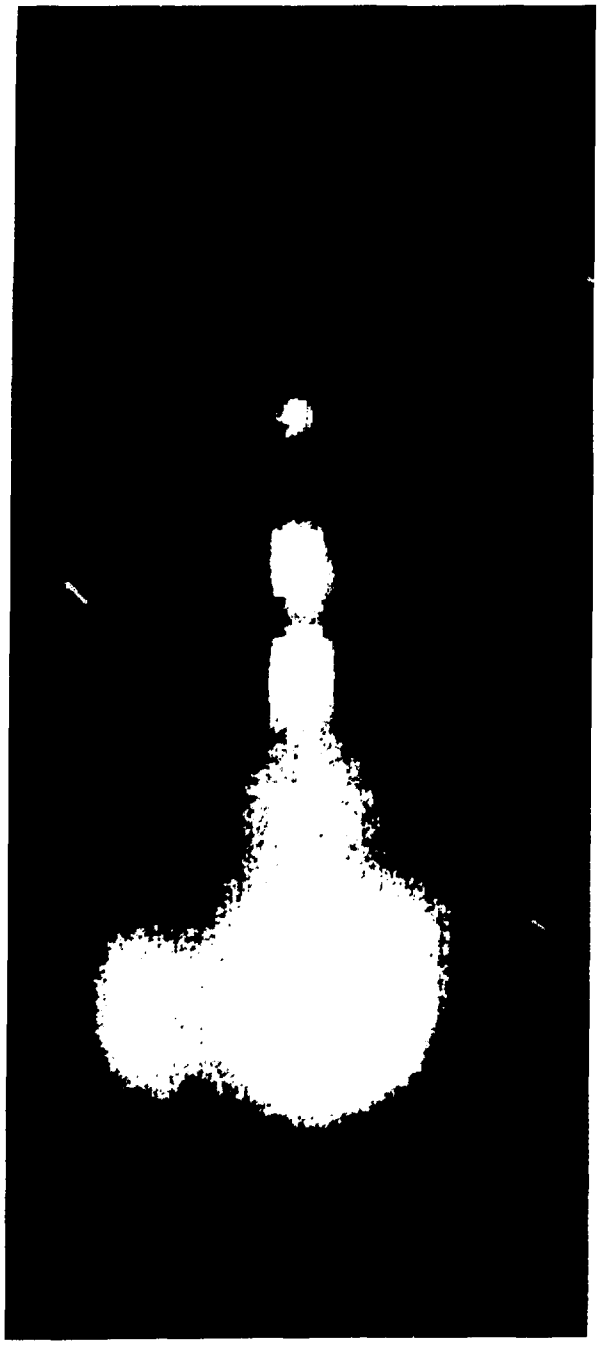

Fig. IV-20.
Single-pinhole x-ray picture of a laser-driven compression of a DT-filled GMB scaled to correspond to the image shown in Fig. IV-21.

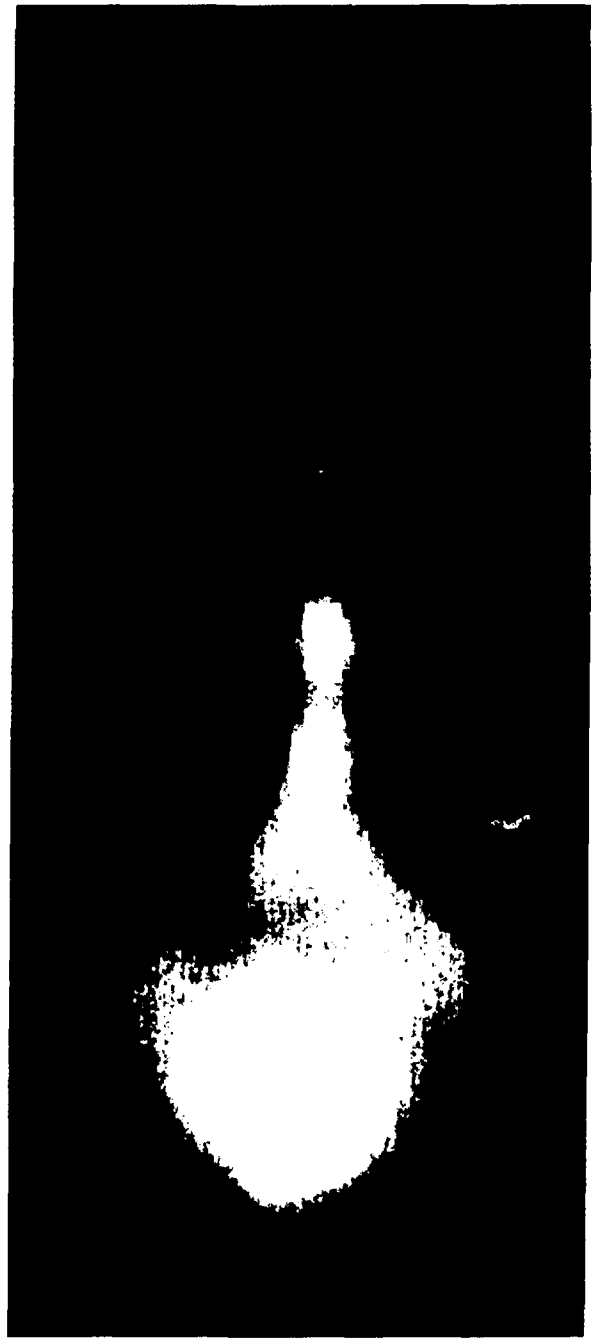

Fig. IV-21.
URA x-ray of a target like that shown in Fig. IV-20.

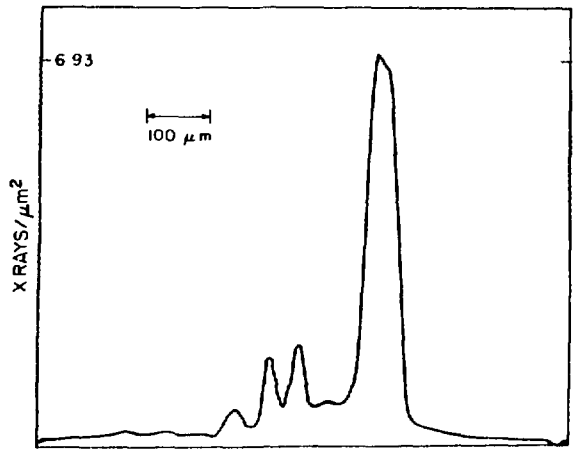

Fig. IV-22.
Densitometer trace of image in Fig. IV-20.

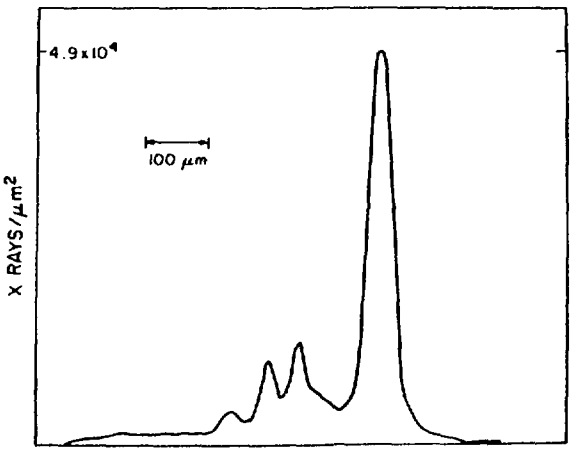

Fig. IV-23.
Densitometer trace of image in Fig. IV-21.

Fig. IV-24.
Telephotography system consisting of a 90-mm-diam telescope and a modified tri-plane camera used as a film holder. The assembly is rigidly mounted on a plate attached to a vacuum flange.

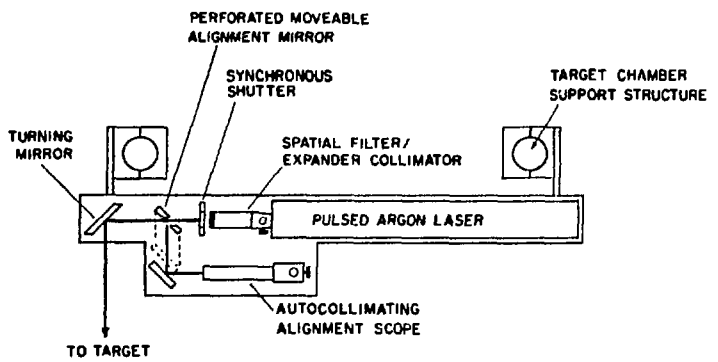

Fig. IV-25.
Optical probe source assembly.

transport, and laser-driven shock propagation in transparent media.

Incoherent, uv-Triggered Spark Gap (R. Carman, N. Clabo, F. Wittman)

We are pioneering in the development of fast high-voltage switching and triggering for use with various diagnostics such as optical probe beams, x-ray and visible streak cameras, and x-ray backlighting.

A pressurized spark gap with low-interelectrode capacitance was used in this investigation. A double-electrode trigger was used with a uv-grade quartz tube to isolate the trigger electrons from the main gap. Sulfurhexafluoride (SF_6) at 5 psi was mixed with argon at 400 psi to pressurize the spark gap. A 75-MΩ charge resistor was used in series with the spark gap and a 20-kV pulse was used for the trigger. Peak outputs and pulse widths for several different values of applied voltage and spark-gap pressure are shown below. The low-output peak with respect to applied voltage was attributed to corona or leakage current from anode to ground and to the cathode of the gap causing a large voltage drop across the 75-MΩ resistor. A new cavity is being designed to withstand 2000 psi and have less capacitance and a longer leakage path to ground. This should allow us to use higher voltage, decrease pulse width, and increase efficiency.

Voltage Applied to Charge Resistor (kV)	Spark-Gap Pressure (psi)	Peak Output Voltage (V)	Pulse Width (FWHM) (ns)
4	67	700	0.48
6	~110	1080	0.64
6	~125	~1000	0.60
$>V_{breakdown}$	~125	800	0.64

High-Voltage, Short-Pulse Technology (F. Wittman, R. Carman, N. Clabo)

We continued to develop technology to produce low-jitter, fast-risetime, short electrical pulses of high-voltage output. Several areas were explored, including the use of overvoltaged spark gaps to sharpen the pulse risetime, the use of pulsed charging techniques for krytrons, and the design of very low capacitance, electrically triggered spark gaps for producing electrical pulses of <300 ps. Also, several practical applications of this technology were identified, one of which will be discussed in this report.

Because laser-triggered spark gaps require careful alignment and a large amount of maintenance, it would be desirable to develop a simple, electrically triggered krytron circuit that would produce a subnanosecond output pulse of 15-20 kV. This could replace the optically triggered spark gap used for pulse generators in Pockels cell optical pulse selectors and pulse-clipping systems. With this in mind, we attempted to understand the process of pulsed charging of a krytron switch. We found that KN22 krytrons (EG&G) were not useful in this application because the pulsed charging process caused them to trigger uncontrollably. Further, by exceeding the maximum anode applied voltage rating, it was necessary to take into account the internal characteristic 50-Ω impedance of the KN22, as well as the increasing inductance of this impedance above 100 A. In practice, a larger external load impedance was required as the pulse charged voltage applied was increased.

The current capacity of the KN6B is ~3000 A, and the principal use is in ~50-ns risetime applications, therefore, we decided to try pulsed charging in this tube. We found that while the dc applied voltage limit on the KN6B anode was 8 kV, at least 20 kV could be applied in a pulsed mode for up to ~100 ns. Then, we noted that if the applied voltage is pulsed to 50 or 60 kV, internal conduction occurs. However, the resulting output pulse from the KN6B can be very short. A pulse charging circuit was built using 10 series KN22B tubes to apply an ~60-kV pulse to the anode of one KN6B. No keep-alive voltage is used on the KN6B so that full-charge voltage is developed on the anode before the tube starts to conduct. Figure IV-26 shows a 519 (Tektronix) oscillogram where the pulse is ~900-ps FWHM with an 18.75-kV peak. Notice that the trace does not return to the baseline, but rather should be ~5% of the peak due to the steady-state discharge of the large anode capacitor used in the KN22 string, while the output is taken into a piece of 50-Ω coaxial cable. In many applications, this feature is of no consequence, but when it is important, a crowbar system could be used to eliminate it. The pulser lifetime appears to be quite high, including the KN6B, even though ~375 A must flow to develop the full output voltage. We are packaging one such pulser to use as a pulse driver for a CdTe CO_2 pulse clipper. We intend to pursue the answer to why 60 kV must be applied to the

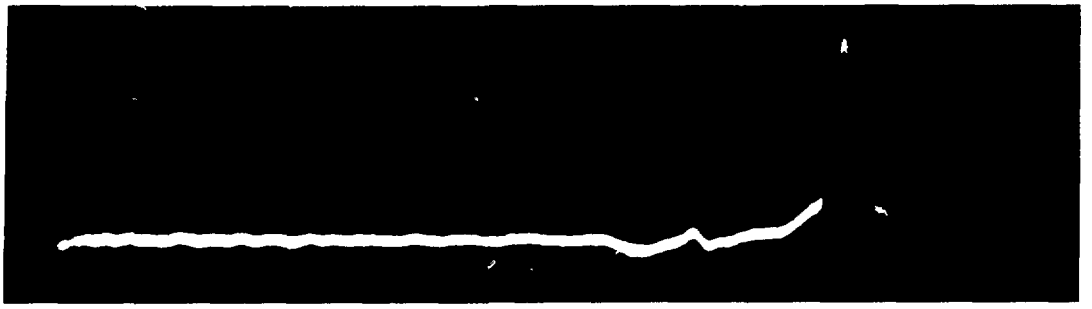

Fig. IV-26.
Oscillogram of an electrically triggered krytron pulser output as recorded on a Tektronix 519 scope. The amplitude corresponds to 18.75-kV peak and the pulse width is 900-ps FWHM with a risetime of ≤ 50 ps.

KN22 krytron string in order for the KN6B to produce a pulse of 18.75-kV peak.

Electrical pulses of 900-ps FWHM are interesting, but other Pockels cell applications require 15- to 20-kV electrical pulses with ~100-ps risetime and ~200-ps FWHM. At this time, we do not believe that a krytron system can be built to satisfy this requirement. On the other hand, we wish to retain electrical initiation of the pulse output.

CO_2 Laser System for Hydrodynamic Studies (R. L. Carman, F. Wittman, N. Clabo)

The study of the self-consistent evolution of electron density profiles near the CO_2 critical density is fundamental to understanding laser-plasma interactions. The ponderomotive force apparently ameliorates many of the deleterious effects once assumed to be present with long-wavelength lasers. This conclusion has been deduced from indirect measurements but should be confirmed directly. To do so, careful interferometric measurements with high spatial and temporal resolution are required. We determined that the most effective way to perform such measurements is with a small laser dedicated to this experiment. To this end, operation of a small CO_2 laser system began during the later part of 1978, but there are several problems that must be remedied before we can use the laser as a facility for interferometric measurements. All six cw CO_2 oscillators operated successfully in early summer 1978, delivering ~25 W total. Upon arrival of the Ar:Ge detectors, we demonstrated the piezoelectric translator (PZT) scheme of oscillator output frequency and amplitude stabilization. In this scheme, the front mirror is translated to adjust the cavity length to provide automatic feedback. The specific CO_2 line and band are controlled with the grating rear reflector. The diameter of the intercavity apertures was determined by manually translating the PZT-controlled mirror to cause more gain in the off-axis cavity modes and then stopping down the intercavity apertures until lasing ceases. Although each cavity has an independent feedback system and controller, no difficulties were encountered in obtaining the same relative amplitudes from the six lasers.

The beam-combining optics described in Ref. 13 were installed in the summer of 1978. We demonstrated adjacent line operation in the 10-μm P-branch shortly thereafter. Alignment was carried out in two phases. First, one beam was aligned to pass through the amplifier chain. Each of the other beams was centered and aligned to the first using the quadrant detector sensors developed for Helios. We achieved a centering accuracy of ±20 μm for several beams and determined that the angular drift of the beam-combining system was within the required tolerance of ±25 μrad.

The first GaAs Pockels cell could not withstand the cw beam. A large movable beam stop was then inserted in series with the two gates ahead of it to accomplish reliable 50- to 200-ns adjustable pulse generation.

The low-pressure amplifier chain can be divided into two parts. The first consists of five amplifiers, each 50 cm long, operating with a 1:1:1 mix of CO_2:N_2:He at an absolute pressure of 15 torr. By varying the duration of

the input laser pulse, we established that pulse durations <75 ns were required for the 10-μm (P20) gain to be independent of other lines in the 10-μm band.

The second GaAs Pockels cells separated the low-pressure amplifier sections and was synchronized with the first GaAs Pockels cell. The second portion of the low-pressure amplifier chain consisted of four amplifiers, each 50 cm long, also operated with a 1:1:1 mix of CO_2:N_2:He, but at an absolute pressure of 25 torr. We reliably obtained ~1 mJ for 75-ns pulse widths.

Firing only the 9- to 60-kV Marx banks for the low-pressure amplifier and the 10-kV GaAs Pockels cell pulse driver caused no timing problems; however, timing problems did arise when the 60- and 120-kV Marx banks of the TEA amplifiers were included.

Fig. IV-27.
High-pressure reinjection oscillator with four-pass optics integrated into the Invar-stabilized structure.

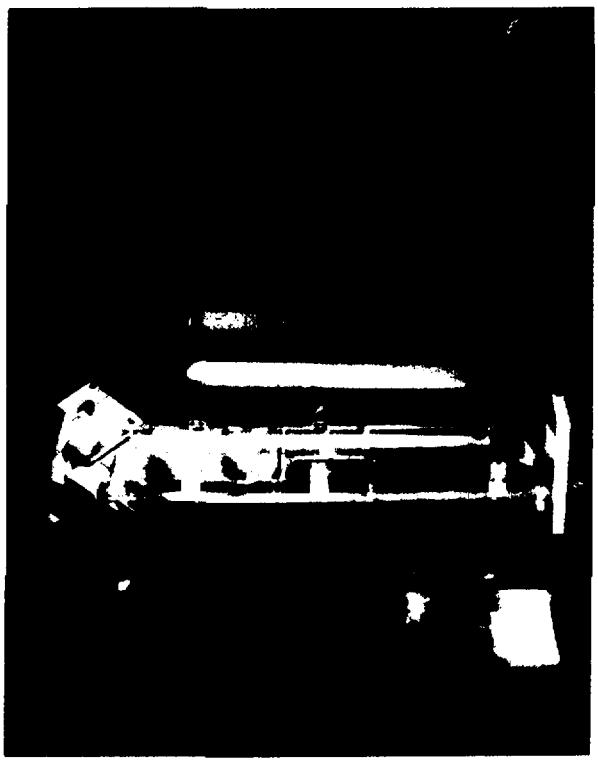

Fig. IV-28.
High-pressure laser components.

High-Pressure Reinjection Laser (E. S. McLellan)

Introduction. CO_2 laser oscillators capable of highly reproducible spectral content will be required in our future laser fusion systems. A multiatmosphere preamplifier is also required for efficient generation of high-power subnanosecond pulses. Such signals are needed for diagnostics development and materials studies, as well as for power-amplifier drivers. We developed a highly reliable, high-pressure reinjection oscillator that satisfies both requirements. The reinjection concept permits a single gain medium to be used as both oscillator and preamplifier.[13] Here, we discuss numerous improvements made during the present reporting period, and in particular, those leading to reliable operation at pressures up to 7600 torr. Measurements of spectral and spatial gain uniformity for various pressures, and of output-energy reproducibility are presented. Figures IV-27 and -28 show the Invar-stabilized reinjection oscillator assembly. This system integrates the oscillator and four-pass amplifier optical components into a single, stable structure that includes the pressure vessel for the high-pressure discharge.

Hardware Design Considerations. In our design, a simple capacitor and spark-gap system replaces the conventional Marx system for laser gas pumping. This simple system was found to enhance the laser reliability. The 0.075-μF main discharge capacitor is charged to 75 kV, regardless of gas pressure. High-pressure operation is facilitated by adjusting the laser gas mixture to take advantage of the $V \propto PR^{2/3}$ dependence of the self-sustained discharge voltage on total pressure P and proportion R of nonhelium laser gas components. Figure IV-29 plots the maximum arc-free operating pressure as a function of helium fraction in the laser mixture.

Our data show that with 60- by 5-cm electrodes separated by 1.5 cm, stable operation is obtained for $PR^{2/3} = 1.19$.

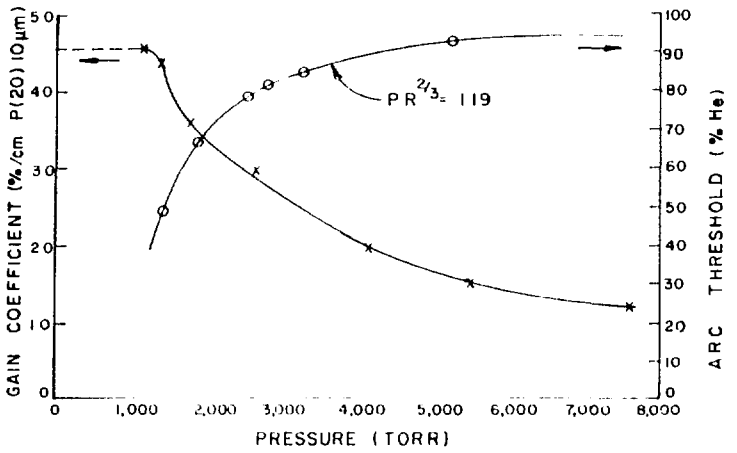

Fig. IV-29.
Maximum pressure obtained before arcing between the electrode as a function of helium fraction in the laser mix and measured small-signal gain at that pressure.

Laser Performance. The measured pressure-dependence of P-20 (10-μm) centerline gain is shown in Fig. IV-29 and in Table IV-II. Gain variation vs operating wavelength is described in Table IV-III, and measurements of gain variation with radial position within the aperture are presented in Fig. IV-30 and Table IV-IV. Greater gain homogeneity than that shown in Fig. IV-30 was obtained by series rather than parallel operation of the two preionizer circuits located behind the anode screen.

Specific stored optical energy was determined by measuring the energy extracted from a 0.5-ℓ discharge volume by gain-switched oscillation. When the entire 1.5- by 5-cm aperture was illuminated, 12 J was produced with a 36% reflecting output coupler. An uncoated NaCl output coupler (4% single-surface reflectance) produced $\geq$ 9 J.

Tests were conducted to determine whether shock and vibration caused by laser operation resulted in misalignment of the oscillator optics. Results of a 4000-shot test

TABLE IV-II

DEPENDENCE OF P20 CENTERLINE GAIN FOR 10.4-μm BRANCH OF VARIOUS LASING MIXES

	Gain at Various Pressures, torr, and $He:N_2:CO_2$ Mixes (%/cm)						
	1185 37:25:38	1420 50:20:30	1800 68:14:19	2645 80:10:10	4200 91:4:5	5500 95:2:3	7600 96:2:2
	4.52	4.40	3.55	3.06	1.98	1.50	1.24
	4.59	4.41	3.49	3.00	2.01	1.49	1.17
	4.55	4.39	3.49	2.95	2.00	1.51	1.19
	4.56	4.36	3.49	2.96	1.99	1.52	1.25
	4.46	4.41	3.57	2.92	2.01	1.52	1.19
Mean Gain	4.54	4.40	3.52	2.98	2.00	1.51	1.21
Gain, Standard Deviation	0.05	0.02	0.04	0.05	0.02	0.01	0.03

TABLE IV-III

P- AND R-LINE DEPENDENCE OF GAIN AT CENTERLINE OF CAVITY FOR 67:14:19::He:N_2:CO_2 AT 1800 torr

	Gain at 10.4-μm P-Lines (%/cm)				
	12	16	18	22	24
	2.88	3.16	3.24	3.04	3.05
	2.87	3.25	3.18	3.11	3.06
	2.93	3.24	3.28	3.12	2.97
	2.87	3.22	3.33	2.99	2.98
	2.93	3.22	3.35	3.14	2.95
Main Gain	2.90	3.22	3.28	3.08	3.00
Gain, Standard Deviation	0.03	0.03	0.07	0.06	0.05

	Gain at 10.4-μm R-Lines (%/cm)				
	14	16	18	20	22
	2.85	2.95	2.93	2.75	2.61
	2.84	2.91	2.93	2.79	2.63
	2.87	2.94	2.94	2.73	2.62
	2.90	2.99	2.97	2.75	2.60
	2.93	2.97	2.95	2.76	2.60
Mean Gain	2.88	2.95	2.94	2.76	2.61
Gain, Standard Deviation	0.04	0.03	0.02	0.02	0.01

	Gain at 9.4-μm R-Lines (%/cm)						
	20	16	14	14	15	18	20
	3.18	3.34	3.14	2.93	3.10	3.18	3.21
	3.17	3.31	3.38	2.92	3.10	3.12	3.20
	3.19	3.26	3.37	2.92	3.11	3.11	3.20
	3.23	3.30	3.36	2.98	3.22	3.21	3.19
	3.14	3.23	3.39	3.02	3.07	3.15	3.21
Main Gain	3.18	3.29	3.38	2.95	3.12	3.15	3.20
Gain, Standard Deviation	0.03	0.05	0.02	0.04	0.06	0.04	0.01

conducted during a 6-day period are shown in Fig. IV-31. No drop in laser energy was observed after 4000 shots within the 1% resolution of the measuring system. These results show that mechanical coupling of the discharge and optical structure in this design did not degrade system reliability.

During this test, there were 6 shot failures in a 4000-shot sequence. This 99.85% reliability was obtained

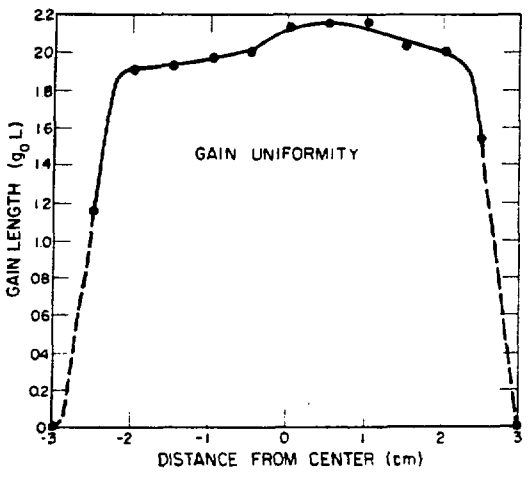

Fig. IV-30.
Gain uniformity across the discharge measured parallel to electrodes at 1800 torr with 67:13:20::He:N_2CO_2 laser mixture on P-20 lines of 10-μm branch.

without warmup or purging of the laser. Start-up time was determined entirely by the time required to reach operating pressure. This laser will be used in the GWTF upgrade. In this application, previous experience at high pressure predicts pulse widths of 0.1 to 0.5 ns with peak powers of 1.0 to 5.0 GW.

MILITARY APPLICATIONS (J. H. McNally)

Introduction

During the past 2 years (January 1977 to December 1978), the two-beam glass laser facility was used for a variety of experiments most of which are related to military applications. The laser can deliver a pulse to the target chamber from two temporally and spatially coincident opposing beams. The pulse width can be 70, 300, or 1000 ps. Normally, a 300-ps pulse is used to deliver 15-50 J on target for a power density of $\sim 10^{14}$ W/cm^2.

Two series of experiments not directly connected with military applications involve calibrating the GEAR Pico-X streak camera and obtaining spectroscopic data in the vacuum uv of highly ionized metals. The laser is used to produce a short burst of x rays of known duration for calibrating the camera. The laser beam impinging on a variety of flat metallic targets produces a high-temperature plasma for spectroscopic measurements.

The following experiments were directly related to weapons applications.

1. Equation-of-state studies. By observing high-pressure laser-generated shock fronts, an improved version of the equation of state (EOS) can be deduced.

2. Multiburst simulation and blast wave interactions. Laser fireballs created from single or multiple targets simulate full-scale nuclear events with respect to density and temperature.

TABLE IV-IV

DEPENDENCE OF GAIN ON RADIAL POSITION WITHIN APERTURE, 67:14:19::He:N_2:CO_2

	Gain at Various Distances from Centerline (%/cm)										
	+2.5	+2.0	+1.5	+1.0	+0.5	0	−0.5	−1.0	−1.5	−2.0	−2.5
	2.15	3.30	3.14	3.35	3.52	3.52	3.21	3.15	2.81	3.00	1.40
	2.26	3.25	3.10	3.38	3.48	3.55	3.22	3.04	2.96	2.86	1.62
	2.25	3.34	3.13	3.34	3.47	3.55	3.26	2.85	2.81	3.21	1.50
	2.18	3.24	3.32	3.35	3.45	3.55	3.21	3.12	2.91	2.78	1.53
	2.19	3.35	3.08	3.32	3.44	3.60	3.25	2.91	2.96	3.11	1.45
Mean Gain	2.21	3.30	3.16	3.35	3.47	3.56	3.23	3.01	2.89	2.99	1.50
Gain, Standard Deviation	0.05	0.05	0.09	0.02	0.03	0.03	0.02	0.13	0.07	0.18	0.08

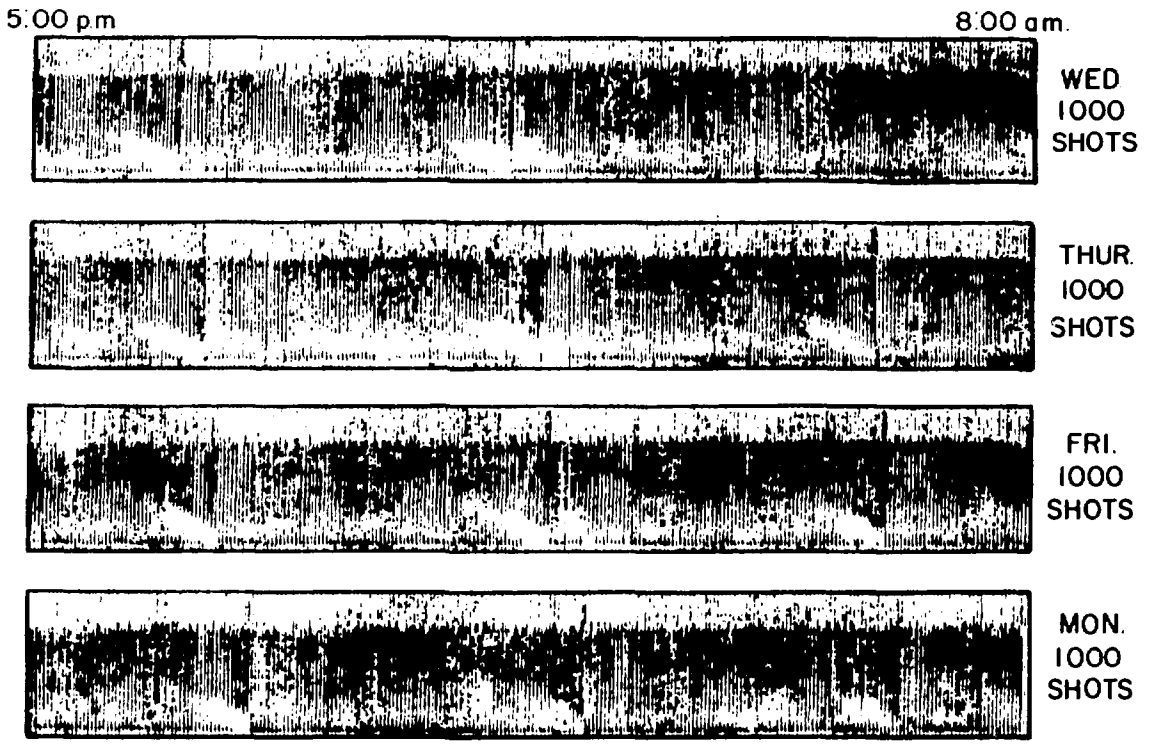

Fig. IV-31.
Chart recorder output showing the relative energy obtained for each of 4000 shots fired during the integrated structure stability test.

3. Opacity experiments. The laser-produced plasma fireball is observed in the visible region at various angles through a series of filters to gain information on isotropy.

Equation-of-State Studies (L. Veeser, J. Solem, A. Lieber—P Division)

We did not have a suitable streak camera during most of the past 6 months, therefore, we spent considerable time upgrading our optics to collect more light from the targets and to reduce the background light. When we received a GEAR Pico-V camera late in December, we decided to begin using it immediately and to postpone detailed studies of camera sensitivity and sweep speeds. This was dictated by the laser schedule, by our desire to move as quickly as possible toward our goal of an impedance-match equation-of-state measurement, and by the lack of a convenient calibration facility.

Our new camera is very reliable. Image magnification to about 25x on the streak camera slit still leaves enough intensity and resolution to see more than one step on a target foil. Therefore, we can measure how the shock velocity changes with target thickness. We looked at an impedance-match foil made of a 3-μm step of gold and a 4-μm step of aluminum on a 13-μm-thick aluminum substrate. Although these data have not been analyzed, the streaks indicate that we can observe the quantities needed to demonstrate an impedance-match experiment. We also made some risetime measurements for aluminum foils, finding risetimes of ~50 ps measured with ~15-ps resolution. Such risetimes imply a viscosity at 2 Mbar of $\sim 10^2$ P, which is three orders of magnitude less than Mineev and Savinov[15] measured in 1967. We feel that our numbers are more reasonable.

Future projects include upgrading the diagnostics and the laser beam quality for high-quality impedance-match measurements, improving the beam spot uniformity and measuring its size for each shot, and studying the time dependence of the pulse.

Multiburst Simulation and Blast Wave Studies (S. N. Stone, M. D. Wilke—X Division)

We continued laboratory experiments of laser-driven simulations of the nuclear multiburst environment. Our optical diagnostic techniques were expanded during this reporting period with the successful introduction of two wavelength experiments. Records were obtained of shockwaves in 50- and 580-torr air for laser energies of 10 and 30 J, delivered with pulse durations of 300 ps, at times ranging between 0.5 and 50 μs. Maximum electron densities near the center of the shocked region, as deduced from the observations, are about an order of magnitude lower than calculations based on thermal equilibrium conditions. On the other hand, maximum gas densities observed in the shock front differ from calculations by only ~30%.

We improved our set up geometry for observing shock coupling experiments from air into transparent plexiglass blocks, with the result that shock-coupling strengths were considerably lower than observed earlier.

For the first time in our MAL experiments, one-dimensional and two-dimensional shocks were generated in air at very low pressure (1 torr). Previously, the lowest pressures were 10 and 20 torr. The fast-framing emission pictures of the 1 D shocks showed luminous plasma to relatively large radii (>1 cm) and late times (>1 μs) with substantial deviations from uniform spherical shape.

In the 2-D case of two colliding shocks at 1 torr, we observed an appreciable increase in luminosity from the plasma ring formed by the intersection of the two spherical shock waves; this luminosity was ~33% greater than the sum of the light from the separate shock waves.

Laser Opacity Equipment (N. M. Hoffman, L. W. Miller, J. M. Mack, H. W. Kruse—X Division)

During this period, data from our August 1978 experiments were reduced and analyzed. These experiments used a channel-plate-intensifier (CPI) camera gated at 5.7 ns to image the optical self-emission from the back of aluminum foil targets simultaneously along a 30° and a normal LOS (see Fig. IV-32). We saw, for the first time, a time-dependent anisotropy in this emission, which we discuss below.

The two-dimensional images on film were scanned with a densitometer, and film densities were converted to relative intensities. The resulting two-dimensional array of intensity values was smoothed and then searched for the peak value of intensity in each LOS. The vertical axis shown in Fig. IV-33 shows the anisotropy R, which is the ratio of peak intensity in the 30° LOS to the peak intensity in the normal LOS. The horizontal axis is Δt, the time difference between the laser pulse (300-ps FWHM) and the trailing edge of the gate; i.e., at Δt = 0, the gate just begins to overlap the laser pulse. Increasing Δt means the gate is delayed with respect to the laser pulse. The ratio R was corrected for progressive differential

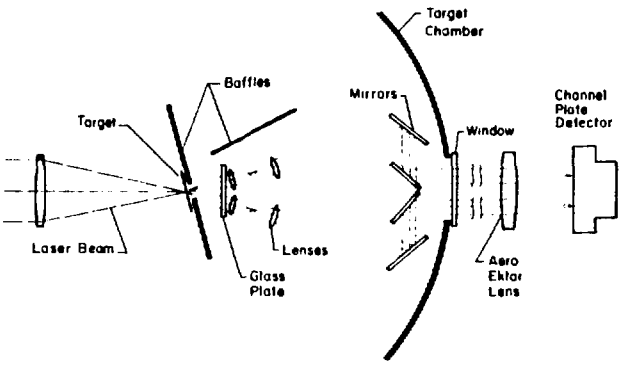

Fig. IV-32.
Schematic of experiment showing channel-plate-intensifier camera gated to image optical self-emission from the back of aluminum foil targets simultaneously along a 30° and a normal LOS.

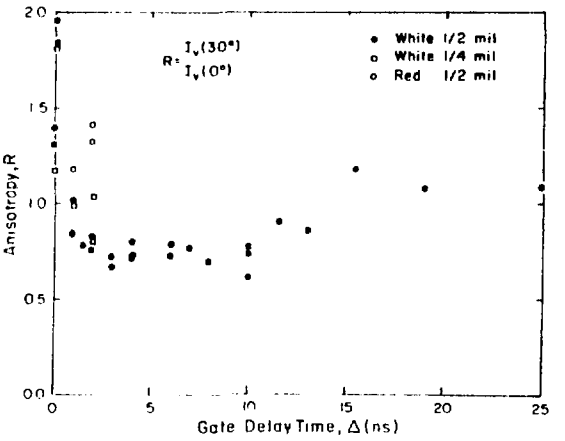

Fig. IV-33.
Anisotropy in self-emission along the 30° and normal LOS vs gate delay time.

obscuration of the glass plate protecting the optics; this effect is always <12%. Each point represents a single laser shot; pulse energies range between 9 and 40 J.

Most of the data in Fig. IV-33 are for an unfiltered band of white light, defined essentially by the S-20 response of the CPI photocathode. However, 3 points were taken using a red filter which passed only $\lambda \geq 6000$ Å. These points are shown as open circles.

These data reveal a trend from "limb-brightening" ($R > 1$) to "limb-darkening" ($R < 1$) as the gate is delayed with respect to the laser pulse. At late enough times ($\Delta t \geq 10$ ns), R returns roughly to unity. The 1/4-mil foils behave much like the 1/2-mil foils, although we have little data for them. Interestingly, red light seems to be "limb-brightened" at the same time that white light is "limb-darkened" at $\Delta t = 2$ ns.

Figure IV-34 shows relative intensity in the normal LOS vs gate delay time for laser pulses with energies between 26 and 31 J striking 1/2-mil foils. This profile is what one expects from smearing the true intensity history of the target backside with the ~6-ns FWHM gate: from earlier streak camera observations we know that the intensity history consists of a bright flash of <1-ns duration, followed by a fainter tail of >10-ns duration.

Comparing Fig. IV 33 with Fig. IV-34 shows that the limb-darkening ($R \simeq 0.75$ at 2 ns $\leq \Delta t \leq$ 10 ns) is associated with the smeared-out bright flash. Also, the return of R to roughly unity is associated with the faint tail at $\Delta t \geq 10$ ns. This is expected as the plasma

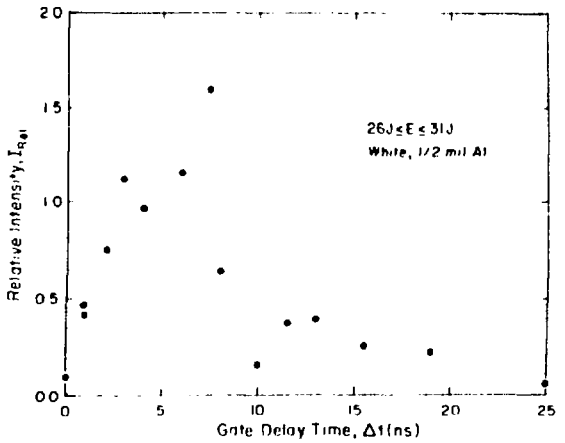

Fig. IV-34.
Relative intensity in the normal LOS vs gate delay time.

becomes nonplanar, which certainly occurs by 10 ns after the laser pulse.

The limb-brightening for $\Delta t < 2$ ns has been a mystery, though we now believe it may be an instrumentation effect. We can rule out a straightforward interpretation using any isotropic source function in a planar plasma: it is impossible to get limb-brightening stronger than $1/\cos\theta$ in this way. At $\theta = 30°$, $1/\cos\theta = 1.15$, whereas we have R between 1.5 and 2.0.

Thus, we are led to consider a dynamic instrumentation effect as a source of spurious limb-brightening. Suppose that the CPI tube does not gate simultaneously across its surface. Specifically, suppose that the portion of the tube viewing the 30° LOS gates "off" slightly later than the portion of the tube in the normal LOS. Then for $\Delta t \simeq 0$, the 30° view will integrate more of the rising edge of the bright flash than will the normal view, giving a spurious limb-brightening. If this does happen, and it probably does (see below), it nevertheless does not invalidate our observations of limb-darkening.

If the back-side emission were not intrinsically limb-darkened, then the spurious limb-brightening caused by nonsimultaneous gating would persist at least until the leading edge of the gate is moved later than the laser pulse; i.e., until $\Delta t \simeq 6$ ns. After $\Delta t \simeq 6$ ns, it might be possible for nonsimultaneous gating to give spurious limb-darkening; then the emission intensity is decreasing with time over most of the gate duration. This argument does not affect the limb-darkening for 2 ns $\leq \Delta t \leq 6$ ns, except possibly to make the observed limb-darkening somewhat weaker than the intrinsic limb-darkening.

Recent experiments show that, in fact, the CPI tube does not gate simultaneously across its surface. It appears that the outer edge of the circular tube gates "on" about 1 ns before the center of the tube; the edge gates "off" slightly earlier, too, so that the total gate duration is about the same across the tube. The gating pattern is circularly symmetric about the center of the tube; thus, to remove this effect one could simply ensure that the two target images are equidistant from the tube center. We are reviewing the data to determine how far the two images were from being centered.

Vacuum uv Spectroscopy of Highly-Ionized Metals (J. Reader and G. Luther, NBS, Washington, DC)

In October 1978, researchers from the National Bureau of Standards used LASL's high-power Nd:glass

laser to observe spectra of highly ionized atoms belonging to isoelectronic sequences important to the diagnosis of fusion plasmas generated in tokamaks. These observations were made by photographing the spectra of laser-produced plasmas of various metals with a 2-m grazing-incidence spectrograph. Spectra of the following metals were obtained: Fe, Sr, Y, Zr, Nb, Mo, Ru, Rh, Pd, Ag, Cd, Sn, Ba, La, Nd, Sm, Gd, Dy, Er, Yb, Ta, and W. All spectra were obtained with a laser pulse width of 300 ps at a total energy of ~25 J. Six laser pulses were generally required to produce a usable spectrum. The preliminary results are catagorized by isoelectronic sequence.

Zinc sequence. Figure IV-35 summarizes the NBS/LASL observations for the $4s^2\ {}^1S_0 - 4s4p\ {}^1P_1$ resonance line. Z_c is the net charge of the atomic core seen by the valence electron, or stage of ionization. The point for Xe is from tokamak observations by Hinnov.[16] The points for Rb^{6+} to Sb^{21+} are from recent work at

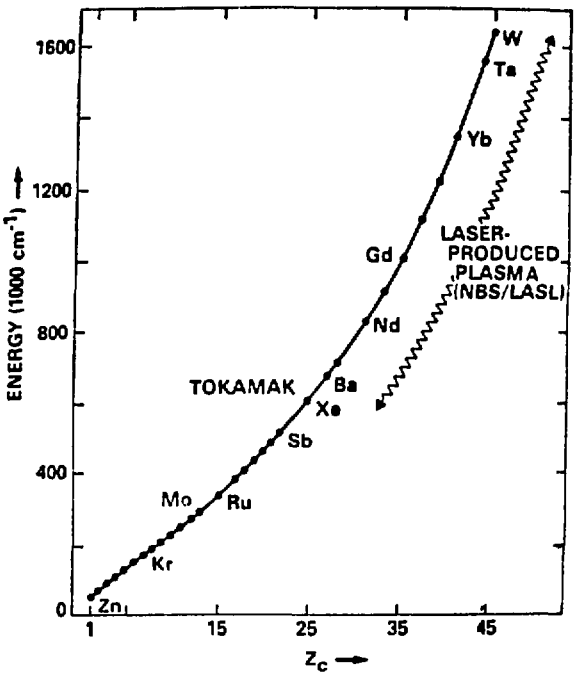

Fig. IV-35.
Energy transitions for the $4s^2\ {}^1S_0 - 4s4p^1p_1$ resonance line for the zinc sequence. Zc is net charge of the atomic core seen by the valence electron, or stage of ionization.

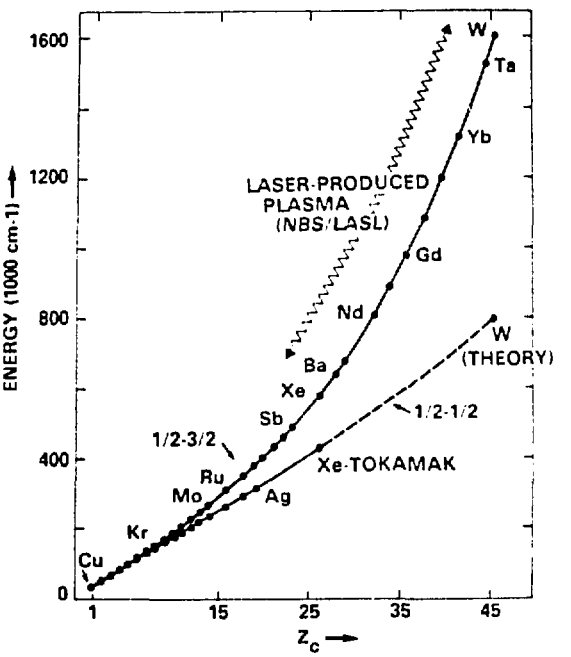

Fig. IV-36.
Energy transitions for the 4s-4p resonance lines for the copper sequence.

NBS with low-inductance sparks[17] and laser-produced plasmas.[18]

Copper sequence. Figure IV-36 summarizes the NBS/LASL observations for the 4s - 4p resonance lines. The Xe points are again tokamak observations from Ref. 16. Previous NBS work[17,18] on these ions covered Rb^{7+} to Sb^{22+}. The present observations for W^{45+} represent the highest charge states ever observed with diffraction gratings.

Comparisons with theory for the copper and zinc sequences from Br and Kr to W are given in Figs. IV-37 and -38. The points for Xe (with error bars) represent interpolated corrections to the theory, which permit derivations of accurate semiempirical wavelength values.

Sodium sequence. In a recent NRL/NBS/LASL collaboration involving spectra for molybdenum obtained with a Nd:glass laser at the Naval Research Laboratory in Washington, DC,[19] two close lines were observed in the neighborhood of a strong tokamak line[16] at 129 Å. This was attributed to the $3s\ {}^2S_{1/2} - 3p\ {}^2P_{3/2}$

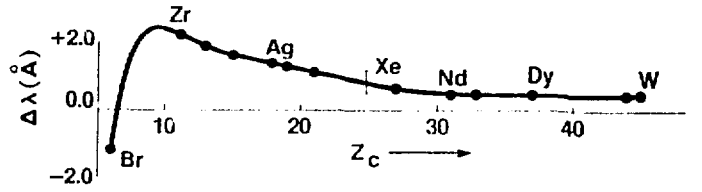

Fig. IV-37.
Comparison of theory with observed wavelength for the zinc sequence.

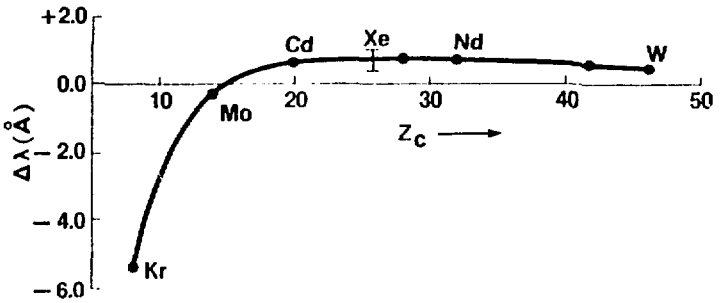

Fig. IV-38.
Comparison of theory with observed wavelength for the copper sequence.

transition of Mo^{31+} Figure IV-39 gives the new NBS/LASL results for this sequence (Sr to Pd). They show that the lower energy line of the two close lines in the laser-produced plasma is the $3s\ ^2S_{1/2} - 3p\ ^2P_{3/2}$ transition of Mo^{31+}, and the higher energy line, the $3p\ ^2P_{3/2} - 3d\ ^2D_{5/2}$ transition of this ion. The Kr^{25+} point is a tokamak observation of Hinnov.[16]

Magnesium sequence. In Fig. IV-40, the points between Sr and Rh represent the NBS/LASL results. They confirm the identifications in Ref. 19 for Mo^{30+} for the three transitions shown. The Kr point is due to Hinnov.[16] Figure IV-41 gives a comparison between theory and experiment for the Mg isoelectric sequence. The point for Kr represents an interpolated correction to the theory, from which an accurate semiempirical wavelength may be derived.

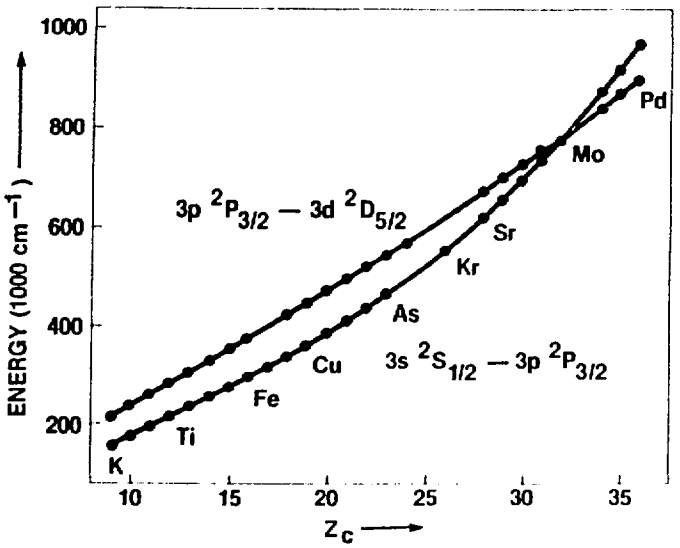

Fig. IV-39.
Energy transitions for the sodium isoelectronic sequence showing two transitions of Mo^{31+}.

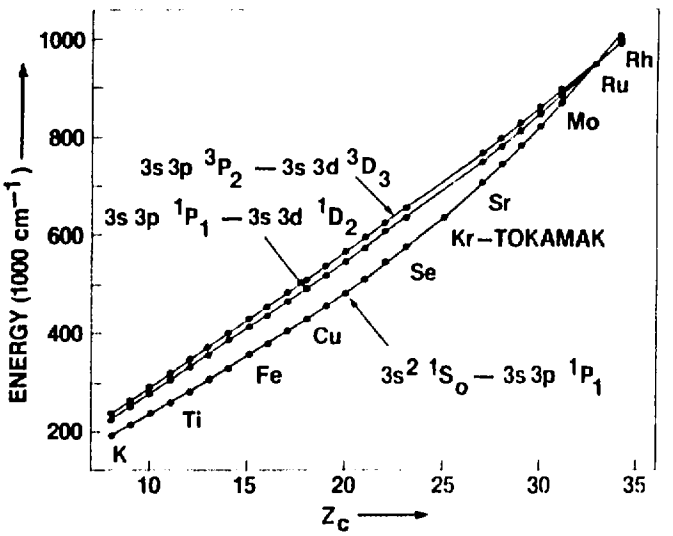

Fig. IV-40.
Energy transitions for the magnesium isoelectronic sequence showing three transitions of Mo^{30+}.

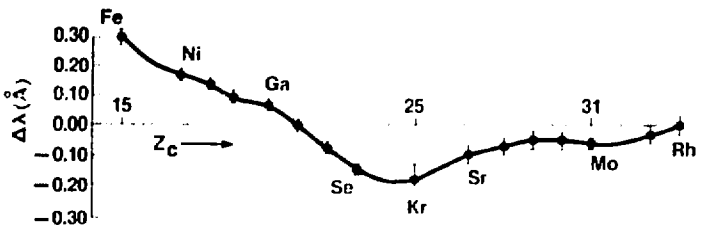

Fig. IV-41.
Comparison of theory with experiment for transition wavelengths in the magnesium isoelectronic sequence.

REFERENCES

1. D. B. vanHulsteyn, P. Lee, K. B. Mitchell, and P. D. Rockett, "X-Ray Continuum Spectra," in "Laser Fusion Program, July 1—December 31, 1977," Los Alamos Scientific Laboratory report LA-7328-PR (December 1978).

2. D. Giovanielli and C. W. Cranfill, "Simple Model for Exploding Pusher Targets," Los Alamos Scientific Laboratory report LA-7218-MS (May 1978).

3. V. Cottles, D. Giovanielli, L. White, and A. Williams, "Absorption Measurements-10.6 μm CO_2 Laser Light," in "Laser Fusion Program, July 1—December 31, 1977," Los Alamos Scientific Laboratory report LA-7328-PR (December 1978).

4. F. Young, "Thomson Parabola Measurement of Fast-Ion Spectra and Population of Ion-Charge States," in "Laser Fusion Program, July 1—December 31, 1977," Los Alamos Scientific Laboratory report LA-7328-PR (December 1978).

5. D. Giovanielli, J. Kephart, and A. H. Williams, "Spectra and Angular Distributions of Electrons Emitted from Laser-Produced Plasmas" J. Appl. Phys. **47**, 2907 (1976).

6. R. F. Benjamin, G. H. McCall, and A. Wayne Ehler, "Measurement of Return Current in a Laser-Produced Plasma," Phys. Rev. Lett. **42**, 890 (1979).

7. T. H. Tan, "Inertial Fusion Program, January 1—June 30, 1978," Los Alamos Scientific Laboratory report LA-7587-PR (May 1980).

8. J. G. Crow, J. Plasma Phys. **14**, Part 1, 65 (1975).

9. D. Forslund, J. M. Kindel, and K. Lee, Phys. Rev. Lett. **39**, 284 (1977).

10. V. Cottles, "Inertial Fusion Program, January 1—June 30, 1978," Los Alamos Scientific Laboratory report LA-7587-PR (May 1980).

11. T. H. Tan, "Inertial Fusion Program, January 1—June 30, 1978," Los Alamos Scientific Laboratory report LA-7587-PR (May 1980).

12. P. B. Lyons, S. E. Caldwell, L. P. Hocker, D. G. Crandall, P. A. Zaganiro, J. Cheng, G. Tirsell, and C. R. Hurlbert, IEEE Trans. Nucl. Sci. **NS-24** (1977) p. 177.

13. F. Skoberne, Comp., "Inertial Fusion Program, January 1—June 30, 1978," Los Alamos Scientific Laboratory report LA-7587-PR (May 1980).

14. C. M. Vest and D. G. Steel, "Reconstruction of Spherically Symmetric Objects from Slit-Imaged Emission: Application to Spatially Resolved Spectroscopy," Opt. Lett. **3**, 54-6, (1978).

15. V. N. Mineev and E. V. Savinov, Sov. Phys. JETP **52**, 629 (1967).

16. E. Hinnov, "Highly Ionized Atoms in Tokamak Discharges," Phys. Rev. **14A**, 1533 (1976).

17. J. Reader and N. Acquista, "4s-4p Resonance Transitions in Highly Ionized Cu- and Zn-like Ions," Phys. Rev. Lett. **39**, 184 (1977).

18. J. Reader, G. Luther, and N. Acquista, "Spectrum and Energy Levels of Thirteen-Times Ionized Molybdenum (Mo XIV)," J. Opt. Soc. Am. (December 1978).

19. P. G. Burkhalter, J. Reader, and R. D. Cowan "Spectra of Mo XXX, XXXI and XXXII from a Laser-Produced Plasma," J. Opt. Soc. Am. **67**, 1521 (1977).

V. LASER FUSION THEORY AND TARGET DESIGN

(D. B. Henderson)

Our theoretical support activities are closely coupled to our experimental efforts, with the intent of gaining a fundamental understanding of laser-target interactions, particularly of the relevant plasma physics and hydrodynamics. The close coupling of theory and experiments has made it possible to eliminate theories that are not supported by experiment. In general, basic studies have shown that the design difficulties associated with long wavelength are less severe than believed earlier, and that breakeven target designs are attainable even in the presence of a hot-electron spectrum. These results have increased our confidence that scientific breakeven can be demonstrated with our efficient, inexpensive CO_2 lasers.

THEORETICAL SUPPORT

Introduction (D. W. Forslund)

The supporting physics section continued its efforts to develop models for laser light absorption and transport of the resulting deposited energy. The effects of deliberate or inadvertent targeting error on the absorption of light by spherical targets in the Helios system were calculated. The calculations indicate that absorption may be enhanced by off-center focusing. The validity of the empirical scaling model of hot-electron temperature was further verified, as well as the detailed acceleration mechanism of the hot electrons. A more accurate Monte Carlo treatment of hot-electron transport was developed, which includes important cross-coupling terms between the hot and cold electrons. Finally, a more precise calculation of the loss of fast ions from the tails of the fuel-ion distribution in low pR pellets is presented.

Light Absorption by a Spherical Target as a Function of Laser Focal Shift (H. Brysk, A. J. Scannapieco)

The illumination of a sphere by a system of finite laser beams and the associated energy deposition were discussed previously.[1] However, the complete computation of the amount of light absorbed by a spherical target requires further consideration of the time variation in the laser pulse and of the motion of the critical surface under hydrodynamic expansion. On the basis of a two-dimensional study, the expansion velocity can be approximated by

$$v = 200\ \pi\ I^{1/3}\ ,$$

where I is the largest absorbed irradiance up to that time in the problem, and where the numerical factor has been evaluated with the energy expressed in kilojoules, time in picoseconds, and distance in microns (thus, the units of v are 10^8 cm/s and those of I are 10^{23} W/cm^2).[2]

Laser light absorption by spherical targets in Helios was computed with the LISP code (Laser Illumination of Spherical Pellets). The initial target radii were 100 and 200 μm (i.e., the bracketing current design values). The targets were assumed to expand during irradiation (total beam energy, 4 kJ) to ~1000 μm. The focal spots were aimed in unison at the center of the target or at various lateral distances from the center, both along and perpendicular to the polarization direction, to illustrate the impact of deliberate or inadvertent targeting. The focal spot was assumed Gaussian with a width of 68 μm, and the temporal pulse as triangular, with a risetime of 200 ps and a fall time of 1 ns.

The fractional absorption (integrated over the pulse length) as a function of the displacement of the focal spot from the center of the target is plotted in Fig. V-1 for the two initial target sizes and for P, the displacement along the polarization direction, and S, perpendicular to P. With the focal spot at the center of the target, there is, of course, no polarization dependence; also, there is no sensitivity to the initial target radius because the target quickly grows to a size much larger than the focal spot (and to about the same size for both initial radii). Note that the absorption changes little for focal shifts (in any direction) of the order of the focal spot, so that the quality of targeting cannot be safely inferred from target performance. When the beam is shifted perpendicularly to the polarization direction, there is a monotonic decrease in absorption with displacement. On the other hand, for shifts along the polarization direction there is

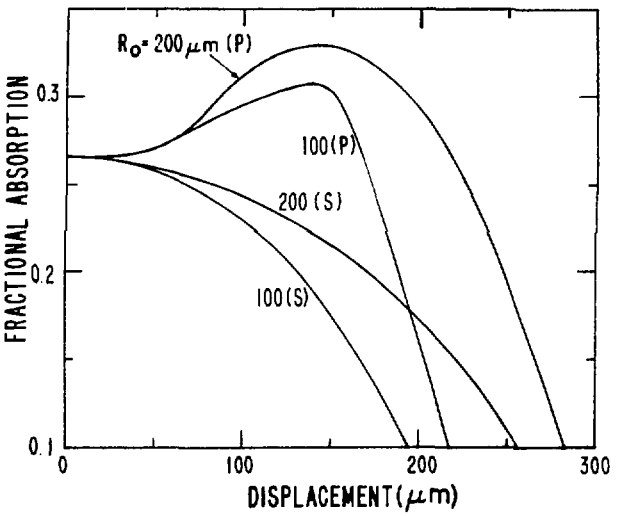

Fig. V-1.
Light absorption by a spherical target vs beam shift P along polarization direction, and S perpendicular to polarization.

an absorption maximum (as much as 25% higher) for an off-center position. More significant may be the fact that this maximum occurs with a displacement ~150 μm away from the specular point; there may, then, also be an enhancement of laser output because of suppression of parasitics.

Target performance depends not only on total energy absorption but also on its time dependence. Figures V-2 and -3 display the temporal profile of the absorbed power for the two target sizes with various focal spot displacements. With the focal spot at the center of the target, the absorbed power profile is quite similar to the triangular incident power profile. For displacements smaller than the initial target radius, the pulse shape is only moderately altered while the amplitude changes, so that Fig. V-1 approximately presents the relative performance. As the displacement increases, the pulse rise is slowed because only the wing of the beam pattern is incident on the target until the latter has expanded enough to intercept a major part of the beam; hence, the relative performance for displacements greater than the initial target radius is expected to be worse than Fig. V-1 suggests. At late times, the absorption becomes insensitive to the shift because the target has then expanded so much that its size is much larger than the displacement and the beam size.

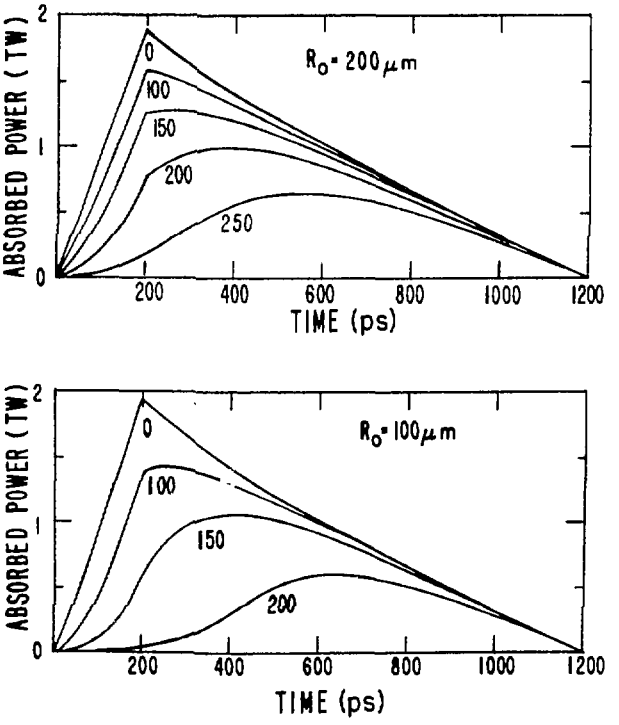

Fig. V-2.
Absorbed power profile for beam shifts (μm) perpendicular to polarization; (a) for R_0 = 200 μm; (b) for R_0 = 100 μm.

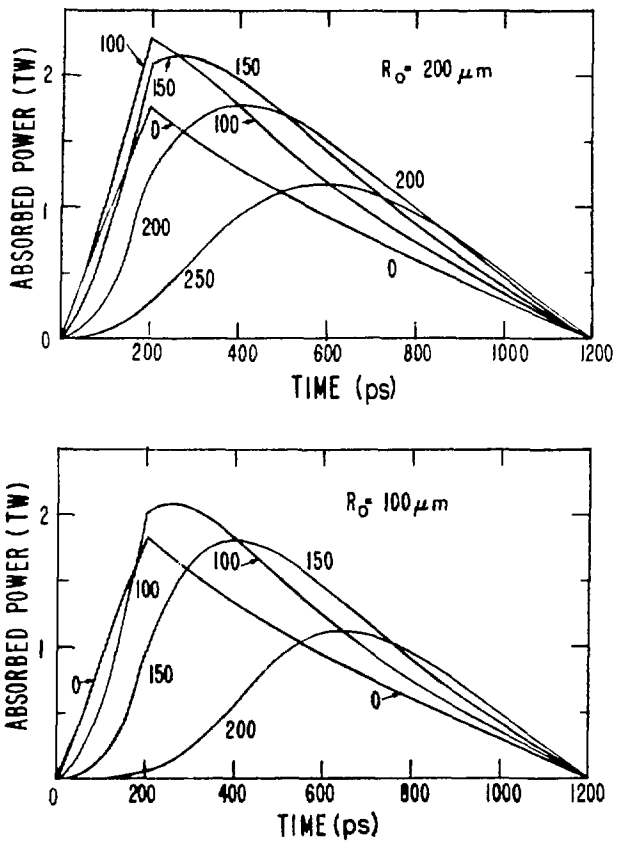

Fig. V-3.
Absorbed power profile for beam shifts (μm) along polarization (a) for R_0 = 200 μm; (b) for r_0 = 100 μm.

Extension of Suprathermal Electron Scaling Law (D. W. Forslund)

Of great importance in the performance of laser-driven targets is the spectrum of the suprathermal electrons generated in the absorption process. We previously reported[3] a scaling law that fits the suprathermal electron spectrum produced in two-dimensional WAVE simulations and agrees rather well with the experimental data. We verified that this scaling law is valid over an intensity range an order of magnitude wider than reported previously, now ranging from 10^{15} to 2×10^{17} W · μm²/cm². This result was obtained on the CRAY-1 computer, which accepts grid sizes and performs at speeds unattainable on the CDC 7600. At the highest intensity run, $I\lambda^2 = 1.6 \times 10^{17}$ W · μm²/cm², still below the maximum attainable intensities in Helios, the measured hot temperature T_H (for T_c = 0.625 keV) was 35 keV, whereas the formula[3]

$$T_H = 30(I\lambda^2)^{1/3}T_c^{1/3} ,$$

yields 30 keV; here $I\lambda^2$ is in units of 10^{17} W · μm²/cm², and T_H and T_c are in keV. At the lowest intensity of 1.2×10^{15} W · μm²/cm², T_H was 9.3 keV, in agreement with the above formula. The new data points are shown in Fig. V-4. This result increases our confidence in using the formula to predict the hot-electron temperatures.

Other noteworthy features of the highest intensity run illustrate that the absorption process is extremely nonlinear. First, the hot-electron temperature is less than the oscillating energy of 41 keV of an electron in the vacuum electromagnetic field; it would be interesting to see whether this behavior continues at higher intensities. Second, the hot-electron density is three times higher than the critical density, indicating that the hot-electron pressure gradient at that density is insufficient to overcome the balance between the cold-electron pressure gradient and the laser pressure gradient. This situation exists even though the hot pressure exceeds the cold pressure by more than a factor of 3. The absorption remains above 25% over the entire intensity range.

Coherent Acceleration Of Hot Electrons (P. Bezzerides, D. DuBois, D. Forslund)

In an effort to understand the physical mechanisms responsible for the high-energy tails observed in simulations of resonance absorption, we developed a simple model of the acceleration process. The ultimate goal of this work is to identify the controlling factors in the development of the hot-electron spectrum and thereby to determine the extent to which the spectrum can be modified experimentally.

The model was studied numerically and analytically. Basically, it assumes that the heating is due to coherent acceleration when an electron passes through a large-amplitude, localized, traveling wave with spatially varying phase velocity. Our numerical work, particularly the phase-space plots, illustrates that the particle in the field oscillates at large amplitudes about its guiding center, and that this coherent oscillatory motion is interrupted by resonant acceleration in the neighborhood of the

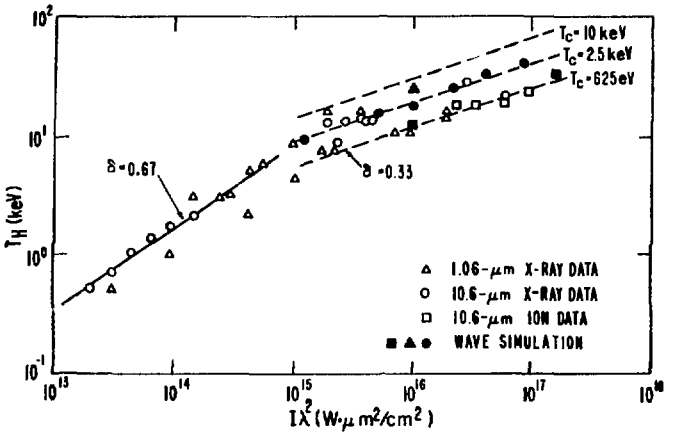

Fig. V-4.

Hot-electron temperature vs laser intensity. The solid data points are WAVE simulation points and the rest are experimental data. The new points are at 1.2×10^{15} and 1.6×10^{17}. The dashed curves are the empirical scaling laws for three different background electron temperatures, $T_c = 0.625$, 2.5, and 10.0 keV. The solid squares correspond to $T_c = 625$ eV, the solid circles to $T_c = 2.5$ keV, and the solid triangles to $T_c = 10$ keV.

resonance where the velocity is equal to the phase velocity, leading to the final velocity of the particle. The final time-averaged distribution function in v_2 is obtained from the $v_1 - v_2$ transform plots, where v_1 is the velocity at which the electron was injected into the field at early time to exit the field with value v_2 at a given final time.

Most attempts to understand the heating analytically have invoked the transit-time heating effect, which is the only way to explain how particles that are already fast can acquire still higher energies. We derived a general formula relating v_1 to v_2 by using a generalization of guiding-center theory, which allows for large-amplitude adiabatic motion, resonant interaction, and transit-time effects. We found that

$$v_1 = v_2 \exp\left\{ \int_{\tau}^{t(v_2,t)} d\tau \; \partial/\partial x(\tau) \; u_H(x(\tau),\tau) \right\} , \qquad \text{(V-1)}$$

relating the velocities of the velocity transform plot for a given time t at which v_2 is attained, where τ is the injection time. In Eq. (V-1), $u_H[x(\tau),\tau]$ is the oscillatory velocity of the particle at its position $x(\tau)$ at time τ. Equation (V-1) reduces to the well-known limits of guiding-center motion, resonant heating, or transit-time heating, but more important, it shows how the acceleration scales with the inhomogeneity of the field. Evaluating the integral in Eq. (V-1) is, in general, as difficult as obtaining the detailed trajectories. For the envelope of the $v_1 - v_2$ transform corresponding to maximum acceleration for a given v_2, we find

$$v_1 = v_2 \exp\{ - (v_2 - v_1)/v_{ph}(x_r) \} , \qquad \text{(V-2)}$$

with $v_{ph}(x_r)$ denoting the phase velocity at the resonant point given by $v_{ph}(x_r) = v_2 - \Delta v$, where $\Delta v = 4/\pi\sqrt{v_{os}(x_r)v_{ph}(x_r)}$. The most important limit occurs when, in the frame moving with the phase velocity, the acceleration due to the field is greater than that due to the spatial phase inhomogeneity. Note that Δv is equivalent to the scaling result for $T_H \simeq eE\ell$, where ℓ^{-1} is to be understood as k, the spatial phase. The predictions of Eq. (V-2) compare favorably with the numerically determined $v_1 - v_2$ envelope for the velocity transform plot; we believe, therefore, that the coherent-acceleration model is well understood. Progress is being made in uncovering the role of coherent acceleration in our simulations.

Hot-Electron Transport (R. Mason)

Elsewhere we described a double-diffusion scheme[4] for hot-electron two-dimensional transport in which the suprathermal electrons were treated as a fluid. This treatment, however, limited the precision of preheat predictions. The need for accurate preheat calculations has renewed our interest in Monte Carlo modeling.

The one-dimensional Monte Carlo transport code of earlier reports (see LA-6245-PR) has been improved significantly. As before, the hot electrons are treated as area-weighted PIC particles, whereas the cold electrons are treated as a fluid. The hot electrons are scattered, in accordance with Jackson's Gaussian distributions for both angular deflections in Coulomb interactions and decelerations from Coulomb drag. Their energy loss is deposited in the cold electrons, which are also accelerated in the local area-weighted electric field.

As an important new feature, we have calculated E from Poisson's equation in the "current" form, i.e.,

$$\frac{\partial E}{\partial t} = 4\pi\varepsilon\left(j_s^{(m+1)} + n_c u_c\Big|^{(m+1)}\right) , \qquad \text{(V-3)}$$

in which j_s is the suprathermal number flux, and $n_c u_c$ is the flux of cold electrons. We accumulate j_s as a particle property at the end of each cycle; $n_c u_c$ is obtained from the momentum equation for the cold electrons

$$n_c u_c\Big|^{(m+1)} = n_c u_c\Big|^{(m)} - \frac{1}{m}\left[\frac{\partial P_c^{(m)}}{\partial x} + n_c e E^{(m+1)}\right]\Delta t - \nu\Delta t n_c u_c\Big|^{(m+1)} . \qquad \text{(V-4)}$$

In general, with strong collisions (when $\nu\Delta t \gg 1$), Eq. (V-4) reduces to Ohm's law, so that, in steady state,

$$\frac{\partial P}{\partial t} \approx 0 ,$$

with $\partial P_c/\partial x$ small, Eq. (V-3) yields

$$j_s^{(m+1)} = -n_c u_c = \frac{neE^{(m+1)}}{m\nu} ,$$

determining $E^{(m+1)}$.

Alternatively, for extremely high collision frequencies so that the cold-electron velocities are nearly zero, or if there are very few cold electrons present ($\nu \to \infty$, so that $u_c \to 0$, or for $n_c \to 0$), Eq. (V-4) becomes

$$\frac{\partial E}{\partial t} = 4\pi\varepsilon j_s^{(m+1)} ,$$

which could lead to enormous fields on a typical fluid dynamic calculation mesh in which the cells are many Debye lengths wide. To avoid such large E-fields, we locally decrease the electron charge ε so as to stretch the local Debye length up to the calculational mesh dimensions. This ensures that the E-field is of the order

$$E \approx -(e n_s)^{-1}\frac{\partial(n_s T_s)}{\partial x} ,$$

which we would derive near steady state from a moment treatment of the suprathermal electrons.

This new Debye stretching technique is extremely important because, for the first time, we can track Monte Carlo or multigroup electron transport in the low-density corona around a pellet, where the density of suprathermal electrons exceeds the density of cold electrons. In practice, the E-fields calculated by this technique establish quasi-neutrality over one or two calculational cells. The stretched Debye length is somewhat akin to the stretched mean free path employed with von-Neuman artificial viscosity.

Figure V-5 shows typical ouput from a run with the Monte Carlo code. A fixed gold profile has been illuminated with 10^{16} W/cm^2 of 1.06-μm light with 20% absorption for 2 ps. Frame 1 shows the density profiles for hot and cold electrons and the critical density Zn_i. Suprathermal electrons are created at the critical density ($Zn_i = 10^{21}$ cm^{-3}) and are emitted toward the laser beyond the corona. Frame (d) shows the phase space for suprathermal electrons. They have been reflected by the self-consistent E-field and flow with $u < 0$ out the left side of the problem area. Electrons with $u > 0$ in $x < x_{crit}$ ($x_{crit} \approx 31$-μm point) have been either scattered by the ions or retarded by the E from Ohm's law. Frame (b) *shows the reflecting* $E > 0$ *field in* $x > x_{crit}$ *and the* retarding ohmic E-field in $x < x_{crit}$. Frame (c) shows the hot and cold temperatures set up in the plasma at 2 ps. The hot electrons are at roughly 20 keV. They are generated in accordance with $T_H = 31.6\,(I\lambda^2)^{1/3}\,T_c^{1/3}$, and the increasing background temperature of cold electrons can, therefore, affect T_H. To model this dependence with a fixed number of simulation particles emitted during

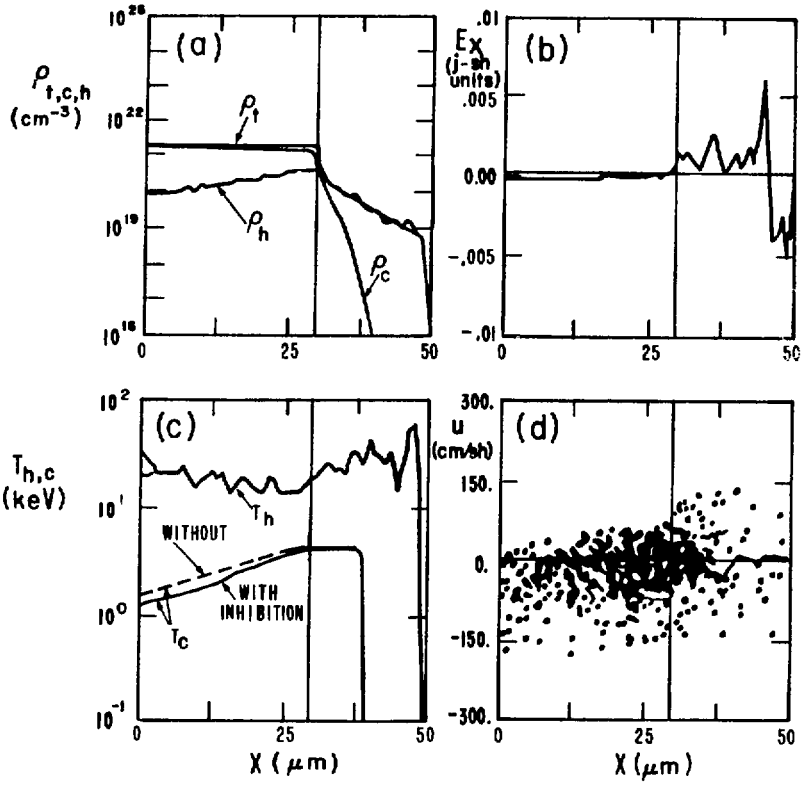

Fig. V-5.
Typical results from the Monte Carlo code with Debye stretching after 2 ps. See text for description of individual plots.

each cycle, we found it necessary to weight the PIC particles. Finally, two temperature profiles for cold electrons are shown. The higher T_c curve is for thermal diffusion alone, whereas the lower curve plots diffusion plus thermal inhibition stemming from enhanced thermoelectric effects and convective heat-flow effects, due to the strong cold return currents in response to the incident suprathermal current.

To treat the above flow effect of cold electrons with precision, the model now performs complete donor-cell[5] fluid dynamics calculations for the cold electrons. Thus, we avoid flux-limiters in the transport of cold electrons, rendering accurate drift velocities for the calculations of convective thermal transport, PDV work, and joule heating.

High-Energy Ion Losses In Laser Fusion Pellets (A. G. Petschek,* D. B. Henderson)

The mean free path for the 90° deflection of a test ion in a hot plasma of identical ions is

$$\lambda = M_i^2 v^4 (\varepsilon_T n Z^4 e^4 \ell n \Lambda)^{-1} , \qquad \text{(V-5)}$$

where M_i is the mass, v the velocity, n the background density, Ze the ion charge, and $\ell n\Lambda$ the Coulomb logarithm. Thus, high-energy ions have long mean free paths and will be preferentially lost from a finite plasma.

*Consultant: Permanent address, New Mexico Institute of Mining and Technology, Socorro, NM 87801.

On the other hand, in the quadratures leading to the reaction rate

$$\langle \sigma v \rangle = 1/2 \int_0^\infty g_1(v_1) v_1 dv_1 \int_0^\infty g_2(v_2) v_2 dv_2 \int_{|v_1 - v_2|}^{v_1 + v_2} v^2 \sigma(v) dv , \tag{V-6}$$

high relative velocities v are emphasized because of the rapid increase of the cross section σ. Other symbols in Eq. (V-6) are g_1 and g_2, the distribution functions of the reactants, and their velocities v_1 and v_2. The emphasis on high velocities is most easily seen if g_1 and g_2 are Maxwellian so that they can be replaced by a Maxwellian g of the relative velocity and by another of the center-of-mass velocity. Integrating, we obtain

$$\langle \sigma v \rangle = 1/2 \int g(v) v^3 \sigma(v) dv \quad . \tag{V-7}$$

If σ involves a simple Gamow penetration formula appropriate to DT, the integrand has a maximum at a relative energy of $E/kT = 6.8(keV/kT)^{1/3}$. Hence, loss of the high-energy tail of the distribution function might be expected to have a substantial effect on <σv>. In an earlier publication,[6] this effect was estimated by truncating the distribution g at the velocity above which the ions could transit the pellet radius with less than one 90° scattering. Because the values of <σv> presented in Ref. 6 are erroneous, we give, in Fig. V-6, <σv> as a function of the temperature and cutoff, which is for distributions that are Maxwellian at some temperature up to a cutoff and zero beyond. Reference 6 used Eq. (V-7) rather than Eq. (V-6) and showed a much larger effect than Fig. V-6.

To better calculate the effect of ion tail loss, we used a computer to solve the Fokker-Planck equations, as outlined by Rosenbluth et al.,[7] and have added an ion loss term using a diffusion approximation, assuming

$$\nabla^2 n(\underset{\sim}{x}, v) = (\pi^2/R^2)\, n(\underset{\sim}{x}, v) \quad , \tag{V-8}$$

where n is the density of fast ions as position $\underset{\sim}{x}$ and speed v. This leads to a loss per unit time independent of position

$$\frac{1}{n}\frac{dn}{dt} = \frac{\pi^2}{3}\frac{\lambda v}{R^2} \quad . \tag{V-9}$$

Our distribution function is, therefore, also independent of position.

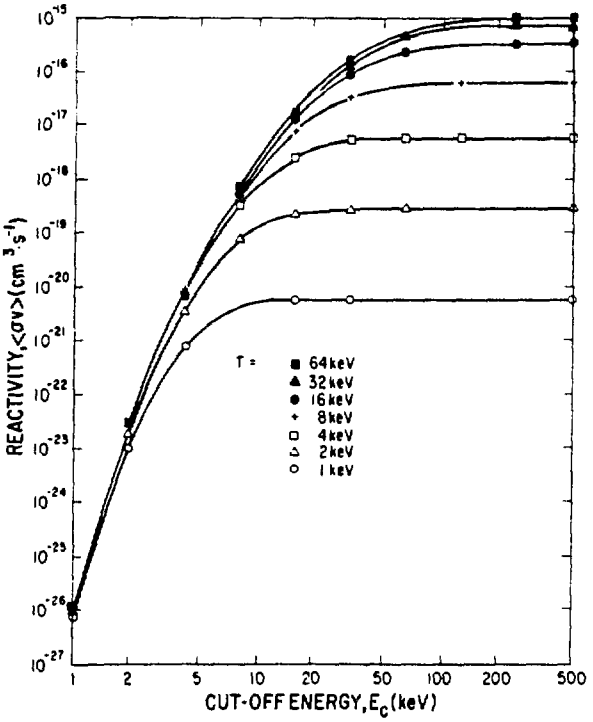

Fig. V-6.
Fusion reactivity <σv> integrated to cutoff energy E_c for various temperatures T.

A problem arises as to what to assume for the fate of the lost particles. Should they be returned to the pellet or lost permanently, and if they are returned, with what distribution of speeds? Clearly, the answer depends on complicated dynamics in the pusher surrounding the thermonuclear fuel. We chose to return the lost ions to the fuel with the speed distribution of the fuel. That is, after the loss calculation, we rescaled the distribution to reach the original particle number. This assumption undoubtedly affects the reaction rate and the mean ion kinetic energy, but probably has much less effect on the shape of the distribution function and on the deviation of <σv> from its Maxwellian value. For simplicity we also used a single ion of mass 5/2 instead of carrying D and T ions separately. We calculated $\ell n \Lambda$ following deWitt,[8] using the mean ion energy, and thus, ignoring some of the energy dependence of $\lambda n \Lambda$. We have also neglected collisions with electrons because ion-ion collisions are much more important than ion-electron collisions for both the momentum and energy change of the ions.

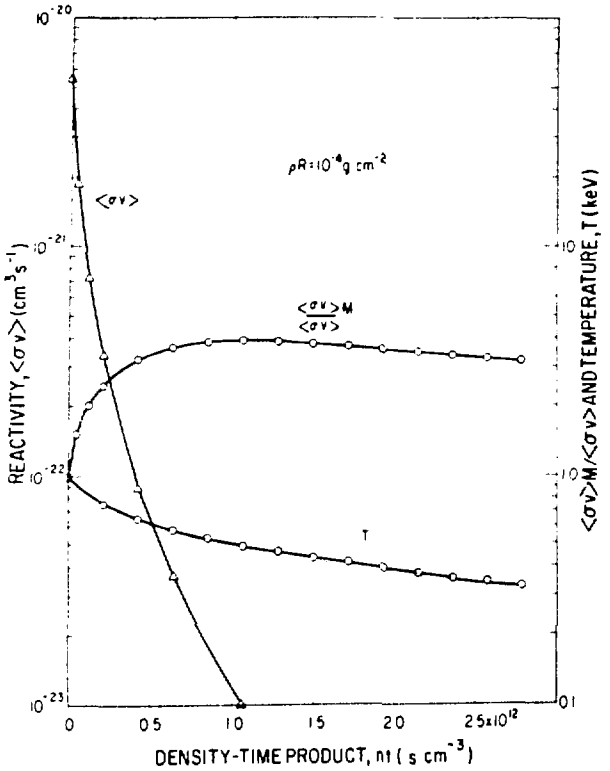

Fig. V-7.
Evolution of fusion reactivity <σv>, temperature T, and the ratio $<\sigma v>_M(T)/<\sigma v>$, for an initial Maxwellian distribution at T = 1 keV. Evolution includes ion losses for ρR = 10^{-4} g cm^{-2}.

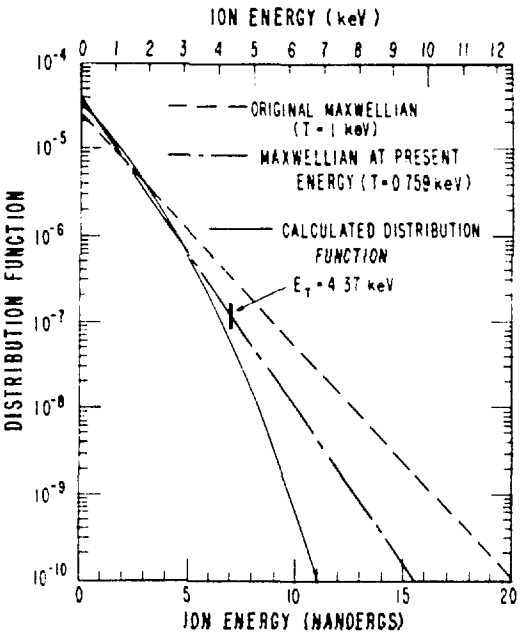

Fig. V-8.
Distribution function for case of Fig. V-7 at time nt = 2.01 × 10^{11} s cm^{-3}. Also shown are the original 1-keV Maxwellian and the Maxwellian at the present energy. The latter yields a <σv> equal to the evolving distribution function if truncated at E_T = 4.37 keV.

Figure V-7 presents the reaction history of a pellet with a density of 180 g/cm³, a density-radius product ρR of 10^{-4} g/cm², and a 1-keV Maxwellian initial ion distribution. The <σv> average drops very rapidly, due, largely, to a decrease in the average ion kinetic energy. The ratio $<\sigma v>_M/<\sigma v>$, where the numerator is calculated with a Maxwellian distribution at the mean ion kinetic energy and the denominator is calculated with the distribution from the Fokker-Planck code, reaches a maximum of 3.9 at a density-time product nt ≈ 10^{12} s.cm^{-3} when the mean ion kinetic energy has dropped by a factor of 2 and <σv> has dropped by a factor of ~600. Thus, the dominant effect is energy loss, but the tail loss is not altogether negligible. Earlier in the history it is relatively more important. For example, at nt = 2.01 × 10^{11} s.cm^{-3} when the mean ion kinetic energy is 0.76 of the starting value, <σv> is down by a factor of 14.8, of which a factor of ~6 is due to kinetic energy loss and 2.4 is due to tail depletion. Figure V-8 shows the distribution function for this case, together with a Maxwellian distribution of the same mean energy. To reduce <σv> by a factor of 2.4 at this temperature would require a cutoff at 4.37 keV, which is also shown.

To summarize, we have shown that losses from the tail of the distribution function in small laser targets (those with an areal mass = ρR 10^{-2} g/cm²) significantly affect the reaction rate, partly because of the decrease in ion kinetic energy and partly because of the deviation from a Maxwellian distribution that results from preferential loss of fast ions.

TARGET DESIGN

Exploding-Pusher Target Designs for Helios (W. P. Gula)

From the time Helios became operational, we have needed the capability to predict the performance of various targets. Accordingly, we performed numerous calculations. The two main purposes of the study are to aid in the design and interpretation of experiments on Helios and to calibrate our codes with the experimental results.

Single-shell DT-filled GMBs were chosen for this study because they are relatively simple and have only a few variable parameters, the targets are easy to diagnose experimentally, and we understand the physics of these exploding-pusher targets. In our one-dimensional calculations the glass shells were perfect spheres with an initial density of 2.4 g/cm^3, filled with an equimolar mixture of deuterium and tritium.[9]

Many parameters of the laser pulse and of the targets were varied. The results show that the GMBs should have a shell thickness of ~1 μm, a radius of 75 to 300 μm, depending on the laser power, and a fill pressure of 10 atm or less. The neutron yield as a function of laser peak power for a given target and pulse width is shown in Fig. V-9. The steepness of these curves emphasizes the importance of the dependence on peak power of the exploding-pusher targets in this regime. The one exception is the curve for targets of 100-μm radius; its slope is much less steep, consistent with data from earlier work with pulses of lower power. The steepness is less because the implosion time of a 100-μm target is so short that only limited amounts of energy can be transferred to the fuel before disassembly begins, even for very high peak powers.

Preliminary target shots on Helios were made at low powers (2 to 5 TW). Neutron yields ranged from 2 to 3 × 10^{8}n, in agreement with calculations for the specific targets used.

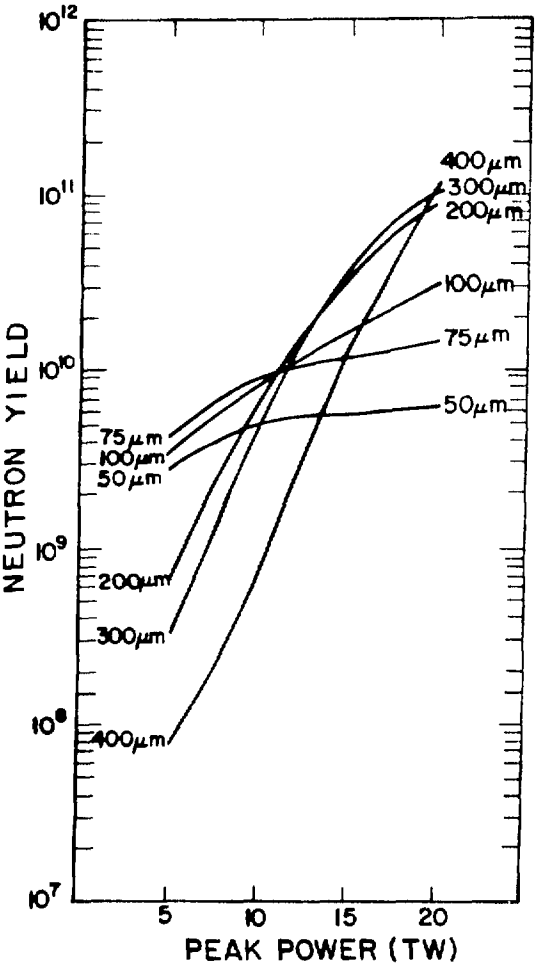

Fig. V-9.
Neutron yield as a function of laser peak power.

CODE DEVELOPMENT

Introduction (K. A. Taggart)

The two major efforts in code development during the past 6 months were the incorporation of nonlocal thermodynamic-equilibrium physics for opacity calculations, and the rewriting of the laser ray-trace package to allow for rays that do not pass through the coordinate Z-axis. The effort to adapt some codes to the CRAY-I computer was redirected slightly to aim at FTN compilation. This effort is progressing well and will be finished in late summer 1979.

Off-Axis Ray-Trace Routine (G. A. Rinker)

The laser ray-tracing routine in previous versions of our codes required that each ray pass through the Z-axis at some point for the sake of simplicity. If we view a cylindrical coordinate system in three dimensions and imagine representing a laser beam by a bundle of

straight-line rays, we can see that a general description may be obtained only if some rays are allowed to miss the Z-axis. The on-axis description can be complete only for a beam focused to an infinitesimal spot size on the axis.

Although a complete three-dimensional ray trace (in Cartesian coordinates, for example) would increase execution time significantly, a suggestion made earlier may be used to exploit the cylindrical symmetry of the target and remove analytically the angular degree of freedom.[10] This treatment does not introduce additional physical approximation because the noncylindrically symmetric ray path is effectively averaged over all angles when coupled to the cylindrical target.

The geometrical ray-trace equation is

$$\ddot{\vec{r}} = \frac{1}{2}\nabla n^2(\vec{r}) \quad , \tag{V-10}$$

where $\vec{r}$ describes the position of the unit-mass particle whose path describes the ray trajectory, and

$$n^2(\vec{r}) = 1 - \varepsilon_e(\vec{r}) \tag{V-11}$$

is the index of refraction, where $\rho_e(\vec{r})$ is the electron density measured in units of the critical density. The speed of the particle has been set to 1. For a cylindrically symmetric target, $\rho_e(\vec{r})$ does not depend on θ, so that the above equation becomes

$$\ddot{r} = -\frac{1}{2}\frac{\partial}{\partial r}\left[\varepsilon_e(r,z) + L_z^2/r^2\right]$$

and

$$\ddot{z} = -\frac{1}{2}\frac{\partial}{\partial z}\left[\rho_e(r,z) + L_z^2/r^2\right] \quad , \tag{V-12}$$

where

$$L_z = r^2\dot{\xi} \tag{V-13}$$

is the conserved angular momentum. Thus, the complete three-dimensional solution may be obtained from the former restricted solution merely by the addition of a new term to the density, yielding an effective density $\rho_e(r,z) + L_z^2/r^2$. In vacuum, the equations may be solved analytically, with the resulting ray path

$$r^2\cos^2 y = L_z^2\cot^2 y + (z\sin y - r_B)^2 \quad . \tag{V-14}$$

where y and r_B are parameters that describe the ray asymptotes. The distance of closest approach of the ray to the Z-axis is

$$r_{min} = -L_z/\sin y \quad . \tag{V-15}$$

The ray-trace equations are reduced to those used previously in our design codes when $L_z = 0$.

This new capability was implemented in the codes. A given ray is traced in vacuum according to the hyperbolic path given in Eq. (V-14). When a material boundary is intersected, the ray is traced through with linear approximations to the term L_z^2/r^2 in each cell as is normally done for the true density. This overall procedure suffers from a numerical problem due to the singularity in L_z^2/r^2 as r approaches zero, with the result that rays are not traced accurately in the cells adjacent to the z-axis. However, this inaccuracy has little physical significance, because there is very little volume in such cells. Further problems arose in implementing this capability because the previous critical-surface turning-point detector is not valid in the new context. This situation was corrected, and an approximation to the observed angular-dependent resonance absorption was added at the same time.

The problem of physical interest concerns a laser beam focused to some finite spot. To approximate this situation by using geometrical ray-trace optics, it is necessary to produce a bundle of rays distributed according to some intensity pattern in the focal plane. This pattern is obtained in the following way. A nominal focal point is described as before in the (r,z) plane; then random fluctuations in L_z and the angle y are imposed to yield an intensity pattern corresponding in the limit of an infinite number of rays to a Gaussian of specified FWHM. More general intensity patterns may be obtained with superpositions of such Gaussians, subject always to the cylindrical averaging process mentioned before, which transforms off-axis focal points into rings. These fluctuations are rerandomized at each cycle. Additional random fluctuations in L_z and y may be imposed at reflections within the target.

An example of the effects of these modifications is shown in Figs. V-10 through V-13. Figure V-10 shows a ball with a laser focused to a point on each side of the

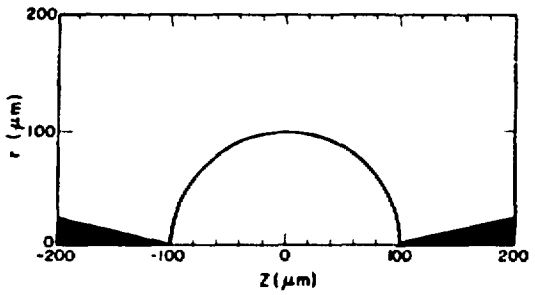

Fig. V-10.
On-axis laser illumination of spherical target.

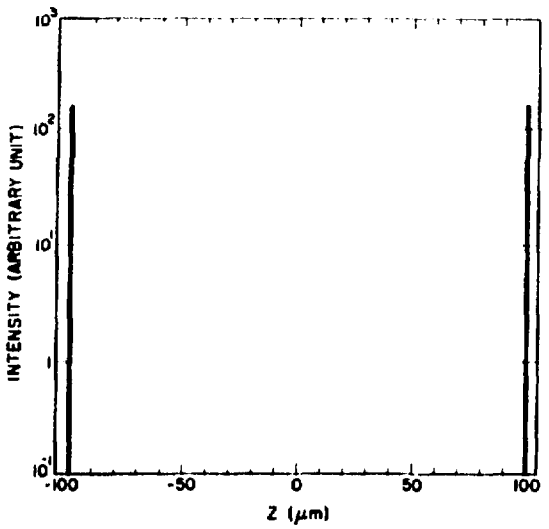

Fig. V-11.
Laser intensity on sphere of Fig. V-10 as a function of z.

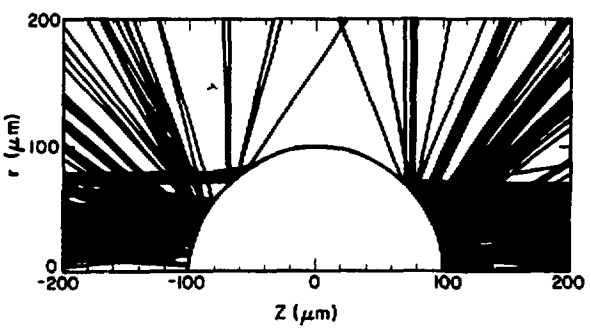

Fig. V-12.
Off-axis laser illumination of sphere in Fig. V-10.

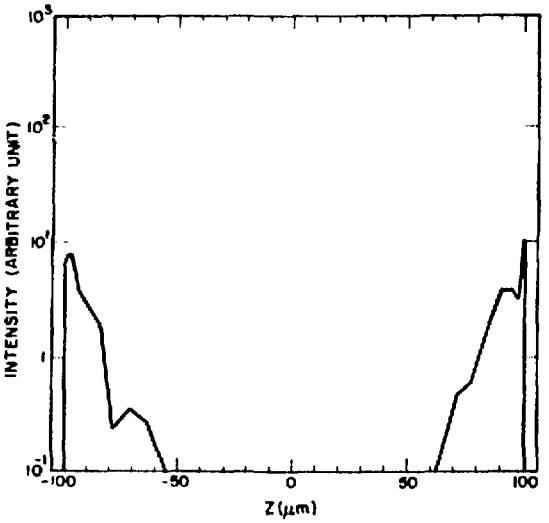

Fig. V-13.
Laser intensity on sphere of Fig. V-12 as a function of z.

sphere: the corresponding intensity as a function of z is shown in Fig. V-11. Figures V-12 and -13 show the same configuration except that finite focal spots of 100 μm have been imposed. A significant change in overall illumination is evident from the trend of the graph in Fig. V-13. Note that the fluctuations are statistical and tend to disappear over time because of the rerandomizing carried out during each cycle. The increase in symmetry is the most obvious manifestation that our new laser ray-tracing capability reflects the physics of pellet irradiation more accurately.

REFERENCES

1. H. Brysk and A. J. Scannapieco, Bull. Am. Phys. Soc. 23, 750 (1978).

2. M. A. Stroscio, D. B. Henderson, and A. G. Petschek, Nucl. Fusion *18*, *142.5* (*1978*).

3. D. W. Forslund, J. M. Kindel, and K. Lee, Phys. Rev. Lett. 39, 284.

4. R. J. Mason, "Double Diffusion in Hot Electron Transport in Self-consistent E and P Fields," Phys. Rev. Lett. 42 (1979).

5. R. A. Gentry, R. B. Martin, and B. J. Daly, "An Eulerian Differencing Method for Unsteady Compressible Flow Problems," J. Comp. Phys. **1**, 87 (1966).

6. D. B. Henderson, Phys. Rev. Lett. **33**, 1, 142 (1974).

7. M. N. Rosenbluth, W. M. McDonald, and D. L. Judd, Phys. Rev. **107**, 1 (1957); and W. M. McDonald, M. N. Rosenbluth, and W. Chuck, Phys. Rev. **107**, 350 (1957).

8. H. deWitt, *Lectures in Theoretical Physics* Vol. IX, Part C (Gordon and Breach, 1967) p. 621.

9. C. W. Cranfill, "One-Dimensional Computer Simulations of the Implosion of Single-Shell Targets with the Los Alamos Two-Beam CO_2 Laser," Los Alamos Scientific Laboratory report LA-6827-MS (1977), Fig. II.5.

10. F. Tappert, University of Miami, Florida, and E. Lindman, Los Alamos Scientific Laboratory, private communication (1978).

VI. LASER FUSION TARGET FABRICATION
(R. J. Fries)

Our target fabrication effort, supported by extensive theoretical investigations, supplies thermonuclear fuel containing pellets for laser driven compression and heating experiments. These targets, which range from simple, deuterated, flat plastic films to complex, multilayered structures containing cryogenic solid DT fuel, are optimized for use with high power CO_2 lasers. After a target has been designed, we develop the technologies to produce the materials and properties desired. Then, we fill the target with thermonuclear DT fuel, assemble the necessary parts, and develop methods to measure and characterize all these properties. Finally, we insert the target in the target chamber and position it at the exact laser focal spot.

INTRODUCTION (E. H. Farnum, R. J. Fries)

Our target fabrication effort has two objectives:

(1) We supply targets of current design to satisfy the needs of the experimental program. Targets of various designs are used: thermonuclear compression targets for Main Sequence experiments, partial and modified compression targets for Target-Essentials experiments, a wide variety of targets for Support-Physics experiments, and several types of targets for Military Applications experiments. All are irradiated in one of our laser systems.

(2) We develop new techniques as needed for the fabrication of future thermonuclear compression targets envisaged in the Inertial Fusion Program plan. Because these target designs are not fixed, we must continue to investigate all materials that have a high probability of being used in the final designs. We also develop methods of measuring and characterizing these materials and of assembling them into required configurations.

In addition to these goals, we provide micromachining, microassembly, and materials fabrication services to other groups.

A recent design for the Polaris-A multishell laser fusion target is shown in Fig. VI-1. Laser fusion targets have evolved slowly to this stage. Initial targets, called Sirius, comprised only one shell filled with room-temperature DT gas. This single shell acts as an exploding pusher in which the fuel is preheated as it is compressed. Most of these shells are GMBs with only a few atmospheres of DT gas fill. Although these designs cannot lead to a high yield, they do produce some thermonuclear reactions and neutrons. The target is improved by adding a 100-μm-thick layer of plastic, which is vaporized by the laser pulse causing the glass shell to implode hydrodynamically. By coating the GMB with molybdenum or other high-Z metal before plastic deposition we reduce preheat, and thus, make the desired adiabatic hydrodynamic compression possible. Such a design will be used to attain our 20XLD milestone.

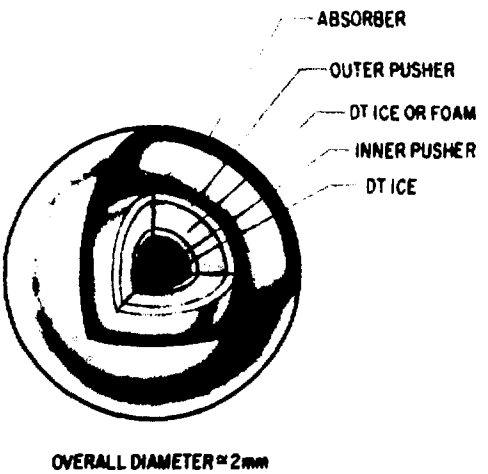

Fig. VI-1.
Polaris-A, a multilayer multishell target designed for Antares and Helios.

In our Polaris-A target, this high-Z metal coating is added as a heat shield for the fuel, the ablator layer is changed to low-density plastic foam to provide a hydrodynamic cushion, and a second pusher layer is added outside the foam.

Initial targets will irradiate the outer pusher shell directly, but in subsequent experiments other layers will be added to provide further thermal insulation, to

enhance laser absorption, and to improve hydrodynamic coupling of the laser energy to the target.

In all these targets, from the simple Sirius to Polaris (Fig. VI-1), the fuel will be frozen as a solid layer of DT ice onto the inside surface of the innermost pusher shell. Calculations show that this cryogenic modification will improve the yield substantially. We are developing techniques to freeze such layers in place within the Helios target chamber.

These and other targets of recent design call for the development of high-Z metal shells with diameter and wall-thickness uniformity deviations of not more than 1% and a surface smoothness tolerance of <1000 Å. They also require low-density, small-cell-size plastic foams, thick layers of plastic loaded with metals of low or high Z, metal foams, and smooth metal layers of moderate or low Z. In addition, we are developing methods to prepare alternative fuels that are solid at room temperature and contain fuel atoms at high density (e.g., polyethylene, lithium hydrides, or ammonia borane, in which the hydrogen is replaced by an equimolar mixture of deuterium and tritium). Even though the nonfuel atoms in these compounds dilute the nuclear fuel and reduce target performance, the fact that these materials are solid at room temperature may be an advantage, especially in designs that require fuel-containing layers in the outer parts of the target.

Because any target must be characterized completely to understand its performance, we have devoted much of our effort to measuring and documenting all targets we deliver and to developing new, automated high-resolution methods of characterizing target parts. We are developing a surface acoustic-wave resonator-driver to sort batches of target shells for diameter and wall uniformity using the efficiency (Q-value) and frequency at which the shells bounce as an indicator of quality. We are also automating our x-ray microradiographic method for observing defects and nonuniformities in opaque shells.

TARGET FABRICATION (R. J. Fries, E. H. Farnum)

General

Our primary assignment in target fabrication is the assembly, delivery, and postshot analysis of targets for our three operating laser systems. We therefore devote whatever fraction of our effort is required to meet delivery requests from experimenters on these systems. In addition, we try to maintain a large and very flexible inventory of materials and techniques so that we can respond rapidly to changes in target design or specifications. As part of target assembly, we also mount and align the targets on the appropriate target-changing mechanism to eliminate the need for any further position adjustment in the target chamber. If desired, we photograph and analyze any remnants to supplement target diagnostics.

The process of target fabrication typically includes the following steps. A type of GMB is chosen that is most suitable for the desired diameter, wall-thickness, and gas-permeation characteristics. These GMBs are available from the 3M Company, KMS Fusion, Inc., or the Lawrence Livermore Laboratory. The GMBs are precision-screened to the desired size on an air-jet sieve, separated according to density by flotation in SF_6 gas, crushed by external pressurization (only for cases where the desired wall thickness is greater than 1.5 μm), and cleaned by flotation in ethanol. The refined batch is optically preselected with an interference microscope and then filled with DT or DT:Ne gas mixtures by permeation through the wall at elevated temperature and pressure. The filled GMBs are cleaned in ethanol and examined carefully with an interference microscope. Targets passing optical inspection are examined and measured in three planes. Coatings of metal and/or plastic are then applied. These coatings are examined in three views by x-ray microradiography to determine coating smoothness and uniformity, often after each successive layer has been applied. In the meantime, other parts are being fabricated. For example, for the two-shell vacuum insulation target (see Fig. VI-2), we form the outer plastic shell by coating an appropriately sized copper ball bearing with plastic (by our low-pressure plasma polymerization method described below), cutting the coating into two halves with a laser knife, and etching the copper mandrel away in nitric acid to leave the plastic hemispheres. When the central fuel container is opaque, we use x-ray microradiography to determine shell uniformity.

Fabrication Activity (B. Cranfill, V. Woods, M. Calcote, J. Feuerherd)

We supplied more than 1000 targets for our three operating laser systems and made more than 100 parts for diagnostic devices. About 320 targets were fabricated

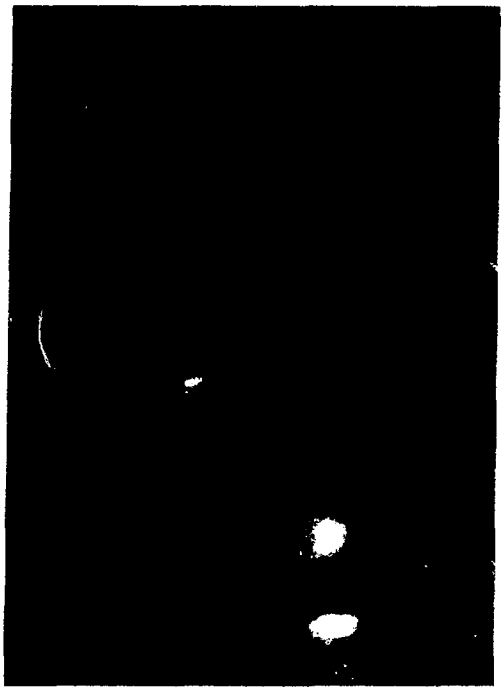

Fig. VI-2.
A two-shell target consisting of a GMB and a single concentric plastic shell.

for main-sequence experiments. Another 340 targets were supplied for a wide variety of Target-Essentials and Support-Physics experiments, including preliminary shots on the Helios laser, and over 400 were made for military applications experiments.

We completed the development of fabrication techniques for the current Vega-B target. We also improved our low-pressure plasma polymerization technique and can now coat mounted GMBs with over 350 μm of parylene for the 20XLD milestone target. The surface smoothness of this coating is acceptable (± 1 μm). We solved the problem of perturbations near the mounting stalk, which are introduced because both the GMB and the stalk are coated simultaneously in the coating process. We are replacing the coated stalk with a new, uncoated one by micromachining with a single-point diamond tool that has a concave tip. This technique produces a smooth spherical surface at the cutoff. We successfully fabricated several targets for an x-ray point-source experiment which requires a tungsten needle suspended behind an aperture in the configuration shown in Fig. VI-3.

Gas Analysis of Laser Fusion Targets

General. To predict the performance of hydrogen-, deuterium-, and DT-filled microballoons correctly, we must be able to measure the gas fill with a high degree of accuracy. Also important are the permeation rates of the hydrogen isotopes through thin layers (shells) of a variety of coating materials at various temperatures. This information will be helpful in deciding under what conditions a given target type can be filled in real time. Permeation data at room temperature and below will also be important in selecting the best storage temperature for targets filled with the desired quantity of fuel gas.

Filling Large-Aspect-Ratio Shells for the 20XLD Milestone Target (Betty S. Cranfill). The 20XLD milestone target requires 300-μm-diam, 1-μm-wall GMBs filled to 30 atm (3 MPa) of DT gas at room temperature. Two problems were encountered in filling these targets. (1) Commercially available batches of 300-μm-diam GMBs are of very poor quality and of a glass composition that permits high DT loss rates even when stored at −80°C (193 K); and (2) the aspect ratio (diameter/wall thickness) of these shells was so large that they collapsed by elastic buckling during the fill (the resulting shock wave and/or fragments break other nearby shells) with the result that even with precrushing and careful staging, only ~10% of the GMBs loaded for DT fill survived. Both problems were solved during this reporting period; we are now filling 300-μm-diam, 1-μm-wall GMBs with 30 atm of DT and achieving 90% recovery.

In trying to solve the first problem, we obtained some GMBs from KMS Fusion Inc., that were not only of very high quality with respect to wall uniformity and surface finish, but also had very low permeability to DT at room temperature due to ~1.% CaO content in the glass. We measured the outgassing rate of GMBs from KMS Fusion, Inc., with and without CaO addition by monitoring the x-ray emission of a number of shells over a period of time; the results are shown in Fig. VI-4. The high quality of these shells significantly reduces the time needed for selection and improves the gas-filled yield by reducing elastic buckling failure.

We solved the buckling problem by isolating the GMB during fill and measuring buckling failure so that fill-staging might be optimized. Isolation was provided by a

Fig. VI-3.
An x-ray backlighting target. The tungsten needle pointed toward the hole emits x-rays from its tip when heated by the laser.

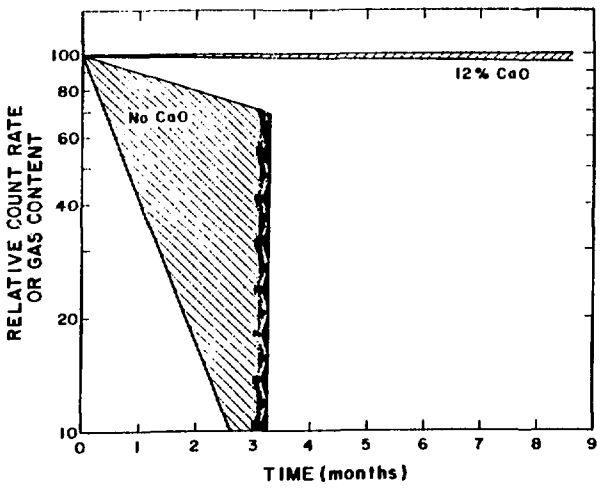

Fig. VI-4.
X-ray count rate data from KMS Fusion, Inc. GMB as a function of time. The relative time for DT outgassing is shown for GMB with and without CaO.

wire with holes drilled into it, each of which acts as an individual container for a GMB during the DT filling process. Thus, each GMB is shielded from its neighbor. The wire containing the GMBs is then placed into a close-fitting glass capillary which retains the GMBs in their holes. Another advantage (other than 90% recovery from 30-atm DT fill) of this technique is that the identity of the GMB is maintained during fill, which permits the recovery of precharacterized shells. Because the fill gas contributes to the wall thickness measured by optical interferometry and must be subtracted, wall thickness can be measured more accurately on an empty GMB. In addition, wall thickness carefully measured before and after filling can be compared to obtain a nondestructive, quantitative gas assay. Although this method is much more tedious than x-ray counting, we used it as an aid in calibrating the x-ray counting system for glass shells. Variations among different shells indicated an x-ray calibration error of ~±7%.

Data for interferometrically measured gas content in GMBs at several fill pressures are plotted with the expected fill density in Fig. VI-5. All these GMBs, which were held at fill conditions for 24 h, showed a lower-than-expected gas content. In contrast, a 10-day fill to an expected 28 amagat at the same temperature showed

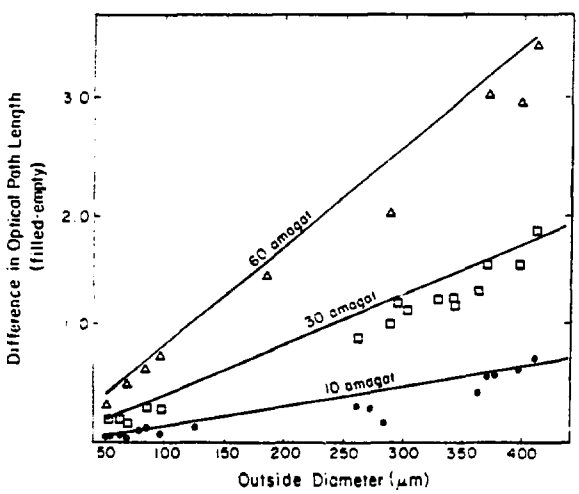

Fig. VI-5.
Interferometric measurements of the amount of DT gas in GMB. The difference in optical path length before and after DT fill in a GMB is plotted against the outside diameter of the shell for several fill pressures and is compared to the curve expected for the fill conditions used.

29.8 ± 1.4 amagat in 10 shells. These data, which would indicate a permeation time longer than 24 h conflict with those of still another experiment in which similar GMBs were emptied of gas by heating in air for only 4 h. Further experiments to resolve these contradictions are in progress.

Buckling Failure in Large-Aspect-Ratio Shells (John V. Milewski). The tensile strength of shells determines the design limitations on the maximum achievable fuel loading. A method of testing for tensile strength was discussed in the last report (LA-7587-PR). However, the current limitation in loading shells with fuel is not the tensile stress from internal gas pressure but rather compressive buckling failure during diffusion-fill. The low buckling strength of larger diameter spheres with thinner walls severely limits the external filling pressure that can be applied to the shells during diffusion-filling. For example, at present, we use 100-psi fill stages for 300-μm-diam, 1-μm-wall GMBs; to achieve a fuel density of 30 amagat at 673 K, we must use 11 stages at 24 h each. Because relatively few preselected GMBs are filled in a single run, optimizing the fill staging is obviously very important.

We built an apparatus for measuring the crushing strength of shells and determined the room-temperature crush strength for GMBs in the size range currently being used for targets. These data agree very well with the theoretical relationship for elastic buckling (Fig. VI-6) given by

$$P_{exx} = \frac{2\ Y\ \Delta r^2}{r^2\ \sqrt{3(1-\nu^2)}} ,$$

where P_{exx} is the externally applied pressure at which buckling occurs, Y is Young's modulus, ν is Poisson's ratio, Δr is wall thickness, and r is shell radius. Note that the buckling-failure pressure is inversely proportional to the square of the aspect ratio (diameter:wall thickness) and that an increase in diameter from 100 to 300 μm at constant wall thickness should reduce the buckling-failure pressure by a factor of 9. For example, 100-μm-diam shells with 1-μm-thick walls do not fail by compressive buckling at room temperature until ~5000 psi of external pressure is applied, whereas 300-μm-diam, 1.0-μm-thick targets fail when ~550 psi of external pressure is applied.

We do not expect this relationship to apply at elevated temperatures because the glass becomes plastic rather

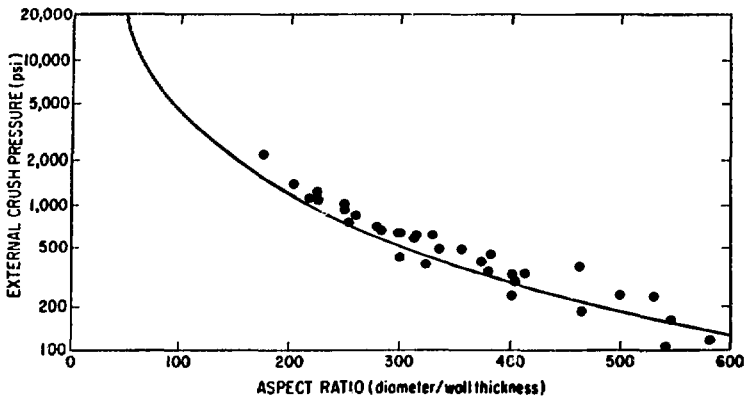

Fig. VI-6.
Data obtained by hydrostatically crushing GMB at room temperature are plotted for shells of different aspect ratio and are compared to the theoretical curve for elastic buckling failure.

than remaining an elastic material. It is, therefore, impossible to predict the properties of thin-walled glass shells at elevated temperatures; they must be measured directly. We are adding a furnace to our apparatus, which will allow crush strength determinations up to 650°C (923 K).

INORGANIC COATINGS DEVELOPMENT (A. T. Lowe)

General

Because future targets will require layers and shells of metal or plastic, we continued to develop a wide variety of coating techniques. Metal coatings were applied by the wet chemical methods of electro- and electroless plating, by chemical vapor deposition (CVD), by physical vapor deposition, and by sputtering. We focused our attention on high-quality coatings and on the coating and recovery of a small number (~100) of preselected GMBs.

Electroless Plating (S. Armstrong, W. Doty)

Previous electroless nickel plating studies used either Solacels or CVD nickel-coated GMBs as the substrates. We developed simple and reliable chemical treatment steps that allow us to plate thin layers of electroless nickel onto GMBs without the need for CVD nickel coating. To carry out the chemical treatments on small numbers of GMBs, special glassware and handling techniques were also developed. We applied these chemical pretreatment steps—which consist of cleaning in a hot aqueous solution of Na_2CO_3, followed by sensitizing and activating with $SnCl_2$ in HCl—to GMBs made by 3M, LLL, and KMS, and achieved metallization. However, this initial electroless nickel coating is very fragile, and adhesion to the glass surface is very low. Suspension and movement of the GMBs during electroless nickel plating is essential, yet too hard an impact against the retaining screens, or against each other, can cause surface defects. Another cause of defects on GMB surfaces is the presence of gas in the form of air, H_2, or water vapor from near-boiling solutions, which causes the GMBs to align themselves at the gas-liquid interface and results in rough, pitted deposits.

An all-fluorocarbon plastic electroless nickel-plating fixture that will fit into a 1-ℓ beaker and that contains an 0.83-mℓ plating chamber was constructed. GMBs were agitated by a slow uniform up-and-down motion through Teflon screens of 74-μm opening. Two frequent types of defects were observed: small holes and tearing. We believe these defects are caused by collisions with the screen and by poor adhesion to the glass substrate. If the damage occurs in the very early stages of deposition, a small piece of electroless nickel is completely removed and a hole is left. At a later time, the electroless nickel deposit is thicker and a screen impingement produces a tear, but not complete removal of a piece of nickel. This

flap of nickel will lie unevenly on the surface and subsequent deposition forms a rough modular part. We are investigating ways of improving the adhesion between the GMB and the initial nickel coating.

Chemical Vapor Deposition (G. J. Vogt)

We completed construction of the fluidized-bed CVD reactor designed to allow us to quantitatively analyze the fluid bed. This reactor system, designed specifically to study the WF_6+H_2 reaction, is also useful for other CVD reactions. We are investigating the system controls and diagnostics.

Experimental work on a Solacel fluidized bed was started with the WF_6+H_2 CVD reaction to ascertain operating conditions for the optimum coating qualities and to relate these conditions to fluid-bed parameters.

We also completed the literature search for available thermodynamic and molecular data for the WF_6+H_2 reaction. The subsequent computation for the thermodynamic yield of CVD tungsten as a function of H_2 and WF_6 feed ratio was performed by using these collected data. In general, for all pressures and temperatures, a 99% tungsten metal yield can be obtained at equilibrium for an input ratio of H_2 to WF_6 between 3.0 and 3.3. Note that the stoichiometric input ratio of H_2:WF_6 is 3.0, as given in the reaction

$$WF_{6(g)} + 3H_{2(g)} \rightleftarrows W(s) + 6HF_{(g)}.$$

Because CVD is generally a nonequilibrium process due to a short residence time in the reaction zone, additional H_2 is necessary to ensure a high W(s) yield. Also, the yield of tungsten metal by CVD appears to be specifically dependent on the kinetics of the process.

A similar thermodynamic analysis for $W(CO)_6$ CVD is being considered as an alternative to WF_6 CVD for GMBs because, in the earliest stage of the WF_6 process, the GMBs are quite susceptible to HF attack, yielding badly damaged bed material. We could alleviate this problem by either fully coating the GMBs with the $W(CO)_6$ process or by flash-coating the glass with the $W(CO)_6$ process before further coating with the WF_6 process.

Sputter-Coating, a Gas-Jet Levitator Development (A. T. Lowe, C. Hosford)

We continued our development of sputter coatings on GMB and other spherical mandrels. By using the gas-jet levitator described in the previous progress report,[1] we have successfully applied molybdenum and gold to levitated GMBs. The configuration that allowed successful GMB levitation is shown in Fig. VI-7.

The GMB is observed from outside the chamber through a 10-cm-diam viewport with a Questar telescope, and illumination of the sphere is maintained throughout the run with a 4-mW He:Ne laser whose beam passes through a second viewport and is directed onto the GMB with mirrors inside the sputtering chamber.

The gas flow (measured with a mass flowmeter) required to levitate a GMB is between 0.1 and 0.2 cm^3/min at sputtering pressures from 20 to 100 mtorr. At these flow rates, additional argon must be added to the bell jar to establish sputtering pressures of 40 mtorr.

Initial liftoff of the GMB from the collimated hole structure (CHS) is difficult because of static charging of the GMB. Increasing the gas flow sufficiently to lift the sphere would often blow the GMB away (typical GMB weight, 2 μg). However, an electromechanical driver (as used for the shaker table) attached to the CHS vibrated the structure sufficiently to gently dislodge the GMB and

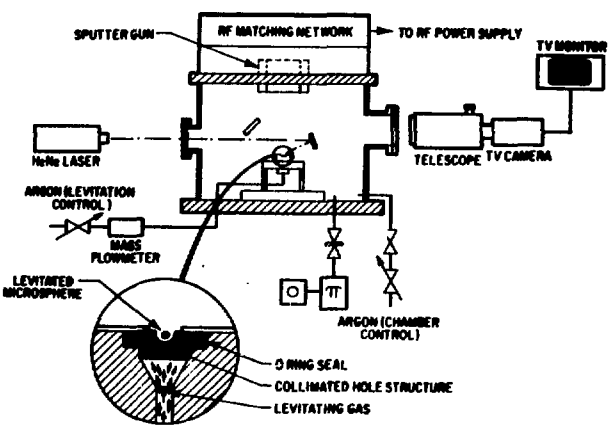

Fig. VI-7.
Schematic of rf sputtering unit with its gas-jet levitator.

to permit liftoff at low gas flows. To keep static charges to a minimum, the GMB must be coated with a thin (200- to 500-Å) metallic layer before levitation, stored in metal containers, and treated with commercial electrostatic-charge-eliminating devices.

The metallographic cross section of a gold coating 1.4 ± 0.2 μm thick is shown in Fig. VI-8. This coating was deposited at a rate of 4.2 nm/min onto a 200-μm-diam GMB with a 2.0-μm-thick wall.

To keep the sphere levitated, a delicate balance must be maintained between the two counteracting forces of gravity and levitation-gas pressure. Therefore, the levitation-gas flow must be increased as the weight of the GMB increases during coating. For the gold coating in Fig. VI-8, we had to increase the flow from an initial rate of 0.1 cm^3/min by 0.02 cm^3/min for every 100 nm of gold film added. Preliminary coatings made with this technique show much cleaner, smoother surfaces than the vibrating-table scheme used previously.[1]

The disadvantage of this technique is the low deposition rate achievable at the high pressures necessary for stable levitation. Finer gas-flow controls and improved designs of directional jets, which should allow operation at higher rf power and lower pressures, are being tested.

Microflow Valve (J. R. Miller, J. Feuerherd)

The need for precise gas flow with a controllable rate of 0.001 to 1.0 std cm^3/min for the gas-jet levitator coupled with the lack of a suitable commercial device led to our development of a microflow valve.

The simple device, shown in Fig. VI-9, relies on the thermal expansion difference between a precisely lapped tungsten plug and the surrounding brass body. As the temperature of the assembly is raised by the resistance heater coiled around the valve body, the brass expands more than the tungsten and a gap forms around the plug, allowing gas to flow through the device. Typical flow rate vs temperature at three pressure differentials for one

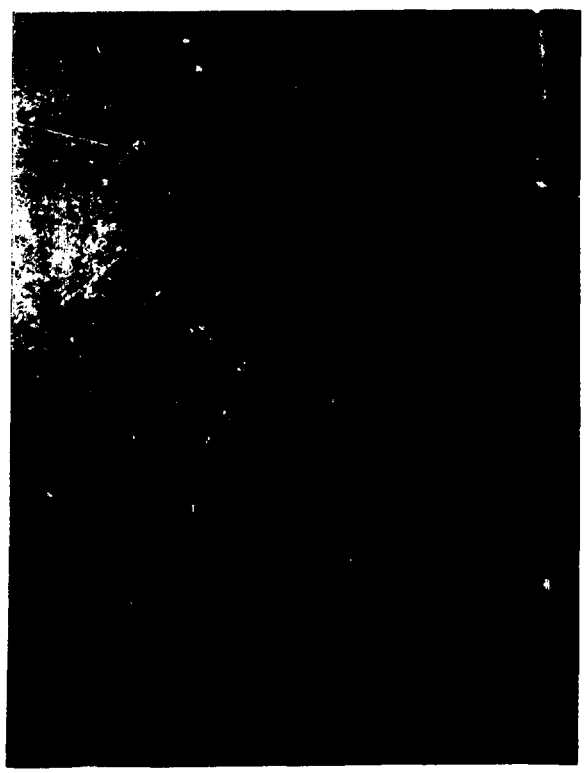

Fig. VI-8.
Optical metallograph of the cross section of a 1.4-μm-thick gold coating sputtered onto a levitated GMB. 2500X

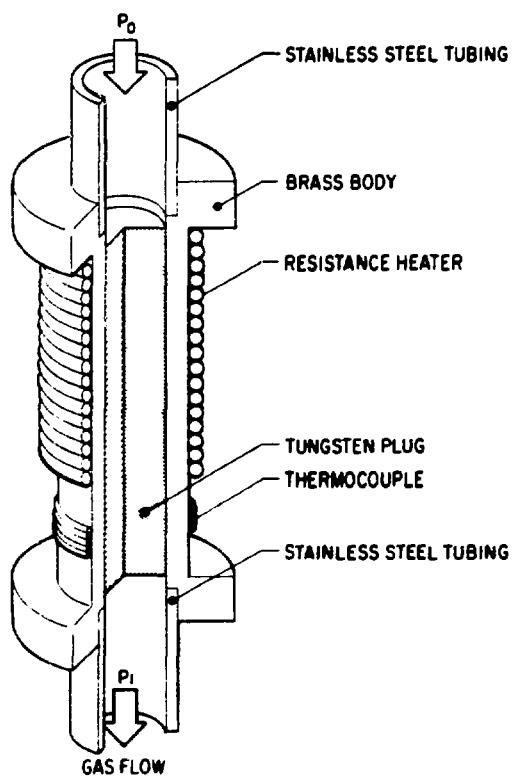

Fig. VI-9.
Schematic of temperature-controlled microflow valve.

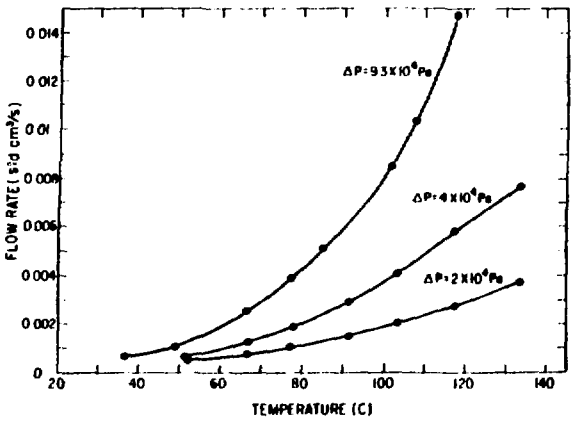

Fig. VI-10.
Flow rate for helium gas as a function of orifice temperature for the microflow valve.

of these valves is shown in Fig. VI-10. The sensitivity of this valve can be changed by choosing plug and body materials that have either greater or less difference in their thermal expansion coefficients.

Mandrel Development (S. Butler, M. Thomas)

Work toward making mandrels for metal microballoons continued. This effort should produce microspheres that can be coated with nickel by chemical vapor deposition (CVD), and that can be removed through the coating, leaving a shell strong enough for additional coating. The resulting product is a free-standing metal microballoon, with the inside diameter dependent upon the mandrel size and the wall thickness determined by the coating process. We further investigated conditions for spherical droplet formation, using water in the droplet generator described in Ref. 1. The size of the drops was measured by viewing them in free fall with a telescope, video-camera assembly, and stroboscopic light, which have been calibrated for such measurements. Droplet size measured for a 140-μm orifice agrees well with that predicted from mass balance, liquid-jet velocity, and excitation frequency. However, drops formed with a 68-μm orifice are substantially larger than predicted (by 1.5 to 2.5 times) and the measured size does not correspond to any overtone or simple divisor of the excitation frequency. We cannot offer an explanation for the discrepancy yet.

Sodium nitrite spheres ~250 to 500 μm in diameter were produced by dropping the molten material at 563 K through a 300-μm orifice. Although the drops solidified in the 1.5-m drop length, some spheres contained bubbles. We have not yet metal-coated this product. Polymethyl methacrylate (PMMA) spheres were CVD nickel-coated at ~355 K. Although the PMMA does dissolve through a thin (~2-μm) coating without adverse swelling, most of the shells crumple without mandrel support. Observation with an optical microscope showed that some shells with a wall thickness of 1.1 to 1.4 μm remained intact after removing the PMMA. Because high-energy radiation is known to decompose PMMA, promoting dissolution, this fact may allow easier removal of the mandrel material through the nickel wall. Therefore, we have irradiated some PMMA spheres with a linac electron beam. Evidence of decomposition of the material appears at doses of ~50 Mrad, but quantitative analysis of the change in solubility is not yet complete.

ORGANIC COATINGS DEVELOPMENT (R. Liepins)

General

Many of our multilayered laser fusion targets use an outer shell of low-density, low-Z material as an absorber/ablator layer. This layer absorbs energy from the incident laser, is heated and vaporized, and streams away from the pusher shell causing the pusher shell to implode via the rocket reaction forces. For target pellets that do not depend on the strength of this absorber/ablator to contain the fuel-gas pressure, we generally use plastic. We also provide free-standing cylindrical and spherical shells of plastic as targets and for special diagnostic measurements. These latter specimens are generally fabricated by coating appropriate mandrels, which are then dissolved in acid to leave the free-standing plastic shells, but we are also trying to make plastic shells by using our droplet generator described earlier. Finally, because the Polaris-A target requires a shell of low-density small-cell-size plastic foam, we are developing techniques for making this foam in the form of spherical shells that can be placed around target cores.

Gas-Phase Coatings (R. Liepins, M. Campbell)

General. The primary problems encountered in coating GMBs with plastic are obtaining uniform coating thickness and high surface smoothness. Of the three general coating approaches (solid, liquid, and gas phase) the gas-phase coating approach gave the most promising results. Two gas-phase techniques were investigated: (1) a low-pressure plasma (LPP) process, and (2) a vapor-phase pyrolysis (VPP) process, i.e., the p-xylylene process.

The primary requirements for coatings on laser fusion targets are sphericity and uniformity of better than 5% and smoothness or defects less than 1 μm. We achieved these requirements with a low-pressure plasma process, and are approaching success with a vapor-phase pyrolysis process. In addition, we can now apply these coatings to a few preselected GMBs with 100% recovery.

Low-Pressure Plasma Process (LPP).

Introduction. Previous work demonstrated that many different coating effects were caused by electrostatic charge build-up on the GMB support structures. We have used this electrostatic charge effect to enable us to coat as few as eight free-standing GMBs in the LPP process, a feat not previously possible. A study that correlated the electrical power in the plasma with deposition rate and chemical structure of the coating revealed that the ionization potential of the organic species is one of the most important parameters affecting the deposition rate. Similarly, the ionization potential of the background gas strongly affects the plasma density, and thereby affects the deposition rate as follows: the lower the ionization potential the higher the plasma density and the faster the deposition rate. As a result, we were able to double the thickness of smooth, uniform coatings (up to 15 μm thick) by changing the background gas in the plasma from argon to xenon, which has a lower ionization potential.

Coating a Few Preselected GMBs. In all previous LPP coating work, batches of many hundreds of GMBs were coated at one time. The large number facilitated bouncing in the plasma. Attempts to coat fewer than 100 GMBs failed because the GMB could not be made to bounce. We can now coat as few as eight GMBs by precoating the aluminum plate electrodes with a thin ($\lesssim$0.5-μm) coating of poly(p-xylene). Apparently, this dielectric coating leads to a rapid charge build-up on the plates, which stimulates bouncing of the GMB.

Effects Caused by the Ionization Potential (IP) of the Background Gas and Monomer. Previous LPP work used an argon background gas because the presence of argon produced stiffer, stronger coatings and higher survival rates for thin shells than coatings made without background gas. We studied the deposition rate and maximum thickness of smooth-surface coatings for argon (IP = 15.8 eV), nitrogen (IP = 14.5 eV), and xenon (IP = 12.1 eV). We found that substituting xenon for argon triples the deposition rate, doubles the maximum smooth-coating thickness, and improves the achievable surface finish. The data for nitrogen lie between those of argon and xenon, as expected from its ionization potential.

To determine the effect of the ionization potential of the monomer on deposition rate and smoothness, we made coatings with p-xylene, 1,3-butadiene, and ethylene at an input power of 700 mW. Increased ionization potential reduced the coating rate as follows.

Monomer	Ionization Potential (eV)	Coating rate (nm/min)
p-Xylene	8.45	25.8
1,3-Butadiene	9.1	11.9
Ethylene	10.5	3.6

Note that plasma polymerization differs strikingly from free-radical chain-reaction polymerization in which 1,3-butadiene polymerizes almost explosively and p-xylene will not polymerize at all.

Vapor-Phase Pyrolysis Process (VPP).

General. To extend our capability in the preparation of thick coatings with precise control of coating thickness and surface smoothness, we also developed the VPP process. In principle, the process has no coating-thickness limitation and inherently leads to a conformal coating of high surface smoothness and uniformity. The coating p-xylylene possesses high mechanical strength, good thermal stability, and high resistance to most solvents and chemicals. We increased the thickness of

coatings on GMBs to greater than 350 μm, with surface smoothness approaching 100 nm. This coating can be applied to mandrels that are etched out through a small hole, thus leaving free-standing shells with aspect ratios greater than 22 and wall thicknesses at least as thin as 20 μm. We also installed a gas-jet levitator in a VPP apparatus and coated some levitated GMBs.

Thick, Smooth Coatings. To apply thick coatings, a cold chamber with a wide temperature and gas-flow capability was constructed (Fig. VI-11). Coating deposition rates from 40 to 500 nm/min and deposition temperatures from 283 K (+10°C) to 238 K (−35°C) were explored. Deposition rate has a direct effect on the coating surface smoothness—the higher the rate, the rougher the surface. By going from a deposition rate of 180 nm/min to 40 nm/min, the surface roughness decreases from ±1 μm to <±0.05 μm. Thus, in preparing very thick coatings a compromise must be made among coating thickness, surface smoothness, and deposition time. Typically, a 100-μm-thick coating with a 1-μm peak-to-valley surface roughness can be obtained in 8 h. A GMB with an 86-μm-thick coating of p-xylylene applied at a rate of 177 nm/min and showing 1-μm surface smoothness is illustrated in Fig. VI-12.

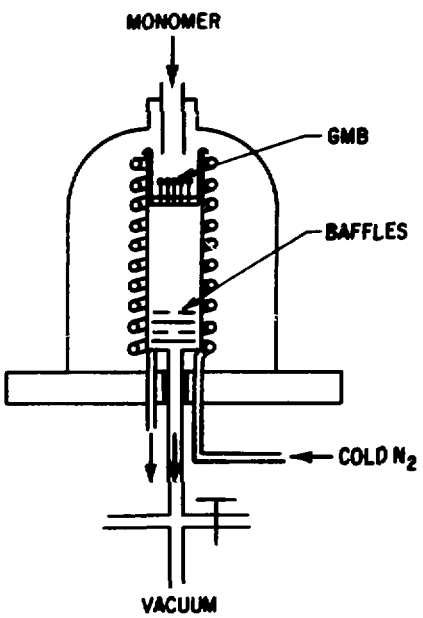

Fig. VI-11.
Schematic of vapor-phase pyrolysis (VPP) coating apparatus used to obtain thick (>350-μm), ultrasmooth (±100-nm) coatings on GMBs.

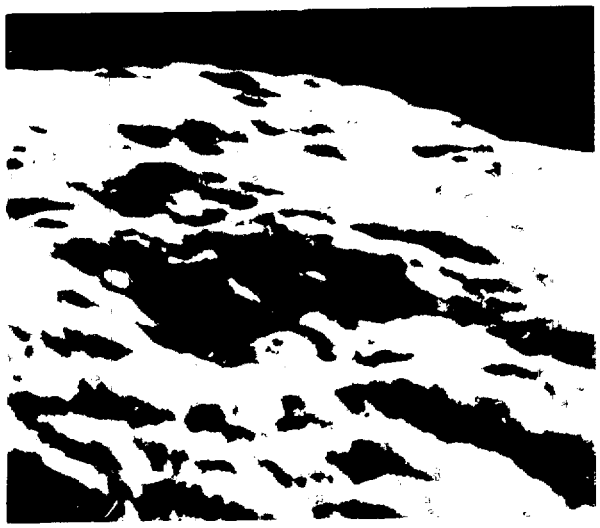

Fig. VI-12.
Scanning-electron micrograph of the surface of an 86-μm-thick VPP plastic coating deposited at 177 nm/min. 5000X

We found two techniques that will improve surface finish even at high deposition rates. One uses a comonomer that interferes with the crystallization process and the other uses a substrate coating with a relatively low number of nucleating sites. Addition of the comonomer 2-chloro-p-xylylene to p-xylylene dramatically improves surface finish even at high coating rates. Figure VI-13 shows an 87-μm-thick coating polymerized with 33 wt% of the above comonomer at a rate 1.9 times faster than the coating in Fig. VI-12. To obtain an equivalently smooth surface with only a single monomer, we would have to use a deposition rate less than 40 nm/min, which is eight times slower than the comonomer rate used for the coating shown in Fig. VI-12. A similar, but somewhat less effective smoothing can be achieved by applying a smooth aluminum coating to the GMB before plastic deposition. A GMB mounted on an Aramid fiber was coated with 20 nm of sputtered aluminum and then with 41 μm of p-xylylene at a rate of 150 nm/min. The resulting surface (shown in Fig. VI-14) is better than that of a similar coating on a bare GMB (Fig. VI-12) but not as smooth as a comonomer deposition (Fig. VI-13).

Plastic Coatings on Levitated GMBs (with A. Lowe and C. Hosford). To coat VPP plastic on a GMB for 20XLD targets, we must mount the GMB on an Aramid

Fig. VI-13.
Scanning-electron micrograph of the surface of an 87-μm-thick VPP plastic coating deposited at 336 nm/min, but with a comonomer added to reduce crystallite growth. 4250X

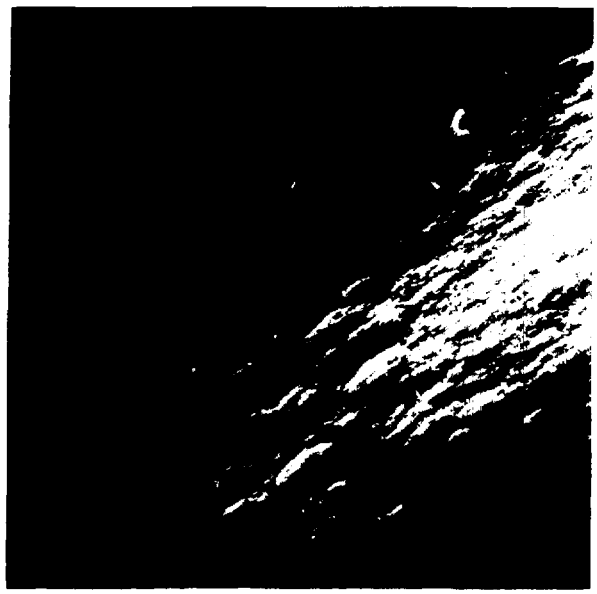

Fig. VI-14.
Scanning-electron micrograph of the surface of a 41-μm-thick VPP plastic coating deposited at 150 nm/min on a GMB passivated with a thin sputtered coating of aluminum. 4450X

fiber, apply the coating, and then machine the coated fiber off to produce a smooth, spherical target. This is a difficult, time-consuming process which, at best, only marginally meets target specifications for sphericity and coating uniformity. Therefore, we are trying to find a way to apply thick plastic coatings to unmounted GMBs. Although we can apply LPP plastic up to 15 μm thick on bouncing, unmounted GMBs, we were unable to keep a number of unmounted spheres in motion during the VPP process which will allow thicker coatings. To solve this problem, we installed a microballoon levitator in our VPP cold chamber and applied up to 5-μm-thick coatings of VPP plastic to levitated GMBs. This levitator is similar to that developed for sputter-coating (described above). We are optimizing the coating and levitation parameters to allow application of thick, smooth-surfaced coatings.

Chemical Analysis of Plastic Coatings by ir Spectrometry. Qualitative and quantitative chemical analysis of as-applied plastic coatings provides necessary data to obtain better control of coating uniformity, aging characteristics, and composition, especially for the high-Z-loaded plastics. This information has been difficult to obtain because of the very small size and spherical geometry of the substrate. Consequently, we were forced to analyze samples taken from the coater wall or from a large number of shells, even though we knew that these samples might not be representative of the coating on a single selected shell. We recently developed a technique for analyzing plastic coatings on GMBs as small as 600 μm in diameter by measuring the ir spectrum of a single shell on a Fourier transform spectrometer. Because this instrument has the capability of subtracting the spectrum of the GMB substrate from that of the coated GMB, we are able to obtain spectra, and hence, to identify the qualitative chemical composition of the coating *in situ*. We are trying to calibrate the instrument so that we may obtain quantitative data.

ORGANOMETALLIC COATINGS DEVELOPMENT (R. Liepins, M. Campbell)

General

The outer pusher of the Polaris target requires a high-Z, low-density (1.3 to 3 g/cm^3) material as an x-ray and hot-electron shield for the DT fuel. We are investigating both metal-loaded plastic and high-Z metal foam for this layer. By using easily vaporizable organometallic monomers, we have successfully deposited layers of metal-loaded plastic with both the VPP and LPP processes.

Lead and Tantalum Organometallics

We applied LPP organometallic coatings to GMBs with tetraethyl lead $(CH_3CH_2)_4Pb$ and with pentaethoxy tantalum $(CH_3CH_2O)_5Ta$, both pure and mixed 50 wt% with p-xylene. Although very little tantalum was incorporated in the applied film in any case, preliminary coatings made with tetraethyl lead showed up to 30 wt% lead. In the VPP process we introduced 10 wt% iron via the organometallic compound ferrocene into the p-xylylene vapor stream and observed 9.3% iron inclusion in the resulting film. Because some of this iron could be extracted by soaking the film in hot methanol we believe that at least some of the iron was molecularly dispersed but did not react with the p-xylylene. These results are summarized in Table VI-I.

POLYMER FOAM DEVELOPMENT

General

Several advanced laser fusion target designs require ~250-μm-thick spherical shells of low-density foam (<0.05 g/cm^3) with very small cells (<1 μm). Ideally, the foams should consist only of carbon and hydrogen. However, to increase the chances for producing the desired foams, we also used polymers containing nitrogen and/or oxygen atoms. This broadened the choice of polymers greatly, although heavy metals and other elements with atomic numbers higher than 20 are generally considered undesirable. Because the foams should have a uniform structure throughout, cell size and density should be uniform.

Summary of Small-Cell-Size Foam Development at Monsanto (J. L. Schwendeman, Monsanto Research Corporation)

We have supported a development effort at Monsanto Research Corporation to form small-cell-size, low-density plastic foam shells. The desired goal was a cell size less than 2 μm and a density less than 0.1 g/cm^3. This contract terminated in October 1978. Three materials were investigated for meeting cell size and density requirements in foam coatings for small spheres, with the following results.

TABLE VI-I

FORMATION OF HIGH-Z METAL-LOADED PLASTIC COATINGS

	Appearance		Coating Thickness	Metal (wt%)	
	Reflected light	Transmitted light	(μm)	Calculated	Found
50:50 Pb:p-Xylene	Dark brown, metallic	Brown	7.9	---	13.3
50:50 Ta:p-Xylene	Tan	Tan	1.4	---	0.13
Tetraethyl lead	Black, metallic	Dark brown	5.8	64.1	30.7
Pentaethoxy tantalum	Dark brown, metallic	Brown	7.3	44.5	<1.0
Ferrocene:p-Xylylene	Bright orange	---	107.0	10.0	9.3

Evaluation of cellulose acetate asymmetric membranes proved that these foam films have the required small cell size. These films can be prepared at room temperature and lend themselves to molding parts in matched positive-pressure molds and, possibly, to vacuum-forming of the desired foam shells. However, we were unable to produce these foams in the desired density range. At present, 250-μm-thick cast foam films, when dried, are 70 to 80 μm thick, with 2.0-μm and smaller cells and a density greater than 0.30 g/cm^3.

Aropol water-extended polyester foam systems (WEP 661-P® and D-WEP 123®) were also evaluated as a possible means of forming small-cell-size foams. We succeeded in making water-extended polyester foams with a density as low as 0.12 g/cm^3, but failed to form foams having cell sizes less than the required maximum of 2.0 μm. We could mold these foams into small spheres.

Gelatin/water/toluene emulsion foams were also investigated. Upon film draw-down, foams of small cell size were produced. However, work on this material was stopped because of concern as to the reproducibility of the properties of gelatin and its relatively low thermal stability.

As a result of the failure of all experiments in this contract, we are reconsidering alternative possibilities for making foams that meet requirements for both density and cell size and using pressurized gas in place of foam for the buffer.

CRYOGENIC TARGET DEVELOPMENT (J. R. Miller)

General

Laser fusion targets fueled with cryogenic liquid or solid DT offer the advantage of high initial fuel density without the disadvantage of diluent atoms being present as they are in room-temperature solids having a high hydrogen density [e.g., lithium in Li(D,T), carbon in $(\text{-CDT})_n$, or boron and nitrogen in NH_3BH_3]. In addition, calculations indicate that the yields from targets fueled with liquid or solid DT can be considerably higher than those from targets of the same design, but fueled with high-pressure DT gas. Therefore, we actively pursued the development of cryogenic targets despite the significant experimental complications encountered in their fabrication and in their use in laser-target interaction experiments. We also tested a cryogenic insertion mechanism for loading and cooling these targets in the Helios target chamber.

Cryogenic targets receiving the greatest attention are uniform, hollow shells of solid DT condensed onto the inside surface of a glass or metal microballoon that serves as the pusher shell. We previously developed techniques to freeze the DT into a uniformly thick layer on the inside surface of the glass and to measure the thickness uniformity of the condensed DT shell. Because high-yield targets require metal pusher shells and we are not able to directly measure the uniformity of DT layers inside opaque shells, we made a calculational analysis of the FIF technique.

Fast Isothermal Freezing (FIF) (J. R. Miller, W. J. Press, R. J. Fries)

The investigation of any possible limitations of the fast isothermal freezing (FIF) technique for producing uniform, solid DT layers in target fuel cores continued. As reported in LA-6616-PR and LA-6834-PR, the FIF method forms layers of solid DT on the inner surface of bare GMB fuel cores with a uniformity that is better than can be determined interferometrically (±10% variation in layer thickness). Because laser fusion targets of advanced design have multiple shells and multiple layers around the cryogenic fuel core, we continued the investigation of inherent limitations that may apply to the FIF technique.

Because it is not possible to measure the solid DT layer's uniformity in opaque, multishell targets interferometrically, and because no other diagnostic techniques are available to measure the uniformity of a thin, low-Z shell (DT) inside one or more opaque high-Z shells (gold, for example), we developed a computer model to calculate how long liquid exists in the fuel core as it is cooled. This time can then be used to predict the gravitationally induced nonuniformity (NU) produced in the frozen DT shell.

The NU produced in the frozen DT shell, defined as the difference between the maximum and minimum shell thicknesses divided by the average shell thickness, depends on the length of time liquid is present in a given fuel core. For example, a 100-μm-diam fuel core filled with DT to 10 MPa and frozen in 25 ms, or a 500-μm-diam fuel core filled to 10 MPa and frozen in 100 ms will each produce a NU of 0.095.[2] Our heat-flow model

calculates the cooling rate of the fuel core, and hence, the expected thickness uniformity of the solid DT layer.

Although laser fusion targets are radially symmetric and therefore can be modeled mathematically in one dimension, the cooling rate of a multishell target cannot be solved analytically. This inability stems from the strong temperature-dependence of both the thermal conductivity and the specific heat of most materials over the temperature range of 4 to 40 K and from the thermal interaction of each layer in a multimaterial target.

The problem of calculating the length of time liquid exists in a fuel core can be separated into two parts. The first part consists of determining the time required to condense all the DT gas into a liquid shell, and the second part, determining the time required to freeze this liquid shell. The sum of these two times is the quantity used to predict the NU of the frozen DT shell. Physically, this partition of the problem assumes that the heat released by the condensing gas prevents the liquid from cooling below the triple point until all the DT has condensed.

An exact numerical solution to the heat equation for gas condensation in a multishell sphere with temperature-dependent thermal properties was obtained from a standard finite-difference formulation.[3,4] Stable, physically realistic results for all times were obtained with a Crank-Nicholson scheme using a time-dependent weighting factor.[5] With a constantly spaced nodal mesh, the transient target temperature distribution had minimal dependence on the time step used. Therefore, incorporation of a variable time step into the finite-difference scheme had the added benefit of minimizing the computational effort. Less than 1 min of CDC 6600 cpu (central processing) time was needed for each multishell target evaluated.

The numerical solution for the DT condensation time in a simple two-shell target is shown in Fig. VI-15. The family of curves, reduced temperature vs reduced radius, plots the condensation time of DT gas in a 100-μm-diam, 1-μm-thick glass fuel core positioned inside a second 1-μm-thick glass shell. The target, initially at $T_I = 40$ K, cools to $T_F = 19.7$ K in 63 ms. In general, thicker shells or larger target diameters increase the DT condensation time.

Because the DT condensation time is strongly affected by the helium diffusivity, and because thermal-property data for cryogenic, gaseous helium at low pressures are scarce,[6] the temperature-dependence of the thermal diffusivity for helium was obtained by matching calculated

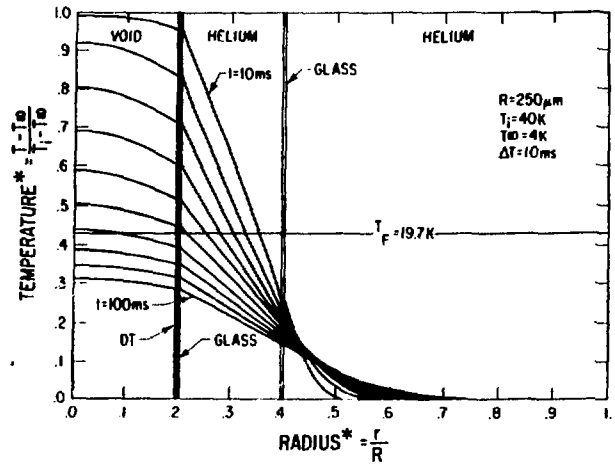

Fig. VI-15.
DT condensation-time calculation for a target with two concentric glass shells separated by 50 μm of helium exchange gas. the temperature of the DT is plotted against radial position.

and experimental results of the freezing time for a bare 100-μm-diam glass fuel core. The condensation time is also a function of the density of the gaseous helium.

Although metal shells are not considered in Fig. VI-15, condensation-time results for such shells were obtained. The effect on condensation time of adding a metal shell is minimal: no significant time increase is seen because of the relatively high thermal conductivity of metals compared to that of other target materials.

The time required to freeze a liquid DT shell is the second part of the liquid-existence-time problem. As stated, when the freezing time is added to the condensation time, we can predict the layer nonuniformity of solid DT in a target fuel core.

An approximate solution to the heat-flow problem involving a liquid-solid phase change in spherical bodies has been formulated.[7] This approximate solution was used to compute freezing times of liquid DT shells. The results of this calculation indicate that the DT fusion time is short (<1 ms) compared to typical DT condensation times (≥10 ms). Consequently, layer nonuniformities arise during the DT condensation time rather than during the DT solidification time.

Model calculations were performed to determine the length of time liquid DT is present during the formation of cryogenic laser fusion targets. Our results make it possible to predict the thickness uniformity of solid DT

shells in opaque, multishell targets. As shown, gas condensation occurs at a much slower rate than does the subsequent solidification of the liquid shell.

Helios Cryogenic Target-Producing Prototype (J. R. Miller, J. K. Feuerherd, H. E. Tucker, C. Cummings, R. Day)

The experimental apparatus designed to produce cryogenic targets for the Helios laser system was tested extensively. Three specific areas investigated were (1) the heat load to the apparatus, (2) the cryogenic-shroud retraction system, and (3) the seals between the target mount and the cryogenic shroud.

To cool the apparatus to the desired 6 K, we had to redesign the liquid-helium transfer system, the thermal standoff between the target mount, the target cart, and the target holder. In addition, a new cryogenic-shroud retraction system was designed, fabricated, and assembled. Evaluation of the performance of this device with high-speed motion pictures, discrete position sensors, and an accelerometer showed that it needs 6.8 ms to move the required 3 cm. We expect this time to be sufficiently short. However, work is continuing on the shock-absorber subsystem needed to stop the rapidly moving cryogenic-shroud retraction device with uniform, constant deceleration, which is needed to minimize mechanical fatigue in the entire system and vibration in the Helios target chamber.

REFERENCES

1. F. Skoberne, Comp., "Inertial Fusion Program, January 1—June 30, 1978," Los Alamos Scientific Laboratory report LA-7587-PR (May 1980).

2. Extrapolated from T. M. Henderson, R. J. Simms, and R. B. Jacobs, "Cryogenic Pellets for Laser-Fusion Research—Theoretical and Practical Considerations," Adv. Cryog. Eng. 23, 682 (1977).

3. M. N. Ozisik, *Boundary Value Problems of Heat Conduction* (International Textbook Co., 1968), p. 413.

4. B. Carnahan, H. A. Luther, and J. O. Wilkes, *Applied Numerical Methods* (John Wiley and Sons, Inc., 1969), 462.

5. S. V. Patonkar and B. R. Baliga, "A New Finite/Difference Scheme for Parabolic Differential Equations," Numerical Heat Transfer 1, 27 (1978).

6. D. C. Pickles and B. Colyer, "Heat Transfer Through Low Pressure Helium Gas at Temperatures Below 4.2 K," Rutherford High Energy Laboratory report RHEL/R 145 (1967).

7. Sung Hwang Cho and J. E. Sudderland, "Phase Change of Spherical Bodies," J. Heat Mass Transfer 13, 1231 (1970).

VII. APPLICATIONS OF LASER FUSION—FEASIBILITY AND SYSTEMS STUDIES

(L. A. Booth and T. G. Frank)

Our feasibility and systems studies are being performed to analyze the technical feasibility and economic aspects of various commercial and military applications of lasers and laser fusion. Commercial applications include electric power generation, fissile-fuel production from fusion-fission hybrid reactors, and production of synthetic fuels such as hydrogen. Our studies also include assessments of advanced technologies that require development for the ultimate commercialization of laser fusion. The general objectives of these studies are the conceptualization and preliminary engineering assessment of laser fusion reactors and other energy production subsystems; the development of computer models of integrated plant systems for economic and technology tradeoff and comparison studies; and the identification of problems requiring long-term development efforts.

REACTOR DESIGN STUDIES

Introduction

Our reactor design studies determine the fundamental engineering feasibility of reactor design concepts and establish scaling laws for the sizing of reactors in integrated plant designs for energy production applications. In converting pellet output energy to useful forms, two primary design considerations prevail: (1) protection of the reactor chamber structural wall from x rays and ion debris generated by the pellet, and (2) conversion of these energy forms and of the high-energy neutrons to useful energy while producing the fuel constituent, tritium.

In general, these design considerations are essentially independent of each other. Because ~80% of the pellet output is in the form of high-energy neutrons, this energy is most conveniently converted to thermal energy in a "blanket" surrounding the cavity and containing lithium or lithium compounds for tritium breeding; the design of this blanket is essentially not dependent upon the first-wall protection scheme. Likewise, means of protecting the first wall are generally not dependent upon the blanket design. Therefore, a variety of blanket designs can be incorporated with a particular wall-protection scheme and vice versa.

We are studying three methods of first-wall protection: (1) a lithium wetted wall,[1] (2) a magnetically protected wall with a low-Z sacrificial liner,[2] and (3) a magnetically protected wall with a background fill gas. In the lithium wetted-wall concept, the x-ray output and ion debris are absorbed by the ablation of a thin film of lithium that coats the inside surface of the first wall. In the second concept, the ion debris is ducted out the ends of a cylindrical configuration where the ions are either collected on large surface areas or slowed down by MHD decelerators. The x-ray energy is absorbed by ablation of small amounts of the low-Z sacrificial liner. In the third concept, the ion debris is converted in the same manner as above, but the x-ray energy is attenuated and converted into a blast wave, which beneficially increases the interaction time of this energy fraction with the first wall.

Our studies of blanket concepts include (1) a low-temperature (<1000 K) liquid-lithium blanket for electric power generation, (2) a high-temperature (1500-2000 K) boiling-lithium blanket for high-efficiency electric power generation and as a high-temperature process heat source for hydrogen production, and (3) a lithium-cooled array of elements containing fertile ^{238}U and/or ^{232}Th for the production of fissile fuel and electricity as a byproduct.

Reported below are results from our studies on the magnetically protected wall concept, on the high-temperature boiling-lithium blanket concept, and on a low-power-density fissile-fuel production blanket (hybrid) concept.

Magnetically Protected Cavity Phenomena Modeling (I. O. Bohachevsky, J. J. Devaney)

We have programmed the mathematical description[3] of the new plasma model representing the magnetically protected reactor cavity for use on the CRAY computer. The part of the code that solves the coupled ion-transport and electromagnetic field equations has been tested successfully; the part describing the behavior of the continuum background medium is being tested. In addition to completing these time-consuming tasks, our theoretical analysis has led to an improved understanding of the physics of cavity phenomena and of implications of the postulated cylindrical symmetry.

We have derived expressions for the momentum transfer from the high-velocity ions to the background medium. Some results are summarized in Table VII-I, where we have used Γ_1 as the drag force in dynes acting on an alpha particle moving with the energy E(keV) through helium at the density of $\rho g/cm^3$. Although our expressions are currently valid only for neutral gases, their use may be justified in cases of low background ionization. In addition, their availability in a form suitable for computation enables us to test the code and provides assurance that additional results will be derived when needed.

MHD Decelerators for the Magnetically Protected Wall Concept (I. O. Bohachevsky)

The use of structured pellets in inertial confinement fusion (ICF) reactors and of a buffer gas for cavity wall protection[4] implies that a significant fraction of fuel-pellet microexplosion energy will be deposited in the cavity environment. Therefore, there is a need to investigate methods of removing and recovering this energy. Calculations indicate that the sputtering erosion of energy sinks,[5,6] proposed for the removal of pellet-debris ion energy in the magnetically protected reactor cavity design, may be unacceptably high. Consequently, we had to seek alternative methods. We found that the energy may be removed and recovered from the pellet debris and the cavity medium by means of magnetic fields in a magnetohydrodynamic (MHD) energy converter that decelerates the ions without suffering excessive wall erosion and that even generates electric energy in the process.

Previous studies[7] assessing the applicability of MHD generators for energy removal from the fusion fuel-pellet debris led to a more extensive analysis[8] of these devices, as summarized below.

There are conventional and induction-type MHD generators. In a conventional generator, the electrodes

TABLE VII-I

DRAG FORCE ON AN ALPHA PARTICLE IN HELIUM AT DENSITY $\rho g/cm^3$

$$\Gamma_1 = \rho \times 2.4113 \times 10^{-4}$$

$$S_H = \frac{6300}{E} \ln 1 + \frac{1.3 \times 10^5}{E} + 0.04407E$$

$$S_L = 0.58E0.59$$

$$S = S_H \qquad E > 10 \text{ MeV}$$

$$S = \frac{S_H S_L}{S_H + S_L} \qquad 50 \text{ keV} \leq E \leq 10 \text{ MeV}$$

$$S = \frac{S_H S_L}{S_H + S_L} + \Delta S \qquad 5 \text{ keV} \leq E \leq 50 \text{ keV}$$

$$S = 2 \qquad 1 \text{ keV} \leq E \leq 5 \text{ keV}$$

E (keV)	50	40	30	20	10	8	5
ΔS	0.10	0.15	0.20	0.33	0.50	0.60	0.70

are exposed to the high-energy plasma flow and therefore tend to be eroded rapidly. In an induction-type generator, the power is extracted with induction coils located behind insulating refractory walls, which, therefore, are not exposed to the destructively hot plasma environment.

The plasma exiting from the reactor differs from that in a conventional MHD generator in two respects. (1) Its conductivity is very high because it contains a large proportion of metallic ions in high ionization states, and (2) it can be collimated with the magnetic field into a high-velocity beam.[5,9] Consequently, the magnetic Reynolds number in the MHD channel will be high (≥ 1) and the energy density will not be less than in a conventional (electrode) generator. These conditions make it possible to exploit the engineering advantages of the induction-type generator without penalties commonly associated with low-energy density and efficiency if a conventional combustion-generated plasma is used in this device.

To investigate the compatibility of magnetically protected reactor cavity designs with MHD generators we imposed two performance requirements. (1) The generators should reduce the ion exit velocity so that the debris, possibly with the aid of diffusers, could be used in conventional heat exchangers, and (2) they should generate sufficient amounts of electricity to energize their own magnets.

In our analysis we solved the one-dimensional channel-flow equations, determined the magnet parameters, and estimated the cost of MHD deceleration. Representative results summarized in Tables VII-II and -III and in Figs. VII-1 and -2 show that nearly 65% of the ion kinetic energy has been either extracted in the form of electric power or converted into thermal energy. In our illustrations, Q_{IDEAL} denotes the power residing in the moving plasma, $Q_{\Omega MC}$ is the power dissipated in magnet coils, and Q_{ICP} is the power developed in the induction coil for an arbitrarily prescribed load current of 500 A. None of the cases calculated was optimized in any way, and therefore, significant improvement in performances can be gained by simple parameter improvement.

To determine the economic effectiveness of MHD decelerators, we compared their cost with the cost of graphite energy sinks. It is convenient to arrive at the decelerator cost by estimating the magnet and channel costs separately. The cost estimate for a conventional magnet (including core, winding, cooling, and some support structure) is based on a unit cost of 100 000 \$/m^3;

TABLE VII-II

CONSTANT-AREA SUPERSONIC DECELERATOR
0.35- by 0.35- by 1.00-m CHANNEL

	Case[a]		
	1	2	3
Plasma Conductivity (mho/m)	1000	500	100
Magnetic Field (T)	0.134	0.219	0.576
Exit Velocity (m/s)	5784	5767	5812
Exit Pressure (N/m^2)	1.94×10^5	1.81×10^5	1.95×10^5
Exit Mach Number	1.007	1.001	1.006
Ideal Power (W)	5.35×10^4	3.62×10^4	1.01×10^4

[a]In all cases:

Instantaneous Mass Flow Rate (kg/s)	5
Pulse Rate (Hz)	10
Ion Pulse Duration (s)	1.24×10^{-4}
Inlet Velocity (m/s)	10^4
Inlet Pressure (N/m^2)	10^5

TABLE VII-III

EFFECTS OF EXIT HEIGHT ON CHANNEL PARAMETERS OF A DIVERGING AREA SUPERSONIC CHANNEL FOR PLASMA CONDUCTIVITY EQUAL TO 1000 mho/m CHANNEL INLET, 0.35 by 0.35 m; CHANNEL LENGTH, 1 m

	Case[a]				
	1	2	3	4	5
Channel Height, Exit (m)	0.35	0.4	0.5	0.6	0.7
Mach Number, Exit	1.007	1.187	1.298	1.335	1.341
Exit Velocity (m/s)	5784	6738	7320	7523	7563
Exit Pressure (N/m^2)	1.94×10^5	1.42×10^5	1.04×10^5	8.40×10^4	7.17×10^4
Ion Pulse Duration (s)	1.24×10^{-4}	1.20×10^{-4}	1.15×10^{-4}	1.12×10^{-4}	1.10×10^{-4}
Ideal Power (W)	5.35×10^4	5.91×10^4	6.98×10^4	8.03×10^4	9.05×10^4

[a]In all cases:

Inlet Velocity (m/s)	10^4
Magnetic Field (T)	0.134
Inlet Mach Number	1.844

the channel costs are estimated at less than $100 000. The cost of energy sinks is based on the graphite (cheapest energy-sink material) cost of 11 $/kg. A more accurate cost model of MHD decelerators has been constructed and will be used when a more extensive and reliable economic data base becomes available.

The conclusions inferred from our investigation may be summarized as follows.

- MHD decelerators are a competitive alternative to energy sinks if the sink erosion rate exceeds ~1 to 2 cm/yr.
- Net electric power production with steady-state magnet operation appears possible only when the plasma conductivity is greater than ~100 mho/m. For lower conductivities, pulsed or superconducting magnets must be used; however, the low power outputs obtained at such low conductivities indicate that these designs may be economically infeasible.
- Power output and cost of the MHD decelerators are both proportional to their size; therefore, a tradeoff investigation must be carried out to determine the most cost-effective configuration.
- Performances of induction and electrode-type decelerators are approximately equal. The induction-type decelerators generate slightly more power because the average magnetic Reynolds number along the channel is slightly higher than unity for the conditions. However, the electrode-type decelerators may not be feasible because of limited electrode lifetime in the plasma environment anticipated for ICF reactors.

High-Temperature-Lithium Boiler Blanket Concept (J. H. Pendergrass)

An artist's rendition of the high-temperature-lithium boiler concept, described in a preliminary form previously, is shown in Fig. VII-3. The concept's operating principles are as follows. Highly penetrating 14-MeV fusion neutrons give up only a modest fraction of their kinetic energy in passing through cavity walls of moderate thickness, and only a small fraction is absorbed by nuclear interactions. Most of the fusion-neutron kinetic and interaction energy is deposited in a boiling, lithium-containing, liquid-metal blanket. Transport of vapor to, and its condensation on, heat-exchanger transfer surfaces constitutes the primary blanket heat-transport mechanism, which would be self-pumping if provisions were made for gravity return of the condensate. The concept offers two significant advantages: (1) the presence of lithium in the blanket allows tritium breeding ratios of

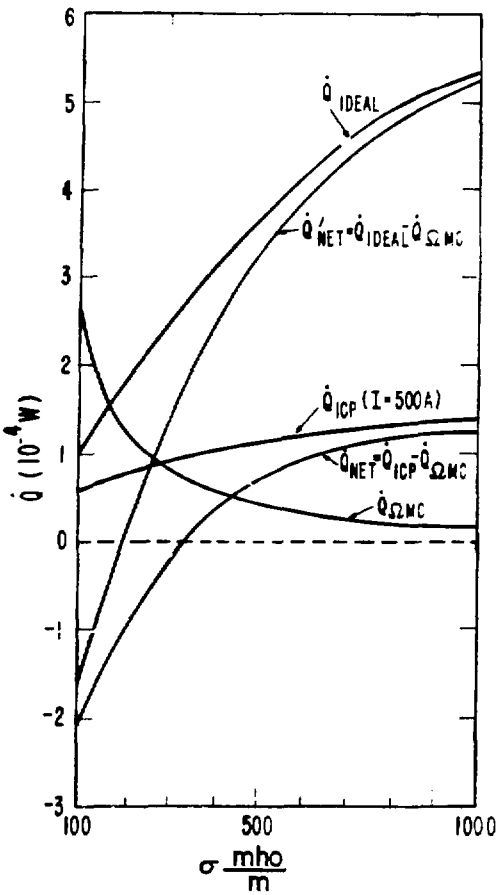

Fig. VII-1.
Effect of conductivity on power allocation for a constant-area supersonic duct.

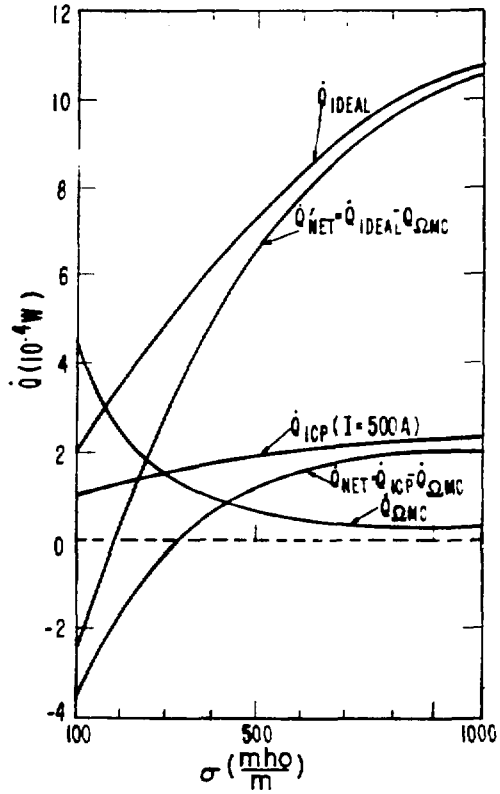

Fig. VII-2.
Effect of conductivity on power allocation for a diverging-area supersonic duct.

1.0 or greater, hence tritium self-sufficiency is achieved; and (2) pure lithium and lithium-containing molten alloys considered for use have relatively low vapor pressures (0.4 atm at 1500 K rising to ~15 atm at 2000 K for pure lithium) so that structural requirements are not severe.

The preliminary description of the concept[3] listed a number of potential advantages over other high-temperature fusion reactor blanket concepts. We have attempted to further assess the possibility of achieving these benefits and have developed conceptional solutions to important design problems.

Design aspects considered include

- The containment of molten lithium-containing alloys at elevated temperatures;
- The recovery of most neutron kinetic and interaction energy as high-temperature heat;
- An allowance for differential thermal expansion and for routine, periodic replacement of neutron-damaged first-wall structures while maintaining all other reactor functions;
- The design of the primary heat exchanger, with emphasis on limiting the tritium escape rates through primary heat exchangers into power-cycle or process loops to acceptable values;
- Neutronics and tritium breeding performance;
- The distribution of boiling and steady-state vapor volume fractions;
- The recovery of bred tritium by methods that take advantage of high blanket temperatures; and
- Electric power conversion cycles for topping, which can take advantage of the high heat delivery temperatures.

As blanket containment structural materials, we considered ceramics, glass-ceramics, and graphites, all of which possess the required strength and resistance to creep in the 1500 to 2000 K temperature range. As a

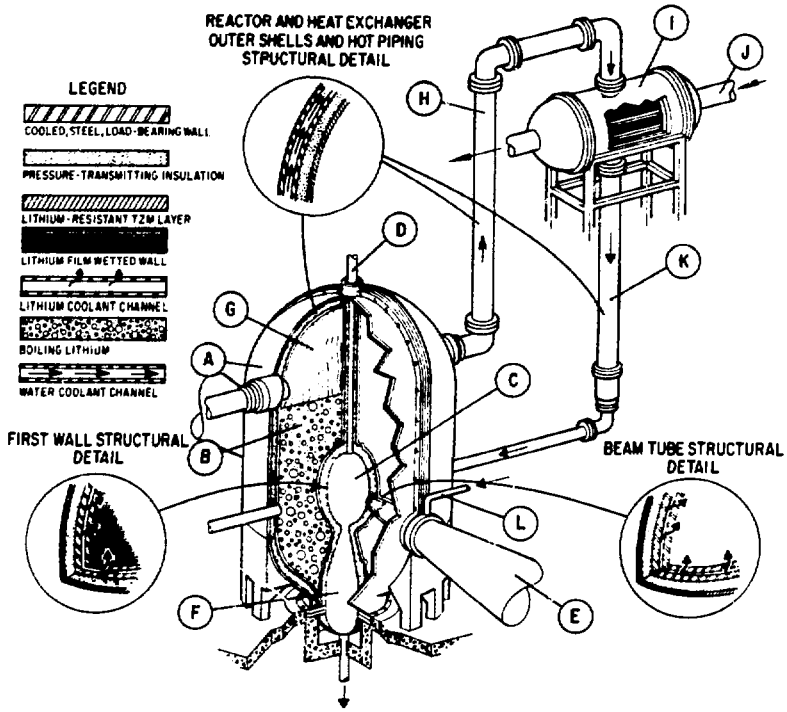

Fig. VII-3.

Artist's rendition of lithium boiler high-temperature tritium-breeding blanket and primary heat-transport concept. (A) Outer containment clamshell, (B) boiling lithium, (C) inner lithium-cooled blanket containment clamshell including wetted-wall first-wall protection, (D) pellet injection tube, (E) laser beam tube, (F) supersonic condenser, (G) lithium vapor, (H) vapor conduit, (I) process heat or power cycle heat exchanger, (J) process heat or power cycle stream, (K) condensate return line, (L) first-wall and beam-tube lithium coolant feed.

protection from attack by the liquid metal, we considered coating these materials with thin adherent layers of TZM (0.5:0.08:99.42 wt% Ti:Zr:Mo) or protecting the structure with thicker, nonadherent TZM liners. Reflux experiments of 1000-h duration at 1923 K indicated that TZM is not attacked by pure lithium under these conditions.[10] First walls operating at blanket temperature could permit the recovery of x-ray and pellet debris energy at high temperature. However, TZM liners, supported by cooled steel walls with insulation between liner and structure and possessing sufficient compressive strength to transmit internal pressure loads to the load-bearing structure without collapsing, appear more attractive.

A carbon foam, made by sintering together hollow spheres manufactured from petroleum pitch, which has a density of 0.39 g/cm^3, a thermal conductivity of only $\sim 10^{-3}$ W/cm·K, and a compressive strength of 1500 psia at room temperature, has been identified as a potentially attractive insulating material.[11] However, lack of knowledge concerning high-temperature physical properties and behavior under 14-MeV neutron irradiation to high fluences compels us to examine other insulation concepts as well.

Provisions for accommodating differential thermal expansion and periodic, routine replacement of first-wall structure are indicated in Fig. VII-3.

Most neutrons passing through the first-wall structure can be absorbed in a liquid, pure-lithium blanket less than 2.0 m thick, and tritium breeding ratios greater than 1.5 can be achieved with such thicknesses. However, the blanket will actually be thicker because of significant fractional vapor volume. Boiling is expected to be unusual because energy is deposited volumetrically rather than transferred into the blanket through solid surfaces.

Because most theory and experiments concerned with ordinary nucleate boiling are of limited applicability, experiments will probably be required to clarify this issue.

With liquid-lithium thicknesses of this order of magnitude, significant amounts of gamma energy, produced primarily by (n,γ) reactions of neutrons with reactor structure and blanket fluids, and of neutron energy can escape from the blanket. While deposition of as much fusion energy as possible in the high-temperature zone may be desirable because lower temperature heat can be used less efficiently, capture of the last few percent of escaping energy is generally more difficult than capture of all the rest. On the other hand, greater gamma and neutron energy leakage means that thicker reactor shielding and a greater capacity to cool the shield will be required. Exploratory neutronics calculations for 1.5-m-thick, 20-vol%-vapor, pure-lithium blankets indicate that gamma-energy leakage is more than 10% of neutron wall loading.

In an attempt to retain more gamma and neutron energy within the blanket without large increases in blanket thickness, we investigated the use of lithium-rich boiling lead-lithium mixtures. Preliminary neutronics calculations for 1.5-m-thick blankets indicate that gamma- and neutron-energy leakage can be reduced substantially, i.e., by a factor of about 2, that the total of neutron kinetic plus interaction energy is increased, and that the tritium breeding ratio is relatively insensitive to lead content up to large lead concentrations. Although there is little compatibility experience for high-temperature materials with lead and much less for lead-lithium mixtures, all indications are that no particular problems will be encountered. Lead-lithium alloys have lower vapor pressures than lithium and are projected to have lower tritium solubilities, thereby further lowering containment structural stresses and blanket tritium inventories.

Conservative calculations, which assume that the only significant resistance to tritium permeation through heat exchangers is that of bulk materials to diffusion, indicate that the use of double-walled heat-transfer equipment with ceramic permeation barriers and removal of tritium escaping through the first wall by a helium sweep gas between the two walls will limit tritium escape rates to acceptable levels, i.e., to 1.0 Ci or less per day. The helium sweep gas also aids heat transfer by providing a conductive mechanism operating in parallel with thermal radiation, to which helium is essentially transparent, and permits ready adjustment of pressure differential loading between inner and outer walls. Because readily fabricable metals of acceptable cost creep excessively in the temperature range of interest, the use of ceramics, glass-ceramics, and graphites for construction of primary heat exchangers will probably be necessary. Protection from blanket fluid attack by coating or cladding such materials with, e.g., TZM, is necessary. On the process-fluid side, heat-transfer surfaces must be protected from attack by oxidizing gas mixtures with oxides, e.g., alumina or silica, as structural materials or protective layers. Double-walled heat-transfer equipment construction affords both protection against catastrophic heat-exchanger failure due to sudden rupture and the possibility of detecting small leaks before they assume serious proportions. Because the largest resistance to heat transfer to gaseous process or power-cycle streams is the gas film resistance, a large temperature-drop penalty is not paid for double-walled heat-exchanger construction in such cases.

If permeable windows are used for tritium recovery, tritium window performance is enhanced by higher temperatures and their simplicity is attractive. However, high-temperature distillation can also take advantage of the high temperatures provided by lithium boiler blankets and offers other advantages, including the removal of other volatile blanket impurities such as helium generated by (n,α) reactions of blanket and structural materials, oxygen, and nitrogen. Distillation for tritium recovery has been rejected in the past because at low temperatures (below ~1230 K), the liquid is enriched in deuterium and protium relative to the vapor. At higher temperatures the opposite is true, with the atom ratio of deuterium in the vapor to deuterium in the liquid rising to 10 at ~1850 K, corresponding roughly to an enrichment by a factor of 10 for each equilibrium stage, so that only a few stages would be required. Also, side-stream drawoffs of only a few percent of the blanket boilup are required, heat can be recovered at temperatures only a little below the blanket operating temperature in overhead condensers, column shell construction would be similar to blanket containment, and the device would be self-pumping.

Preliminary indications are that thermionic diode designs developed for topping fossil-fuel-fired steam power plants[12] can be readily adapted for mating with lithium boiler blankets to improve overall plant thermal conversion efficiencies or to provide dc power for electrochemical processes such as the bismuth-oxide hybrid cycle described below.

Fusion-Fission Hybrid Reactor Studies (W. A. Reupke, H. S. Cullingford)

Interest in proliferation-resistant fuel cycles has stimulated the development of hybrid fusion-fission concepts based on the resource-efficient thorium fuel cycle. Previous studies have identified a high-power-density hybrid concept that produces a large amount of byproduct electricity[13] as well as fissile fuel. Our studies have turned to quasi-symbiotic concepts that maximize fissile-fuel production and minimize heat production—so-called fissile-fuel factories. Such concepts shift the burden of electric power production from the hybrid reactor to a host system of fission reactors. We have adopted the following conditions as our design basis: (1) electrical self-sufficiency, (2) tritium self-sufficiency, and (3) maximum fissile-product output per unit of blanket heat.

Our studies of fissile-fuel factories are based on laser-driven ICF reactor concepts. The specific designs investigated are spherical and use the wetted-wall reactor cavity, which is enclosed by spherical shells consisting of breeding materials, coolant, and structure. Liquid lithium is used as the fertile material for breeding tritium and as the reactor coolant. The fissile breeding material is thorium metal.

Neutronics calculations were performed with our one-dimensional S_N code ONETRAN-DA. Multigroup cross sections and kerma factors were processed from ENDF/B-IV using the NJOY processing system to form a coupled 30/12 group neutron/gamma-ray set. Several blanket compositions and configurations were investigated. Calculated quantities of interest include the tritium breeding ratio R_T, the fissile conversion ratio or number of fertile atoms converted per thermonuclear source neutron R_F, the blanket energy deposition per thermonuclear source neutron Q, and the ratio of fissile-equivalent thermal energy to blanket energy 180 R_F/Q. A typical reactor geometry and blanket composition is given in Table VII-IV. Selected results of the neutronics calculations are presented in Table VII-V. Only cases that satisfy the requirement for tritium self-sufficiency are included in Table VII-V. For Case 1, a 4-cm-thick beryllium neutron-multiplier region was included adjacent to the reactor cavity and the allowable volume fraction of thorium, while retaining sufficient lithium coolant for a tritium breeding ratio of 1.1, was determined. The fissile breeding region for Case 2 includes the maximum volume fraction of thorium consistent with requirements for structure and coolant. Sufficient beryllium neutron multiplier (11 cm) was included to obtain a tritium breeding ratio of 1.1. Case 3 is similar to Case 2 except that the beryllium-region thickness was reduced to 4 cm and sufficient lithium was added between the beryllium and thorium regions to obtain a tritium breeding ratio of 1.1. For Case 4, the beryllium was eliminated and the lithium-region thickness was increased sufficiently to obtain an adequate tritium breeding ratio. The effects of using a carbon reflector outside the fissile breeding region are illustrated by Case 5 (see also Table VII-IV).

The most attractive designs are Cases 2 through 5. The use of a beryllium neutron multiplier results in smaller overall systems (Cases 2 and 3) than the design with sufficient lithium for adequate tritium breeding without the neutron multiplier (Case 4). For Case 5, the thickness of the fissile breeding region is reduced from 50 to 30 cm, but the fissile fuel production per thermonuclear neutron R_F, is almost as large as for Case 4. Thus, the average rate of production of fissile fuel per unit volume of fissile blanket is larger by ~70% for Case 5 than for Case 4. This may have important implications for optimum processing cycles.

TABLE VII-IV

CARBON-REFLECTED BLANKET

Outside Radius (cm)	Composition[a]
199.9	Void
200.0	Li
201.0	50% Li, 50% SS[b]
230.0	Li
232.0	50% Li, 50% SS
262.0	68.6% Th, 16.5% Li, 14.9% SS
282.0	C
284.0	50% SS, 50% Li
292.0	Li
296.0	SS

[a]Compositions in vol%.
[b]SS = stainless steel.

TABLE VII-V

SUMMARY OF BLANKET NEUTRONICS EVALUATION

Case	Beryllium Multiplier (cm)	Breeding Region 1	Breeding Region (Vol%) 2		R_T	R_F	Q (MeV)	$180\,R_F/Q$
1	4	---	12 Th	50 cm thick	1.1	0.30	22	2.5
2	11	---	69 Th		1.1	0.78	35	4.1
3	4	20 cm Li	69 Th		1.1	0.71	28	4.6
4	---	29 cm Li	69 Th		1.1	0.67	27	4.6
5	---	29 cm Li	69 Th 30 cm 100 C 20 cm		1.1	0.63	26	4.4

The minimum pellet gain requirement for electrical self-sufficiency can be estimated from an energy balance, i.e.,

$$P = f\,G\,E_L\,\eta_L\,\eta_B\,\eta_{th}(0.2 + 0.8\,M_B) - f\,E_L \quad .$$

where P is the net electric power produced by the fuel factory, f is the microexplosion repetition rate, G is the pellet gain (thermonuclear energy released/laser energy on target), E_L is the electric energy input to the laser per pulse, η_L is efficiency of the laser system, η_B is the beam transport efficiency, η_{th} is the thermal-to-electric conversion efficiency, and M_B is the blanket energy multiplication factor. For electrical self-sufficiency, P = 0. Inserting estimates of $\eta_L = 0.06$, $\eta_B = 0.95$, $\eta_{th} = 0.33$, and $M_B = 2$, we find $G \geq 30$. Thus, electrically self-sufficient fissile-fuel factories can operate with relaxed pellet gain requirements compared to pure commercial fusion for which $G \geq 100$.

The number of converter reactors with a thermal power equivalent to the thermal power of the fissile-fuel factory at 100% burnup is

$$N_{equiv} = R_F\eta_R(E_{fiss}/E_{fus})/(1 - C)(0.2 + 0.8\,M_B) \quad ,$$

where R_F is defined as above, η_R is the efficiency of recovery of fissile material from the blanket, E_{fiss}/E_{fus} is the ratio of energy release of fusion events to fission events, and C is the reactor conversion ratio. Inserting $R_F = 0.65$, $\eta_R = 0.90$, $E_{fiss}/E_{fus} = 180/17.6$, $M_B = 2$, and $C = 0.9$, we find $N_{equiv} = 33$.

We have coordinated the investigation of specific engineering features by means of a generic point design. Areas receiving our attention included the fusion driver or core, blanket geometry and construction, materials selection, heat-removal considerations, and system layout.

The metallic thorium is contained in 0.38-mm-thick stainless steel cladding. The outside diameter of the fuel pins is 13 mm; they are supported in hexagonal modular arrays of 37 fuel pins each. The minimum pitch-to-diameter ratio of the fuel pins is 1.05. Each module is cooled by liquid lithium at an inlet temperature of 773 K and an inlet velocity of 1 m/s, the maximum time-averaged thorium centerline temperature is 780 K, and the time-averaged outlet temperature is 778 K. Compared to the requirements of net-electric-power producing blankets, the heat-removal requirements of electrically self-sufficient fissile-fuel factories are moderate.

Figure VII-4 shows the layout of a generic system. Two square modules and eight hexagonal modules contain lithium-cooled thorium. The remaining four lithium-cooled square modules of the truncated octahedron are dedicated to pellet injection (1), beam transport (2), and cavity exhaust (1). The entire assembly is enclosed in a shielded cell with remote manipulators for blanket-module assembly and disassembly.

Our studies have established that a CO_2-laser-driven lithium wetted-wall ICF fissile-fuel factory concept is technically feasible. Neutronics calculations have shown that lithium prebreeding regions or beryllium multipliers offer a high output of fissile material with minimum

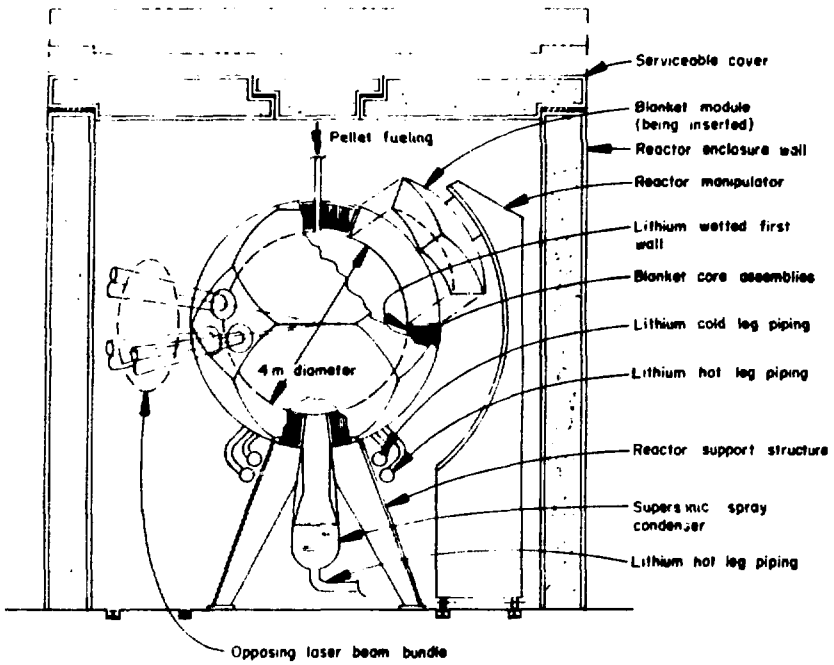

Fig. VII-4.
Low-power-density hybrid reactor design using lithium wetted-wall protection concept.

residual heat. Engineering studies have identified a consistent system of ICF core, conversion blanket, and heat-removal components.

INTEGRATED PLANT DESIGN STUDIES

Introduction

We are studying three commercial applications of laser fusion: (1) electric-power generation, (2) synthetic-fuel (hydrogen) production, and (3) fissile-fuel production. Integrated plant systems for these applications are described by the computer model TROFAN, in which plant subsystems are described analytically, and important parameters may be varied for design tradeoff and optimization studies.

We have previously defined preliminary electric generating plant concepts[14] based on lithium wetted-wall and magnetically protected wall reactor concepts. Our current efforts include updating TROFAN with more definitive analytical models of reactor concepts and electric generating plant subsystems, and by incorporating a capital cost data base, being developed under contract by Burns and Roe, Inc., Oradell, New Jersey.

Our hydrogen production studies are coordinated with a parallel study, also supported by the Office of Fusion Energy, on thermochemical hydrogen production using a tandem-mirror reactor as a fusion energy source. This study is further supported at LASL by the Division of Energy Storage for experimental verification of our bismuth-oxide electrothermochemical cycle. Our studies include integration of the electrothermochemical process with the high-temperature lithium boiler concept described above, and the production of hydrogen by high-temperature electrolysis.

Reported below are results from our studies of electric-power generation and hydrogen production.

Electric-Power Generation (E. M. Leonard, J. H. Pendergrass)

We are extensively modifying our laser fusion systems code TROFAN. The modifications involve improvements in our criteria for determining reactor cavity sizes and structural requirements. Cavity sizing is based on allowable temperature rises in cavity structures, allowable rates of material loss from surfaces by evaporation and

sputtering, and times required for restoration of cavity conditions to those necessary for initiation of the next pellet microexplosion. Cavity structural requirements are based on calculated loads. The loads considered are pellet debris impact, blast-wave reflections, evaporation and sputtering recoil, blanket thermal expansion, static pressures, and thermal stresses.

TROFAN is also being restructured to be compatible with a capital cost account structure for laser fusion, which we have developed, and with a capital cost and cost-scaling-law data base being developed for us by Burns and Roe, Inc. The cost data base and cost-scaling laws are for laser fusion electric-power generating stations incorporating the lithium wetted-wall and magnetically protected wall reactor concepts. We adapted a list of cost accounts for laser fusion power plants from a list of capital-cost accounts, which was developed for magnetic confinement fusion for uniform use throughout the magnetic-confinement fusion community to report capital-cost estimates. This cost account system is a modification of earlier fossil-fuel and fission power-plant capital-cost account lists.[15,16] The modifications involved the addition of accounts to cover features peculiar to laser fusion and the elimination of accounts that cover items peculiar to magnetic confinement fusion.

Costs are expressed in 1978 dollars for a mature fusion-power-plant construction industry. While costs representative of the time frame of a mature fusion economy are desirable, uncertainties associated with the projection of costs so far into the future are too great to justify such attempts and they were not made. However, other advanced technology is subject to similar cost escalation, and cost comparisons made in terms of current dollars are reasonable, especially if periodically updated. Wherever the development of completely new technology is involved and technological barriers to construction of facilities or manufacture of equipment with required characteristics at acceptable costs based on present industrial capabilities were perceived, an effort was made to determine whether the technological barriers are insurmountable (e.g., due to obvious materials limitations) or can be eliminated (e.g., by constructing manufacturing facilities of increased capacity).

Design tradeoff and parameter studies, for which the cost data base will be used, require cost-scaling information, rather than cost estimates of point designs, over wide ranges of principal plant parameter values, some of which are listed in Table VII-VI. The cost-scaling equations were developed to involve as few parameters as possible consistent with high accuracy for futuristic technology at the conceptual stage of development to provide compatibility with a systems code of manageable proportions.

Initially, we hoped that for each reactor concept, a single cost-scaling law could be developed for each plant component or system, which would cover the entire plant parameter space of interest. Such laws would involve

TABLE VII-VI

RANGES OF SOME PRINCIPAL ELECTRIC POWER PLANT PARAMETERS COVERED BY THE COST DATA BASE

	Wetted-Wall Reactors	Magnetically Protected Wall Reactors
Number of reactor cavities	1-20	1-4
Cavity thermal powers (MW)	150-3000	750-6000
Laser amplifier pulse repetition rate (Hz)	1	10
Laser amplifier pulse total energy, (MJ)	1-5	1-5
Nominal plant net electric-power output (MWe)	1000-2000	1000-2000
Reactor materials of construction	Stainless steels and refractory alloys	Stainless steels and refractory alloys

scaling relative to a single-point plant design for each reactor concept. However, large changes in plant capacity and/or in the number of reactor cavities within the ranges of interest necessitated qualitative as well as quantitative changes in plant layout, plant equipment, and facility conceptual design. In addition, the ranges of parameter values for which accepted scaling laws or new scaling laws developed during the present study are accurate about point designs are quite limited. Therefore, more than one conceptual point design, plus scaling about the point designs, for the two reactor concepts proved necessary for accurate coverage of the entire parameter space of interest. The point conceptual designs upon which the scaling laws are based are (1) a 3000-MWt plant with 20 wetted-wall reactor cavities, (2) a 3000-MWt plant with 4 wetted-wall reactor cavities, (3) a 3000-MWt plant with 1 wetted-wall reactor cavity, (4) a 5600-MWt plant with 4 magnetically protected wall reactor cavities, and (5) a 5600-MWt plant with 1 magnetically protected wall reactor cavity.

Different approaches were used to develop the cost data for various plant facilities, components, and systems. For some, especially those peculiar to laser fusion and involving technology that is only in the conceptual stage, more detailed conceptual designs were developed and basic unit material, fabrication, assembly, and installation costs were estimated. For example, raw-materials costs for large refractory-metal reactor vessels were obtained from suppliers, and fabrication, assembly, and installation costs were based on information from various manufacturers, reviews of published information, and Burns and Roe in-house expertise. Fabrication costs for such vessels include assembly (primarily by welding using advanced technology such as electron beams or lasers) of factory-constructed subassemblies in the reactor service building or wing, and final assembly in reactor cells. Because the same facilities and equipment are required for scheduled maintenance and repair of damaged equipment, their cost is included in a maintenance equipment account.

In other cases, e.g., for such relatively conventional plant equipment as turbine generators and steam generators, design and cost information was obtained from manufacturers. Designs for some major plant systems, e.g., ultimate heat rejection, service cooling water, chilled water, emergency tritium removal, radwaste, and building service systems, which are relatively conventional and insensitive to nuclear island characteristics, were adapted from existing facilities and designs, such as 1000-MWe light-water reactor and breeder-reactor power plants, and costs for such systems were appropriately adjusted.

The scope of the data base includes two steam cycles, one subcritical with maximum temperature of 730 K and pressure of 2270 psia, and the other, an 810 K, 3500-psia supercritical cycle. Cost data were developed for only a single type of bred-tritium recovery system, refractory-metal tritium windows, and a single type of ultimate heat-rejection system—dry cooling towers.

Synthetic-Fuel (Hydrogen) Production (J. H. Pendergrass)

Based on a preliminary investigation of applications of fusion energy to hydrogen production by thermochemical water splitting,[17] we conclude that tritium must be bred in the high-temperature blanket zone if a tritium breeding ratio BR >1 and a fraction of high-temperature thermal energy >0.5 is to be attained. In this study[17] of a provisional blanket concept, tritium breeding was accomplished in a low-temperature zone, and high-temperature heat was generated in a separate graphite zone. The high-temperature heat was transferred to the thermochemical process via a helium coolant loop.

The constraints that all tritium breeding be accomplished in a low-temperature blanket zone and that BR ≥ 1 result in the conversion of only 33.8% of fusion reactor energy release to stored chemical energy of hydrogen. In addition, 8.7% of total energy release is exported as electric power if low-temperature heat or electric power generated from this heat cannot be used to drive the thermochemical cycle.

Although the provisional blanket concept does not permit a good match between fusion-energy delivery characteristics and thermochemical-cycle energy requirements, indications are that the combination is competitive with other nuclear-energy-driven synthetic-fuel production concepts. Furthermore, the high-temperature lithium-boiler concept described above offers the possibility of a better match between energy delivery characteristics and energy requirements.

A fusion-energy synthetic-fuels econometric model[17,18] was developed as part of this study to facilitate examination of the tradeoffs arising from considerations of tritium breeding, electric-power production, and hydrogen production. Important conclusions were

- The lowest hydrogen production costs are achieved with plants that do not export electricity.

- Hydrogen production cost depends on thermochemical-cycle efficiency in a roughly hyperbolic fashion, so that high efficiency in the thermochemical portion of the plant is essential for low-cost production.
- Hydrogen production cost increases approximately linearly with capital costs of fusion-energy source, electric generating plant, and thermochemical plant, with the first projected to be the highest.
- If other chemical fuels are available at low cost, or if electricity can be freely substituted for hydrogen energy, a selling price for hydrogen commensurate with its energy content alone would make electric-power production more attractive in an infinite market situation. However, the first circumstance is not projected to continue for long; free substitution of electricity for hydrogen as a chemical feedstock is not possible; and substitution for many hydrogen fuel uses may not be economic.
- Despite inevitable uncertainties, comparison with published hydrogen production cost estimates using light-water fission reactors (LWRs), high-temperature fission reactors (HTRs), and liquid-metal-cooled fast breeder reactors (LMFBRs) as energy sources, as well as conventional electrolysis, advanced electrolysis, or thermochemical cycles for water-splitting suggests that fusion-driving of our reference cycle will be competitive, with HTRs combined with a pure thermochemical cycle offering the most formidable competition.

Our reference thermochemical cycle,[19] illustrated schematically in Fig. VII-5, consists of six basic steps: (1) production of hydrogen (H_2O) and aqueous sulfuric acid (H_2SO_4) by electrolysis of aqueous sulfur dioxide (H_2SO_3) at low temperature (~300 K); (2) reaction of solid bismuth oxide (Bi_2O_3) with aqueous sulfuric acid to form bismuth oxide sulfate ($Bi_2O_3 \cdot 3\ SO_3$) and liberation of water (H_2O) at low temperature (~300 K); (3) thermal decomposition of bismuth oxide sulfate to reform the bismuth oxide and release sulfur trioxide (SO_3) at higher temperature (maximum, ~1250 K); (4) thermal decomposition of sulfur trioxide (SO_3) to sulfur dioxide and oxygen at highest cycle temperature (maximum, 1450 K); (5) rapid quenching of the dissociated gas mixture to prevent back reaction, followed by separation of sulfur dioxide and oxygen; and (6) formation of sulfurous acid by dissolution of the sulfur dioxide in water to close the cycle.

A preliminary conceptual process design was developed for our reference cycle to permit preliminary estimation of thermal efficiency and future hydrogen production cost if this cycle continues to be promising. Except for the electrolyzers, the low-temperature operations are relatively conventional. Similarly, many of the high-temperature steps of the cycle also involve standard process technology, with a few important exceptions. Inadequate thermodynamic, kinetic, solids-characteristics, and materials-compatibility data made necessary a number of assumptions and approximations, which may not be very accurate when experimental data from the concurrent experimental program at LASL become available.

Although the reference cycle still appears promising, the process design exercise has revealed a few shortcomings, but lack of data makes assessment of the seriousness of these shortcomings impossible. Alternatives, described in Table VII-VII, within the bismuth oxide cycle family, in which fewer than three sulphur trioxide groups are added to and removed from the bismuth oxide molecule, permit avoidance of some of these potential problems at a cost primarily of increased solids circulation. Process designs for these alternative cycles are partially completed.

ENGINEERING DEVELOPMENT STUDIES

Introduction

Our engineering development studies include the assessment of advanced technologies unique to long-life, high-repetition-rate ICF subsystems, and the analysis and development of conceptual subsystems for inclusion in our integrated plant systems studies. These studies include methods of increasing the overall efficiencies of CO_2 laser systems, laser gas-handling and cooling systems, pulsed-power systems, pellet injection/tracking and beam firing synchronization, beam transport, and pellet fabrication.

Reported below are results from our studies on increased efficiency of energy extraction in CO_2 lasers and on lifetimes of cryogenic pellets in a reactor environment, and from a study under contract to United Technologies Research Center (East Hartford, Connecticut) on pellet injection, tracking, and laser-beam synchronization.

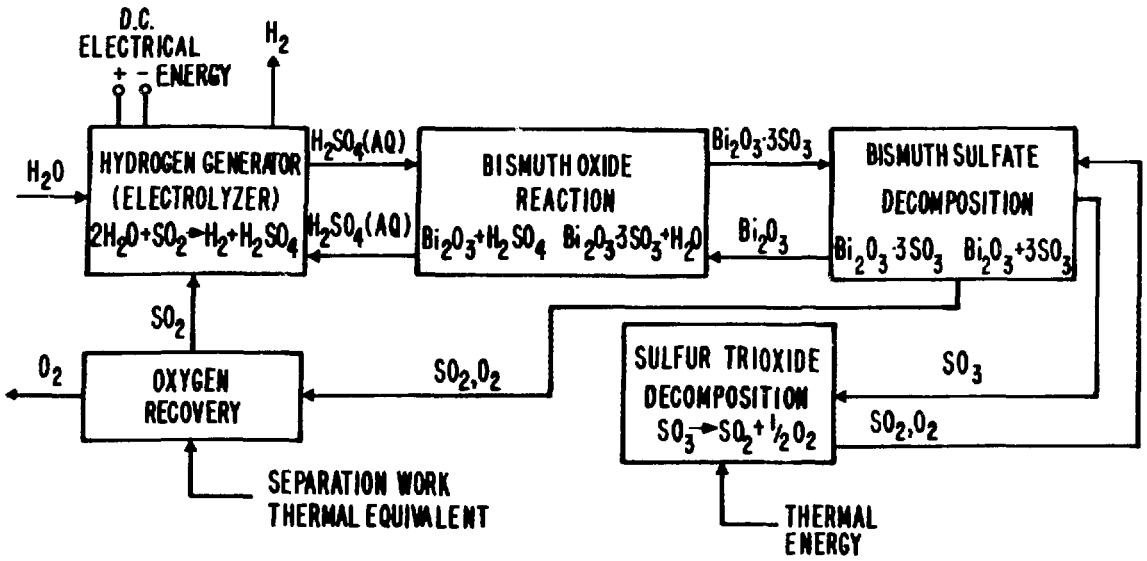

Fig. VII-5.
Bismuth-sulfate/sulfuric-acid hybrid thermochemical hydrogen cycle.

TABLE VII-VII

REFERENCE ELECTROTHERMOCHEMICAL BISMUTH OXIDE SULFATE CYCLE AND ALTERNATIVES WITHIN THE SAME FAMILY[11]

Alternative Number	Reactions Involving Bismuth Oxide and Bismuth Oxide Sulfates	Sulfuric Acid Concentration Required for Sulfur Trioxide Addition Step (wt%)	Required Solids Circulation Rate (mols Solids Circulated per mol H_2 Produced)	Molten Salts Must be Handled at High Temperature
1	$Bi_2O_3\ 3SO_3(s) \rightarrow Bi_2O_3(l)+3SO_3(g)$ $Bi_2O_3(s)+3H_2SO_4(aq) \rightarrow Bi_2O_3\ 3SO_3(s)+3H_2O(l)$	53-59	1/3	yes
2	$Bi_2O_3\ 3SO_3(s) \rightarrow Bi_2O_3\ SO_3(?)+2SO_3(g)$ $Bi_2O_3\ SO_3(s)+2H_2SO_4(aq) \rightarrow Bi_2O_3\ 3SO_3(s)+2H_2O(l)$	53-59	2/3	?
3	$Bi_2O_3\ 3SO_3(s) \rightarrow Bi_2O_3\ 2SO_3(s)+SO_3(g)$ $Bi_2O_3\ 2SO_3(s)+H_2SO_4(aq) \rightarrow Bi_2O_3\ 3SO_3(s)+H_2O(l)$	53-59	1	no
4	$Bi_2O_3\ 2SO_3(s) \rightarrow Bi_2O_3(l)+2SO_3(g)$ $Bi_2O_3(s)+2H_2SO_4(aq) \rightarrow Bi_2O_3\ 2SO_3(s)+2H_2O(aq)$	5-20	2/3	yes
5	$Bi_2O_3\ 2SO_3(s) \rightarrow Bi_2O_3\ SO_3(?)+SO_3(g)$ $Bi_2O_3\ SO_3(s)+H_2SO_4(aq) \rightarrow Bi_2O_3\ 2SO_3(s)+H_2O(l)$	5-20	1	?
6	$Bi_2O_3\ SO_3 \rightarrow Bi_2O_3(l)+SO_3(g)$ $Bi_2O_3(s)+H_2SO_4(aq) \rightarrow Bi_2O_3\ SO_3(s)+H_2O(l)$	5	1	yes

Energy Extraction with Long Pumping Discharges (H. C. Volkin)

Pulsed-power systems tend to be cheaper and more reliable as the required pulse duration increases and the delivered voltage decreases. This consideration favors long discharge times in pulsed electrical excitation of gas lasers and is compatible with multiple optical-pulse energy extraction in CO_2 laser amplifiers. In multipulse laser operation, a sequence of two or more light pulses passes through the amplifier in the time interval between the start of successive electrical discharges. Between optical pulses, amplifier gain is restored by vibrational

relaxation and (within the discharge time) by further discharge pumping. Laser efficiency can be increased because vibrational energy stored in the nitrogen of the lasing gas mixture and in the higher levels of the CO_2 asymmetric-stretch (AS) mode can be extracted by later pulses and because less excitation energy in the AS mode is lost by intramolecular transfer to the other modes of CO_2. The gain recovery time is the time required after an optical pulse has traversed the amplifier for the gain to reach its maximum value in the absence of any external pumping. The rate parameters for vibrational energy transfer are temperature-dependent. Hence, gain recovery time varies somewhat with the translational temperature and the modal vibrational temperatures.

A given gas mixture has an optimum ratio of electric field E to molecular number density N for efficient discharge pumping. The pressure-scaling law for electrical excitation kinetics can be stated as follows. With a given gas mix and value of E/N, if energy deposition per unit volume W_o and population inversion density ΔN_o occur at the pressure P_o in a time T_o with the current density J_o, then at pressure P in the time $(P_o/P)T_o$ with the current density $(P/P_o)J_o$, the energy deposition is $(P/P_o)W_o$ and the inversion density is $(P/P_o)\Delta N_o$. Because an optical cross section at pressure P differs by the factor (P_o/P) from that at P_o, the saturation energy at P differs by the factor P/P_o, but the small-signal gain coefficient is the same. Under this pressure scaling, the efficiency of converting electrical energy to energy stored in the inversion remains constant. A known discharge efficiency at some higher pressure carries over to a lower pressure with the indicated increase in discharge time, along with the proportionate decrease in E and J. However, the smaller inversion density obtained at the lower pressure necessitates a correspondingly larger volume of laser gas to produce a given laser output energy.

To assess the laser-system tradeoffs involved in these considerations, parameter studies were made to determine laser efficiencies, multipulse sequencing, and optical pulse energies associated with long discharge times. In all cases the fill pressure and temperature were 760 torr and 300 K; the discharge time was ~4 μs, and the first optical pulse occurred when the gain coefficient reached 2%·cm^{-1}. We assumed that energy extraction occurred only on the 10.6-μm band, but that all the available energy was extracted by each pulse. For each gas mix, current densities of 6, 4, and 2 A·cm^{-2} were considered, and three time periods used between successive optical pulses were 0.2, 0.4, and 0.8 μs. With the longer interpulse periods, fewer pulses are obtained with generally higher average energies. Smaller current densities also lend themselves to fewer optical pulses, because the gain coefficient reaches 2%·cm^{-1} later in the discharge and less energy is deposited in the gas. Of four gas mixes investigated, the mixture 3:1:1::He:N_2:CO_2 gave good efficiency with a 0.5-μs discharge time and 20 A·cm^{-2} at 1800 torr. In addition, three helium-free N_2:CO_2 mixes, namely, 0:1:4, 0:1:2, and 0:1:1, were examined to provide data for tradeoffs involving the cost reduction inherent in eliminating helium from the system.

We define a single-pulse efficiency for a given case as the efficiency obtained under the following circumstances: the discharge continues until the gain reaches the peak value that can occur under the prescribed conditions, at which point all the energy available on the 10.6-μm band is extracted by the single optical pulse. The single-pulse efficiencies for the various gas mixes are 3.71% (3:1:1), 3.05% (0:1:1), 3.58% (0:1:2), and 3.77% (0:1:4). Typical gain recovery times are shown in Table VII-VIII.

If no restriction is placed on the number of pulses, the 3:1:1 mix is again markedly superior in efficiency to the helium-free mixes. Limiting the number of pulses by the requirement that the energy of the final pulse be about half that of the initial pulse, we find that efficiencies around 22% are attainable with the 3:1:1 mix in 12 to 14 pulses with an interpulse period of 0.4 or 0.2 μs. This corresponds to a sixfold increase over single-pulse efficiency. By comparison, efficiencies around 16% are obtained with 0:1:1 in 17 pulses (0.2-μs period), and with 0:1:2 in 16 pulses (0.2-μs period). In all these cases, the discharge current was 4 A·cm^{-2}; the efficiency and pulse energy (J/ℓ·atm) at various pulse times are shown in Table VII-IX.

TABLE VII-VIII

GAIN RECOVERY TIMES FOR GAS MIXTURES AT VARIOUS TEMPERATURES

He:N_2:CO_2 Mix	Gain Recovery Time (μs)
3:1:1	0.83 (312 K) 0.71 (330 K)
0:1:1	0.27 (301 K) 0.19 (315 K)
0:1:2	0.24 (301 K) 0.18 (318 K)
0:1:4	0.17 (304 K) 0.12 (322 K)

TABLE VII-IX

SOME EFFICIENT MULTIPLE-PULSE ENERGY EXTRACTION SEQUENCES[a]

	Pulse Number (in Parentheses), Efficiency (%), and Pulse Energy (J/ℓ·atm) for $He:N_2:CO_2$ Mix			
	3:1:1	3:1:1	0:1:1	0:1:2
Discharge Current (A cm^{-2})	4	4	4	4
Energy Deposition (J/ℓ-atm)	92.4	92.4	162	134
Interpulse Period (μs)	0.2	0.4	0.2	0.2
	(1) 5.04,1.99	(1) 5.04,1.99	(1) 5.12,2.08	(1) 6.04,2.27
	(2) 8.26,1.64		(2) 8.24,1.93	(2) 9.45,1.93
	(3)10.6,1.50	(2) 8.15,1.94	(4)11.7,1.76	(3)11.5,1.72
	(5)13.9,1.39	(3)10.4,1.98	(6)13.4,1.62	(5)13.7,1.45
	(7)16.2,1.34	(4)12.0,2.02	(8)14.4,1.51	(7)14.7,1.30
	(9)17.8,1.31	(5)13.4,2.06	(10)148,1.42	(9)15.2,1.20
	(11)190,1.29	(6)14.5,2.08	(12)15.1,1.33	(11)154,1.13
	(12)195,1.28		(14)15.1,1.26	(13)155,1.07
	(13)208,1.14	(7)15.4,2.11	(16)15.1,1.18	(15)154,1.02
	(14)219,0.98	(8)17.4,1.85	(17)15.7,0.95	(16)160,0.73
	(15)229,0.83	(9)19.1,1.54	(18)16.1,0.72	
		(12)224,0.83		

[a]Efficiency and pulse energy are given for selected optical pulses in a sequence, where the pulse number is shown in parentheses. Pulses in the discharge time occur between the double horizontal lines, and their efficiencies refer to the cumulative electrical-to-optical efficiency up to the time of the pulse.

At 9 or 10 optical pulses, efficiencies of 19 to 20% can be attained with the 3:1:1 mix by using an interpulse period of 0.4 μs and a discharge current of 4 A·cm^{-2}. With helium-free mixes, an efficiency of 15.5 to 16% is found with the 0:1:1 mix using a period of 0.2 μs and 2 A·cm^{-2}, and 13.5 to 14% is found with the 0:1:2 mix using 0.4 μs and 4 A·cm^{-2}. If four or five optical pulses are desired, then 2 A·cm^{-2} and interpulse periods of either 0.4 or 0.8 μs give efficiencies of 14 to 16.5% with 3:1:1, and 11 to 12% with either 0:1:1 or 0:1:2 mixes.

Cryogenic Pellet Lifetimes and Temperatures (J. J. Devaney)

Lifetimes of several typical cryogenic pellets were calculated for several customary environments inside and outside laser fusion reaction chambers. Optimum cooling and resulting temperatures of multishell pellets were computed. Pellets of 50:50 at.% solid D:T generally contain 31 to 46% of the DT in the form D_2, so that pellet destruction commences when the D_2, which has the lowest triple point, begins to melt. The triple point of D_2 is 18.71 K. Heat mechanisms affecting the pellet are internal tritium radioactivity, external radiation into the pellet, forced convection, and conduction into the pellet.

Although the beta radioactivity of tritium is exceedingly weak, with a half-life of 12.26 yr and a mean beta particle energy of only 5.7 keV, attempting to keep a tritium-containing pellet at very low temperatures—where the efficiencies of radiative and conductive cooling as well as the heat capacities are extremely low—is difficult and in some cases impossible. Radiation, of course, varies as absolute temperature to the fourth power; specific heats of crystalline (Debye) solids drop as temperature to the third or higher power at low temperatures; below 4 K the

conduction-electron contributions to the specific heat are significant and are proportional to temperature; the specific heats of many plastics are roughly proportional to temperature over a wide low-temperature range; and last, low-temperature thermal conductivities all show decreases with decreasing temperature, very roughly directly proportional to the temperature. In fact, radiation-cooling has dropped to such a low level around 4 to 20 K that typical pellet designs containing appreciable amounts of solid DT within a vacuum cannot exist at all. Steady-state DT temperatures calculated for such pellets at absolute zero in vacuum range from 88 to 114 K, well above the D_2 triple point.

Such pellets, therefore, need direct cooling of inner DT-containing structures and have lifetimes away from such cooling of typically 26 to 80 s if initially at 10 K, and of 30 to 95 s if initially at 4.2 K. However, in multishell pellets, even a low-density interstitial gas such as hydrogen or helium is very effective in cooling inner shell structures. Ironically, too low a coolant temperature will condense too much of the conductive gas, and so allow inner DT structures to melt. For example, one of our pellet designs will survive only if the outer shell structure is kept between 7.9 and 18.2 K. In this design the minimum inner DT temperature of 9.4 K is achieved for an outer cooling bath of 9.0 K. All other coolant temperatures lead to a higher inner DT temperature.

The high external temperatures of a laser fusion reactor cavity further restrict the lifetime of a pellet. However, the pellet designer has considerable control over the melting of restrictive parts, i.e., solid DT, by rather modest pellet design changes. For example, by aluminizing exposed plastic parts, he can reduce the acquisition of radiative energy, or by using low-conductivity materials, he can restrict the heat flow; these changes can account for extensive lifetime changes. We examined the survival of laser fusion pellets in two extreme reaction-chamber atmospheres, marking the upper and lower bounds of expected chamber lifetimes for the pellets investigated, namely, 10^{17} atom/cm^3 of argon at 773 K and a vacuum at the same temperature. A high pellet injection speed of 13 700 cm/s was assumed. We found that Rayleigh-Benard instabilities do not develop and that all relevant flows are laminar. Our worst case, a pellet moving at 13 700 cm/s in 10^{17} atoms/cm^3 at 773 K with sensitive areas exposed and with an initial temperature of 10 K, will last 0.048 s. A protected pellet (aluminized, baffled—best case for this general design) will live 64 s in a 773 K vacuum if initially at 10 K.

Pellet Injection and Tracking (J. J. Devaney)

A preliminary investigation of potential pellet and laser beam space-time interaction systems for inertial confinement fusion reactors, with emphasis on CO_2 laser-driven reactors, was completed under contract to United Technologies Research Center.[20]

We examined the synchronization requirements; velocity requirements; accelerators, including gravitational, mechanical, pneumatic, and electrical; tracking, including accuracy required, degrees of freedom, measurement resolution, reference frame stability, and some merits of tracking both within and without the chamber; guidance, including trajectory correction required, types of guide tubes, and electrostatic guidance; beam pointing, including active-optics techniques and capabilities and nonlinear phase conjugation; and pellet velocity tradeoffs. Three systems that may have merit were identified: (1) adaptive laser optics operated in a predictive mode, with pellet tracking inside and outside the reactor; (2) feedback-controlled electrostatic guidance of the pellet, with high-precision tracking and guidance external to the reactor; and (3) a combined adaptive optics-electrical guidance system, with relaxed operating parameters for both subsystems. The primary critical issue was identified as the ability to make the position and velocity tracking measurements with the required speed and accuracy. Other critical issues include reference frame motion, injector accuracy, and injector reliability.

Based on the information developed in this study, system recommendations shown in Table VII-X are made for 100-m/s injection velocities. Such high velocities are needed if high repetition rates are desired. The preferred system uses adaptive optics to point and focus the laser beams on the pellet. Due to insufficient slew rate, the adaptive optics must operate in the predictive mode, whereby the pellet trajectory at the focus is predicted based on precise tracking data, and the laser beams are aimed and focused before the arrival of the pellet at the focal region. Errors between tracking and adaptive-optics reference frames (due to, e.g., noise and vibration) are assumed to be less than errors in trajectory measurement. In practice, this implies active tracking between reference frames and precise autoalignment of all beams. Guidance in this system is provided only by the rough constraint of inherent angular scatter of the pellet accelerator imposed by a mechanical guide tube. The accelerator is a pneumatic gas gun, and pellets are

TABLE VII-X

PELLET/LASER BEAM SPACE/TIME SYSTEM RECOMMENDATIONS
(Pellet Velocity, 100 m/s)

	Recommended			Not Recommended	
Beam Pointing	Active	None	Active	Active	Phase conjug.
Mode	Predictive	Predictive	Predictive	Active	Passive
Guidance	Guide tube	Electro-static	Electro-static	None	Guide tube
Tracking	Inside & outside	Outside	Inside & outside	Inside & outside	Inside
Propulsion	Pneumatic	Pneumatic	Pneumatic	Pneumatic	Pneumatic

tracked both outside and inside the reactor for adaptive optics control and synchronization of laser fire. Some autoalignment and initial trajectory measurement requirements are relaxed if final tracking can be performed inside the reactor through each beam line using shared apertures.

An alternative system with fixed optics relies on electrostatic guidance of electrically charged pellets to place pellets on the correct trajectory to pass through the focal region. The tracking requirements on this system are very severe and must be sufficiently precise to function solely on measurements outside the reactor.

A hybrid system that combines adaptive optics and electrostatic guidance is also possible. This approach relaxes performance requirements on both systems, but at the cost of increased system complexity.

The above system recommendations are based on the assumption that the injection velocity is 100 m/s. If the reactor could be designed so that the injection velocity were significantly reduced, then the above conclusions would be altered. Such a design would change the means of (1) propulsion, (2) tracking, and (3) pellet irradiation.

If the injection velocity were 25 m/s or less, gravitational acceleration is a reasonable and preferred means of target propulsion. (A velocity of 25 m/s requires a drop tower of only 32 m in height.) Pellet motion during a pulse round trip through the laser system (which takes 2 μs) would be 50 μm or less so that phase conjugation—passive focusing by nonlinear optics—is not ruled out on the basis of pellet motion.

If the injection velocity were ~10 m/s or less, the required mirror slew rates are low enough so that actively tracking adaptive optics could be used for pellet trajectory-beam direction relative angles of less than 10°. This case would apply to each beam in the polar illumination case when the pellet is injected along the beam-direction axis. Autoalignment system requirements would again be eased by shared aperture tracking on all beams, but in addition, low pellet velocity would eliminate the need to predict pellet position at the focus and should produce more accurate pellet irradiation.

Pellet tracking and trajectory measurement requirements are greatly eased by lower velocities. The time interval during which position determination must be made increases and the accuracy with which the velocity must be measured may decrease. This last factor increases the feasibility of a system that does not include tracking inside the reactor for synchronization. At lower velocity, the voltage or the length of the guide-plate region required to electrostatically correct trajectory errors, is also less.

In summary, many benefits in reducing pellet injection system complexity and cost would be derived from lower pellet injection velocities. Furthermore, the nature of the preferred system is a strong function of pellet velocity.

Finally, this preliminary study should be interpreted as a first exploration of conventional state-of-the-art techniques, and not be considered a definitive review of all possibilities including highly innovative techniques.

REFERENCES

1. L. A. Booth, Comp., "Central Station Power Generation by Laser-Driven Fusion," Los Alamos Scientific Laboratory report LA-4858-MS, Vol. 1 (February 1972).

2. J. J. Devaney, "Magnetically Protected First Wall for a Laser-Induced Thermonuclear Reaction," Los Alamos Scientific Laboratory report LA-5699-MS (August 1974).

3. "Inertial Fusion Program, July 1—December 31, 1978," Los Alamos Scientific Laboratory report LA-7587-PR (May 1980).

4. R. W. Conn et al., "Solase, A Conceptual Laser Fusion Reactor Design," University of Wisconsin report UWFDM-220 (December 1977).

5. I. O. Bohachevsky and J. F. Hafer, "Sputtering Erosion of Fusion Reactor Cavity Walls," Los Alamos Scientific Laboratory report LA-6633-MS (December 1976).

6. I. O. Bohachevsky and J. F. Hafer, "Dependence of Sputtering Erosion on Fuel Pellet Characteristics," Los Alamos Scientific Laboratory report LA-6991-MS (November 1977).

7. "Laser Fusion Program at LASL, January 1—June 30 1977," Los Alamos Scientific Laboratory report LA-6982-PR (April 1978), p. 135.

8. S. Chow and I. O. Bohachevsky, "MHD Deceleration of Fusion Reaction Products," Los Alamos Scientific Laboratory report in preparation.

9. J. C. Goldstein, I. O. Bohachevsky, and D. O. Dickman, "Ion Motion in Laser Fusion Reactor Studies," Paper 9P7, Bull. Am. Phys. Soc., Series II 21 (October 1976).

10. G. A. DeMastry, "Corrosion Studies of Tungsten, Molybdenum, and Rhenium, in Lithium," Nucl. Appl. 3, 127 (1967).

11. Y. Amagi, Y. Nishimura, and S. Gomi, "Hollow Carbon Microspheres from Pitch Material and their Applications," Materials '71, 16th National Symp. and Exhibit. Soc. of Aerospace Material and Process Engineers, Anaheim, California (April 21-23, 1971), p. 315.

12. G. V. Fitzpatrick and E. J. Britt, "Thermionic Central Station Power—The THX Approach—Topical Report," Rasor Associates, Inc., report NSR 2-6 (February 1977).

13. T. G. Frank, "A Thorium-Uranium Cycle ICF Hybrid Concept," Proc. 3rd Topical Meeting on the Technology of Controlled Nuclear Fusion, Santa Fe, New Mexico (May 1978).

14. L. A. Booth and T. G. Frank, "Commercial Applications of Inertial Confinement Fusion," Los Alamos Scientific Laboratory report LA-6838-MS (May 1977).

15. "Guide for Economic Evaluation of Nuclear Power Plant Designs," NUS Corporation report NUS-S31 (January 1965).

16. United Engineers and Constructors, Inc., "1000-MW(e) Central Station Power Plants—Investment Cost Study," WASH-1230, Vols. I-IV (June 1972).

17. L. A. Booth, M. G. Bowman, G. E. Cort, K. E. Cox, D. J. Dudziak, R. A. Krakowski, J. H. Pendergrass, and A. S. Tar, "Production of Electrothermochemical Hydrogen using a Fusion Source of High-Temperature Process Heat," Proc. 3rd ANS Topical Meeting on the Tech. of Controlled Nuclear Fusion (to be published).

18. A. Tai and R. Krakowski, "Generalized Energy—Balance and Economic Considerations for Thermochemical Hydrogen Production from Fusion Reactor Blankets," Trans. Am. Nucl. Soc. Winter Meeting, Washington, DC (1978).

19. K. E. Cox, "Thermochemical Processes for Hydrogen Production," Los Alamos Scientific Laboratory report LA-6970-PR (October 1977).

20. R. G. Tomlinson et al., "Pellet and Laser Beam Space-Time Interaction System Study," UTRC R78-954373-1, Los Alamos Scientific Laboratory Contract LP8-2822E (November 1978).

VIII. RESOURCES, FACILITIES, AND OPERATIONAL SAFETY

The design and construction of HEGLF facilities continued. Safety policies and procedures continued to be successful in minimizing the hazards of operating high-energy lasers.

MANPOWER DISTRIBUTION

The distribution of employees assigned to the various categories of the DOE-supported Laser Fusion Research Program is shown below.

APPROXIMATE STAFFING LEVEL OF LASER PROGRAM

December 31, 1978

Tasks	Direct Employees
CO_2 Laser Development	77
CO_2 Laser Experiments	115
Target Design	27
Target Fabrication	41
Diagnostics Development	40
Systems and Applications Studies	8
Advanced Technology	3
Weapons Application	9
TOTAL	320

High-Energy Gas Laser Facility (HEGLF)

Construction Package I, including the laser building, the mechanical building, the office building, and a warehouse is 40% complete, with a scheduled completion date of September 1979.

Construction Package II, including the target building, the power-transmission system, and miscellaneous construction is 42% complete with a scheduled completion date of August 1979.

In the interest of continuity, we have presented details in HEGLF Design and Construction in Sec. II.

New Laboratories

The contract for the High-Voltage and Optical-Evaluation Laboratories was awarded in January 1978; construction is essentially complete, with a scheduled occupation date of January 22, 1979.

OPERATIONAL SAFETY

General

Laser Fusion Research Program activities have never caused biological damage to any employee from laser radiation. The excellent lost-time injury rate was also maintained, despite increased activities and additional staff.

Laser Protective Eyewear Movie

A 16-mm color movie, "Lasers and Your Eyes," was produced for indoctrination of new employees and for use by industry and Academe to demonstrate the potential ocular hazards of lasers and to share information about available protective eyewear developed in the Laser Fusion Program for lightweight corrective spectacles from a series of colored filter glass.

IX. PATENTS, PUBLICATIONS, AND PRESENTATIONS

PATENTS

Serial numbers, filing dates, patent numbers, and issue dates may not be shown for several months after they are assigned. Therefore, for any given period, cases may be missing from these listings if patent activity occurred late in the reporting period.

S. N. 928,027— "Laser Target Fabrication, Structure and Method for Its Fabrication," E. H. Farnum and R. J. Fries, filed July 25, 1978.

S. N. 942,227— "Enhancement of Laser Pulse Contrast Ratios Via Transient Response of Narrow Band Resonant Interferometers," R. A. Fisher and B. J. Feldman, filed September 14, 1978.

S. N. 945,376— "Fiber Optic Solid State Switch," M. E. Thuot, filed September 25, 1978.

S. N. 951,203— "Vacuum Aperture Isolator for Retroreflection from Laser-Irradiated Targets," R. F. Benjamin and K. B. Mitchell, filed October 13, 1978.

S. N. 951,543— "High Power Laser Amplifier," W. T. Leland and T. F. Stratton, filed October 13, 1978.

S. N. 960,410— "Beam Heated Linear Theta-Pinch Device for Producing Hot Plasmas," I. O. Bohachevsky, filed November 13, 1978.

PUBLICATIONS

E. R. Grilly, "Development of Cryogenic Targets for Laser Fusion," TIC (1977), 13 pp. MN, and Adv. Cryog. Eng. 23 (1978), pp. 676-81.

A. T. Lowe and R. J. Fries, "Plasma Polymerized P-Xylene as a Laser Fusion Target," Sur. Sci. 76, pp. 252-56.

K. B. Mitchell and R. P. Godwin, "Energy-Transport Experiments in 10 Micrometer Laser-Produced Plasmas," J. App. Phys. 49, pp. 3851-4.

K. B. Reipe and M. Kircher, "Design of the Energy Storage System for the High Energy Gas Laser Facility at LASL," Engineering Problems of Fusion Research 7th Symp. Proc. 2, M. S. Lubell, Ed., Knoxville, Tennessee (1977), pp. 1053-5.

B. E. Newnam and D. H. Gill, "Damage Resistance of Ar-Coated Germanium Surfaces for Nanosecond Carbon Dioxide Laser Pulses," TIC (1977), 19 pp.

B. E. Newnam, "Damage Resistance of Coated Optics for Pulsed Carbon Dioxide Lasers," SPIE, Proceedings of Optical Coatings—Applications and Utilization II, TIC (1978), 18 pp.

S. J. Gitomer, "Laser Induced Fusion, IEEE Minicourse, 2nd, Proc., G. H. Miley, Ed., Troy, New York (1977), pp. 10-20.

E. E. Bergmann, I. J. Bigio, B. J. Feldman, and R. A. Fisher, "High-Efficiency Pulsed 10.6 Micrometer Phase—Conjugate Reflection Via Degenerate Four-Wave Mixing," Opt. Lett. 3 (1978), pp. 82-4.

F. D. Wells and D. Remington, "Mirror Position Display Equipment for the Target Chamber Mirror Mounts of the 8-Beam Laser Fusion Research Facility," Cube Symp. Abst. J. J. Ruminer, Comp. (1978), pp. 81-2.

E. E. Stark, "Overview of Laser Fusion," Los Alamos Scientific Laboratory Mini-Review LASL-77-24 (1978).

M. J. Campbell, "Device for Microparticle Array Preparation," Rev. Sci. Instrum. 49 (1978), pp. 1488-9.

M. E. Thuot, "Fiber Optics and Microprocessors—A Control-System Solution for the Laser-Fusion Environment," TIC (1978), 16 pp.

J. E. Sollid, S. J. Thomas, E. Foley, and C. R. Phipps, "Threshold of Detection for Various Materials at 10.6 Micrometers," Appl. Opt. 17 (1978), pp. 2670-1.

J. J. Devaney, "Injection of Laser Fusion Pellets. Part 1. Accuracy Required, Acceleration, and Residual Gas Deflections," Los Alamos Scientific Laboratory report LA-7477-MS (1978).

J. E. Sollid, "Diffraction Measurement for LASL's Antares Laser System," Los Alamos Scientific Laboratory report LA-7443-MS (1978).

C. W. Cranfill, and R. More, "IONOS. A Fast, Analytic, Ion Equation-of-State Routine," Los Alamos Scientific Laboratory report LA-7313-MS (1978).

R. L. Whitman, R. H. Day, R. Kruger, and D. M. Stupin. "Analysis of Laser Fusion Targets Using Monochromatic X-Ray Microradiographs," Los Alamos Scientific Laboratory report LA-7534-MS (1978).

M. A. Stroscio, D. B. Henderson, and A. G. Petschek, "Numerical Computation of the Density Profile Produced by 10.6 Micrometer Irradiation of a Silicon Dioxide Microballoon," Nucl. Fusion 18 (1978). pp. 1425-30.

R. K. Ahrenkiel, "Properties of Cobalt Chromium Sulfide Applicable to Faraday Rotators for Carbon Dioxide Laser Systems," IEEE Trans. Magn. 14 (1978), pp. 454-6.

E. E. Stark, "Lasers and Power Systems for Inertial Confinement Fusion Reactors," TIC (1978), 24 pp.

E. E. Stark, "Carbon Dioxide-Laser Fusion," Proc. 13th Intersociety Energy Conversion Engineering Conf., August 20-25, 1978, pp. 1362-1365.

A. J. Scannapieco and E. W. Cranfill, "Derivation of the Physical Equations Solved in the Inertial Confinement Stability Code DOC," Los Alamos Scientific Laboratory report LA-7214-MS (1978).

W. T. Leland, "Design Engineering of Large High Pressure Gas Laser Amplifiers," TIC (1978).

W. T. Leland, "Advances in Laser Technology (Emphasizing Gaseous Lasers)," (Proc. SPIE Seminar, D. Finkleman, Ed., Washington, DC, 1978), pp. 38-45.

R. K. Ahrenkiel, J. F. Figueira, C. R. Phipps, and D. Dunlavy, "New Saturable Absorber for the Carbon Dioxide Laser Using Doped KCl," Appl. Phys. Lett. 33 (1978), pp. 705-7.

J. L. Lyman, R. G. Anderson, R. A. Fisher, and B. J. Feldman, "Absorption of Pulsed CO_2 Laser Radiation of SF_6 at 140 K," Optics Lett. 3 238 (1978).

J. E. Sollid, C. R. Phipps, Jr., and E. J. McLellan, "A Lensless Method of Measuring Gaussian Laser Beam Divergence," Appl. Opt. 17 3527 (1978).

PRESENTATIONS

The following presentations were made at the Annual Meeting of the Optical Society of America, San Francisco, California, October 30—November 3, 1978.

R. A. Fisher, E. E. Bergmann, B. J. Feldman, and I. J. Bigio, "Phase Conjugate Reflections at 10.6 μm via Intractivity Degenerate 4 Wave Mixing in Germanium."

S. C. Stotlar, E. J. McLellan, and A. J. Gibbs, "Ultra-Fast Pyroelectric Detectors for CO_2 Laser Measurements."

R. A. Fisher and B. J. Feldman, "Phase Conjugation in Inverted CO_2."

J. E. Sollid, "A Lensless Measurement of Gaussian Laser Beam Divergence."

W. C. Sweatt and V. L. Zeigner, "Antares Target System Optical Design."

D. M. Stupin, M. A. Winkler, M. J. Campbell, and R. Liepins, "Radiographic Selection of Laser Fusion Targets: Hollow Metal Shells and Plastic Coatings."

The following presentations were made at the 1978 International Laser Conference, Orlando, Florida, December 11-15, 1978.

R. K. Ahrenkiel, D. Dunlavy, J. F. Figueira, and C. R. Phipps, Jr., "A New 10.6 μm Saturable Absorber: KCl Doped with $KReO_4$."

S. J. Czuchlewski, E. J. McLellan, J. F. Figueira, E. Foley, C. E. Knapp, and J. A. Webb, "A High-Power (~10 GW) Short-Pulse (<1 ns) CO_2 TEA Amplifier."

I. J. Bigio, B. J. Feldman, R. A. Fisher, and E. E. Bergmann, "High Efficiency Phase-Conjugate Reflection in Germanium and in Inverted CO_2."

E. J. McLellan, "A Reinjection CO_2 Oscillator."

The following presentations were made at the Electro-Optics Laser '78 Conference, Boston, Massachusetts, September 19-21, 1978.

E. J. McLellan and S. C. Stotlar, "Sub-One-hundred-ps Pyroelectric Detector Research and Evaluation Program at LASL."

R. A. Fisher, E. E. Bergmann, B. J. Feldman, and I. J. Bigio, "Phase-Conjugate Reflection at 10.6 μm via Degenerate 4-Wave Mixing in Germanium."

K. C. Jones, J. L. Munroe, W. H. Reichelt, and J. E. Sollid, "Antares CO_2 Laser System, Optics and Components."

The following presentations were made at the Twentieth Annual Meeting of the Division of Plasma Physics of the American Physical Society, Colorado Springs, Colorado, October 30—November 3, 1978.

C. W. Cranfill and R. Moore (H-Division, LLL, California), "IONEOS: A Fast, Analytic, Ion-Equation of State Routine."

S. J. Gitomer and R. J. Mason, "A New CO_2 Laser Target with Burnthrough Shields,"

A. J. Scannapieco and H. Brysk, "Symmetry of Energy Deposition by a Multibeam Laser System."

S. J. Gitomer, "Spectral Analysis Techniques Applied to Subnanosecond Laser."

R. A. Kopp, "High Compression Ablative Targets for the Helios Laser System."

R. J. Mason, "Laser Generated Hot Electron Transport in Self-Consistent E and B Fields."

A. J. Scannapieco, "Illumination and Energy Deposition in a Multi-Beam Laser-Fusion System."

A. J. Scannapieco and K. A. Taggart, "Stability of Laser Fusion Targets."

W. S. Varnum and E. L. Lindman, "Antares Design Concepts II."

The following presentations were made at the ANS 1978 Winter Meeting, Washington, DC, November 12-17, 1978.

J. J. Devaney and L. A. Booth, "Laser-Fusion Pellet Injection Accuracies, Accelerations and Deflections."

I. O. Bohachevsky, D. O. Dickman, and J. C. Goldstein, "A New Plasma Model for the ICF Magnetic Wall Reactor Cavity Concept."

J. H. Pendergrass and C. E. Cort, "Lithium Boiler High-Temperature Fusion Reactor Blanket Concept."

In addition, the following presentations were made at various institutions.

R. K. Ahrenkiel, "A New Saturable Absorber for the CO_2 Laser Using Doped KCl," Seminar, University of Rochester, August 21-22, 1978.

J. H. Birely, J. L. Lyman, G. Quigley, R. A. Fisher, and B. J. Feldman, "Multiple Photon Absorption Measurements," National Conference on Nonlinear Optics and Lasers, Lenigrad, USSR, July 1978.

R. A. Fisher, B. J. Feldman, I. J. Bigio, and E. E. Bergmann, "Infrared Wavefront Reversal in Germanium," National Conference on Nonlinear Optics and Lasers, Leningrad, USSR, July 1978.

B. J. Feldman, R. A. Fisher, E. E. Bergmann, and I. J. Bigio, "Infrared Phase Conjugation," Massachusetts Institute of Technology, July 1978.

R. A. Fisher, B. J. Feldman, "Infrared Phase Conjugation," Seminar, Sandia Laboratories, Albuquerque, July 1978.

R. A. Fisher and B. J. Feldman, "10-μm Photoplasma Formation in Germanium," Seminar, Sandia Laboratories, Albuquerque, July 1978.

R. A. Fisher, B. J. Feldman, I. J. Bigio, and E. E. Bergmann, "Infrared Phase Conjugation Via 4-Wave Mixing in Germanium," Seminar, Physics Department, University of California, Berkeley, November 1, 1978.

B. J. Feldman, R. A. Fisher, I. J. Bigio, and E. E. Bergmann, "Infrared Phase Conjugation," Seminar, Lawrence Livermore Laboratory, November 3, 1978.

R. A. Fisher, B. J. Feldman, I. J. Bigio, and E. E. Bergmann, "Phase-Conjugate Optics in the Infrared," Seminar, Stanford University, Palo Alto, California, November 5, 1978.

R. A. Fisher, E. E. Bergmann, B. J. Feldman, and I. O. Bigio, "Phase Conjugation: the Wave of the Future," Seminar, Physics Department, Lehigh University, Bethlehem, Pennsylvania, October 18, 1978.

B. J. Feldman, R. A. Fisher, E. E. Bergmann, and I. J. Bigio, "Infrared Phase Conjugation," Seminar, Stanford Research Institute, Menlo Park, California, October 27, 1978.

R. A. Fisher, B. J. Feldman, E. E. Bergmann, and I. J. Bigio, "Infrared Phase Conjugation," Seminar, Optical Sciences Center, University of Arizona, October 17, 1978.

B. J. Feldman, R. A. Fisher, I. J. Bigio, and E. E. Bergmann, "Wavefront Reversal in Nonlinear Optics," Seminar, Westinghouse Research Laboratories, Pittsburgh, Pennsylvania, October 16, 1978.

J. P. Hong, "Experiments in Minimum Length Representation of Text," Third Berkeley Workshop on Distributed Data Management and Computer Networks, Berkeley, California, August 29-31, 1978.

J. P. Hong and S. Johnson, "Minimum Length Representation of Text," Seventeenth IEEE Computer Society International Conference (COMPCON 78), Washington, DC, September 5-8, 1978.

W. H. Reichelt, "Damage Considerations in Short Pulse CO_2 Laser Systems," 10th Annual Symposium on Optical Materials for High-Power Lasers, Boulder, Colorado, September 12-14, 1978.

R. Williamson, "A 60-Inch Annular Pitch Polisher for LASL's Laser Fusion Effort," Abstract of talk given at Optical Society of America Optical Fabrication and Testing Workshop, Dallas, Texas, November 1-10, 1978.

T. F. Stratton, "Antares Overview," Los Alamos Chapter of the Laser Institute of America, Los Alamos, New Mexico, November 14, 1978.

A. T. Lowe and C. D. Hosford, "Magnetron Sputter Coating of Microspherical Substrates," National American Vacuum Society Meeting, San Francisco, California, November 27—December 1, 1978.

I. O. Bohachevsky, "Elements to be Considered in Planning Heavy Ion Fusion Program—A Summary," Proc. Heavy Ion Fusion Workshop, Argonne National Laboratory, September 19-26, 1978.

E. E. Stark, "CO_2-Laser Fusion," Thirteenth Intersociety Energy Conversion Engineering Conf., San Diego, California, August 20-25, 1978.

T. G. Frank and L. A. Booth, "Commercial Applications of Thermionic Conversion Using a Fusion Reactor Energy Source—A Preliminary Assessment," Thirteenth Intersociety Energy Conversion Engineering Conf., San Diego, California, August 20-25, 1978.

A. R. Larson and C. D. Cantrell, "An Application of Nonequilibrium Quantum Statistical Mechanics to Homogeneous Nucleation," 11th International Symposium on Rarefied Gas Dynamics, Cannes, July 3-8, 1978.

C. R. Phipps and S. J. Thomas, "10-μm Photoplasma Formation in Germanium," Seminar, Sandia Laboratories, Albuquerque, July 1978.

☆U.S. GOVERNMENT PRINTING OFFICE: 1980—777-069/10